THE SPATIAL EXTENT AND CORRELATIONS OF QSO ABSORBERS

by

Nadine Dinshaw

A Dissertation Submitted to the Faculty of the

DEPARTMENT OF ASTRONOMY

In Partial Fulfillment of the Requirements
For the Degree of

DOCTOR OF PHILOSOPHY

In the Graduate College

THE UNIVERSITY OF ARIZONA

1 9 9 6

INFORMATION TO USERS

THE SPATIAL EXTENT AND CORRELATIONS OF QSO ABSORBERS

by

Nadine Dinshaw

A Dissertation Submitted to the Faculty of the

DEPARTMENT OF ASTRONOMY

In Partial Fulfillment of the Requirements
For the Degree of

DOCTOR OF PHILOSOPHY

In the Graduate College

THE UNIVERSITY OF ARIZONA

1 9 9 6

UMI Number: 9713430

UMI
300 North Zeeb Road
Ann Arbor, MI 48103

THE UNIVERSITY OF ARIZONA ®
GRADUATE COLLEGE

As members of the Final Examination Committee, we certify that we have

read the dissertation prepared by Nadine Dinshaw

entitled The Spatial Extent and Correlations of QSO Absorbers

and recommend that it be accepted as fulfilling the dissertation

requirement for the Degree of Doctor of Philosophy

30 Jul, 1996
Date

7/30/96
Date

7/30/96
Date

7/30/96
Date

Date

Final approval and acceptance of this dissertation is contingent upon
the candidate's submission of the final copy of the dissertation to the
Graduate College.

I hereby certify that I have read this dissertation prepared under my
direction and recommend that it be accepted as fulfilling the dissertation
requirement.

Dissertation Director

7/30/96
Date

STATEMENT BY AUTHOR

This dissertation has been submitted in partial fulfillment of requirements for an advanced degree at The University of Arizona and is deposited in the University Library to be made available to borrowers under rules of the Library.

Brief quotations from this dissertation are allowable without special permission, provided that accurate acknowledgment of source is made. Requests for permission for extended quotation from or reproduction of this manuscript in whole or in part may be granted by the head of the major department or the Dean of the Graduate College when in his or her judgment the proposed use of the material is in the interests of scholarship. In all other instances, however, permission must be obtained from the author.

SIGNED: _____

ACKNOWLEDGMENTS

TABLE OF CONTENTS

List of Figures

LIST OF TABLES

ABSTRACT

The lines of sight to QSOs are powerful probes of large-scale structure from redshifts corresponding to the most distant QSOs to the local universe. In this thesis, spectroscopy of QSO pairs and groups are used to study superclustering at high redshift and to estimate the tranverse dimensions of the Lyα absorbers.

We present high resolution (~ 30km s^{-1}) echelle spectra obtained with the CTIO 4-m telescope of the wide QSO pair Tol 1037–2704 ($z_{em} = 2.193$) and Tol 1038–2712 ($z_{em} = 2.331$), as well as two neighboring quasars. The quasars exhibit a large number of apparently correlated C IV absorption systems over a narrow redshift range $1.48 \leq z \leq 2.15$ which is thought to be produced by an intervening supercluster. The velocity correlation function of C IV absorbers distributed among the four lines of sight show significant clustering signal on comoving scales out to $\sim 30\,h^{-1}$ Mpc at redshift $z \sim 2$ ($h \equiv H_0/100$ km s^{-1} Mpc^{-1}; $q_0 = 0.5$). The spatial correlation function shows a marginally significant peak on scales of $< 18\,h^{-1}$ Mpc. The clustering amplitude on these scales is larger than that predicted by current theories of the formation of large scale structure.

We present spectroscopy of three close pairs of quasars with angular separations $10''$ to $2'$ in order to measure the sizes of the Lyα forest absorbers from scales of a few tens of kpc out to hundreds of kpc. Ground-based estimates of the pair Q1343+2640A ($z_{em} = 2.029$) and B ($z_{em} = 2.031$) imply a characteristic radius of the Lyα absorbers of $\sim 100\,h^{-1}$ kpc at $z \simeq 2$. Ultraviolet FOS spectra of the pair Q0107–025A ($z_{em} = 0.956$) and B ($z_{em} = 0.952$) in the redshift range $0.5 < z < 0.9$ show a number of Lyα absorption features common to both spectra as well as several features which are not in common, and imply characteristic radii of $400\,h^{-1}$ kpc to bigger than $1\,h^{-1}$ Mpc. Furthermore, the rms velocity difference between the common systems between the two lines of sight is only about 100 km s^{-1}. These measurements lead to a picture of absorbing clouds that are larger in extent than previously thought and surprisingly quiescent. Using a new statistical

technique, we tested the relative likelihood of three geometric models, namely, spherical absorbers, with and without a distribution in size, as well as filamentary and disk-like absorbers. Spherical absorbers with uniform radius cannot represent the observations and are ruled out. Randomly-inclined disks and filaments match the data comparably, with disks being slightly favored over filaments. Our results are in remarkable agreement with hydrodynamical simulations in which the Lyα absorption is found to arise in diverse structures with coherence lengths as great as 1 Mpc. Finally, we present FOS observations of a second pair of quasars, LB 9605 ($z_{em} = 1.834$) and LB 9612 ($z_{em} = 1.898$), over the redshift range $1.1 < z < 1.7$ from which we placed an 95% confidence *upper* limit on the radii of the Lyα absorbers of $280\,h^{-1}$ kpc. The estimates span the redshift range $0.5 < z < 2$, corresponding to roughly a third of the age of the universe, and provide tantalizing evidence for evolutionary growth in the size of the Lyα absorbers.

CHAPTER 1

INTRODUCTION

1.1 Motivation

Most of our understanding of the universe has come from observations of our Galaxy and other nearby galaxies. With the discovery of QSOs three decades ago, it has become possible to study the universe beyond our local neighborhood. As the light emitted from a distant QSO traverses the universe, the gas at each intervening epoch along the line of sight to the QSO leaves a characteristic imprint in the spectrum of the light that reaches us. This imprint appears in the form of discrete absorption features, which contain important information about the distribution and composition of the gas at different cosmic times that cannot be obtained in any other way. The most distant QSOs are observed to redshifts $z \simeq 5$, allowing us to trace the properties of the gas from the time when the universe was just 10% of its current age to the present.

QSO absorption lines are broadly classified according to their column density, metallicity and clustering properties. Two types of QSO absorption lines that are thought to represent a class of cosmologically-distributed, intervening systems[1] are the heavy element and Lyman-α (Lyα) forest systems. Because they share many of the properties of galaxies in the local neighborhood, it has long been thought that the heavy element systems arise

---

[1] That is, they do not arise from material ejected or physically associated with the QSO.

in the halos of normal galaxies. The most compelling evidence has come from direct optical imaging of the intervening galaxies responsible for the absorption. The relationship between the Lyα absorbers and galaxies is much less certain. Because they appeared to be randomly distributed along the lines of sight to QSOs and relatively free of metals, the Lyα systems have traditionally been thought to arise in the more pristine environment of intergalactic space. Thus, the heavy element and Lyα absorption systems provide an unique opportunity to learn about the physical conditions in two possibly very different environments. From the heavy element systems, we can study the distribution and kinematics of the gas in galaxies and their precursors at different evolutionary stages, as well as the clustering properties of the galaxies which have implications for large-scale structure. On the other hand, from the Lyα systems, we can learn about the distribution of and physical conditions in unprocessed, primordial material belonging to the intergalactic medium. The QSO absorption lines are not only important for the understanding of the nature of the absorbing clouds, but also provide clues about the development of large-scale structure in the universe over a substantial interval of cosmic time.

1.2 QSO Absorption Line Systems

1.2.1 The Heavy Element Absorption Systems

1.2.1.1 Properties of the Heavy Element Systems

The heavy element systems include the metal-line absorption systems, the damped Lyα systems (DLA), and the Lyman limit systems (LLS).[2] Each has a characteristic spectral signature that makes it easily identifiable in QSO spectra. The DLA systems are indentified by prominent Lorentzian damping wings that broaden and dominate the Lyα line profile. By definition, these systems refer to objects with $N(\mathrm{H\,I}) \geq 3 \times 10^{20}$ cm^{-2}, comparable to the column densities in the disks of present-day spiral galaxies (Wolfe et $al.$

---

[2]The LLS and DLA systems almost always show associated metal lines and therefore have been classified with the heavy element absorption systems.

1986; Lanzetta *et al.* 1991). The LLSs indicate systems with $N(\text{H\,I}) > 2 \times 10^{17}$ cm^{-2}, which make them just optically thick in the Lyman H I continuum. The signature of the LLS is an unmistakable discontinuity in the QSO continuum at 912 Å in the rest frame of the absorber. An optical depth of unity is also required to have appreciable absorption of Mg II (Bergeron & Stasinka 1986; Steidel & Sargent 1992), which is thought to arise in the same population of absorbers as the LLS. The absorption systems with the largest cross section are the C IV systems, which exhibit a large range in H I column density from $N(\text{H\,I}) = 10^{15.5}$ to $\gtrsim 10^{21}$ cm^{-2}. The metal-line systems are usually detected by the presence of the strong resonance-line doublets of C IV $\lambda\lambda$1548, 1550 or Mg II $\lambda\lambda$2796, 2800. The absorption features are relatively strong which mades them easy to detect, even in moderate resolution and low signal-to-noise data.

There is considerable evidence that the heavy element systems are associated with galaxies. Just the presence of elements heavier than H and He indicates that the lines originate in systems where some nucleosynthetic processing of the gas must have occurred. It is clear from statistical analyses of large unbiased samples of heavy-element absorption systems, whether selected by H I, C IV, or Mg II, that the absorbers are consistent with a cosmological distribution. This is expected if the absorption arises in intervening galaxies, as opposed to gas somehow associated with the QSO itself. The C IV absorbers appear to cluster on the same scale and with the same amplitude as the luminous galaxies in the local universe. The two-point correlation function of C IV absorption systems shows significant clustering of the absorbers on velocity scales of $\Delta v \leq 1000$ km s^{-1}, similar to the scales on which galaxies cluster (Sargent *et al.* 1988a; Heisler, Hogan & White 1989). On smaller scales ($\Delta v \leq 300$ km s^{-1}), structure is almost always observed in the absorption systems at high resolution. The velocity spread in the absorption features is similar to the typical velocity dispersion of galaxies, which tends to support the interpretation that the absorption systems arise in the extended halos of intervening galaxies.

The most compelling evidence for the connection between metal-line absorption sytems

and normal galaxies is the direct identification of the galaxies responsible for Mg II absorption (Bergeron & Boisse 1991; Steidel & Dickinson 1992; see Steidel 1993 for a review), which is observable from the ground over the redshift range $0.2 < z < 2$. The observations involve looking for a galaxy near the QSO line of sight having the same redshift as the Mg II absorption system. Steidel and his coworkers were able to identify a candidate or confirmed absorbing galaxy in every case examined (Steidel 1993). The identified galaxies have optical-infrared colors consistent with mid- to late-type spiral galaxies, exhibiting modest evolution in luminosity since $z \simeq 0.9$. Their sample shows a significant inverse correlation between impact parameter and luminosity of the galaxy, consistent with the interpretation that the absorber responsible for the Mg II absorption is indeed the identified galaxy. If the absorption were instead produced by a nearby unseen dwarf of low surface brightness galaxy, such a correlation would *not* be expected. The impact parameter, or projected distance from the QSO line of sight to the center of the absorbing galaxy, is typically $\sim 30\,h^{-1}$ kpc ($q_0 = 0$). The implication of these results is that selection by Mg II absorption picks out a population of ordinary bright galaxies.

1.2.1.2 Clustering of the Heavy Element Systems

The formation and growth of large scale structure in the universe provide an important discriminant between cosmological models. Already, the existence of coherent structures on scales of $\sim 50\,h^{-1}$ Mpc in the local neighborhood presents a significant challenge to the cold dark matter (CDM) model for the formation of structure (*e.g.*, Loveday *et al.* 1992). The traditional method of investigating structure in the local universe has been to map the three-dimensional spatial distribution of thousands of galaxies to some limiting magnitude (*e.g.*, de Lapparent *et al.* 1986; da Costa *et al.* 1988; see Giovanelli & Haynes 1991 for a review). These studies rely on extensive surveys of thousands of galaxy redshifts that cover large volumes and scales. The surveys have revealed remarkable structure in the galaxy distribution in our local neighborhood. Many of the galaxies are distributed

in filamentary structures and thin sheets, their extents limited only by the size of the survey. The largest sheet detected so far is the "Great Wall", having a minumum area of at least $60 \times 170\,h^{-2}$ Mpc^2 and thickness of only $2\,h^{-1}$ Mpc. The sheets surround large underdense regions, known as voids, which appear empty of bright galaxies. The voids have typical densities of 20% of the mean, and diameters of $\sim 50\,h^{-1}$ Mpc.

The statistical tool used to quantitatively describe the amplitude and scale of this clustering is the two-point correlation function (Peebles 1980). The spatial correlation function[3] $\xi(r)$ is defined by the probability $dP(r)$ of finding an objects a distance r and within volume element dV from another object such that

$$dP(r) = n\left[1 + \xi(r)\right]dV \tag{1.1}$$

where n is the space density of objects in the sample. In other words, the correlation function measures the density of objects *above* that expected from a random distribution. Therefore, $\xi(r) = 0$ for a random distribution of objects, and $\xi(r) > 0$ for clustered objects. The present-day correlation function of galaxies shows strong clustering out to scales of $\lesssim 20\,h^{-1}$ Mpc. That of rich clusters of galaxies reveals order of magnitude stronger correlations out to at least $\sim 100\,h^{-1}$ Mpc (Bahcall 1988).

A limitation of the galaxy surveys comes from the fact that it is extremely difficult to define a sample of normal galaxies at high redshifts. Pencil beam surveys extending to the faintest possible limits, $m_B = 24$, have not yielded galaxies with redshifts above $z > 1$. For this reason, it has been necessary to find alternative techniques for studying large scale structure at $z > 1$. The most promising way of extending the selection of galaxies to higher redshifts is to use the C IV $\lambda\lambda 1548$, 1550 doublet, observed in absorption from the ground over the redshift interval $1.2 < z < 4$. Like the Mg II doublet, the C IV absorption systems are also thought to trace the halos of normal luminous galaxies.

---

[3]We can similarly define angular and velocity correlation functions which measure the level and extent of clustering on angular and velocity scales.

There is considerable evidence for superclustering of the C IV absorbers. Heisler *et al.* (1989) found significant clustering out to velocities of $\Delta v = 10,000$ km s^{-1} in a large sample of C IV systems detected along the line of sight to 55 QSOs (Sargent, Boksenberg & Steidel (1988). The clustering signal is dominated by a single supercluster along the line of sight to the QSO PKS 0237−233, which shows a large overdensity of absorbers at $z \simeq 1.65$ (Heisler *et al.* 1989). The QSO pair Tol 1037−2704 and Tol 1038−2712 similarly shows a highly significant overdensity of absorbers on scales of $20 - 40\,h^{-1}$ Mpc (Jakobsen & Perryman 1992; Sargent & Steidel 1987; Dinshaw & Impey 1996). Another promising strategy has been to define a grid of background QSOs to be used as probes of the three-dimensional distribution of matter (Foltz *et al.* 1993; Williger *et al.* 1996). In one such study, 25 QSOs near the South Galactic Pole were used to map out two absorbing structures with dimensions $13 \times 5 \times 21\,h^{-3}$ Mpc^3 and $7 \times 1 \times 15\,h^{-3}$ Mpc^3 at $z \sim 2.5$ (Williger *et al.* 1996). Coherent structures on supercluster scales form late in the hierarchical models of structure formation (Evrard, Summers & Davis 1994). Therefore, studies of large scale structure at high redshift are important for understanding the formation and evolution of structure in the universe.

1.2.2 The Lyman Alpha Forest

1.2.2.1 Properties of the Lyman Alpha Forest

By far the most common QSO absorption lines are the Lyα forest systems, which are thought to arise in intervening hydrogen clouds. Every $z \geq 3$ QSO line of sight intersects of the order of 1000 Lyα absorbers with neutral hydrogen column densities ranging from $N(\mathrm{H\,I}) \simeq 10^{16}$ cm^{-2} down to the current detection limit (Tytler *et al.* 1995). The Lyα forest systems have historically been differentiated from the heavy element systems by their apparent lack of metals. Their Doppler widths lie in the range $b \simeq 10 - 60$ km s^{-1}, implying absorber temperatures of $T \simeq 40,000$ K, assuming the widths can be attributed entirely to thermal broadening. Their numbers fall off at higher column densities according

to the power law $dn/dN \propto N^{-\beta}$ with $\beta \sim 1.7$ (Carswell *et al.* 1984). On scales greater than 300 km s^{-1}, the high-redshift absorbers are not significantly clustered (Sargent *et al.* 1980; Bechtold 1987). The lack of associated metal lines and spatial structure in the Lyα forest was originally interpreted to imply that the Lyα absorbers constitute a distinct population of *intergalactic* absorbers, independent of galaxies. The distinction between the Lyα and heavy element systems has been called into question in light of recent results from the *Hubble Space Telescope* (*HST*) and HIRES on the Keck 10-m Telescope. High signal-to-noise echelle spectra indicate that the high column density $[N(\mathrm{H\,I}) \gtrsim 10^{14} \, \mathrm{cm}^{-2}]$ systems have significant metal enrichment (Tytler *et al.* 1995; Cowie *et al.* 1996) and are weakly clustered in velocity space (Chernomordick 1995; Christiani *et al.* 1995). At low redshift, there is increasing evidence that the Lyα lines are somehow asssociated with galaxies (Morris *et al.* 1993; Bahcall *et al.* 1993; Lanzetta *et al.* 1995).

Evidence for weak clustering in the Lyα forest was first detected by Webb (1987) on scales less than 300 km s^{-1}, using 0.2 Å resolution data. Recently, Chernomordick (1995) and Christiani *et al.* (1995) have provided some of the strongest evidence for clustering of the Lyα absorbers at high redshift. On scales less than $\Delta v = 350$ km s^{-1}, Christiani *et al.* found $\xi \simeq 0.89 \pm 0.18$ above a limiting column density $N(\mathrm{H\,I}) = 10^{13.8}$ cm^{-2}. Using neighbor counts to compute the correlations for published Lyα samples, Meiksin & Bouchet (1995) found evidence for clustering with similar amplitudes on scales of 100 − 600 km s^{-1}. Although the correlation signal is less pronounced than those found for the metal-line absorption systems and in galaxy surveys, it nevertheless suggests an origin for the Lyα systems from gravitational instabilities. These instabilities are expected to grow with time, resulting in stronger correlations among the low-redshift systems. Strong clustering has been detected in the Key Project catalog of Lyα systems with $0 < z < 1.3$ by Ulmer (1996) on scales of 250 − 500 km s^{-1} (see also Srianand 1996). Furthermore, some studies have found that the strength of the clustering depends on the column density of the lines, as expected in models involving biasing for the formation of structure, since

objects formed at sites with larger potential wells should be more highly correlated (Webb & Barcons 1991).

The existence of a distinct population of Lyα systems depends, by definition, on the metallicity of the absorbers. Detailed abundance determinations are difficult given the typical column densities of the absorbers. For column densities $< 10^{14}$ cm^{-2} and assuming that the gas is highly ionized (n_{HI}/n_H), the detection of metal abundances below about a tenth of the solar metallicity has not been possible until recently because of the limited sensitivity of prior spectrographs. Using HIRES on the W. M. Keck 10-m Telescope, Tytler *et al.* (1995) has reported the detection of C IV absorption in 60% of the Lyα forest systems with N(H I) $> 10^{14.5}$ cm^{-2} at $z \simeq 3$. He also found that 50% of the clouds have [C/H] > -2.5. This result has been confirmed by Cowie *et al.* (1995), who also reported that from the structure of the C IV systems, the Lyα absorbers appear to be comprised of cloudlets with temperatures of $\sim 35,000$ K, and line-of-sight velocity dispersions of ~ 18 km s^{-1}. These results do not necessarily preclude the existence of a population of Lyα absorbers with primordial composition. However, Songalia *et al.* (1996), also using Keck data, have shown that 90% of absorbers with N(H I) $> 10^{15.2}$ cm^{-2} and 75% of those with N(H I) $> 10^{14.5}$ cm^{-2} have associated C IV, consistent with a uniform distribution of [C/H] as a function of N(H I). If, as this result suggests, all the Lyα absorbers contain metals, Tytler *et al.* (1995) have proposed that the Lyα absorbers may have been contaminated by population III stars that formed in the intergalactic medium prior to the formation of galaxies.

Studies of the Lyα absorbers at redshifts below $z = 1.6$, corresponding to the atmospheric ultraviolet cutoff, have become possible with the successful launch of *HST*. One of the first results was the discovery of a larger number of Lyα systems in the spectrum of 3C 273 than expected from a simple extrapolation of the number density of systems (per unit redshift) derived for the high redshift systems (Morris *et al.* 1991). The number density of Lyα absorbers as a function of redshift is usually parameterized as $dN/dz \propto (1+z)^\gamma$,

where evolution in the absorbers is indicated by departures from the no-evolution value of $\gamma = 0.5$ for $q_0 = 0.5$. The results at $z < 1.3$ were derived using only 10% of the data obtained for the *HST* QSO Absorption Line Key Project whose goal is to obtain a large and homogeneous catalog of Lyα absorbers (see Bahcall *et al.* 1996, and papers therein for details of the Key Project). The Key Project found $\gamma = 0.48 \pm 0.50$, consistent with no evolution in the redshift interval $0 < z < 1$. At higher redshifts, the evidence points to rapid number density evolution, although the precise nature of the evolution has not yet been determined. In the redshift interval $1.5 < z < 4$, Lu, Wolfe & Turnshek (1991) derived a value of $\gamma = 2.68 \pm 0.27$, whereas Bechtold (1994) found $\gamma = 1.89 \pm 0.28$ from a homogeneous sample with rest equivalent width greater than 0.32 Å. The slope of the low redshift dN/dz relation differs at the $2 - 4.5\sigma$ level of significance from the slope obtained from ground-based samples (Jannuzi 1996).

The relation between the low redshift Lyα absorbers and individual galaxies, groups or clusters has also been studied using *HST* (Morris *et al.* 1991, 1993; Bahcall *et al.* 1991, 1993; Lanzetta *et al.* 1995; Stocke *et al.* 1995; Le Brun *et al.* 1995; Bowen *et al.* 1996). So far the results are conflicting. Morris *et al.* (1993) concentrated on the 10 Lyα systems detected along the line of sight to 3C 273 out to a redshift of $z = 0.15$. They found that the Lyα absorbers are not distributed at random with respect to galaxies, nor are they clustered as strongly as galaxies. Their results were consistent with only 20% of the Lyα absorbers being associated with normal galaxies (Mo & Morris 1995). On the other hand, Lanzetta *et al.* (1995) reported that at least 32%, and perhaps as many as 60%, of the Lyα absorption systems out of a total sample of 23 systems detected in 6 different fields arise in the extended envelopes of bright galaxies. From their observations, they estimated the impact parameter for producing Lyα absorption to be $\lesssim 160\,h^{-1}$ kpc. From a sample of 8 Lyα lines, Stocke *et al.* (1995) have found the Lyα absorbers to be associated with both large scale structures and voids in the galaxy distribution. More recently, Le Brun *et al.* (1996), in an experiment similar to Lanzetta *et al.*'s, found no anti-correlation

between Lyα equivalent width and impact parameter for their entire sample of absorber-galaxy pairs and only marginally significant anti-correlations for a subsample of strong lines ($W_0 \geq 0.24$ Å). Moreover, they found no correlation between galaxy luminosity and impact parameter. They interpreted their results as indicating that the Lyα absorbers are not intimately connected with individual galaxies, but are distributed in the large scale structure of the galaxy distribution. Using a slightly different approach, Bowen, Blades & Pettini (1996) first identified galaxies within $40 - 500\,h^{-1}$ kpc ($q_0 = 0$) of the lines of sight to QSOs observed with the Faint Object Spectrograph on *HST*, then looked for corresponding Lyα absorption. With only a 25% success rate, they concluded that their results support the picture that the Lyα lines arise in the large-scale filaments or sheets which bridge and contain the galaxies.

Finally, there remains the question of different populations of Lyα absorbers, which has been invoked to explain the fact that some of the aborbers are metal enriched and others are not, the fact that some appear to be associated with galaxies whereas others are distributed in the voids, and the fact that the high redshift absorbers exhibit more rapid number density evolution than those at low redshift. One view holds that there are two populations of Lyα absorbers: a slowly evolving population that is intimately connected with normal galaxies, and a relatively unclustered, rapidly evolving population that dominates the number counts at high redshift. The other view holds that the observations can be described by a single population which exhibits a continuous distribution of properties between the low- and high-column density systems and the low- and high-redshift absorbers.

1.2.2.2 Models of the Lyman Alpha Absorbers

The origin and physical nature of the Lyα absorbers remain unknown. Various models have been proposed including pressure-confined clouds in an expanding intergalactic medium (Ikeuchi and Ostriker 1986), pressure-confined tidal debris built up in small

groups or clusters of galaxies (Morris & van den Bergh 1994), caustics produced by converging velocity flows (McGill 1990), and shocks associated with explosive galaxy formation (Lake 1988). The majority fall under two broad classes delineated by their confinement mechanism, *i.e.*, pressure and gravity. The original model of the absorbers envisioned them as intergalactic, spherical condensations confined by the pressure of a hot, external intergalactic medium (Sargent *et al.* 1980). Further details of this model were explored by Ostriker & Ikeuchi (1983) and Ikeuchi & Ostriker (1986). In order for the clouds to exist in hydrostatic equilibrium, the product of the temperature and density of clouds is in balance with the external pressure. The radius of a cloud with typical column density 10^{14} cm^{-2} can be expressed as (Ikeuchi & Ostriker 1986)

$$R = 24\,h^{-1}\ \text{kpc}\ \left(\frac{N_{\text{H\,\textsc{i}}}}{10^{14}\,\text{cm}^{-2}}\right) T_{4.5}^{11/4}\ J_{-21}\left(\frac{P}{k}\right)^{-2} \tag{1.2}$$

where J_{-21} is the ionizing flux in units of 10^{-21} ergs cm^{-2} s^{-1} Hz^{-1}sr^{-1}, and $T_{4.5}$ is the temperature of the gas divided by 30,000 K. Major shortcomings of the pressure-confined model include: 1) it cannot account for the wide range in column densities, and 2) there is no obvious formation mechanism for the clouds.

In the cold dark matter model, the gas is stably confined by the gravitational field of dark matter "minihalos," which have sufficiently shallow potential to prevent collapse (Rees 1986; see also Miralda-Escudé & Rees 1993). The minihalos are postulated to form in regions of low background density in order to survive for a long time. This naturally accounts for the lack of correlations among Lyα clouds and also between galaxies and clouds. Taking the gas to be in hydrostatic equilibrium and at the same temperature as the dark matter, the impact parameter that produces a column density equal to 10^{14} cm^{-2} can be written as (Miralda-Escudé & Rees 1993)

$$R = 5\,h^{-1}\ \text{kpc}\ \left(\frac{N_{\text{H\,\textsc{i}}}}{10^{14}\,\text{cm}^{-2}}\right)^{-1/3} \left(\frac{b}{30\,\text{km}\,\text{s}^{-1}}\right)^{4/3} \left(\frac{f_g}{0.05}\right) \frac{T_{4.5}^{-1/4}}{J_{-21}^{1/3}} \tag{1.3}$$

where b is the Doppler width and f_b the fraction of mass in baryons to dark matter. An attractive feature of this model is that it naturally produces a wide range of column

densities. *Both models predict the characteristic radius of the absorbers to be of the order of tens of kpc.*

Recent simulations of the Lyα forest which include gravitational and hydrodynamical processes in a cold dark matter universe yield a more complex picture of the absorbers (Cen *et al.* 1995; Hernquist *et al.* 1995; Zhang *et al.* 1995; Miralda-Escudé *et al.* 1996). The high column density [N(H I) $\geq 10^{17}$ cm^{-2}] systems are produced in collapsed high density regions associated with forming galaxies. The Lyα forest systems are produced in the lower column density [N(H I) $\simeq 10^{13-15}$ cm^{-2}] regions resembling sheets and filaments, where the typical size of a filament is 1 Mpc long and 50 $-$ 100 kpc thick (Miralda-Escudé *et al.* 1996), and some Lyα absorbers are found in the voids. The structures giving rise to low column density lines are physically diverse: either filaments of warm gas that traces the dark matter distribution; caustics produced by converging velocity flows; or sheets of cool gas compressed between shocks (Hernquist *et al.* 1995). Because of their low overdensities, the low column density systems are not in dynamical equilibrium, and many are still expanding at some fraction of the Hubble flow implying that their physical densities and neutral fractions decrease with time. In general, the simulations reproduce the properties (*e.g.*, N(H I) and *b*-parameter distributions) of the Lyα forest remarkably well, though detailed comparisons have yet to be made.

1.2.2.3 Observational Constraints on the Lyα Absorber Size

Two fundamental properties of the absorbers that are needed for a full understanding of the nature and origin of the Lyα absorption are the size and internal kinematics of the clouds. Paired lines of sight towards gravitationally-lensed QSOs and physical pairs of QSOs provide a powerful diagnostic of cloud sizes and kinematics as derived from the number of Lyα systems observed to be in common between the two lines of sight and the velocity difference between the common systems. Early observations of paired QSOs established rather uninteresting *upper* limits ranging anywhere from 0.5 $-$ 1 h^{-1} Mpc at

$z \simeq 2$ (Shaver & Robertson 1983; Crotts 1989). Foltz *et al.* (1984) used the occurrence of common Lyα absorption in the components of the gravitational lens 2345+007A,B to set *lower* limits on the cloud diameters of between 10 − 50 kpc. This measurement is extremely uncertain since the lens has never been identified, and some question the lens nature of this object (Steidel & Sargent 1991). In the 10 years since those observations were made, the only significant improvement in our understanding of the cloud sizes is the work of Smette *et al.* (1992) who looked for common absorption in the two lines-of-sight to the gravitationally-lensed QSO UM 673 A,B. Smette *et al.* counted 62 coincident and two anticoincident absorption features in the redshift range $2.1 < z < 2.7$. The two anticoincident lines have a velocity separation close to that of the Mg II resonance doublet, and because of uncertainties in the wavelength calibration, such an identification could not be ruled out. In view of recent estimates of absorber size, it appears more likely that they are due to Mg II. Therefore, one can only deduce that the clouds are bigger than $8\,h^{-1}$ kpc. The most recent estimate based on the gravitationally-lensed QSO HE 1104−1805 (Smette *et al.* 1995) a gave similar result. In that case, 72 coincidences and no anticoincidences were found, implying a 2σ lower limit of the cloud radius of $25\,h^{-1}$ kpc for $q_0 = 0.5$, assuming a power-law relationship between column density and impact parameter.

1.3 Outline of this Thesis

In Chapter 2, we present high resolution ($30\,\mathrm{km\,s^{-1}}$) echelle spectra of the wide QSO pair Tol 1037−2704 and Tol 1038−2712, as well as two neighboring QSOs. We calculate the velocity and spatial correlation functions of the C IV absorbers distributed among the 4 lines of sight, and find significant correlation signal out to scales of $\sim 30\,h^{-1}$ Mpc ($h = H_0/100\,\mathrm{km\,s^{-1}}$ Mpc; $q_0 = 0.5$) at $z \simeq 2$. The clustering amplitude on these scales is larger than is predicted by current theories of the formation of large scale structure. The rest of the thesis presents new estimates of the sizes of the Lyα forest absorbers,

and some of the first evidence for very large absorbers. In Chapter 3, we present spectra obtained with the Multiple Mirror Telescope of the QSO pair 1343+2640A,B. Common absorption features of Lyα were found in the spectra of the pair suggesting cloud radii of at least $\sim 40\,h^{-1}$ kpc at $z \simeq 2$. Interpreted in terms of a simple-minded model for the absorbers, these studies suggested a characteristic radius of $\sim 100\,h^{-1}$ kpc at $z \simeq 2$. The most compelling evidence for large clouds comes from an ongoing program to measure the radius of Lyα clouds with the *HST*. In Chapter 4, we present preliminary results, and, in Chapter 5, a more detailed study of the QSO pair Q0107$-$025A,B. The FOS spectra of the pair in the redshift range $0.5 < z < 0.9$ imply characteristic radii of $400\,h^{-1}$ kpc to bigger than 1 Mpc, considerably larger than predicted by theoretical models. Furthermore, the rms velocity difference between the two lines of sight for the four strongest pairs of lines is only about 100 km s^{-1}. These measurements have yielded the unexpected result of large and surprisingly quiescent Lyα absorbing clouds. In Chapter 6, we present the observations of another QSO pair LB 9605, LB 9612 at intermediate redshift $1.1 < z < 1.7$ which provide tantalizing evidence for evolution in the radii of the Lyα clouds, with the radii increasing with cosmic time. Finally, in Chapter 7, we discuss some ongoing projects and consider possibilities for future work.

CHAPTER 2

TWO-POINT VELOCITY AND SPATIAL CORRELATION FUNCTIONS OF THE CIV ABSORPTION SYSTEMS TOWARD THE TOLOLO QSO GROUP: EVIDENCE FOR SUPERCLUSTERING AT $z \simeq 2$[1]

Nadine Dinshaw[2] and Chris D. Impey[2]

---

[2]Steward Observatory, University of Arizona, Tucson, AZ 85721

Abstract

The large number of apparently correlated C IV absorption systems observed in the lines of sight to the wide QSO pair Tol 1037−2704 (z_{em} = 2.193) and Tol 1038−2712 (z_{em} = 2.331) between the redshifts $1.88 \leq z_{abs} \leq 2.15$ is thought to be produced by an intervening supercluster. We present high resolution echelle spectra of Tol 1037−2704 and Tol 1038−2712, as well as two neighboring QSOs with the aim of searching for absorption associated with the putative supercluster. The lines of sight toward the original pair are separated by 17″9 corresponding to a proper separation of $D_{\perp} \simeq 4.4\,h^{-1}$ Mpc ($h = H_0/100$ km s^{-1} Mpc^{-1}; q_0 = 0.5) at $z = 2$. We confirm the existence of the C IV absorption complexes already reported, and find additional complexes. At a resolution of $\sim$ 30 km s^{-1} FWHM, many of the C IV complexes break up into multiple discrete components with a velocity spread of $\Delta v \simeq 50 - 1000$ km s^{-1}. This brings the total number of C IV absorption systems with secure identifications to 22 in Tol 1037−2704 and 11 in Tol 1038−2712 in the redshift range $1.48 \leq z_{abs} \leq 2.15$, well above the expectation from Poisson statistics. The two neighboring QSOs, Tol 1035−2737 (z_{em} = 2.159) and Tol 1029−2654 (z_{em} = 2.586), are located roughly 40′ ($D_{\perp} \simeq 10\,h^{-1}$ Mpc) southwest and 115′ ($D_{\perp} \simeq 30\,h^{-1}$ Mpc) northwest of the Tololo pair, respectively. We found five C IV systems in the line of sight to Tol 1035−2737, and six toward Tol 1029−2654. Most of these systems appear to match systems in the original QSO pair within a velocity separation of less than 5000 km s^{-1}, though the significance of the matches is not strong. We find a marginal excess of C IV absorption systems in the line of sight to Tol 1029−2654, whereas the number of systems in the line of sight to Tol 1035−2737 agrees with expectation. The inferred proper dimensions of the proposed supercluster are at least $30\,h^{-1}$ Mpc on the plane of the sky and

approximately $80\,h^{-1}$ Mpc along the line of sight.

We examined the clustering properties of the absorbers toward the Tololo QSOs using the two-point velocity and spatial correlation functions. The velocity correlation function of the complete sample of 44 C IV systems shows strong clustering for velocity separations less than 1000 km s^{-1}, which probe clouds in galactic halos as well as individual galaxies in clusters, and significant clustering signal out to scales of 7000 km s^{-1}. In a subsample of 16 systems ($W_{\rm o} > 0.15$ Å) where the power associated with virialized clusters on scales less than 1000 km s^{-1} has been removed, significant correlation signal persists for velocity separations of $4000 - 7000$ km s^{-1}, which correspond to comoving spatial scales of $\sim 30 - 40\,h^{-1}$ Mpc. The spatial correlation function of the same subsample, derived by pairing absorbers between different lines of sight, shows a marginally significant peak on comoving scales of $< 18\,h^{-1}$ Mpc. The clustering amplitude on these scales is larger than predicted by current theories of the formation of large scale structure.

2.1 Introduction

The absorption lines of heavy elements observed in the spectra of QSOs are powerful probes of large-scale structure at high redshift. Since they appear to cluster in velocity space with an amplitude and scale similar to that expected from galaxy clustering (Sargent, Boksenberg & Steidel 1988; hereafter SBS), the absorbers responsible for the heavy element absorption lines are thought to be associated with galaxies or their precursors. Direct evidence for this association comes from recent identifications of the galaxies associated with the Mg II absorption systems (Bergeron & Boisse 1991; Steidel 1993). By analogy with the Mg II results, the C IV absorption systems, observable from the ground for redshifts $1.2 \lesssim z \lesssim 4$, are thought to define a sample of normal galaxies and provide the only means of studying these galaxies at high redshift since optical identifications at $z > 1$ are not yet feasible.

Recent evidence points to very large-scale superclustering of the C IV absorbers. Heisler, Hogan & White (1989; hereafter HHW) detected significant correlation signal in the two-point correlation function out to velocities of $\Delta v = 10,000$ km s^{-1} from the large sample of C IV systems in 55 QSOs published by SBS. The signal is dominated by a single large supercluster along the line of sight to the QSO PKS 0237−233, which shows a large (≥ 20) overdensity of C IV absorbers at $z \simeq 1.65$. In a followup survey for nearby QSOs to be used as background probes, Foltz et al. (1993) found an overdensity of C IV systems in the redshift range $1.57 \lesssim z \lesssim 1.69$ along the lines of sight to 6 QSOs, with most of the absorption seen toward two QSOs. Similarly, Francis & Hewett (1995) discovered two damped Lyα absorption systems at similar redshifts in the spectra of two high redshift QSOs ($z \simeq 3.2$) separated by a comoving distance of $\sim 18\,h^{-1}$ Mpc. Since high column density hydrogen absorbers are believed to be associated with the disks of spiral galaxies, this result suggests the presence of a large coherent structure at $z > 2$. Recent pencil-beam surveys suggest that galaxies cluster on very large scales with an apparent periodicity in their distribution on a characteristic scale of $128\,h^{-1}$ Mpc (Broadhurst et al.

1990), although the significance of the results has been disputed (Kaiser & Peacock 1991).

Another important example of superclustered absorption is observed along the lines of sight to the wide QSO pair Tol 1037−2704 ($z_{em} = 2.193$) and Tol 1038−2712 ($z_{em} = 2.331$), whose spectra exhibit a number of apparently correlated C IV absorption systems (Jakobsen *et al.* 1986; Sargent & Steidel 1987; hereafter J86 and S87). The spectra of the QSOs each exhibit at least five C IV complexes over the narrow redshift range $1.88 \lesssim z \lesssim 2.15$, representing a highly significant overdensity in the number of absorbers above that expected from Poisson statistics. One complex lies at the same redshift in both QSOs and the rest are coincident to within $v \leq 2000$ km s^{-1}. The QSOs have an angular separation of $17\rlap{.}'9$, corresponding to a proper separation on the sky of $4.4\,h^{-1}$ Mpc.

The favored hypothesis for the overdensity of C IV absorption systems is that the two lines of sight intersect material associated with an intervening supercluster (J86; S87). The matter is arranged in a filamentary or sheet-like structure with comoving dimensions of $\sim$ 50 Mpc along the line of sight and $\sim$ 10 Mpc in the plane of the sky, with the implication that we are viewing it from a special direction along the filament (S88; Jakobsen & Perryman 1992, hereafter J92). Such dimensions are consistent with the sizes of superclusters observed in the local universe. Many of the absorption complexes are split into narrower components spanning the velocity range $\Delta v \simeq 50 - 1000$ km s^{-1}. Velocity separations greater than 300 km s^{-1} are probably not due to cloud motions within galaxies but are consistent with the hypothesis that some of the components arise from the halos of individual galaxies in a cluster (S87). In this scenario, the more complex systems arise from the denser central region of a cluster and the single component systems are produced in the less dense outer region.

Although a plausible picture of the absorption being due to an intervening supercluster is emerging, this interpretation is not universally accepted (Christiani, Danziger & Shaver 1987; Robertson 1987). The supercluster hypothesis is complicated by the fact that both Tol 1037−2704 and Tol 1038−2712 display broad absorption line (BAL) char-

acteristics, which are generally thought to have an intrinsic origin, *e.g.* ejection or outflow of material from the QSO (Weymann, Carswell & Smith 1981). S87 have presented physical arguments against ejection based on the energetics required to accelerate material to such great distances that it would be seen along both lines of sight, as well as statistical objections to the hypothesis that the lines could be due to independent ejections from both QSOs.

One recent line of study has been to locate other QSOs in the field surrounding the pair which are bright enough and at high enough redshifts to use as background probes of the hypothetical supercluster (S87; Jakobsen, Perryman & Christiani 1988, hereafter J88; J92). So far, this approach has met with modest success. One nearby QSO, Tol 1038−2707 ($z_{\rm em} = 1.937$) which is 5′ from Tol 1038−2712 shows a strong absorption system with redshift close to the C IV system near $z_{\rm abs} = 1.90$ in both Tol 1037−2704 and Tol 1038−2712 (J88). Another more promising candidate Tol 1035−2737 ($z_{\rm em} = 2.159$) shows matches at $z_{\rm abs} = 1.982$ and 2.125 (S87; J88).

The existence of a supercluster at these redshifts causes problems for the standard cold dark matter (CDM) model for structure formation, since structures of supercluster scales are not expected to form until redshifts closer to unity (Evrard, Summers & Davies 1994). The theoretical implications of the proposed supercluster toward the Tololo QSOs pair makes further research on the pair and surrounding QSOs particularly relevant, since the nature of the superclustering is not only of interest for investigations of the absorption clouds, but also for understanding the formation and evolution of large-scale structure at high redshift.

In this chapter, we present high resolution echelle spectra of the original Tololo pair and two neighboring QSOs within a $2\overset{\circ}{.}5 \times 1\overset{\circ}{.}5$ field, with the aim of searching for absorption associated with the proposed supercluster. The observations and reductions are described in § 2.2, and the technique used to identify the lines is described in § 2.3. In § 2.4, we discuss the QSOs and their absorption lines, and in § 2.5 we investigate the properties of

the C IV systems. In § 2.6, we present and interpret the two-point redshift and spatial correlation functions of the C IV absorption systems. Finally, in § 2.7, we discuss the results in the context of the intervening supercluster hypothesis. Throughout this chapter, we assume $H_0 = 100$ km s^{-1} Mpc^{-1} and $q_0 = 0.5$.

2.2 Observations and Reductions

We obtained high resolution spectroscopy of the QSOs listed in Table 2.1 during the period 1992 February 29 to March 3 UT using the Echelle Spectrograph and Air Schmidt camera on the 4-m telescope of the Cerro Tololo Inter-American Observatory. We used the 79 l mm^{-1} echelle grating and KPGL2 cross disperser with the Reticon CCD to give a wavelength coverage from 3810 − 5130 Å in fifteen echelle orders. The observations were made using a 1.5″ slit which projected onto about 2.2 detector pixels. This gave a spectral resolution of ∼ 30 km s^{-1} FWHM which varied slightly across the echelle orders, as measured from comparison arc lamp lines. The slit was aligned at the parallactic angle between each exposure to minimize light losses due to atmospheric refraction. The seeing was usually better than 1.5″ FWHM. Exposures times of the QSO spectra were typically 5400 s up to a maximum of 8400 s. Table 2.1 lists the epoch 1950 coordinates, apparent blue magnitudes, and emission redshifts of the program QSOs, and Table 2.2 contains a log of the observations. The field in which the QSOs are located is shown in Figure 2.1.

We reduced the data in IRAF using tasks specifically designed for processing echelle spectra. Pixel-to-pixel variations in the detector response were normalized using a quartz lamp exposure. The orders were extracted using the optimal extraction technique of Horne (1986). At the same time, a variance array was determined for each spectrum from the object and sky background counts. Wavelength calibration was carried out using short exposures of a thorium-argon lamp, obtained before and after each object exposure. Bracketing comparison spectra were extracted using the same spatial weights as were used for the object spectrum. Standard errors in the wavelength calibration were not
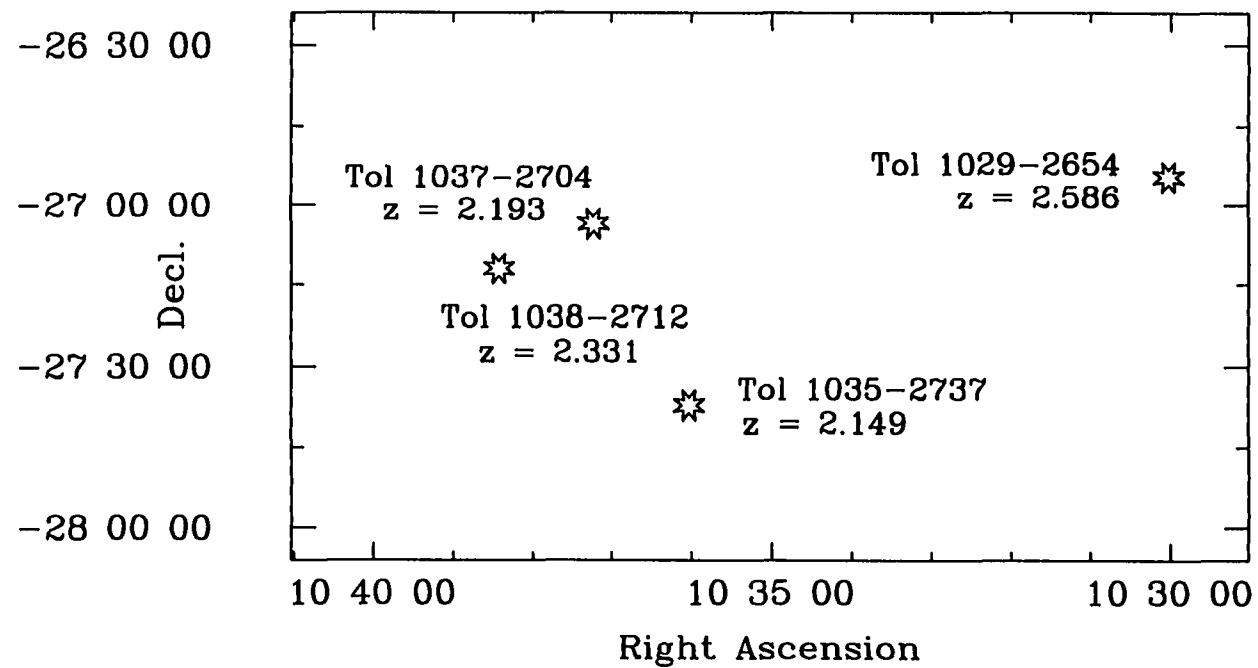
FIGURE 2.1—The field of Tol 1037–2704, Tol 1038–2712, Tol 1035–2737 and Tol 1029–2654. At $z = 2$, $10'$ on the sky is $2.5\,h^{-1}$ Mpc.

more than 0.018 Å.

The individual spectra were then rebinned onto a linear wavelength scale with pixels of 0.15 Å and co-added into a final spectrum for each QSO. A minmax rejection algorithm was used during the summation to eliminate the many cosmic rays spikes, with some resulting reduction of S/N. The variance arrays of the individual spectra were similarly combined into a single array at this stage. The resulting spectra and their 1σ error arrays are shown in Figures 2.2 – 2.5.

The QSO spectra were analysed using software written by J. Bechtold and adapted by T. Aldcroft (cf. Bechtold & Ellingson 1992, for details). The continuum of each spectrum was estimated iteratively by fitting a cubic spline to regions which appeared free of absorption lines and the spectrum was normalized using this fit. Each pixel in the normalized spectrum was then evaluated for the presence of an absorption line by calculating the equivalent width and its uncertainty σ_W in a bin of width 2.5 × FWHM of the instrumental PSF centered on the pixel in question. This effectively excluded spurious features or noise spikes. The pixel was flagged if the equivalent width in the bin exceeded a threshold limit of $5\sigma_W$. Once all the significant lines were determined in this way, their equivalent widths were measured in an interactive manner by marking the beginning and ending wavelengths over which to carry out the summation. The line centers were determined over the same wavelength range using a centroiding algorithm which weights each pixel by the depression with respect to the continuum. For weak lines ($< 10\sigma_W$ in strength), the central wavelengths were derived from Gaussian fits to the lines (cf. Young, Sargent & Boksenberg 1982). The equivalent widths and vacuum wavelengths of all the lines are given in Tables 2.3, 2.4, 2.5 and 2.6. The wavelengths have been referenced to the heliocentric frame.

An attempt was made to separate the lines in complexes or blends by fitting multiple Gaussians only if it was deemed possible to get a good fit. The equivalent widths of these lines were derived from the Gaussian profiles and cannot be considered wholly reliable,
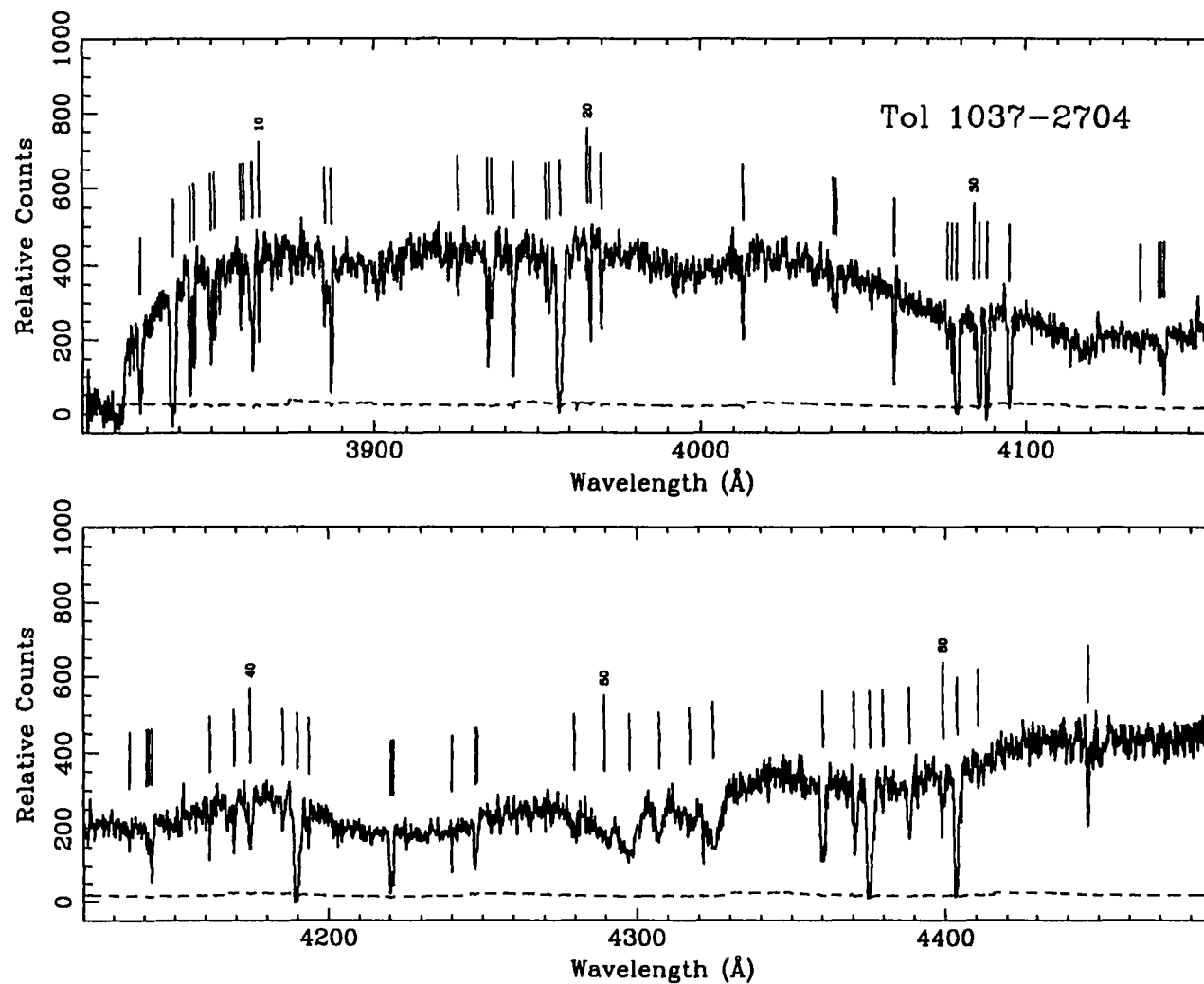
FIGURE 2.2—CTIO echelle spectrum of Tol 1037−2704 as a function of vacuum heliocentric wavelength. The dotted line shows the 1σ errors. The spectral resolution is $30\,\mathrm{km\ s^{-1}}$. Tickmarks indicate all absorption features above the 5σ equivalent width limit listed in Table 2.3.
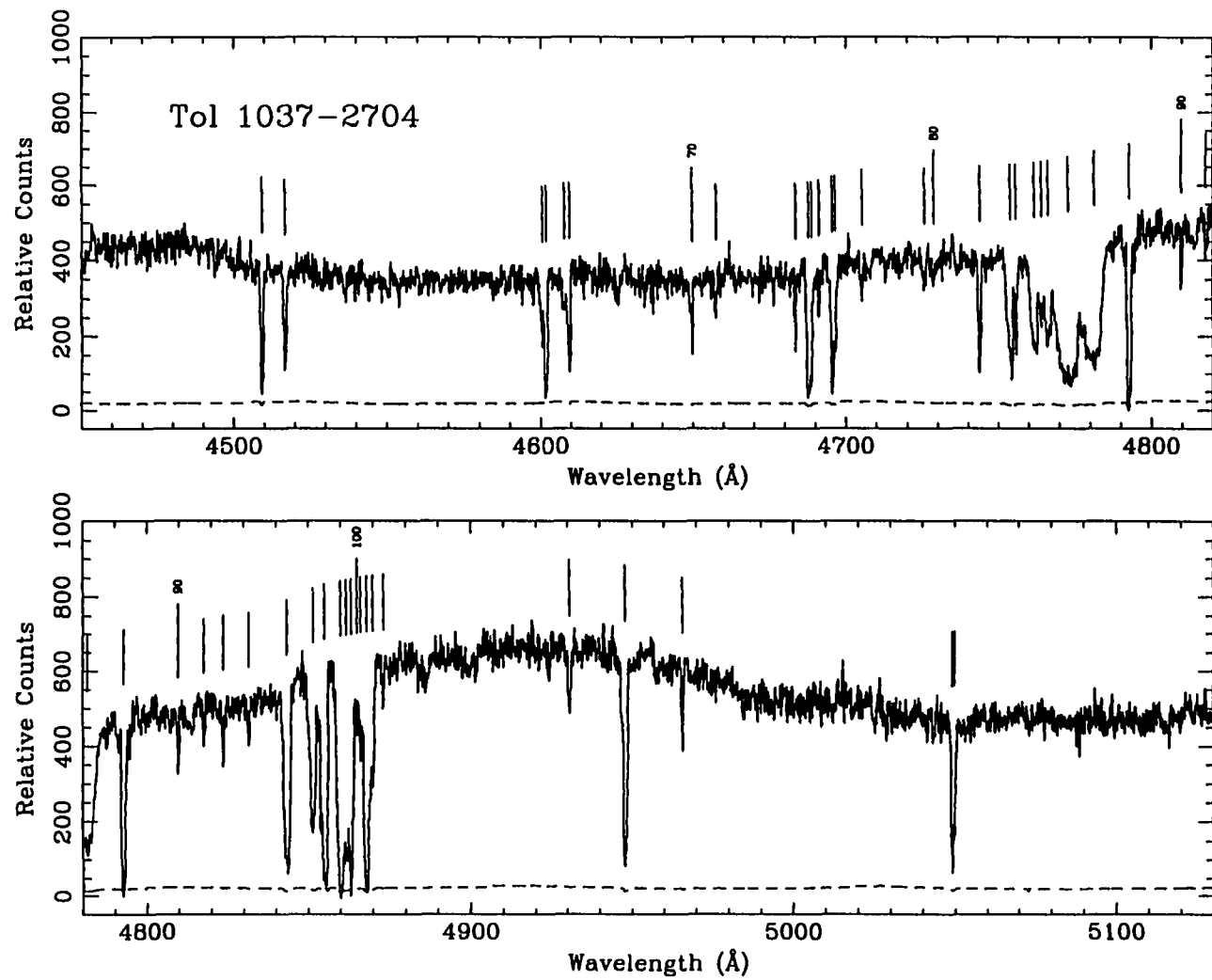
FIGURE 2.2—*continued*.
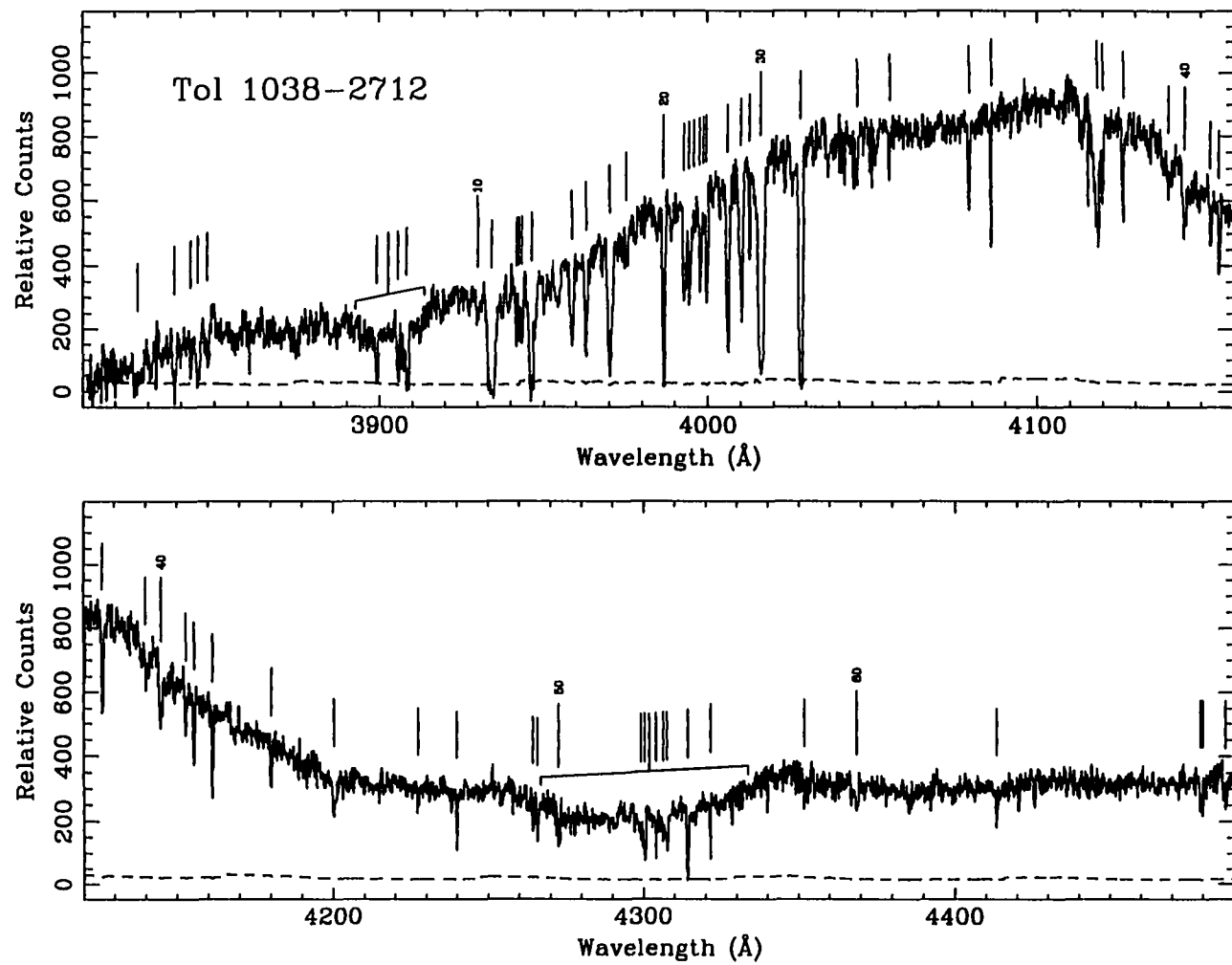
FIGURE 2.3—As Figure 2.2 for Tol 1038–2712. Marked features are listed in Table 2.4.
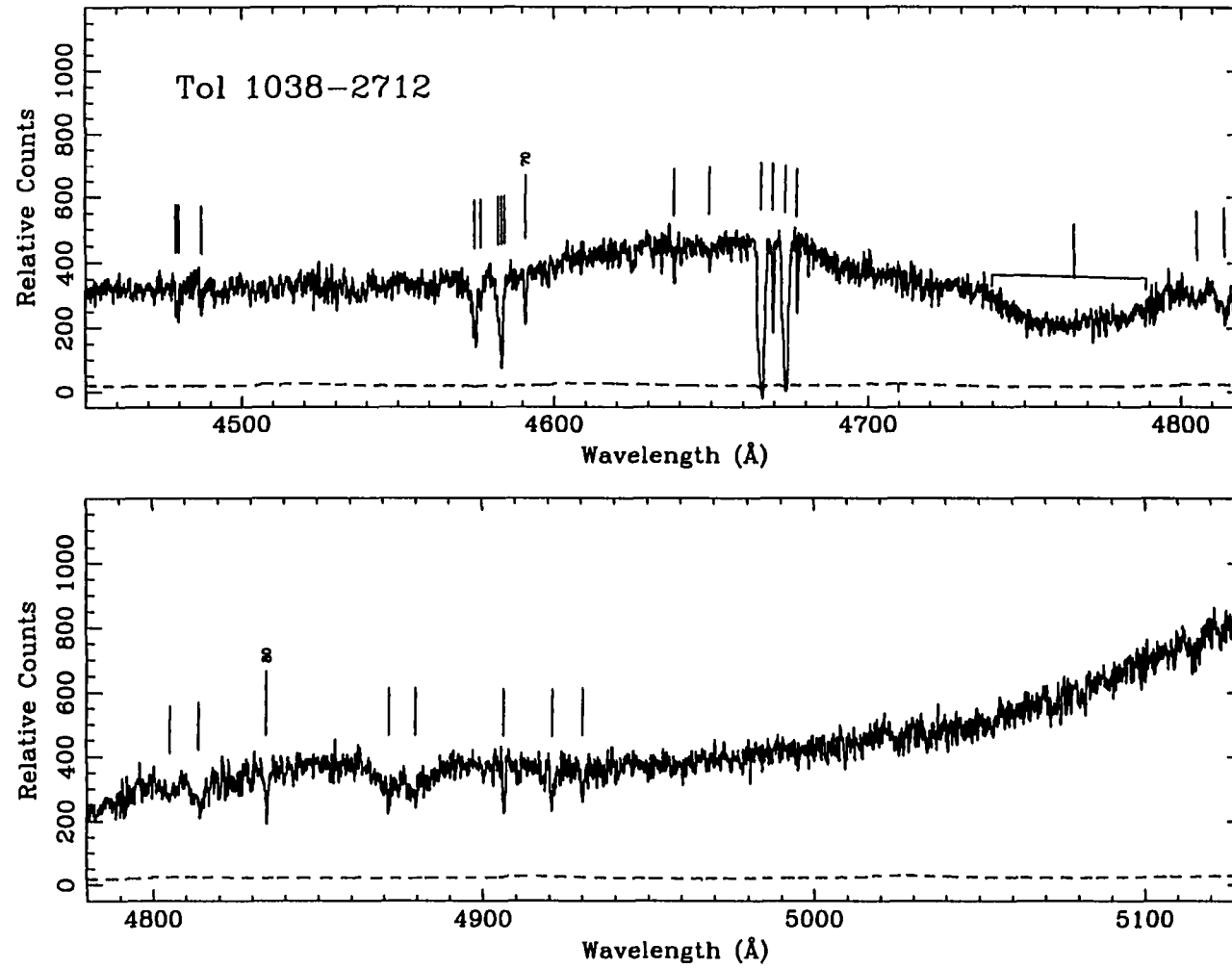
FIGURE 2.3—*continued.*
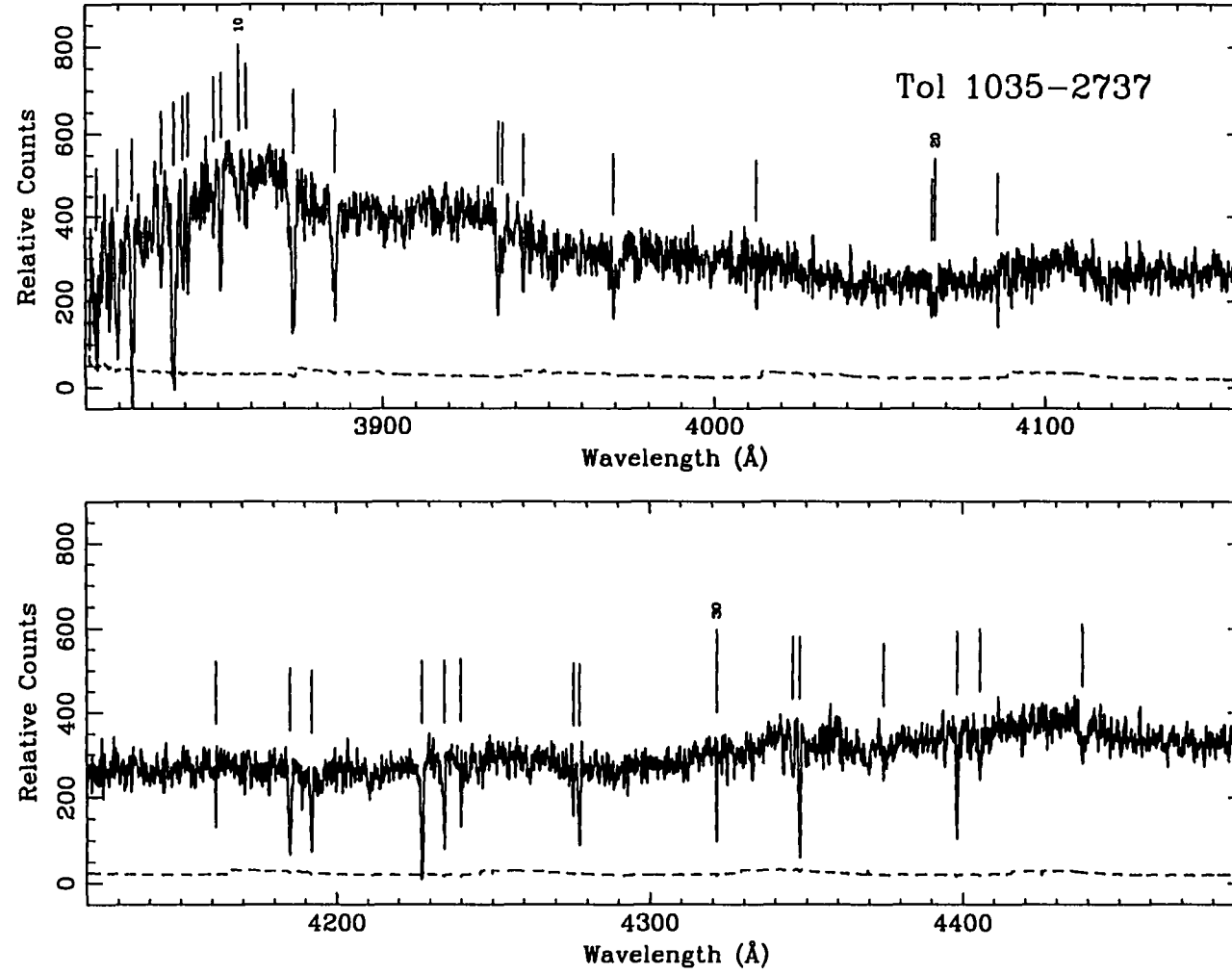
FIGURE 2.4—As Figure 2.2 for Tol 1035−2737. Marked features are listed in Table 2.5.
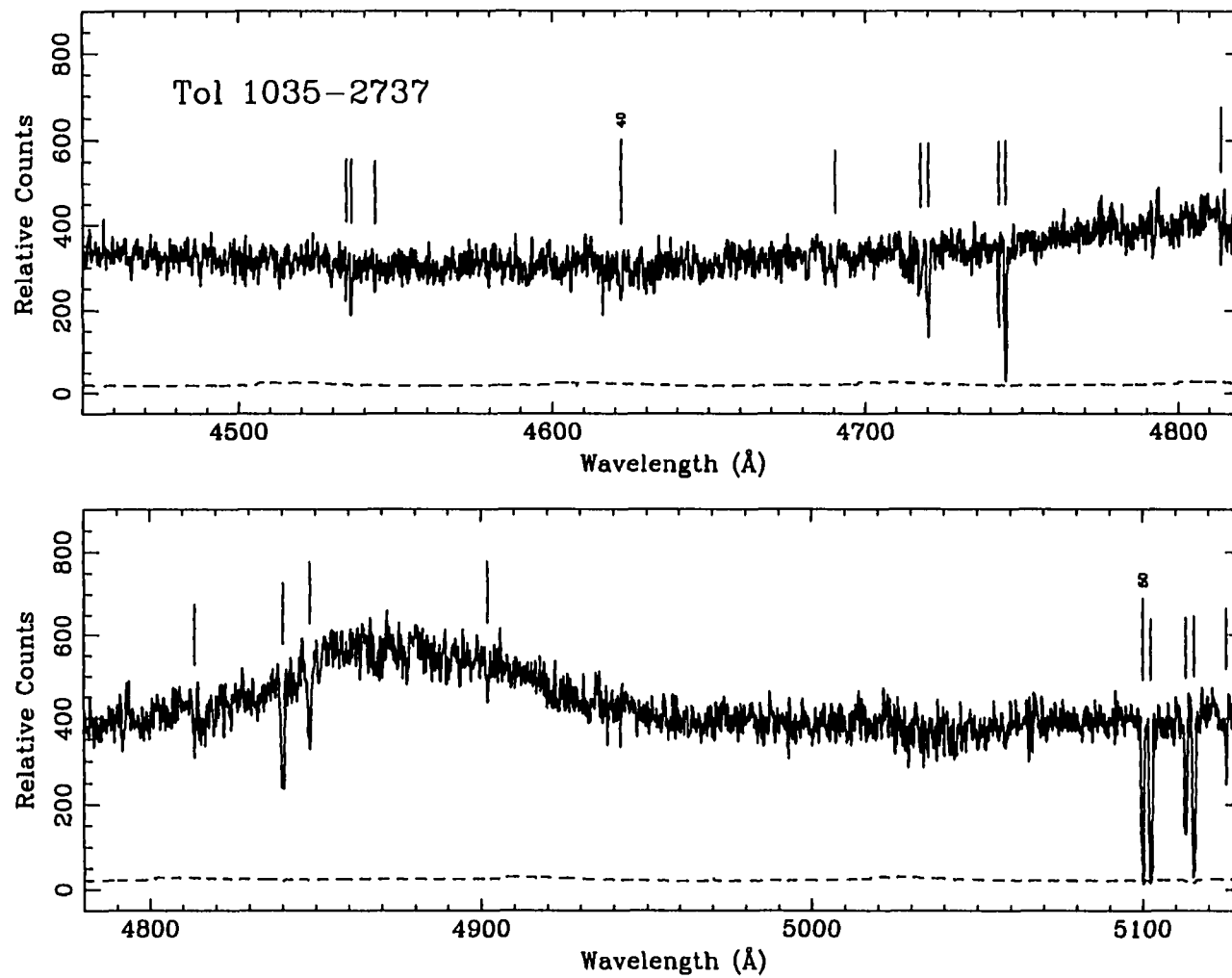
FIGURE 2.4—*continued.*
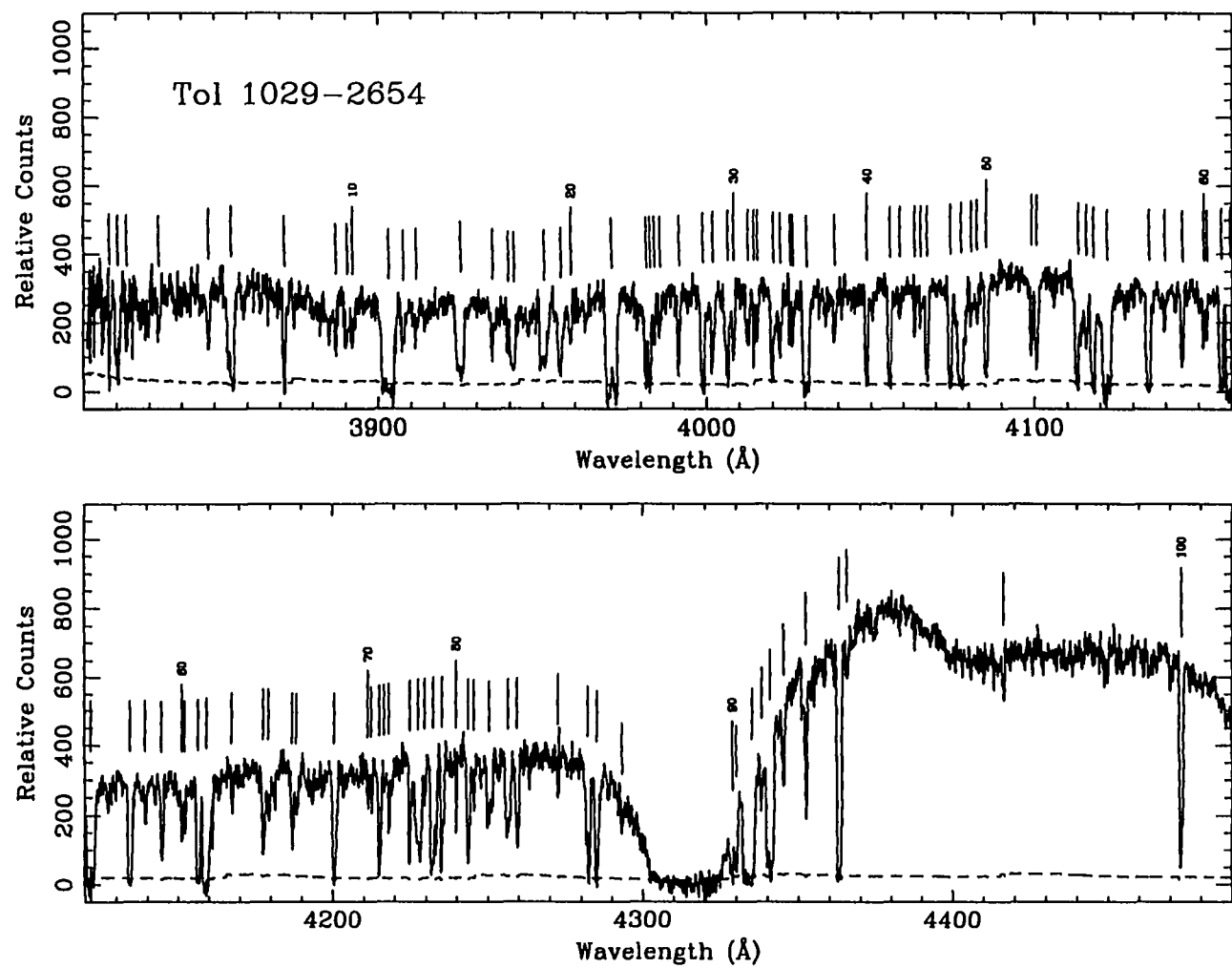
FIGURE 2.5—As Figure 2.2 for Tol 1029−2654. Marked features are listed in Table 2.6.
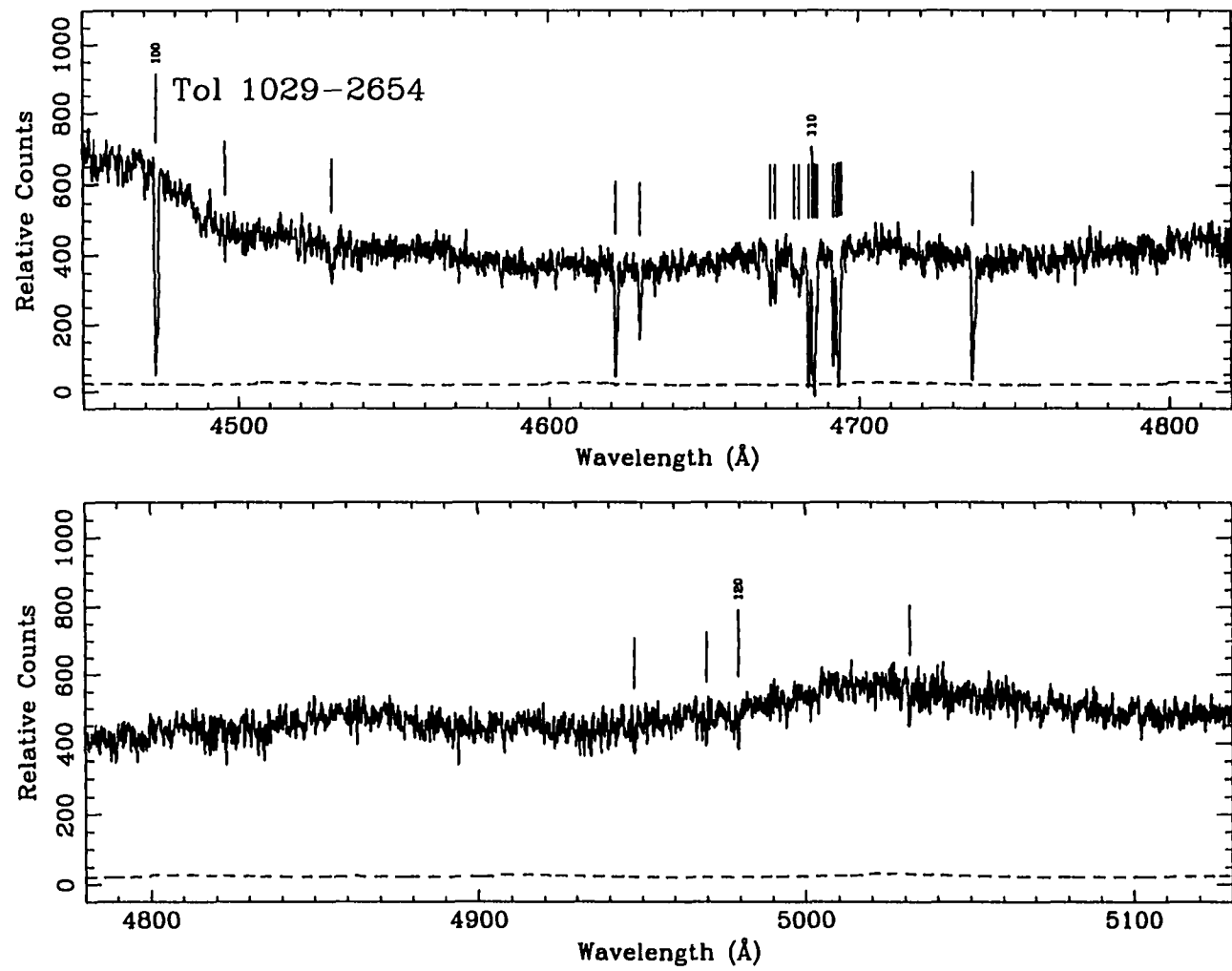
FIGURE 2.5—*continued.*

especially in the broad complexes where the lines are not well-represented by Gaussians. The line centers are nevertheless reliably determined, although their true uncertainties are probably larger than the quoted formal errors from the profile fits.

2.3 Identification of Absorption Lines

We wrote a search program adopting elements of the algorithms described in Bahcall (1968), Aaronson, McKee and Weisheit (1975) and Young *et al.* (1979) to identify the absorption lines automatically. For all observed lines λ_i, all possible redshifts $z_{ij} = \lambda_i/\Lambda_j - 1$ were calculated using a standard set of laboratory wavelengths Λ_j. The redshift range spanned by the z_{ij}'s was then divided into redshift intervals of varying width $\Delta z = (2\delta/3\lambda_c)(1 + z_n)$ where δ is the search acceptance window (0.15 Å) and λ_c is the central wavelength of the spectra (Young *et al.* 1982). Finally, the number $N(z_n, \delta z)$ of redshifts z_{ij} lying within each interval $z_n \pm 2\Delta z$ was counted and those intervals where $N(z_n, \delta z)$ exceeded a certain threshold value were flagged as a possible candidate system. The fact that the intervals overlapped ensured that no systems were missed because of an unfortunate choice of bins. In the automated search, we used a "short" list of ultraviolet absorption lines corresponding to the strongest transitions of the most abundant elements (see Morton, York & Jenkins 1988, Table 4). This list was expanded to include many more lines once a candidate system was accepted.

Once all the candidate systems were identified, we assessed the validity of each candidate according to the probability that the system could have arisen by chance. The statistical analysis adopted is described in detail by Young *et al.* (1979). Wavelength discrepancies of less than three times the estimated 1σ uncertainty in the wavelength determination were considered acceptable in the line identifications. In almost all cases, the wavelength calibration was of sufficient quality that there was little ambiguity over whether the line belonged to a given redshift system, and few candidate systems were rejected because of a poor wavelength match. For the broad absorption systems, we relaxed

the rule to allow wavelength discrepances of as much as $5 - 6\sigma$ since the uncertainties of these systems are probably underestimated. We also checked to make sure that the doublet ratios agreed with expectation, and the relative strengths of lines with a given ion agreed with their known oscillator strengths.

This procedure successfully found all the systems with more than two lines, but was insensitive to systems where only the C IV $\lambda\lambda1548$, 1550 or Mg II $\lambda\lambda2786$, 2803 doublet was present. For this reason, manual searches were made for doublets of C IV, Mg II, N V $\lambda\lambda1238$, 1242, and Si IV $\lambda\lambda1393$, 1402, and as well as the Fe II lines. We also made special searches for pairs of O I $\lambda1302$ and Si II $\lambda1304$ which have a similar wavelength separation as the C IV doublet. In order to minimize the number of misidentifications, we required that for a O I $\lambda1302$/Si II $\lambda1304$ identification to be accepted, C II $\lambda1334$ or Si II $\lambda1260$ must be present at the redshifts of the O I and Si II lines. Otherwise, the C IV identification was accepted. Tables 2.3, 2.4, 2.5 and 2.6 list the suggested identifications for Tol 1037−2704, Tol 1038−2712, Tol 1035−2737 and Tol 1029−2654, respectively.

2.4 The Individual QSOs and their Absorption Line Systems

The increased resolution of our new observations allows us to confirm many of the identifications made by J86 and S87 and to identify a number of new absorption systems. At the resolution of our data, many of the C IV systems are split into narrower components with velocity separations ranging from about $50 - 1000$ km s^{-1}. In total, we found or confirmed 23 C IV systems in Tol 1037−2704 and 13 systems in Tol 1038−2712 in the redshift range $1.41 \lesssim z_{abs} \lesssim 2.15$, and discovered 2 Mg II system in Tol 1037−2704. In addition, we identified 5 C IV systems and 2 Mg II systems in Tol 1035−2737 and 6 C IV systems in Tol 1029−2654. Of the 47 C IV systems found along the four lines of sight, we think that a maximum of only three could be spurious.

2.4.1 Tololo 1037−2704

The spectrum of Tol 1037−2704 ($z_{em} = 2.193$) is shown in Figure 2.2. We call particular attention to the two strong absorption complexes near 4750 Å and 4900 Å which appear broad and troughlike in low resolution data. At 2 Å resolution, S87 were able to decompose the 4750 Å complex into three components and the 4900 Å complex into two components. In our data, we identified four components near 4750 Å and five components near 4900 Å. S87 have used the fact that the broad lines resolve into finer structure at high resolution to argue that Tol 1037−2704 is not a broad absorption line (BAL) QSO. Although the features in the spectrum of Tol 1037−2704 do not remain broad and troughlike at high resolution, BAL QSOs with complex absorption structure are not unknown. Weymann *et al.* (1981) have defined a subclass of QSOs showing complex structure in their BAL troughs. The BAL QSO 1303+308 is an extreme example of this class of QSO (Foltz *et al.* 1987), although Romani, Filippenko & Steidel (1991) suggest that it might be another example of superclustered absorption. On this basis, the classification of this QSO as BAL is still unclear.

$z_{abs} = 0.69636$. This strong, certain Mg II system was previously unidentified, perhaps because the Mg II $\lambda 2803$ line is blended with the C IV $\lambda 1548$ line of the $z_{abs} = 2.07059$ system. The Fe II $\lambda\lambda 2586$, 2600 lines appear to be present with the former blended with Si IV $\lambda 1402$ of the $z_{abs} = 2.12815$ system. The line identified as Fe II $\lambda 2382$ has also been identified as C II $\lambda 1334$ of system $z_{abs} = 2.02847$.

The following two systems are members of a newly identified C IV complex in the Lyα forest. The probability of getting C IV doublet-like matches in the Lyα forest by chance is $\lesssim 0.008$.

$z_{abs} = 1.48248$. The identification of this system is based solely on the presence of the C IV doublet. The components agree within a redshift difference of 0.00002 and have a

doublet ratio [DR = $W_0(1548)/W_0(1550)$] of 1.28 ± 0.06.

$z_{abs} = 1.48323$. As above, this system is identified by it's C IV doublet, with excellent redshift agreement ($\Delta z \lesssim 0.00001$) and a doublet ratio of DR $= 1.29 \pm 0.06$.

The following two systems are members of a another new C IV complex, identified purely on the basis of the C IV doublet. The probability of getting such matches by chance outside the Lyα forest is small, $\lesssim 0.002$.

$z_{abs} = 1.63336$. This is the weaker of the two systems. The redshift agreement between the components of the C IV doublet is better than 0.00005.

$z_{abs} = 1.63434$. This system is identified solely by its saturated C IV doublet. The C IV $\lambda1550$ line was identified as O I $\lambda1302$ and Si IV $\lambda1402$ of other systems by S87 probably because of inadequate resolution. However, it is clear from our data that the C IV $\lambda1550$ of this system and O I $\lambda1302$ of the $z_{abs} = 2.13928$ system are different lines. The Si IV $\lambda1402$ line of $z_{abs} = 1.91249$ is clearly blended and its equivalent width contributes $\lesssim 0.42$ Å to the C IV $\lambda1550$ line. The redshifts of the doublet components are in excellent agreement ($\Delta z \lesssim 0.00002$).

$z_{abs} = 1.91249$. This strong, certain system was identified as $z_{abs} = 1.9122$ by S87. It consists of the C IV doublet, C II $\lambda1334$, Si IV $\lambda\lambda1393$, 1402, Si II $\lambda1526$ and Al II $\lambda1670$. Fe II $\lambda1608$ which was tentatively identified by S87 is not present in our spectrum. The strengths of Si IV $\lambda\lambda1393$ and 1402 are not in their correct ratios; however Si IV $\lambda1402$ appears to be blended with C IV $\lambda1550$ of system $z_{abs} = 1.63434$. Al II $\lambda\lambda1670$ is clearly present, but blended with the absorption complex at $z_{abs} \sim 2.14$. Therefore, although its line center is well-determined, its equivalent width must be considered approximate.

The following two systems appear as a single system in lower resolution data. They were identified as $z_{abs} = 1.9722$ by S87. There is some evidence for an even weaker system shortward of the two at $z_{abs} \simeq 1.9710$ from structure in the C IV doublet and Si IV $\lambda\lambda1393$,

1402 lines.

$z_{abs} = 1.97145$. This is a certain system based on the C IV doublet, C II $\lambda1334$ and Si IV $\lambda1393$. Si IV $\lambda1402$ is present at only the 2.8σ significance level. It is not clear whether Fe II $\lambda1608$ is present because it would be blended with the C IV $\lambda1550$ line of the $z_{abs} = 2.08301$ system. This system would have been blended with the stronger absorption system at $z_{abs} = 1.97216$ in lower resolution data.

$z_{abs} = 1.97216$. This is a strong system, identified by S87 as $z_{abs} = 1.9722$. We can identify the lines of C IV $\lambda\lambda1548, 1550$, Si IV $\lambda\lambda1393, 1402$, C II $\lambda1334$ and Al II $\lambda1670$. As above, Fe II $\lambda1608$ may be present but would be blended with the C IV $\lambda1550$ line of the $z_{abs} = 2.08301$ system.

$z_{abs} = 2.00335$. This new C IV system was probably too weak to have been identified by S87. Both components of the doublet are at $z_{abs} = 2.00335 \pm 0.00003$ and the doublet ratio is 1.30 ± 0.04.

The following three systems were identified as one system at $z_{abs} = 2.0289$ by S87 in their 2 Å resolution spectra. The two strongest systems are severely blended, but all their lines show similar structure.

$z_{abs} = 2.02509$. This system is identified by only a weak C IV doublet. The components of the doublet agree within $\Delta z \lesssim 0.00003$ and the doublet ratio is ~ 2.

$z_{abs} = 2.02786$. This system is certain. In addition to the saturated C IV doublet, the lines of C II $\lambda1334$ and Si IV $\lambda1393, 1402$ are identified.

$z_{abs} = 2.02847$. This system is also certain and shows the same lines as the $z_{abs} = 2.02786$ system.

$z_{abs} = 2.03915$. This is another weak system identified solely on the presence of the C IV $\lambda\lambda1548, 1550$ lines, with redshift agreement better than 0.00003. C IV $\lambda1550$ is

present at the 3.3σ confidence level.

The following complex was identified by S87 as a triple system at z_{abs} = 2.0708, 2.0755 and 2.0825. There is evidence for at least three systems in our spectrum, and probably a fourth from structure in the C IV $\lambda\lambda$1548, 1550 and Si IV $\lambda\lambda$1393, 1402 lines. Many of the lines in these systems are broad and asymmetric, making the line positions and equivalent widths listed in Table 2.3 uncertain.

z_{abs} = 2.07059. The strong C IV $\lambda\lambda$1548, 1550 lines are broad and asymmetric, as are the lines of Si IV $\lambda\lambda$1393, 1402. Despite the difficulty in measuring line positions of such broad lines, the redshifts of all the lines associated with this system agree within 0.0002.

z_{abs} = 2.07716. This probable system is identified from the structure in the C IV doublet lines and is the least certain of this complex. The C IV λ1550 line of the system is severely blended with C IV λ1548 of the z_{abs} = 2.08321 system. The Si IV lines are also blended with those of the z_{abs} = 2.07820 system. The redshift of this system, z_{abs} = 2.07716 $\pm$ 0.00003, is based only on the C IV λ1548 line.

z_{abs} = 2.07858. This certain system is most readily identifiable from the Si IV $\lambda\lambda$1393, 1402 lines, the C IV λ1550 line of the C IV doublet being severely blended with the C IV λ1548 line of the z_{abs} = 2.08321 system. We adopt the redshift of the C IV λ1548 line, z_{abs} = 2.07858 $\pm$ 0.00003, for the system.

z_{abs} = 2.08321. This system is the strongest and broadest of the four systems in this complex. The average FWHM of the C IV doublet lines is $\sim$ 440 km s^{-1}. The C IV λ1548 line is blended with C IV λ1550 of the above system. Identifications of the C IV and Si IV are certain and their redshifts are in good agreement ($\Delta z \lesssim$ 0.0006). The unblended lines give a weighted average redshift of z_{abs} = 2.08321 $\pm$ 0.00003 for the system.

z_{abs} = 2.10663. This probable system was probably not identified in prior studies because of its weakness. It is identified solely on the presence of the C IV doublet. The

doublet components match to within 0.00001.

z_{abs} = 2.11561. This is another new, weak system identified by C IV $\lambda\lambda$1548, 1550, which match in redshift within $\Delta z \lesssim 0.00001$.

The following complex was listed as at least two systems (z_{abs} = 2.1283 and 2.1378) by S87. There was also evidence in their data that the second system was further separable into two subsystems at z_{abs} = 2.135 and 2.139. In our spectrum, the complex is clearly separable into four systems with a probable fifth system present.

z_{abs} = 2.12818. In addition to the strong and broad C IV doublet, we also observe Si II λ1260, C II λ1334 and Si IV $\lambda\lambda$1393, 1402. Si IV λ1402 is blended with Fe II λ2586 of the Mg II system at z_{abs} = 0.69636. All except Si II λ1260 and C II λ1334 agree within 0.00008. The weighted average redshift of the unblended lines is z_{abs} = 2.12818 ± 0.00001.

z_{abs} = 2.13593. This system is certain. Besides a strong C IV doublet, we see N V λ1238, Si II λ1260, C II λ1334 and Si IV $\lambda\lambda$1393, 1402. N V λ1242 and Si II λ1526 appear to be present below the 5σ detection level. From the Si IV doublet lines, this system appears to be made up of two subsystems at z_{abs} = 2.13589 and 2.13645.

z_{abs} = 2.13910. This is another strong, certain system. We identified Si II λ1260, O I λ1302, Si III λ1304, C II λ1334, Si IV $\lambda\lambda$1393, 1402, Si II λ1526, C IV $\lambda\lambda$1548, 1550, and Fe II λ1608. Many of the lines appear saturated and severely blended with lines associated with the z_{abs} = 2.14030 system. The redshift of the system was determined from only the unblended C IV and Fe II lines.

z_{abs} = 2.14030. This system is severely blended with the previous system at z_{abs} = 2.13928, but is definitely real. All the lines observed in the above system are present in this system (except Fe II λ1608). No attempt was made to deblend any of the lines, other than C IV $\lambda\lambda$1548, 1550, of the two systems. Therefore, the redshift of this system was

determined from the C IV doublet lines alone.

z_{abs} = 2.14243. This system is weak, but certain. It consists of C II $\lambda1334$, the C IV doublet and Si IV $\lambda1393$. Si IV $\lambda1402$ is present below the 5σ detection threshold.

2.4.2 Tololo 1038−2712

The spectrum of Tol 1038−2712 (z_{em} = 2.331) is shown in Figure 2.3. It contains broad, troughlike C IV absorption complexes near 4750 Å and 4900 Å similar to Tol 1037−2704. On this basis, Tol 1038−2712 was classified as a marginal BAL QSO by S87. Even in our high resolution data, we were not able to resolve the C IV doublet structure in the complex near 4750 Å; nor were we able to resolve the Si IV doublet structure. The classification of this QSO as a BAL QSO remains uncertain.

The lines associated with the following three systems were identified by S87 as Si IV doublets belonging to three C IV systems at $z_{abs} \simeq$ 2.0652, 2.0768 and 2.0851. The C IV in their data, as in ours, appeared smooth, and the basis of these identifications was the apparent structure in what they interpreted as Si IV lines. We believe the Si IV doublet associated with C IV at $z_{abs} \simeq$ 2.07620 is similarly smooth, and remains unresolved in our data. Furthermore, we believe that the sharp features superimposed on the unresolved Si IV are more accurately identified as C IV doublets.

z_{abs} = 1.75530. This is a new system consisting of an isolated C IV doublet with excellent redshift agreement ($\Delta z \lesssim$ 0.00002). There is evidence for a weaker system at z_{abs} = 1.75442. The C IV $\lambda1550$ line was identified as Si IV $\lambda1393$ from a system identified by S87 as z_{abs} = 2.0652.

z_{abs} = 1.77688. This is a new weak system consisting of the C IV doublet. C IV $\lambda1550$ is blended or affected by a noise spike, but the doublet lines nevertheless show good redshift agreement ($\Delta z \lesssim$ 0.00001).

z_{abs} = 1.77764. This new system is relatively strong. The C IV $\lambda\lambda1548$, 1550 lines show

evidence of structure. The redshift agreement between the doublet lines is $\Delta z \lesssim 0.00001$. The C IV $\lambda 1548$ line was identified as Si IV $\lambda 1402$ of the system $z_{abs} = 2.0646$ and Si IV $\lambda 1393$ of $z_{abs} = 2.0845$.

$z_{abs} = 1.85055$. This system was classified as marginal by S87. The C IV doublet is extremely weak, with the C IV $\lambda 1550$ line present at only the 4.5σ confidence level. Nevertheless, given that the redshift difference between the doublet components is so small, < 0.00001, this system is likely real. Si II $\lambda 1526$ appears to be present at the 5.6σ level. If the Si IV doublet is present, the lines are obscured by blending in the Lyα forest.

The following complex was identified as a single system ($z_{abs} = 1.8936$) and classified as marginal by S87. In our spectrum, the complex is clearly split into two systems.

$z_{abs} = 1.89309$. This system is identified solely by the presence of a very weak C IV $\lambda 1548$. The C IV $\lambda 1550$ line falls below the 5σ equivalent width threshold.

$z_{abs} = 1.89353$. This is the stronger member of the pair. Both C IV doublet lines are present above the 6σ confidence level. The line identified as Al II $\lambda 1670$ is considerably stronger than the C IV doublet and it's identification remains uncertain.

The following complex has been divided into three subsystems based on the structure in the C IV and Si IV doublet lines.

$z_{abs} = 1.95489$. This strong system was identified by S87 as $z_{abs} = 1.955$. The C IV and Si IV doublets show evidence for structure with possible subsystems at $z_{abs} = 1.9543$, 1.9547 and 1.9551. The C IV $\lambda 1550$ line is severely blended with the C IV $\lambda 1548$ line of the $z_{abs} = 1.96047$ system. The line we identify as C II $\lambda 1334$ is almost certainly a chance coincidence with a line in the Lyα forest.

$z_{abs} = 1.95610$. This system is certain, although the C IV doublet is weak and the C IV $\lambda 1550$ line severely blended with the C IV $\lambda 1548$ line of the $z_{abs} = 1.96047$ system. The Si IV $\lambda 1393$ line is present at the 6σ confidence level, but Si IV $\lambda 1402$ falls below the

5σ threshold.

$z_{abs} = 1.96047$. This is a certain system. Besides the C IV doublet, the Si IV $\lambda\lambda1393$, 1402 lines are clearly present. The C IV $\lambda1548$ line is blended with the C IV $\lambda1550$ lines of the $z_{abs} = 1.95489$ and $z_{abs} = 1.95610$ systems.

The following strong and certain complex consists of two subsystems at $z_{abs} = 2.01378$ and $z_{abs} = 2.01623$. S87 identified this complex as one system at $z_{abs} = 2.0144$.

$z_{abs} = 2.01378$. This strong system consists of the C IV $\lambda\lambda1548$, 1550 and Si IV $\lambda\lambda1393$, 1402 lines. The C IV doublet appears saturated. All the lines in this system agree within $\Delta v \lesssim 0.0001$.

$z_{abs} = 2.01623$. This is the weaker system of the complex and was probably blended with the $z_{abs} = 2.01378$ system in the data of S87. The ratio of the C IV doublet is 1.59 ± 0.02 and the redshift agreement is $\Delta z = 0.00001$. There is no evidence for the Si IV doublet in this system.

$z_{abs} \simeq 2.07660$. The C IV doublet of this system remains broad and trough-like, and the components of the doublet unresolved in our high resolution data. This system was identified by S87 as having three components based on structure in the lines they identified as Si IV. We believe the sharp features identified by S87 as Si IV $\lambda\lambda1393$, 1402 are actually C IV doublets superimposed on the smooth unresolved Si IV doublet belonging to this system. We identified the sharp features as members of three new systems, $z_{abs} = 1.75530$, 1.77668 and 1.77764. The FWHM of the unresolved Si IV and C IV doublets are ~ 2400 km s^{-1} and ~ 1600 km s^{-1}, respectively. There is evidence for a broad depression where we would expect to see N V $\lambda\lambda1238$, 1242, but the spectrum does not extend sufficiently blueward to cover the entire feature. Because the Si IV and C IV doublets are unresolved, the redshift of this system is highly uncertain.

$z_{abs} = 2.14674$. This certain system consists of a broad, shallow C IV doublet and Si II

1526 line. There are associated broad, shallow features at the location where N V $\lambda\lambda 1238$, 1242 and Lyα are expected. There is also evidence in our data for the two sharp features in the C IV complex noted by S87. The features show good redshift agreement and are in the correct ratios for identification as C IV at $z_{abs} = 2.1455$. Higher resolution data is required to resolve this complex. The redshift of this system $z_{abs} = 2.14674 \pm 0.00005$ is based on the weighted average redshift of the Si II and C IV lines.

2.4.3   Tololo 1035−2737

The spectrum of Tol 1035−2737 is shown in Figure 2.4. This QSO (#16 of the Bohuski & Weedman 1979 list) is located roughly 40' southwest of Tol 1037−2704 and Tol 1038−2712 (Figure 2.1), corresponding to a projected distance of ~ 10 Mpc. From the peaks of the emission lines, we measured the redshift to be $z_{em} = 2.159 \pm 0.014$ in good agreement with the redshift determined by S87 and J88. At this redshift the QSO lies behind all the common systems seen in the original pair, and is possibly a cluster member situated at the far side of the proposed supercluster. S87, in a footnote added in proof, reported a definite C IV absorption system at $z_{abs} = 2.125$ and two possible systems at $z_{abs} = 2.040$ and $z_{abs} = 1.905$ from a slit spectrum with 4 Å resolution. J88 observed this QSO at 6 Å resolution; they verified the system at $z_{abs} \simeq 2.125$ and identified only one other system at $z_{abs} = 1.982$. These C IV systems coincide with some systems in the original Tololo pair within a velocity separation less than 5000 km s^{-1}. This makes this QSO particularly important for further study.

$z_{abs} = 0.82381$. This is a certain system, based on the presence of the strong Mg II $\lambda\lambda 2796$, 2803 doublet and Fe II $\lambda\lambda 2344$, 2382, 2586, 2600. The ordering of the line strengths correspond well with expectation, except for the Fe II $\lambda 2586$ line which appears to be blended with another (unidentified) line.

$z_{abs} = 0.82467$. As above, this system is certain, based on the presence of a saturated Mg II doublet and Fe II lines. There is evidence for the Fe II $\lambda 2374$ line, but its equivalent

width falls below the 5σ threshold for detection. Fe II $\lambda2382$ may be blended with Fe II $\lambda1608$ from the $z_{abs} = 1.70313$ system.

$z_{abs} = 1.70313$. The identification of this system is primarily based on the presence of a strong C IV doublet, with both members at $z_{abs} = 1.70313 \pm 0.00001$ and a doublet ratio of DR $= 1.54 \pm 0.06$.

$z_{abs} = 1.73058$. This system is identified solely by the presence of a strong C IV doublet. Both lines agree to within $\Delta v \lesssim 0.00003$.

$z_{abs} = 1.84089$. This system is based on the presence of C IV $\lambda\lambda1548$, 1550. The redshift agreement between the doublet members is $\Delta z \lesssim 0.00001$. We identify no other lines associated with this system.

$z_{abs} = 1.92965$. The identification of this system is based solely on the weak C IV doublet. Both members agree within $\Delta z \lesssim 0.00003$ and doublet ratio is ~ 2.

$z_{abs} = 2.12630$. The identification of this system is based on the presence of the C IV doublet and N V $\lambda\lambda1238$, 1242. There is some evidence in the N V lines that the system will split into two components in higher resolution data.

2.4.4 Tololo 1029−2654

The spectrum of Tol 1029−2654 is shown in Figure 2.5. This QSO was discovered in our own survey for nearby QSOs in a $2^\circ.5 \times 3^\circ$ field centered on the original QSO pair using an objective prism plate from the UK Schmidt Telescope. It is situated about 99′ or 24 Mpc northwest of Tol 1037−2704 and roughly 115′ or 28 Mpc northwest of Tol 1038−2712 (Figure 2.1). We estimated $z_{em} = 2.586 \pm 0.018$ from the peaks of the Lyα and Si IV emission lines. An obvious feature in the spectrum of Tol 1029−2654 is the presence of a damped Lyman α system at the redshift $z_{abs} = 2.549$. We observe Si II $\lambda\lambda1190$, 1193, Si II $\lambda1260$, O I $\lambda1302$, Si II $\lambda1304$, C II $\lambda1334$ and Si II $\lambda\lambda1393$, 1402 associated with this damped Lyman α system. We are not aware of any previously published spectra of this

QSO.

$z_{\mathrm{abs}} = 2.01744$. This probable system is identified by a relatively weak C IV doublet, with both members at $z_{\mathrm{abs}} = 2.01744 \pm 0.00001$ and a doublet ratio of DR $= 1.52 \pm 0.04$.

$z_{\mathrm{abs}} = 2.01840$. This is another probable system with a weak C IV doublet. Both lines agree to within $\Delta z \lesssim 0.00001$.

We base our decomposition of the following complex into four systems primarily on the structure in the C IV lines.

$z_{\mathrm{abs}} = 2.02549$. This strong system is certain. In addition to the C IV doublet, we tentatively identify the Si IV doublet although Si IV $\lambda 1402$ is probably blended with another line in the Lyman α forest.

$z_{\mathrm{abs}} = 2.02617$. The strong C IV doublet is severely blended with the system at $z_{\mathrm{abs}} = 2.0268$, but is no doubt real. The redshift agreement between the doublet members is $\Delta z \lesssim 0.00001$. No other lines are observed.

$z_{\mathrm{abs}} = 2.02662$. This system is the most certain, consisting of the saturated C IV doublet, the Si IV doublet and possibly the C II $\lambda 1334$ line. The redshift agreement between the doublets of C IV and Si IV is better than 0.00003, whereas there is a significant discrepancy in redshift between the doublets and the line identified as C II $\lambda 1334$.

$z_{\mathrm{abs}} = 2.02716$. This is the weakest component of this complex. It is severely blended with the C IV lines of the $z_{\mathrm{abs}} = 2.0268$ system, but is most probably real.

2.5 Characteristics of the CIV Absorption Systems

Table 2.7 lists the 47 C IV systems found in the spectra of the four Tololo QSOs. The columns of Table 2.7 list the the minimum (1) and maximum (2) redshifts between which a C IV doublet could have been detected, the weighted mean absorption redshift (3) of the C IV system and its associated uncertainty (4), and the number of lines on which we

based the identification (5). Only the lines that were certain to belong to the system and those that were not blended were used to calculate the mean redshift. Column (6) gives the difference between the absorption redshift of the system and the emission redshift of the QSO in terms of the fraction β of the velocity of light defined as

$$\beta = \frac{(1 + z_{em})^2 - (1 + z_{abs})^2}{(1 + z_{em})^2 + (1 + z_{abs})^2}. \tag{2.1}$$

Columns (7) and (8) list the rest equivalent widths of the components of the C IV doublet. The last column (9) classifies the reliability of the identifications as either certain, probable or possible. A system was considered certain if it contained lines in addition to the C IV doublet; probable if only the doublet was identified, but both lines were present at the 5σ level and the velocity match and ratio of the lines was good; and possible if either only one line of the C IV doublet was observed at 5σ level, but the other line was present at a lower level ($> 3\sigma$), or there was any ambiguity in the line identification.

In order to judge the reliability of the C IV systems whose identifications were based solely on the doublet, we compared the doublet ratios DR $= W_0(1548)/W_0(1550)$ and RMS velocity difference between the doublet components for both the certain and probable systems. The DR and velocity difference distributions, constructed using C IV doublets that are not blended, are shown in Figure 2.6 and 2.7, respectively. The DR histogram of certain systems shows more doublets with ratios of unity than that of the probable systems. This is not unexpected and is due to the fact that the certain systems (defined as those which contain lines other than the C IV doublet) are more likely to have strong and saturated C IV lines. We find a mean value of $< $ DR $>= 1.35$ and standard deviation $\sigma(\text{DR}) = 0.33$ for the certain systems, consistent with the values found by Young et $al.$ (1982) in a sample of 30 QSOs. A χ^2-test indicated that no significant difference exists between the doublet ratio and velocity difference distributions of the certain and probable systems. Similarly, a χ^2-test confirmed that the distribution of velocity differences of the probable systems is consistent with that of the certain systems.

We have defined four samples of C IV systems in Table 2.8. The largest sample S1
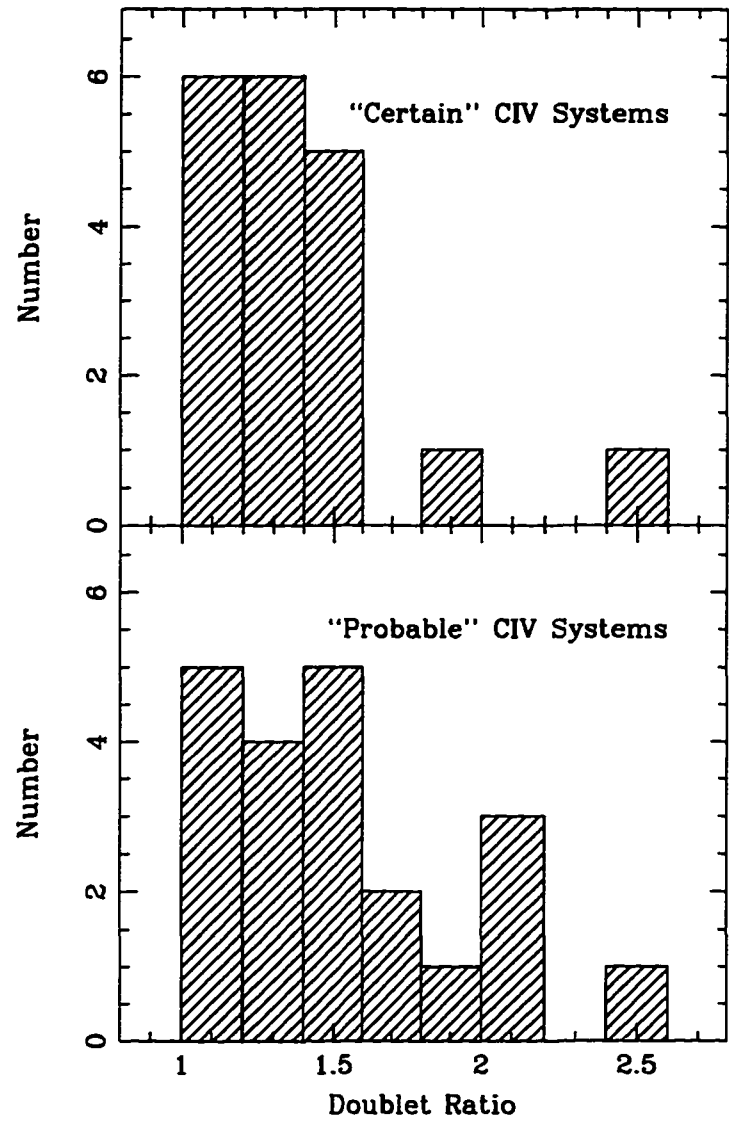
FIGURE 2.6—Histograms of doublet ratios DR $= W_0(1548)/W_0(1550)$ for the certain (*upper panel*) and probable (*lower panel*) systems.
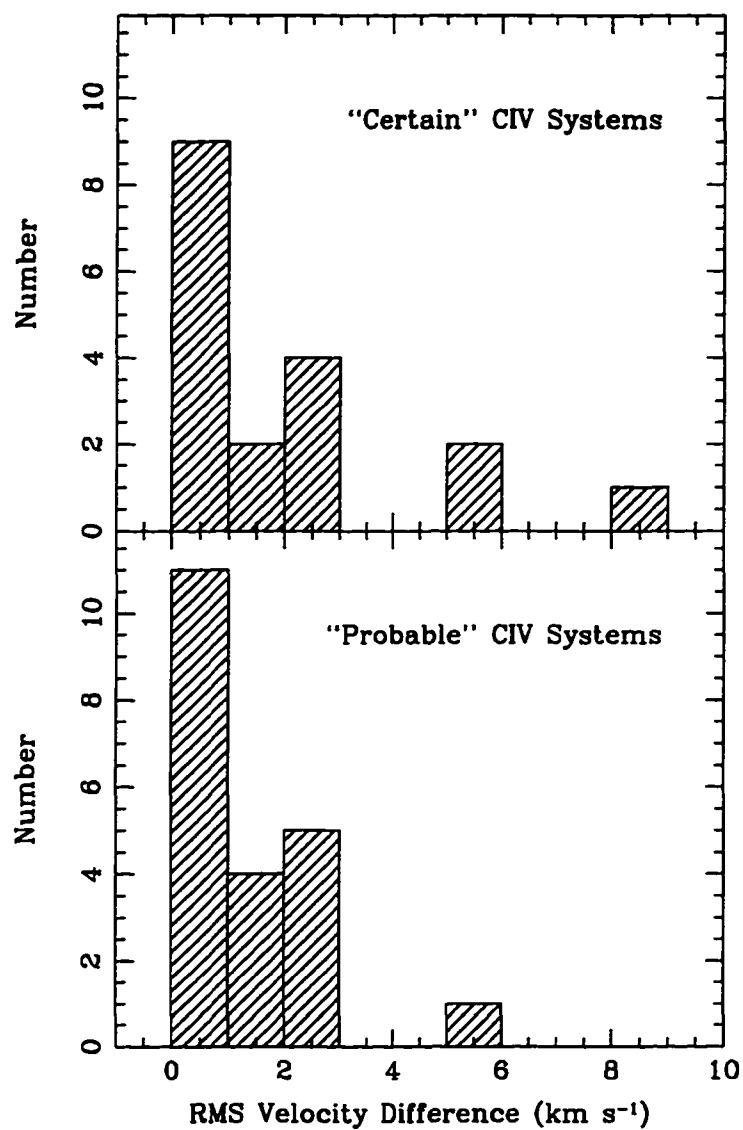
FIGURE 2.7—Histograms of RMS velocity differences between C IV doublet components for the certain (*upper panel*) and probable (*lower panel*) systems.

contains the 44 certain and probable systems listed in Table 2.7. S2 is a subset of sample S1 with all possible associated systems within $\beta c \leq 5000\,\mathrm{km\ s^{-1}}$ of the emission redshift of the QSO excluded (*e.g.* Foltz *et al.* 1986). The third sample S3 contains 21 lines for which the rest equivalent widths of both components in a given C IV doublet exceed 0.15 Å. This sample is most readily comparable to the sample A4 of SBS. In S4, complexes with component separation $\Delta v \leq 1000\,\mathrm{km\ s^{-1}}$ have been collapsed into single systems.

The distribution of rest equivalent widths for C IV absorption lines has been found to be well fitted by an exponential function of the form

$$n(W) = \left(\frac{N_*}{W_*}\right) e^{-W/W_*} \tag{2.2}$$

where $n(W) = \partial^2 N/\partial z \partial W$ is the density of lines per unit ΔW and Δz. Following SBS, we approximated $n(W)$ by counting the number of lines in bins of width ΔW such that $n(W) \simeq \Delta N/\Delta z \Delta W$, where Δz is the total range of redshifts of the sample QSOs.

The binned equivalent width distribution is plotted in Figure 2.8 for sample S3 ($W_0 > 0.15$ Å and $\beta c > 5000\,\mathrm{km\ s^{-1}}$). The vertical error bars give the estimated uncertainty in each bin, and the horizontal bars represent ΔW. The best fit to the equivalent width distribution is an the exponential curve with $W_* = 0.39 \pm 0.04$. Our results agree with SBS who found for their sample A4 ($W_0 > 0.15$ Å), $W_* = 0.46 \pm 0.04$. In order to investigate the trend in the equivalent width distribution for weaker lines ($W_0 < 0.15$ Å), we have plotted in Figure 2.9 the equivalent width distribution for sample S1. It is clear from this plot that a single exponential function is not a good representation of the equivalent width distribution over the entire range of W_0 due to the steep increase in line density for $W_0 < 0.3$ Å. This feature of the distribution is also consistent with the results of SBS. The best-fit values of W_* and N_* for samples S1 through S4 are given in Table 2.8. Thus we are confident that the C IV absorption systems toward the Tololo QSOs are consistent with, and belong to, the same population of absorbers as the SBS systems.
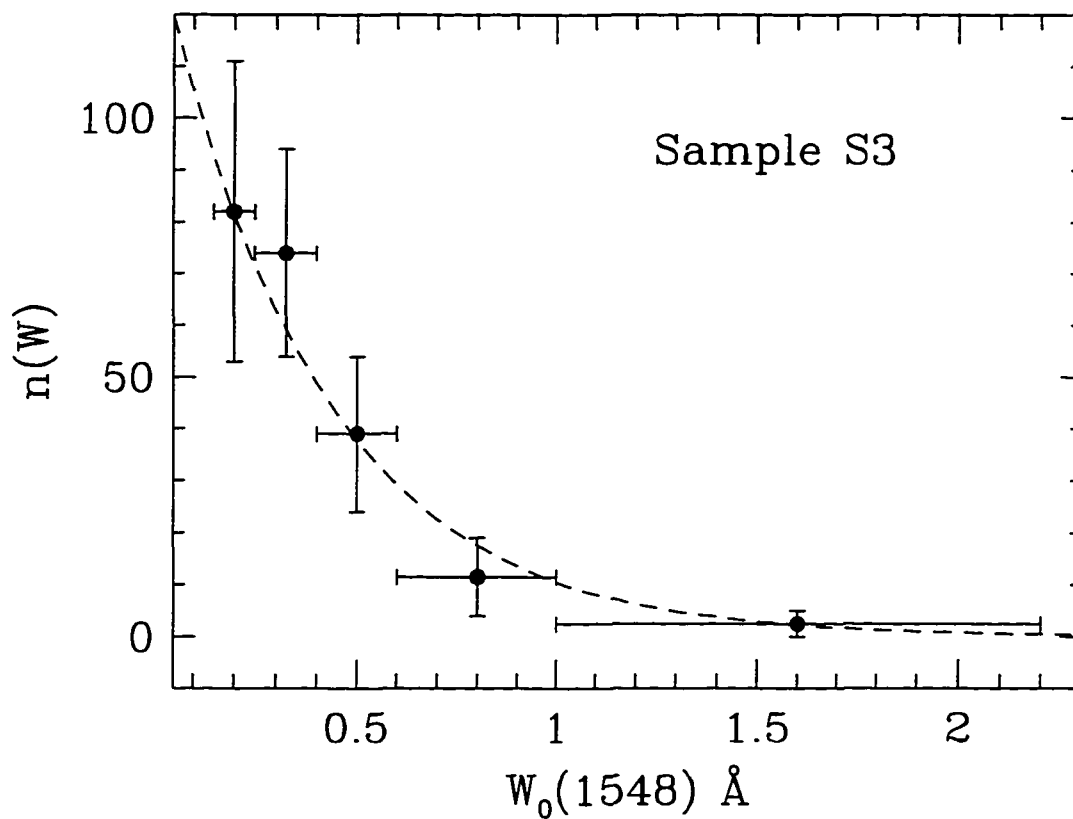
FIGURE 2.8—Distribution of rest equivalent widths for sample S3. The vertical error bars give the estimated uncertainty in each bin, and the horizontal bars represent ΔW. The dashed curve gives the best fit for an exponential function of the form $n(W) = (N_*/W_*)\exp(-W/W_*)$ where $W_* = 0.39 \pm 0.04$ and $N_* = 53 \pm 11$.
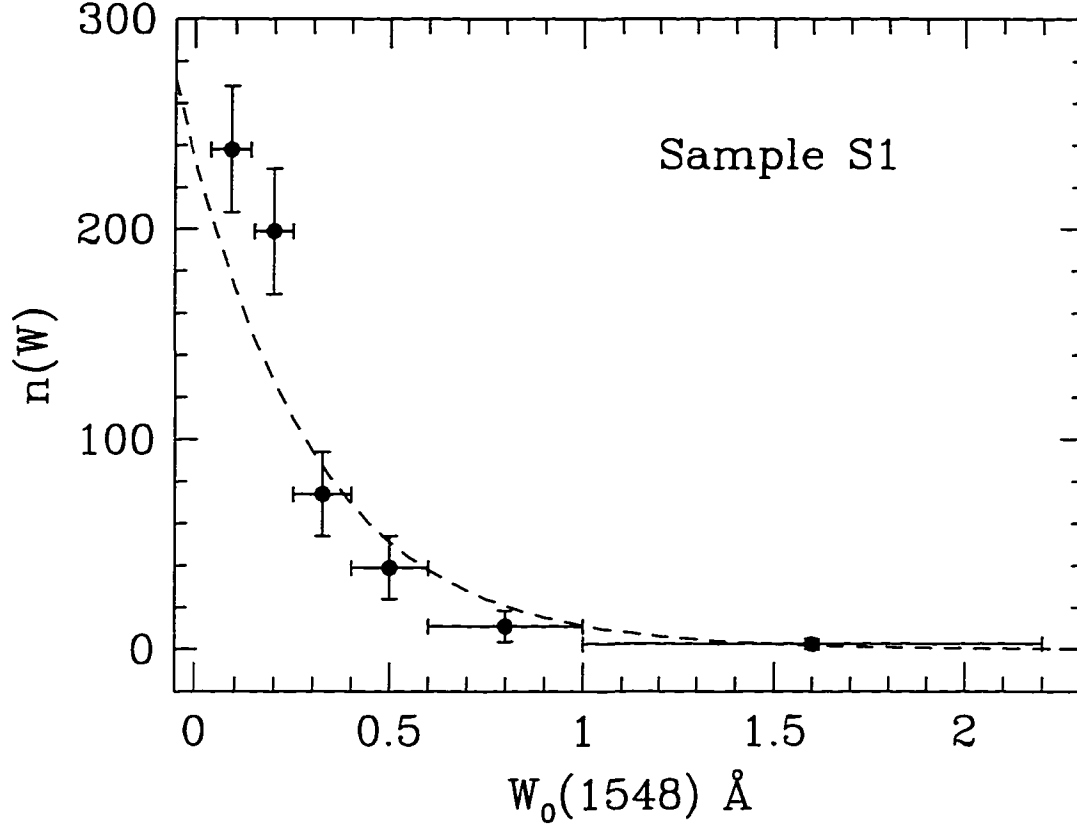
FIGURE 2.9—As Figure 2.8 for sample S1. The dashed curve is the best fit for an exponential function where $W_* = 0.33 \pm 0.04$ and $N_* = 77 \pm 11$.

2.6 The Velocity and Spatial Correlation Functions

The fact that the C IV absorbers are thought to be associated with either galaxies or their precursors makes it of interest to examine the clustering properties of the C IV systems in our sample. There is considerable evidence that the C IV absorbers are clustered on velocity scales out to $\Delta v \simeq 10,000$ kms (SBS, HHW), and that the spatial correlation function of Crotts (1985) appears to show marginal evidence (95% significance level) for clustering on comoving separations of $\lesssim 2$ Mpc. Our high resolution spectra allow us to examine the clustering properties of the C IV absorbers on smaller velocity scales (down to $\Delta v \simeq 30$ km s^{-1}) along the lines of sight to the QSOs and spatially on scales out to $r \simeq 440$ Mpc.

To measure the degree and scale to which the C IV systems cluster spatially and in redshift toward the QSOs, we have computed the two-point correlation function, $\xi(r)$, which is defined such that the probability of finding an absorber at distance r from another in a volume element dV is

$$dP = n\left[1 + \xi(r)\right] dV \tag{2.3}$$

where n is the average number density of absorbers. The correlation amplitude is defined explicitly by the expression

$$\xi(r) = \frac{N_{obs}}{N_{exp}} - 1 \tag{2.4}$$

where N_{obs} is the observed number of line pairs with separations between r and $r + \Delta r$, and N_{exp} is the number of pairs expected for a random distribution of absorbers. For $\xi(r) > 0$, the correlation function measures the *additional* probability over the background of finding an absorber at a distance r from a randomly placed absorber. A similar equation holds for the velocity correlation function, $\xi(v)$.

The usual expression for the variance $\sigma^2 = N_{exp}^{-1}$ in $\xi(r)$ is an underestimate of the true error because the pair count, N_{exp}, is not a Poisson variable even if the redshifts are distributed randomly (Olivier *et al.* 1993). Instead we computed the variance in $\xi(r)$ from

the equation

$$\sigma^2(\xi) = \sigma^2(N_{obs}) \left(\frac{1}{< N_{exp} >} \right)^2 = \frac{< N_{obs}^2 > - < N_{obs} >^2}{< N_{exp} >^2} \tag{2.5}$$

where $< N_{obs}^2 >$, $< N_{obs} >$ and $< N_{exp} >$ were estimated numerically from 1000 Monte Carlo realizations of randomly distributed absorbers in the same redshift range as the data sample and with the same number of redshift systems. The uncertainty calculated in this manner measures the probability that a random distribution of redshifts could lead to the measured value of $\xi(r)$ in a given bin along the identical four lines of sight containing the same number of redshift systems as observed in the sample. Although this is a better measure of the uncertainty per bin, it is still an underestimate where $\xi(r) \gtrsim 1$.

2.6.1 Velocity Correlation Function

We estimated the velocity correlation function $\xi(v)$ using the method described in detail in HHW. First, we decided on a set of bins such that the average occupancy based on randomly distributed absorbers per bin was the same, giving equal sensitivity to departures from a Poisson distribution. Then, we estimated the number of observed pairs in each bin by computing, for each C IV system, the redshift intervals whose velocity separations with respect to that system corresponded to the given bin. We checked that the redshift intervals resided within the redshift range spanned by the data, and, if necessary, adjusted the size of intervals such that they did. Finally, we counted the number of systems in the same line of sight that fell within the redshift intervals to get an estimate of the number of observed pairs.

We estimated the number of expected pairs using the catalogs of C IV systems in SBS and Steidel (1990). We first calculated the number density of systems per unit redshift by counting the number of systems in the catalog lines of sight that fell within larger ($\pm 25,000$ km s^{-1}) redshift intervals centered on the small intervals, and dividing this by the total pathlength intersected by the large intervals for which C IV systems could have been found in the catalog QSOs. Bins of width $\pm 25,000$ km s^{-1} were adopted since

the velocity correlation function shows no evidence of clustering on scales greater than $\sim 10,000\,\text{km s}^{-1}$ (SBS, Steidel 1990, HHW). We then obtained the number of expected pairs by multiplying the average number density of systems by the redshift intervals in which the number of observed pairs was derived.

This procedure was repeated treating each redshift system as the reference system and accumulating the numbers of observed and random pairs in each bin. The method automatically takes into account the non-uniform wavelength coverage of the data sample without having to make an explicit correction. Furthermore, it is designed to be independent of any assumptions about the evolution in absorber population. The velocity separation between absorbers was calculated using the approximation $\Delta v \simeq c\Delta z/(1 + \bar{z})$ where $\Delta z = z_2 - z_1$ and $\bar{z} = \frac{1}{2}(z_1 + z_2)$. We verified our calculations by successfully reproducing the results of HHW. We also generated random datasets, placing systems over the same redshift ranges covered by the QSO data, and verified that $\xi(v)$ scattered about zero as expected for a random distribution of absorbers.

Our calculation of $\xi(v)$ deviates from that of HHW in one important way. HHW used the same sample of redshifts to calculate both the observed and expected number of pairs. It would not be appropriate in our case to do the same because the lines of sight are not typical, having been selected for a detailed study from *a priori* knowledge of their abnormally complex absorption spectra. We modified their procedure to use a sample of C IV absorbers found along the lines of sight to randomly-selected QSOs to estimate the expected number of pairs. The sample was a combination of two homogeneous and complementary surveys for C IV systems described in SBS and Steidel (1990). Together the surveys found 275 C IV absorption systems in the spectra of 66 QSOs, with a sensitivity designed to detect all systems with rest equivalent widths exceeding 0.15 Å. We restricted our attention to a subsample of 138 systems satisfying the criteria $W_0 > 0.15$ Å in both C IV lines and $\beta c > 5000\,\text{km s}^{-1}$. This subsample contains absorbers with redshifts ranging from $1.2 \lesssim z_{\text{abs}} \lesssim 3.6$ and median $z_{abs} = 2.015$.

One disadvantage in using the SBS sample to estimate the number of expected pairs arises because our data were obtained at higher resolution than the data of SBS. This introduces uncertainty into the normalization of the correlation function. It is well-known that the number of C IV systems varies with resolution since many of the systems which appear to be one at low resolution are split into narrower components in higher resolution data (Blades 1988). Therefore, it was necessary to normalize the observed correlation function by the mean overdensity $\bar{\varrho}$ of systems. We estimated $\bar{\varrho}$ numerically from the average ξ of 1000 Monte Carlo realizations of randomly distributed absorbers in the same redshift sensitivity intervals and with the same number of systems as in the relevant data sample. As expected, the correlation function is flat for an unclustered sample and the standard deviation of the amplitude among the bins implies an uncertainty in the normalization of $\lesssim 10\%$.

The velocity correlation function of the 44 C IV systems in sample S2 is shown in Figure 2.10 normalized by $\bar{\varrho} = 6.7$. The error bars are the 1σ statistical errors for a random distribution of absorbers. There are five features of note in Figure 2.10: (1) The strongest correlations appear in the smallest velocity bin with $\Delta v \leq 300$ km s^{-1}. These correlations are thought to be predominantly due to the motions of individual clouds in galactic halos since the typical velocity dispersions of the clouds are about 200 km s^{-1} (Davis & Peebles 1983). (2) We also detect strong signal in the second bin for velocity separations in the range $300 \leq \Delta v \leq 1000$ km s^{-1}, which corresponds to the velocity dispersions of typical galaxy clusters ($\sigma_v \simeq 300 - 1400$ km s^{-1}; Zabludoff et al. 1993). (3) The correlation signal appears to persist out to velocity separations of $\Delta v \lesssim 13,000$ km s^{-1}, though the power in the velocity bin $10,000 \leq \Delta v \leq 13,000$ km s^{-1} is most likely an artifact of the subsplitting of the C IV complexes. We explore this point in more detail below. (4) On velocity scales of $20,000 \leq \Delta v \leq 35,000$ km s^{-1}, there is an apparent 2.8σ deficit of correlation signal, also discussed in more detail below. (5) Finally, in the bins corresponding to $\Delta v \geq 35,000$ km s^{-1}, we find $\xi(v) \simeq 0$ consistent

with no clustering of the absorbers.

Most of the power in Figure 2.10 appears to be confined to well-defined peaks. We investigated the possibility that this is an artifact of the adopted bin boundaries by experimenting with different bin sizes and shifting the centers of the bins. We found that regardless of the location of the bin boundaries, the structure in $\xi(v)$ persisted. Upon close examination of the data, this is not so surprising. Figure 2.11 shows the redshift distribution of C IV systems in the Tololo QSOs. The systems are clearly clustered in five complexes in Tol 1037−2704 and Tol 1038−2712 with roughly equal spacing [though the $z_{abs} = 1.85055$ system in Tol 1038−2712 was classified as a possible system and therefore was not included in the calculation of the $\xi(v)$]. This feature has been pointed out by J86 and S87. The spacing between each cluster of systems is approximately $5000-7000$ km s^{-1} which is consistent with the separation between the peaks in the redshift correlation function. The most likely cause of the pattern of peaks is beating between the five clusters of systems, where the third and fourth peaks represent higher harmonics. Similarly, the deficit in the correlation function between $20,000 \leq \Delta v \leq 35,000$ km s^{-1} is caused by beating between the two clusters of systems at $z_{abs} \simeq 1.48$ and 1.63 and the five clusters of system at the opposite end of the accessible redshift range between $z_{abs} \simeq 1.91$ and 2.14 in Tol 1037−2704 (Figure 2.11).

In order to eliminate the beating effects in $\xi(v)$, we reduced the cluster signal by collapsing complexes with component separations $\Delta v \leq 1000$ km s^{-1} into single systems, consistent with the typical line-of-sight velocity dispersions of clusters of galaxies (Zabduloff et al. 1993, Figure 4). The velocity correlation function was then recalculated for the remaining 16 C IV systems with $W_0 > 0.15$ Å (sample S4), and is shown, normalized by $\bar{\varrho} = 2.1$, in Figure 2.12a. It can be seen that after collapsing complexes into single systems, there is no correlation signal corresponding to the velocity separations of clusters of galaxies. However, significant signal persists for velocity separations of $4000 \leq \Delta v \leq 7000$ km s^{-1}. We simulated this effect by placing systems in the redshift
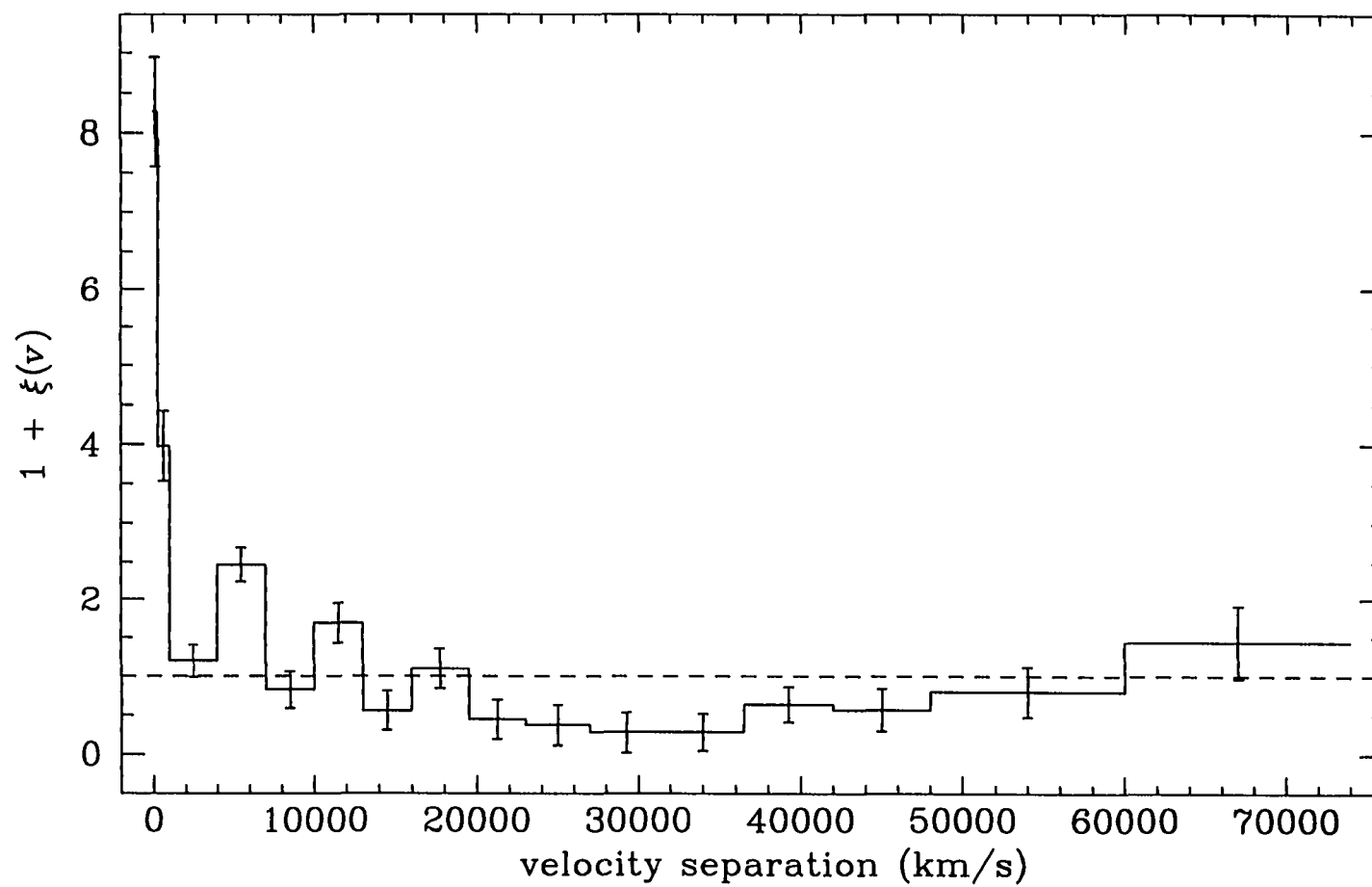
FIGURE 2.10—Two-point velocity correlation function for the 44 C IV absorbers in sample S2. Error bars represent 1σ uncertainties for a random distribution of absorbers.
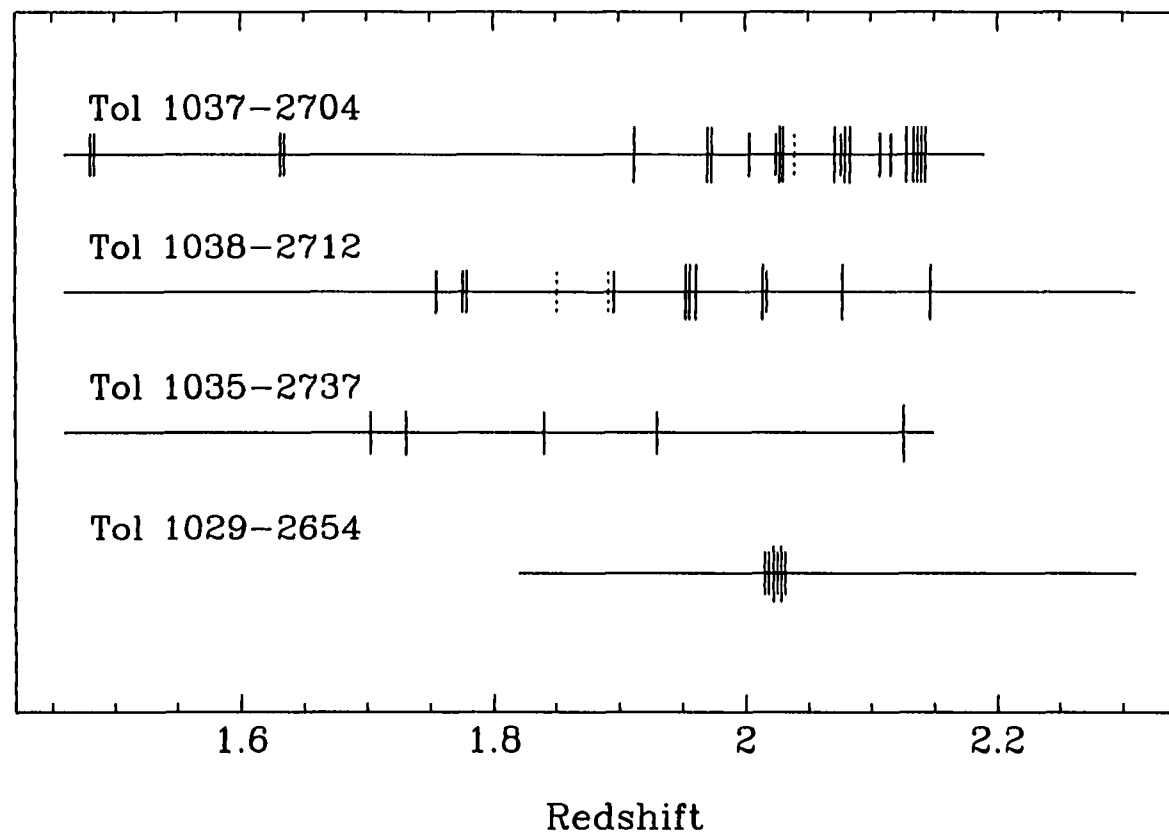
FIGURE 2.11—Redshift distribution of C IV systems toward the lines of sight to the four QSOs. The long vertical lines represent the certain systems, and the short lines represent the probable systems. The possible systems are indicated by dotted lines. Some of the closely spaced systems have been shifted slightly to distinguish them in the plot.

range $1.80 \lesssim z_{abs} \lesssim 2.15$ with velocity separations of 5500 ± 1000 km s^{-1}. We also required that some of the absorbers in the line of sight to Tol 1037−2704 have redshifts $z_{abs} = 1.45$ and 1.65 in order to simulate the apparent deficit of signal in the largest velocity bins. The result of the simulations is shown in Figure 2.12b and shows excellent agreement with the observed correlation function. The peak in the velocity splitting histogram corresponds to a comoving spatial scale of $\sim 30 - 40\,h^{-1}$ Mpc. Since the power associated with virialized clusters on smaller scales has been removed, we can be confident that this highly significant (4.3σ) peak represents power on supercluster scales.

For small velocity separations, there is no easy way to relate the velocity correlation function to the spatial correlation function derived from 3-dimensional surveys without some knowledge of the internal structure, kinematics and small scale clustering properties of the absorbers (HHW). However for large velocity separations, the relationship between the correlation functions is straightforward. Adopting the model of HHW, the velocity correlation function resembles a Gaussian of width σ at small velocities, and tails off as a power law at large velocities. Based on observations of nearby galaxies and clusters, it is reasonable to assume $\sigma \simeq 300$ km s^{-1}. For separations greater than 3σ ($\simeq 900$ km s^{-1}), the contribution to $\xi(v)$ from the Gaussian component becomes negligible and $\xi(v)$ is dominated by the power-law component. Therefore for velocity differences exceeding 1000 km s^{-1}, it is possible to compare $\xi(r)$ directly with $\xi(v)$.

The amplitude of the correlations is estimated to be 2.35 ± 0.55 in the velocity bin $4000 \leq \Delta v \leq 7000$ km s^{-1} where most of the power exists (Figure 2.12). This value was determined from the two-point correlation function for the S4 sample where velocity separations on scales less than 1000 km s^{-1} have been removed. This ensures that the correlation function on large scales is uncontaminated by "clustering" effects that would arise when the splittings are calculated between all the members of a complex and allows direct comparison with the spatial correlation function of clusters of galaxies.

The two-point autocorrelation function $\xi_{cc}(r)$ of 351 Abell clusters for richness classes
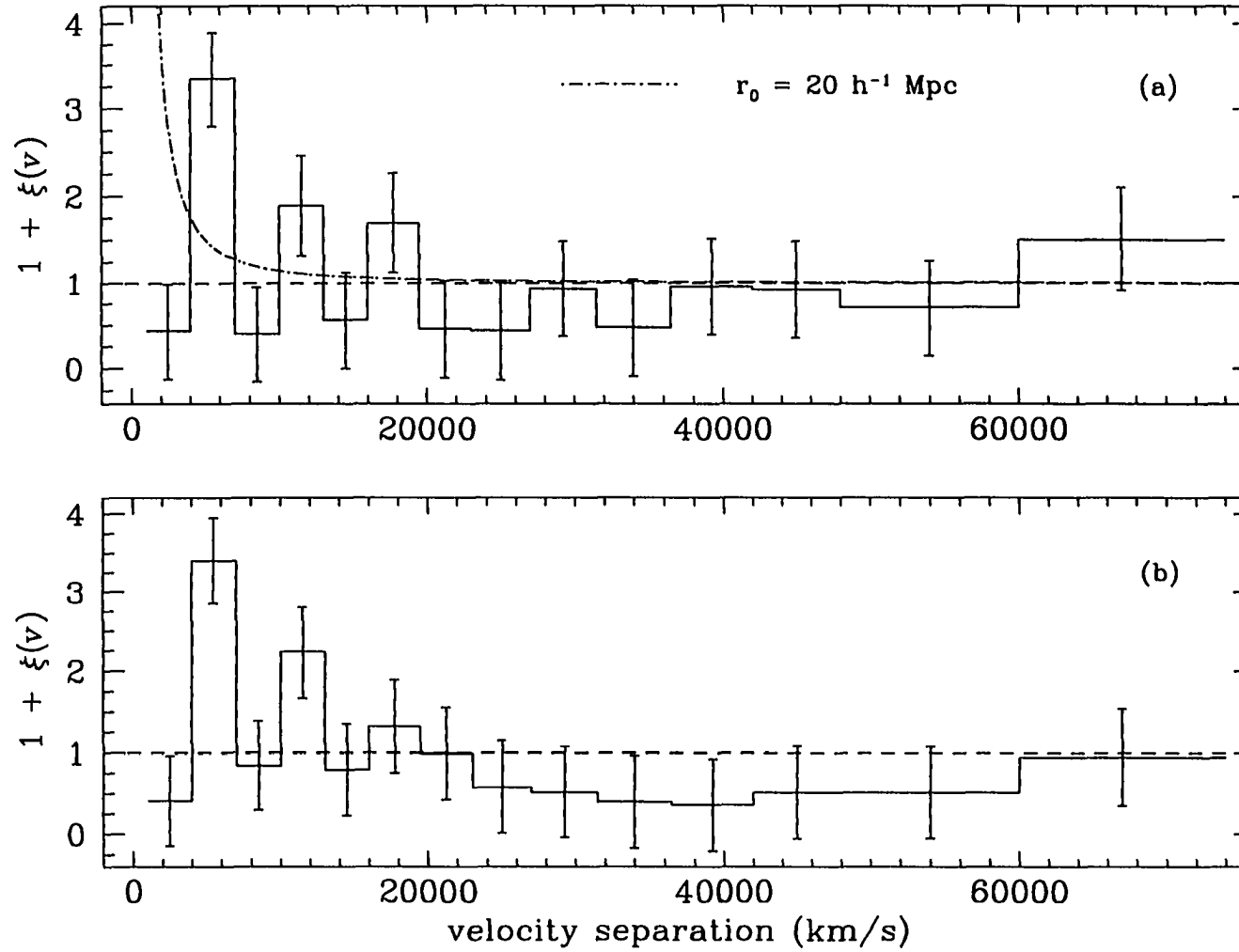
FIGURE 2.12—(a) Two-point velocity correlation function for the 16 C IV absorbers in sample S4. $\xi(v)$ is 2.35 ± 0.55 in the bin corresponding to the velocity separations of $4000 < v < 7000$ km s^{-1}. For $v > 7000$ km s^{-1}, $\xi(v)$ is consistent with no clustering signal. (b) As (a) for simulated samples of aborbers.

RC $= 0$ and RC > 1 is well-described between $r = 10$ and $70\,h^{-1}$ Mpc by a power law $(r/r_0)^{-1.8}$ where $r_0 = 20\,(\pm 4.3)\,h^{-1}$ Mpc (Postman, Huchra & Geller 1992). We have superimposed this relation, assuming a correlation length $r_0 = 20\,h^{-1}$ Mpc, onto the correlation function derived in Figure 2.12a. The amplitude of the correlation function toward the Tololo QSOs at comoving scales of $\sim 30 - 40\,h^{-1}$ Mpc is clearly significantly larger than $\xi_{cc}(r)$ for even the richest (RC > 1) clusters of galaxies.

2.6.2 Spatial Correlation Function

The spatial correlation function $\xi(r)$ was determined in the same manner as the velocity correlation function, but this time pairing systems along *different* lines of sight in order to obtain a measure of the true spatial clustering. Again we decided on a set of bins such that the average number of expected pairs based on randomly distributed absorbers was roughly the same in each bin. This time the bin sizes varied nonuniformly as a function of comoving separation since there is a tendency for the number of observed pairs to accumulate near the perpendicular separations of neighboring lines of sight. To estimate number of observed pairs in each bin, we treated each redshift system along a given line of sight in turn as a reference system and calculated the redshift intervals in each of the neighboring Tololo lines of sight that corresponded to the comoving separation represented by that bin. We then checked that the intervals fell within the redshift range sampled by the data, and counted the number of redshift systems that fell in the respective intervals to get the number of observed pairs.

The number of expected pairs was determined using the same catalog of C IV absorption systems used to estimate the redshift correlation function. Intervals of size ± 200 Mpc were used to estimate the number density of systems per unit redshift since no clustering is evident on spatial scales greater than about 150 Mpc (Bahcall & Soneira 1983). We found the centers of the bins in which N_{obs} was determined, and calculated the redshift intervals with respect to those centers in each of the neighboring lines of sight that corre-

sponded to the comoving separation of the larger (± 200 Mpc) intervals. We then adjusted the intervals so that they fell within the redshift range spanned by the data of the catalog QSOs, and counted the number of redshift systems in each catalog line of sight which fell within the larger intervals. This is equivalent to setting each of the catalog QSOs at the angular separations of the Tololo QSOs. Finally, in a manner analogous to the redshift correlation function, we derived the average number of redshift systems per unit redshift by dividing the total number of redshift systems by the total pathlength spanned by the large bins in which C IV system would have been detected. We then multiplied this average number density of systems by the small redshift intervals to get the number of expected pairs in that bin.

As before, we assumed $q_0 = 0.5$. This simplified the computations, since the spatial separation of any two absorbers is given by the familiar Euclidean law of cosines, $r_{12} = (r_1^2 + r_2^2 - 2r_1 r_2 \cos \alpha)^{\frac{1}{2}}$ where α is the angular separation of the neighboring lines of sight and $r_{1,2} = \frac{2c}{H_0}[1 - (z_{1,2} + 1)^{-\frac{1}{2}}]$ is the comoving distance to the absorbers. We restricted the range of study to $12 \leq r \leq 440$ Mpc where the lower limit corresponds to the perpendicular separation of the closest pair of QSOs.

The resultant spatial correlation function $\xi(r)$ is shown normalized by $\bar{\varrho} = 2.0$ in Figure 2.13 for sample S4, which contains no correlation signal from clusters of galaxies (cf. § 2.6.1). The error bars are the 1σ statistical errors for a Poisson distribution of redshifts (eq. 2.5). There is no convincing evidence for any spatial correlation signal over scales from $18 \leq r \leq 440\,h^{-1}$ Mpc. However a signal of the same amplitude and scale as the velocity correlation function (Figure 2.12), is present in the smallest bin $r < 18\,h^{-1}$ Mpc, although in this case the error bars are larger because of the sparse sampling of this pencil beam experiment. All of the correlation signal in this bin is derived from the systems belonging to the two closest QSOs, Tol 1037−2704 and Tol 1038−2712; the separations of the other two QSOs are too large to make any contribution on comoving scales less than $\sim 30\,h^{-1}$ Mpc. We estimate the amplitude of the correlations to be $\xi(r) = 2.7 \pm 1.2$

between comoving separations $12 < r < 18\,h^{-1}$ Mpc. In order to test whether the signal in this bin is caused primarily by the high density of systems toward Tol 1037−2704 and Tol 1038−2712, we performed Monte Carlo simulations with random datasets keeping the number of systems along each line of sight fixed. In 1000 trials, the measured signal, $\xi(r) = 2.7$, was exceeded 32 times, implying a slightly lower significance (2.1σ) than inferred by its estimated uncertainty.

In Figure 2.13, we have superimposed the power-law solution of the two-point correlation function for rich clusters of galaxies derived by Postman et al. (1992). The amplitude of spatial correlation function for the Tololo grouping is consistent with that of rich clusters.

2.6.3 Superclustering of the Absorbers

The detection of correlation on velocity scales out to $7000\,\mathrm{km\ s^{-1}}$, or comoving spatial scales of $\sim 30 - 40\,h^{-1}$ Mpc, is consistent with the result of HHW, who found significant correlations out to velocity separations of $10,000\,\mathrm{km\ s^{-1}}$ corresponding to spatial scales of $\sim 60\,h^{-1}$ Mpc in the SBS sample of C IV systems. We also find evidence for marginally significant spatial clustering on comoving scales of $r < 18\,h^{-1}$ Mpc. Even for the richest clusters of galaxies, $\xi(r) < 1$ on comoving spatial scales less than $\sim 25\,h^{-1}$ Mpc. Our results suggest clustering on scales larger than that of present-day cluster correlations and appear to be consistent with scales characteristic of superclusters.

The stronger clustering amplitude toward the Tololo QSOs as compared with the observed correlations of the richest clusters of galaxies can be viewed in one of two ways: (1) we are viewing only a small region of space where there is a strong departure from the average clustering properties of galaxy clusters; or, (2) we are seeing evidence for clustering on supercluster scales. Our data do not sample a sufficient volume of space to distinguish between these scenarios.

The spatial correlation functions of clusters of galaxies are calculated in volumes con-
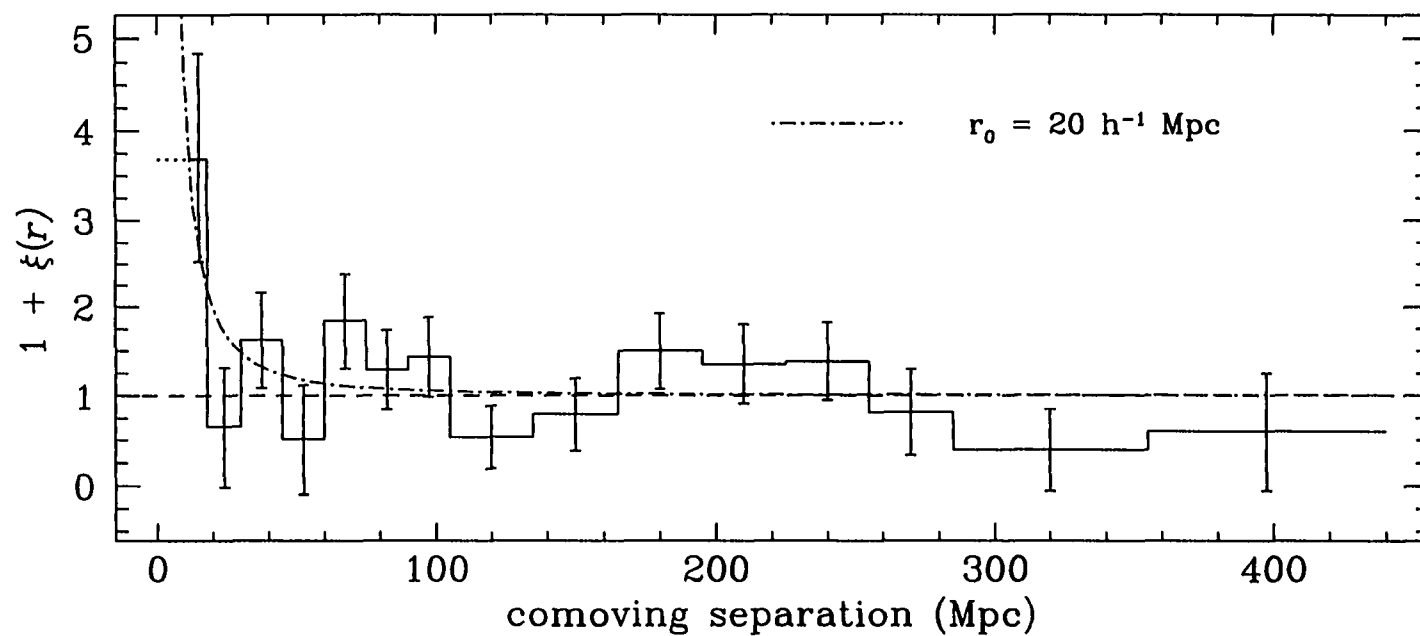
FIGURE 2.13—Two-point spatial correlation function for the 16 C IV absorbers in sample S4. The error bars represent the 1σ uncertainties. $\xi(r)$ is 2.7 ± 1.2 in the lowest bin ($r < 18$ Mpc), corresponding a marginally significant detection of 2.1σ, and is consistent with zero everywhere else.

siderably larger than our pencil-beam study and therefore represent an average $\xi(r)$ over a large volume of space. On the other hand, this work samples only a small fraction of the entire volume and the correlation signal may represent a region of strong biasing. However correlations on such large scales are not unprecedented. For example, HHW attribute the clustering signal out to velocities of $10,000$ km s^{-1} as being due to a large cluster of systems in the QSO PKS 0237−233. In fact, if PKS 0237−233 is replaced by one of the Tololo QSOs, the correlation amplitude between 1000 and $10,000$ km s^{-1} becomes $\xi(v) = 0.26 \pm 0.12$ for Tol 1037−2704 and 0.21 ± 0.12 for Tol 1038−2712 (HHW). Therefore the clustering signal of the individual lines of sight remains significant even in an average sample of C IV absorbers, although the amplitude is diminished from the value computed using only the four Tololo QSOs.

Bahcall & Burgett (1986) have studied the spatial correlation function of a sample of superclusters from the catalog of Bahcall & Soneira (1984). The sample is complete to $z \leq 0.08$ and contains 16 superclusters with $RC \geq 1$ clusters and overdensity factor $f = 20$, and 26 with $RC \geq 0$ clusters and $f = 20$. The results of their study reveal correlations at significance levels of $2 - 3\sigma$ on scales as large as $\sim 75 - 150\,h^{-1}$ Mpc. Fitting a power law of the form $r^{-1.8}$ which best fits the galaxy and cluster correlation functions, they found

$$\xi_{SC} \simeq \left(\frac{r}{60}\right)^{-1.8} \tag{2.6}$$

with a factor of two uncertainty, although it is not obvious that the supercluster correlation function should follow the power law form. The implied correlation scale of superclusters is $\sim 60\,h^{-1}$ Mpc. Similar results have been obtained by Kopylov et al. (1987) who studied the correlation function to $z \lesssim 0.2$.

Assuming the same power law form, the peak in the correlation function in Figure 2.12 implies a correlation scale of $\sim 50\,h^{-1}$ Mpc with an associated uncertainty of $\sim 20\,\%$. The supercluster correlation function of Bahcall & Burgett was calculated between spatial scales of $\sim 70 - 150\,h^{-1}$ Mpc since no meaningful correlation is expected below the typical

separation between superclusters ($\gtrsim 60\,h^{-1}$ Mpc). On the other hand in our pencil-beam experiment correlations on scales $< 60\,h^{-1}$ Mpc can be expected because we are likely viewing the linear distances between superclusters in projection and we estimated the correlation scale from a single point at $35\,h^{-1}$ Mpc. Despite the differences between the methods of calculating the correlation functions, we find the characteristic scale of clustering determined from our data to be remarkably consistent with that derived by Bahcall & Burgett for superclusters in the local universe.

2.7 Discussion

Arguments favoring an intervening supercluster to explain the apparent overdensity of C IV systems in the sightlines to Tol 1037−2704 and Tol 1038−2712 have been presented by S87. They have suggested that in order to get the rich absorption spectra in the two lines of sight, the supercluster must be oriented in such a way that there is an unusually high density of absorbing matter along the lines of sight. The most plausible explanation is that our line of sight coincides with either the long axis of a large-scale "filament" or the plane of a large-scale "sheet" of galaxies. Our results are consistent with, and strengthen the support for, the interpretation of the C IV absorption line systems as arising from material associated with a supercluster.

Our search for C IV absorption line systems in the spectra of the two nearby QSOs, Tol 1035−2737 and Tol 1029−2654, have revealed several new absorption complexes with redshifts coincident to those in the original Tololo pair. In addition to the five matches between the sightlines to Tol 1037−2704 and Tol 1038−2712, at least four of the five complexes in Tol 1035−2737 appear to match systems in Tol 1038−2712, and both complexes in Tol 1029−2654 seem to have redshifts in common with systems in both Tol 1037−2704 and Tol 1038−2712.

As a test of whether the absorbers along the lines of sight to the Tololo QSOs are in any way associated, we evaluated the significance of the apparent correlations in two ways.

First, we calculated the probability of obtaining the observed number of matches between adjacent lines of sight, allowing a system in a given line of sight to match at most one system from each of the other lines of sight to within the redshift window Δz. We took Tol 1038−2712 as the fiducial object since the systems in its spectrum match with the most number of systems along the other three lines of sight, noting that in some cases this gives the more optimistic measure of the significance. At the large angular separations of the neighboring QSOs, larger velocity separations can be expected between the C IV systems due to Hubble flow if the expansion of the absorbing structure has a nonperpendicular component to the line of sight, and the redshift window in which possibly correlated absorption can be found is correspondingly larger, increasing the probability of finding spurious absorption matches.

The velocity shift expected from Hubble expansion between absorbers located on two sightlines separated by the perpendicular distance $D_\perp$ and belonging to a comoving structure of size $R \geq D_\perp$ is given by (J88)

$$\Delta v = H(z)\, D_\perp \tan\alpha = 2\, c\,\theta\, [(1+z)^{\frac{1}{2}} - 1]\tan\alpha \qquad (2.7)$$

where $H(z) = H_0(1+z)^{\frac{3}{2}}$ is the value of the Hubble constant at redshift z and $(-\pi/2) \leq \alpha \leq (\pi/2)$ is the angle between the plane of the sky and the line connecting the two absorbers on the the two sightlines. If the absorbing material is distributed in a thin sheet then the velocity shifts can be arbitrarily large depending on the orientation of the sheet. For example for $|\alpha| \simeq \pi/2$ and the sheet is viewed at a glancing angle then the probability of finding spurious absorption systems within the window will be large. For a spherical distribution, however, we have $|\alpha| \leq \pi/4$ and we can evaluate the probability of the detected systems being correlated against the probability of finding similar acceptable redshift coincidences by chance.

For Tol 1037−2704, the velocity separation expected from the Hubble expansion is $\Delta v \simeq 2000$ km s^{-1} or $\Delta z \simeq 0.02$; for Tol 1035−2737, $\Delta v \simeq 5000$ km s^{-1} or $\Delta z \simeq 0.05$; and for Tol 1029−2654, $\Delta v \simeq 20,000$ km s^{-1} or $\Delta z \simeq 0.20$. We have organized the

C IV absorption systems in Table 2.9 such that they coincide in velocity to better than that expected from the Hubble flow. In fact, as we can see in Table 2.9, the systems in Tol 1038–2712 coincide to better than $\Delta v \simeq 4000$ km s^{-1} and 3000 km s^{-1} with those in Tol 1035–2737 and Tol 1029–2654, respectively, so we adopt these values as our criterion for a match. Nevertheless, a few of the pairings are somewhat arbitrary. For example, the $z_{abs} = 1.7306$ system in Tol 1035–2737 could be matched with either the $z_{abs} \simeq 1.755$ or $z_{abs} \simeq 1.777$ systems in Tol 1038–2712. Similarly the $z_{abs} = 1.9852$ system in Tol 1029–2654 could be associated with the $z_{abs} \simeq 1.972$ and 1.955 systems in Tol 1037–2704 and Tol 1038–2712, respectively, or with the $z_{abs} \simeq 2.003$ system in Tol 1037–2704.

We calculated the significance of the matches in Table 2.9 by distributing the number of systems observed in Tol 1037–2704, Tol 1035–2737 and Tol 1029–2654 over the redshift windows in which systems would have been observed in the spectrum of Tol 1038–2712, and evaluating the binomial probability $P(M, N, q)$ that one would obtain the observed number of coincidences N given the number of systems M in the fiducial line of sight, where q is the probability that a system match within Δz of another in the total red-shift window Δ. For Tol 1037–2704, $\Delta = 0.73$; for Tol 1035–2737, $\Delta = 0.69$; and for Tol 1029–2654, $\Delta = 0.49$. In this calculation, we counted each complex as one system since members of a complex are not independent, and require that each system in a given spectrum coincide with only one other in the reference spectrum Tol 1038–2712. For Tol 1037–2704, the probability is $P(8, 5, 0.055) \simeq 3 \times 10^{-3}$; for Tol 1035–2737, $P(8, 4, 0.12) \simeq 0.3$; and for Tol 1029–2654, $P(8, 1, 0.082) \simeq 0.6$.

The significance of the absorption matches is high between the original pair, but poor for the other two lines of sight. In fact, if we use Tol 1037–2704 as the fiducial object, the probability of obtaining five matches in Tol 1038–2712 becomes $P \simeq 0.02$, consistent with only a marginal significance for those matches. As pointed out by S87, the high density of absorption systems in the narrow redshift range $1.70 \leq z_{abs} \leq 2.15$ increases

the probability that the pattern of redshift matches is due to chance. Moreover, because we have no way of knowing, post hoc, whether we have grouped the systems correctly in Table 2.9, this calculation is prone to significant uncertainty.

An alternative to the probability calculations above, which does not require a fiducial choice, is to take each absorber in turn and find its closest velocity match in each of the *other* lines of sight. Note that this probability calculation allows for a system to match more than one system in the other lines of sight. The histogram of velocity differences is shown in Figure 2.14. We also randomly selected absorbers among the four lines of sight for 1000 realizations, preserving the number of absorbers along each sightline and found their closest velocity match. By using these distributions of δv (observed and simulated), we obtained some idea about the significance of the observed matches.

The simulated distribution (*dashed histogram*) and its standard deviation (*errorbars*) are shown in Figure 2.14a. For velocity differences $\Delta v \leq 2000$ km s^{-1} the observed distribution deviates from randomly distributed redshifts at the $\sim 2.1\sigma$ level. In Figure 2.14b, we have plotted the cumulative distributions for the simulated and observed redshifts. A KS test gives a $\sim 1.7\%$ probability that the observed redshifts are drawn from a random population of redshifts. This agrees with the above probability analysis which showed weak evidence for correlations between pairs of sightlines. We find that the correlation among all four lines of sight considered together is marginal.

There is clearly an overdensity of C IV absorbers toward Tol 1037−2704 and Tol 1038− 2712. Indeed, that is what first called attention to these QSOs. We can estimate the overdensity of these systems from the average background number density of systems per unit redshift given in Steidel (1990). Over the redshifts spanned by our data, the mean number density of systems per unit redshift interval taken from Steidel (1990) is $dN/dz \sim 2.8$ for systems with rest equivalent widths $W_o > 0.15$ Å, leading to an expected number of C IV doublets of ~ 2 in Tol 1037−2704 and ~ 2.5 in Tol 1038−2712, over the pathlengths searched for C IV absorption. The observed number of detections is 12
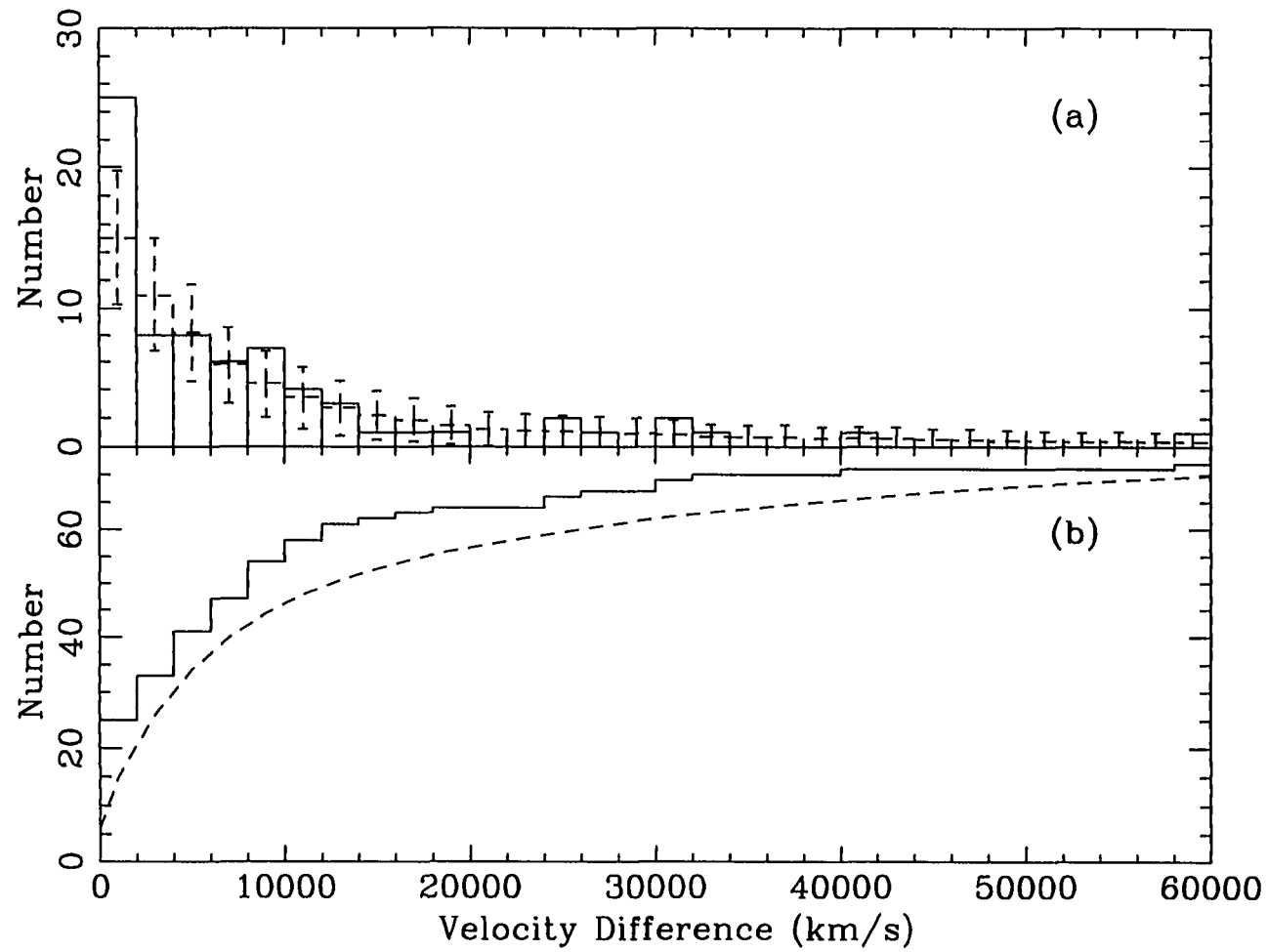
FIGURE 2.14—(a) Distribution of velocity differences between "nearest neighbors" in different lines of sight for the observed (*solid*) and simulated (*dotted*) systems. (b) Cumulative distribution of velocity differences for the observed (*solid*) and simulated (*dashed*) systems.

in Tol 1037–2704 and 5 in Tol 1038–2712 for the same equivalent width limit. This represents a factor of ~ 6 overdensity in Tol 1037–2704 and ~ 2 in Tol 1038–2712.

We can also estimate the overdensity of C IV absorption systems along the lines of sight to Tol 1035–2737 and Tol 1029–2654. Taking the mean number density of systems again from Steidel (1990) and restricting the wavelength range to the region from Lyman α to long wavelength limit of the spectrum, 4360 – 5130 Å, we predict the number of systems to be ~ 1.5 with $W_0 > 0.15$ Å. We observe 2 C IV absorption systems in each of Tol 1035–2737 and Tol 1029–2654 that meet the same equivalent width criterion, evidence of no overdensity in C IV absorbers. However, this calculation ignores the fact that most of the C IV systems observed in Tol 1035–2737 and Tol 1029–2654 lie in the narrow redshift range in which we observe coincidences. Restricting the redshift range to the region exhibiting coincident C IV systems, the predicted number of systems is ~ 1 in each spectrum. The observed number of detections in Tol 1029–2654 over this redshift range could be taken as offering marginal evidence for a factor of 2 overdensity. Finally, we note that the number of detections represent lower limits since the spectra are not sensitive to systems with $W_0 > 0.15$ Åover their entire wavelength range.

The spatial overdensity of intervening clouds toward the Tololo QSOs lend further support for the interpretation that the four lines of sight intersect material associated with an intervening supercluster. The presence of an overdensity in the spectrum of the most distant QSO Tol 1029–2654 in the group suggests a lower limit on the size of the supercluster of $\sim 30\,h^{-1}$ Mpc in the transverse direction. Taking only the redshift range $(1.73 \leq z \leq 2.15)$ in which we observe coincident systems, we estimate the proper linear extent along the line of sight to be $\sim 80\,h^{-1}$ Mpc.

Structures of this size are observed in the local universe. Typical superclusters have dimensions anywhere from $30 - 150\,h^{-1}$ Mpc for the highest to lowest density systems (Bahcall & Soneira 1984). In addition, studies of the spatial distribution of rich clusters show evidence for superclustering on scales of $\sim 50 - 150\,h^{-1}$ Mpc (Bahcall & Soneira

1983, 1984; Postman *et al.* 1992). There is also considerable evidence from surveys of the local galaxy distribution for large coherent structures extending over many tens of Mpc (e.g. de Lapparent, Geller & Huchra 1986). The dimensions of the largest known structure, "The Great Wall", are at least $\sim 60 \times 170\,h^{-1}$ Mpc (Geller & Huchra 1989). If large-scale structures participate in the general Hubble flow, then the dimensions of the observed intervening matter are more like $\sim 90 \times 240\,h^{-1}$ Mpc and the most likely local counterparts are structures such as the "Great Wall".

Recent $\Omega = 1$ cold + hot dark matter (CHDM) N-body simulations which probe scales of ~ 100 Mpc find coherent large scale structures composed of massive galaxy halos to be already in place at $z \sim 2$ (Primack 1995). Smaller scale CDM simulations which incorporate hydrodynamics and form galaxies over a range of masses predict $\xi(r) < 1$ on comoving scales of $10\,h^{-1}$ Mpc at $z \sim 2$ (Evrard *et al.* 1994). In all hierarchical clustering models, the amplitude of large structures is lower at $z \sim 2$ than observed in the local universe. Whether or not the large clustering amplitude seen along the lines of sight towards the Tololo QSOs is in conflict with the standard CDM model depends on what type of galaxy halo is represented by the C IV absorbers. In this chapter, we have focused on a region known to have an overdensity of absorbers. If strong clustering signals are seen along other lines of sight, they could pose a considerable challenge to theories of large scale structure formation.

A remaining complication with the supercluster hypothesis is the presence of the smooth, broad C IV system at $z_{abs} \simeq 2.08$ in Tol 1038−2712, which even our high resolution observations do not resolve into individual C IV doublets. Such systems are most commonly associated with BAL QSOs. An alternative explanation that is consistent with the intervening supercluster hypothesis is if the line of sight to Tol 1038−2712 pierces a cooling flow associated with the cores of clusters and groups of galaxies. The FWHM of the each component of the C IV absorption doublet at $z_{abs} \simeq 2.08$ is ~ 13 Å, corresponding to a velocity spread of ~ 800 km s^{-1}. The expected velocity range from a single cooling

flow seen in absorption is expected to be comparable to the line widths of the emission-line nebulae, or $\sim 500 - 1000\,\mathrm{km\ s^{-1}}$ (Baum 1992). Since all our knowledge of cooling flows comes from low redshift clusters, it is yet to be determined whether the the properties of high redshift cooling flows are consistent with what we observe in Tol 1038−2712. Crawford *et al.* (1987) argue that the covering factor is sufficient for *most* lines of sight to pass through a cooling flow, though their estimate of the cooling radius may be overestimated by factors of $\sim 2 - 10$.

Further mapping of the large-scale distribution of the intervening absorption clouds toward the Tololo QSOs clearly requires a larger grid of absorption probes. The multiplex advantage to multifiber spectrographs offers a promising and efficient means of sampling many QSOs (> 40 in a 1° field) simultaneously with sufficient S/N to be sensitive to C IV absorption. Studies of this kind will provide important information on the growth and evolution of large-scale structure in the early universe.

TABLE 2.1

PROGRAM QSOs

QSO	R.A. (1950)	Decl. (1950)	m_B	z_{em}
Tol 1037-2704.....	$10^h36^m00\overset{s}{.}1$	$-27°03'37''$	17.4	2.193
Tol 1038-2712.....	10 38 10.4	-27 12 08	17.9	2.331
Tol 1035-2737.....	10 35 47.2	-27 37 14	19.0	2.159
Tol 1029-2654.....	10 29 35.4	-26 54 18	19.5	2.586

NOTE.— All coordinates, magnitudes and redshifts are from Jakobsen & Perryman (1992), except for Tol 1029−2654 whose coordinates and magnitude were estimated from our objective prism survey. Details of the redshift determination for this object are given in the text.

TABLE 2.2

JOURNAL OF OBSERVATIONS

QSO	Date	Exposure (s)	Wavelength (Å)	Resolution (Å)
Tol 1037–2704......	1992 Feb 29	5400	3810 – 5130	0.15
	1992 Feb 29	5400	3810 – 5130	0.15
	1992 Feb 29	5400	3810 – 5130	0.15
Tol 1038–2712......	1992 Feb 29	5400	3810 – 5130	0.15
	1992 Feb 29	5400	3810 – 5130	0.15
	1992 Mar 1	5400	3810 – 5130	0.15
	1992 Mar 1	5400	3810 – 5130	0.15
Tol 1029–2654......	1992 Mar 2	5400	3810 – 5130	0.15
	1992 Mar 2	5400	3810 – 5130	0.15
	1992 Mar 2	5400	3810 – 5130	0.15
	1992 Mar 2	5400	3810 – 5130	0.15
	1992 Mar 2	7200	3810 – 5130	0.15
Tol 1035–2737......	1992 Mar 3	5400	3810 – 5130	0.15
	1992 Mar 3	5400	3810 – 5130	0.15
	1992 Mar 3	5400	3810 – 5130	0.15
	1992 Mar 3	5400	3810 – 5130	0.15
	1992 Mar 3	8400	3810 – 5130	0.15

TABLE 2.3

Absorption Lines of Tol 1037–2704

No.	λ_{obs}(Å)	$\sigma(\lambda)$	W_{obs}(Å)	$\sigma(W)$	S/N	ID	z_{abs}	Notes
1	3827.95	0.03	0.91	0.05	17.2	Lyα	2.14884	
2	3837.98	0.06	1.86	0.07	28.3	Lyα	2.15709	
3	3843.38	0.01	0.59	0.03	21.4	C IV 1548	1.48248	
4	3844.53	0.02	0.40	0.03	14.8	C IV 1548	1.48322	
5	3849.74	0.02	0.46	0.03	17.0	C IV 1550	1.48246	
6	3850.92	0.02	0.31	0.03	11.7	C IV 1550	1.48323	
7	3858.95	0.02	0.19	0.02	9.7	Lyα	2.17434	
8	3859.86	0.04	0.12	0.02	5.5	Lyα	2.17509	
9	3862.51	0.02	0.71	0.03	27.5	Lyα	2.17727	
10	3864.56	0.02	0.29	0.02	15.3	Lyα	2.17895	
11	3884.73	0.04	0.24	0.04	6.0	N V 1238	2.13583	a
12	3886.77	0.02	0.59	0.03	17.9	C II 1334	1.91246	
13	3925.76	0.06	0.18	0.03	6.6			
14	3934.82	0.01	0.41	0.02	26.6			
15	3935.97	0.02	0.33	0.02	16.9			
16	3942.58	0.01	0.41	0.02	21.6	Si II 1260	2.12798	
17	3952.56	0.03	0.11	0.02	5.8	Si II 1260	2.13590	
18	3953.84	0.04	0.29	0.03	9.6			
19	3957.12	0.02	1.97	0.04	48.5	Si II 1260	2.13952	b
20	3965.50	0.04	0.09	0.02	5.6	C II 1334	1.97145	
21	3966.35	0.02	0.26	0.02	11.6	C II 1334	1.97209	
22	3969.69	0.02	0.27	0.02	11.5			
23	4012.84	0.01	0.15	0.01	12.5			c
24	4040.77	0.04	0.16	0.02	7.1	C II 1334	2.02785	
25	4041.62	0.03	0.18	0.02	8.2	C II 1334	2.02849	
						Fe II 2382	0.69619	b
26	4059.30	0.01	0.42	0.02	23.1	Si IV 1393	1.91249	
27	4075.72	0.06	0.20	0.03	6.0			
28	4076.98	0.02	0.29	0.02	14.5	C IV 1548	1.63336	
29	4078.48	0.02	1.46	0.03	48.7	C IV 1548	1.63433	
30	4083.83	0.08	0.14	0.02	7.7	C IV 1550	1.63341	
31	4085.28	0.02	1.32	0.03	44.0	C IV 1550	1.63435	b
						Si IV 1402	1.91229	b
32	4087.82	0.02	1.05	0.03	32.1	O I 1302	2.13924	b
33	4094.81	0.03	1.05	0.05	21.1	Si II 1304	2.13930	b
34	4135.09	0.05	0.17	0.03	5.1			
35	4140.82	0.05	0.12	0.02	6.3			
36	4141.47	0.04	0.19	0.04	5.4	Si IV 1393	1.97145	a
37	4142.41	0.02	0.58	0.04	14.3	Si IV 1393	1.97212	
38	4161.39	0.02	0.13	0.02	7.3			c
39	4169.24	0.04	0.28	0.04	7.2	Si IV 1402	1.97215	
40	4174.59	0.05	0.51	0.04	12.0	C II 1334	2.12813	
41	4185.09	0.05	0.18	0.03	5.0	C II 1334	2.13600	
42	4189.77	0.04	2.18	0.06	36.4	C II 1334	2.13950	b
43	4193.54	0.03	0.15	0.03	5.8	C II 1334	2.14233	
44	4220.18	0.03	0.85	0.06	14.7	Si IV 1393	2.02792	
45	4220.96	0.02	0.29	0.05	6.4	Si IV 1393	2.02848	
46	4239.92	0.02	0.16	0.02	8.9			c

TABLE 2.3—*Continued*

No.	λ_{obs}(Å)	$\sigma(\lambda)$	W_{obs}(Å)	$\sigma(W)$	S/N	ID	z_{abs}	Notes
47	4247.50	0.04	0.49	0.06	8.5	Si iv 1402	2.02794	
48	4248.24	0.05	0.12	0.02	5.5	Si iv 1402	2.02847	
49	4279.79	0.12	0.90	0.07	13.1	Si iv 1393	2.07069	
50	4289.57	0.32	2.93	0.23	12.8	Si iv 1393	2.07771	b
51	4297.61	0.13	2.67	0.20	13.1	Si iv 1393	2.08348	
52	4307.15	0.08	0.86	0.05	16.1	Si iv 1402	2.07046	
53	4316.95	0.40	1.52	0.22	6.8	Si iv 1402	2.07745	b
54	4324.55	0.16	2.55	0.20	12.9	Si iv 1402	2.08286	
55	4360.24	0.03	1.06	0.03	35.3	Si iv 1393	2.12841	
56	4370.85	0.04	0.68	0.03	20.0	Si iv 1393	2.13601	
57	4375.59	0.02	2.09	0.03	69.6	Si iv 1393	2.13943	b
58	4379.74	0.04	0.11	0.02	5.7	Si iv 1393	2.14240	a
59	4388.36	0.04	0.63	0.03	21.4	Si iv 1402	2.12835	b
						Fe ii 2586	0.69654	b
60	4399.20	0.06	0.36	0.03	10.6	Si iv 1402	2.13608	
61	4403.76	0.02	1.54	0.03	51.3	Si iv 1402	2.13933	b
62	4410.71	0.04	0.07	0.01	5.4	Fe ii 2600	0.69631	
63	4446.57	0.02	0.28	0.02	15.5	Si ii 1526	1.91252	
64	4509.18	0.01	0.76	0.03	27.5	C iv 1548	1.91253	
65	4516.67	0.02	0.65	0.03	20.3	C iv 1550	1.91253	
66	4600.45	0.06	0.48	0.06	7.9	C iv 1548	1.97148	
67	4601.75	0.03	1.01	0.06	16.8	C iv 1548	1.97232	
68	4607.83	0.10	0.38	0.06	6.8	C iv 1550	1.97131	
69	4609.45	0.03	0.68	0.05	14.7	C iv 1550	1.97235	
70	4649.79	0.02	0.26	0.03	9.0	C iv 1548	2.00335	
71	4657.56	0.05	0.20	0.02	9.4	C iv 1550	2.00338	
72	4683.44	0.01	0.22	0.02	13.3	C iv 1548	2.02508	
73	4687.72	0.02	0.97	0.06	16.2	C iv 1548	2.02785	
74	4688.67	0.03	0.66	0.06	11.5	C iv 1548	2.02846	
75	4691.26	0.02	0.11	0.02	7.0	C iv 1550	2.02511	
76	4695.50	0.02	0.87	0.05	17.6	C iv 1550	2.02782	
77	4696.46	0.03	0.44	0.05	8.9	C iv 1550	2.02846	
78	4705.23	0.05	0.18	0.02	6.4	C iv 1548	2.03915	a
79	4725.65	0.11	0.18	0.03	6.2			
80	4728.64	0.06	0.11	0.02	5.0			
81	4743.70	0.01	0.59	0.02	33.8	Mg ii 2796	0.69639	
82	4753.90	0.05	1.67	0.04	43.5	C iv 1548	2.07059	
83	4755.72	0.02	0.55	0.03	21.9	Mg ii 2803	0.69633	
84	4761.81	0.03	1.43	0.04	35.8	C iv 1550	2.07060	b
85	4764.06	0.05	0.69	0.03	23.0	C iv 1548	2.07716	b
86	4766.26	0.04	1.23	0.05	24.9	C iv 1548	2.07858	b
87	4772.74	0.05	7.61	0.13	59.7	C iv 1550	2.07765	b
						C iv 1548	2.08276	b
88	4781.35	0.05	3.75	0.10	39.0	C iv 1550	2.08320	b
89	4792.73	0.01	1.38	0.02	69.0	Si ii 1526	2.13926	b
90	4809.69	0.03	0.19	0.02	9.2	C iv 1548	2.10663	
91	4817.69	0.03	0.11	0.02	6.4	C iv 1550	2.10664	
92	4823.60	0.02	0.17	0.02	9.5	C iv 1548	2.11561	

TABLE 2.3—*Continued*

No.	λ_{obs}(Å)	$\sigma(\lambda)$	W_{obs}(Å)	$\sigma(W)$	S/N	ID	z_{abs}	Notes
93	4831.61	0.02	0.12	0.02	7.9	C IV 1550	2.11561	
94	4843.36	0.02	1.82	0.03	66.6	C IV 1548	2.12838	
95	4851.47	0.02	1.47	0.03	49.8	C IV 1550	2.12842	
96	4855.04	0.01	2.21	0.03	77.3	C IV 1548	2.13592	
97	4859.99	0.03	2.37	0.05	47.4	C IV 1548	2.13912	
98	4861.69	0.07	0.63	0.03	20.1	C IV 1548	2.14022	
99	4863.20	0.06	1.80	0.06	27.8	C IV 1550	2.13598	
100	4865.05	0.04	0.23	0.03	8.8	C IV 1548	2.14238	
101	4866.11	0.03	0.17	0.02	8.3	Al II 1670	1.91247	
102	4868.03	0.02	2.12	0.05	44.1	C IV 1550	2.13910	
103	4869.92	0.03	0.52	0.04	12.9	C IV 1550	2.14032	
104	4873.25	0.04	0.09	0.01	5.8	C IV 1550	2.14246	
105	4930.69	0.04	0.21	0.02	12.0			
106	4947.84	0.01	1.23	0.02	73.4			
107	4965.74	0.02	0.18	0.01	15.6	Al II 1670	1.97210	
108	5049.05	0.03	0.57	0.06	9.5	Fe II 1608	2.13908	
109	5049.77	0.04	0.42	0.06	7.0			

[a]Doublet component below 5σ equivalent width threshold.
[b]Probable blend.
[c]Possible spurious line.
[d]Probable chance coincidence.

TABLE 2.4

ABSORPTION LINES OF TOL 1038-2712

No.	λ_{obs}(Å)	$\sigma(\lambda)$	W_{obs}(Å)	$\sigma(W)$	S/N	ID	z_{abs}	Notes
1	3826.89	0.14	1.67	0.23	7.4	Lyα	2.14797	
2	3837.96	0.04	1.01	0.08	12.5	Lyα	2.15707	
3	3842.85	0.03	0.41	0.05	7.6	Lyα	2.16110	
4	3844.99	0.04	1.07	0.07	15.1	Lyα	2.16286	
5	3847.84	0.07	0.60	0.07	15.8	Lyα	2.16520	
6	3899.24	0.03	0.62	0.06	10.2	Lyα	2.20748	
7	3904.79	0.17	2.80	0.17	16.5	N v 1238 + 1242	2.14902	b
8	3905.77	0.02	0.56	0.04	12.6	Lyα	2.21285	
9	3908.35	0.03	1.27	0.05	25.4	Lyα	2.21498	
10	3930.19	0.09	0.19	0.03	5.8	Lyα	2.23294	
11	3934.28	0.02	2.71	0.05	54.2	Lyα	2.23631	
12	3941.83	0.02	0.22	0.03	8.7	Lyα	2.24252	
13	3942.53	0.03	0.17	0.03	5.7	Lyα	2.24309	
14	3943.37	0.05	0.36	0.06	6.3	C ii 1334	1.95487	d
15	3946.40	0.04	1.70	0.06	28.3	Lyα	2.24628	
16	3958.79	0.04	0.61	0.04	16.2	Lyα	2.25646	
17	3963.04	0.02	0.52	0.03	18.4	Lyα	2.25996	
18	3970.31	0.02	1.19	0.03	39.4	Lyα	2.26594	
19	3975.31	0.05	0.16	0.02	8.0	Lyα	2.27006	
20	3986.68	0.01	0.80	0.02	49.6	Lyα	2.27941	
21	3992.97	0.02	0.52	0.02	26.9	Lyα	2.28458	
22	3994.45	0.02	0.54	0.02	28.0	Lyα	2.28580	
23	3995.99	0.10	0.17	0.03	5.1	Lyα	2.28707	
24	3997.79	0.02	0.34	0.02	16.1	Lyα	2.28855	
25	3998.77	0.04	0.08	0.01	8.0	Lyα	2.28935	
26	3999.73	0.01	0.40	0.02	21.1	Lyα	2.29014	
27	4006.23	0.01	0.76	0.02	45.1	Lyα	2.29549	
28	4010.30	0.02	0.68	0.02	34.0	Lyα	2.29884	
29	4012.90	0.01	0.10	0.01	9.9	Lyα	2.30098	
30	4016.33	0.03	1.92	0.04	50.9	Lyα	2.30380	
31	4028.45	0.02	1.39	0.02	56.1	Lyα	2.31377	
32	4045.58	0.04	0.08	0.01	5.1	Lyα	2.32786	
33	4055.31	0.03	0.07	0.01	5.9	Lyα	2.33586	
34	4079.25	0.02	0.19	0.01	16.1			
35	4085.82	0.01	0.14	0.01	17.6			
36	4118.38	0.04	0.88	0.04	24.9	Si iv 1393	1.95488	
37	4120.07	0.02	0.10	0.02	6.0	Si iv 1393	1.95609	a
38	4126.22	0.02	0.18	0.01	15.4	Si iv 1393	1.96051	
39	4140.12	0.03	0.06	0.01	5.9			
40	4145.00	0.04	0.28	0.02	12.9	Si iv 1402	1.95487	
41	4152.90	0.04	0.11	0.01	7.4	Si iv 1402	1.96050	
42	4155.47	0.02	0.21	0.01	15.5			
43	4161.47	0.01	0.17	0.01	15.2			
44	4180.22	0.04	0.13	0.02	6.3			
45	4200.32	0.05	0.36	0.03	11.8	Si iv 1393	2.01367	
46	4227.43	0.04	0.11	0.02	5.7	Si iv 1402	2.01363	
47	4239.90	0.02	0.25	0.02	13.5			
48	4264.40	0.04	0.14	0.02	5.6	C iv 1548	1.75442	a

TABLE 2.4—Continued

No.	λ_{obs}(Å)	$\sigma(\lambda)$	W_{obs}(Å)	$\sigma(W)$	S/N	ID	z_{abs}	Notes
49	4265.78	0.04	0.25	0.04	6.4	C IV 1548	1.75531	
50	4272.83	0.03	0.25	0.04	6.4	C IV 1550	1.75529	
51	4299.18	0.08	0.26	0.03	9.8	C IV 1548	1.77689	
52	4300.34	0.08	0.51	0.03	19.9	C IV 1548	1.77763	
53	4301.84	0.24	11.39	0.19	59.9	Si IV 1393 + 1402	2.07656	b
54	4304.09	0.05	0.31	0.04	8.0			
55	4306.32	0.05	0.25	0.03	10.1	C IV 1550	1.77688	
56	4307.49	0.05	0.44	0.03	15.2	C IV 1550	1.77764	
57	4314.17	0.01	0.63	0.02	25.6			
58	4321.47	0.01	0.17	0.02	9.4			c
59	4351.88	0.04	0.11	0.02	5.6	Si II 1526	1.85050	d
60	4368.72	0.07	0.23	0.04	6.4			
61	4413.27	0.03	0.21	0.03	8.2	C IV 1548	1.85058	a
62	4479.09	0.04	0.13	0.02	5.4	C IV 1548	1.89309	a
63	4479.79	0.03	0.15	0.02	6.8	C IV 1548	1.89354	
64	4487.20	0.04	0.13	0.02	6.2	C IV 1550	1.89352	
65	4574.80	0.03	0.87	0.04	23.9	C IV 1548	1.95491	
66	4576.66	0.04	0.13	0.02	6.3	C IV 1548	1.95611	
67	4582.40	0.03	0.61	0.04	14.4	C IV 1550	1.95491	b
68	4583.37	0.02	0.51	0.03	15.8	C IV 1548	1.96045	b
69	4584.26	0.04	0.07	0.02	5.0	C IV 1550	1.95611	
70	4590.99	0.02	0.35	0.02	15.6	C IV 1550	1.96045	
71	4638.29	0.03	0.10	0.02	6.7			
72	4649.63	0.09	0.10	0.02	5.0			
73	4665.98	0.01	2.39	0.03	95.2	C IV 1548	2.01381	
74	4669.74	0.01	0.27	0.01	21.0	C IV 1548	2.01623	
75	4673.68	0.01	1.89	0.02	81.7	C IV 1550	2.01377	
76	4677.48	0.01	0.17	0.01	13.6	C IV 1550	2.01622	
77	4765.69	0.22	11.51	0.16	71.9	C IV 1548 + 1550	2.07662	b
78	4805.20	0.31	0.65	0.09	7.2	Si II 1526	2.14743	
79	4814.01	0.17	1.34	0.09	14.4			
80	4834.50	0.03	0.34	0.03	13.4	Al II 1670	1.89355	d
81	4871.69	0.13	1.31	0.06	21.8	C IV 1548	2.14668	
82	4879.80	0.11	1.26	0.06	21.3	C IV 1550	2.14669	
83	4906.50	0.04	0.29	0.03	9.2			
84	4921.21	0.07	0.42	0.04	10.5			
85	4930.33	0.07	0.26	0.03	8.7			

[a]Doublet component below 5σ equivalent width threshold.
[b]Probable blend.
[c]Possible spurious line.
[d]Probable chance coincidence.

TABLE 2.5

ABSORPTION LINES OF TOL 1035-2737

No.	λ_{obs}(Å)	$\sigma(\lambda)$	W_{obs}(Å)	$\sigma(W)$	S/N	ID	z_{abs}	Notes
1	3813.35	0.08	0.79	0.13	6.2	Lyα	2.13683	
2	3819.61	0.05	0.76	0.09	8.8	Lyα	2.14198	
3	3824.10	0.02	1.09	0.06	17.1	Lyα	2.14567	
4	3832.86	0.07	0.38	0.06	6.3	Lyα	2.15288	
5	3836.64	0.02	1.41	0.07	20.2	Lyα	2.15599	
6	3839.46	0.04	0.36	0.04	10.1	Lyα	2.15831	
7	3840.98	0.03	0.38	0.03	11.4	Lyα	2.15956	
8	3848.86	0.04	0.13	0.02	5.5	Lyα	2.16604	
9	3850.97	0.02	0.38	0.03	13.9	Lyα	2.16778	
10	3856.34	0.07	0.18	0.03	5.6	Lyα	2.17219	
11	3858.63	0.05	0.24	0.03	8.1	Lyα	2.17408	
12	3872.86	0.02	0.89	0.05	17.1	N v 1238	2.12625	
13	3885.44	0.05	0.65	0.07	9.5	N v 1242	2.12635	
14	3934.90	0.02	0.49	0.03	14.3			
15	3936.21	0.06	0.22	0.04	5.9			
16	3942.51	0.02	0.14	0.02	8.3			
17	3969.66	0.04	0.30	0.04	7.0			
18	4012.82	0.03	0.13	0.02	5.3			
19	4065.87	0.04	0.20	0.04	5.6			
20	4066.90	0.06	0.22	0.04	5.5			
21	4085.77	0.02	0.12	0.02	5.2			c
22	4161.39	0.02	0.13	0.02	6.8			c
23	4184.98	0.03	0.63	0.05	11.7	C iv 1548	1.70312	
24	4191.96	0.03	0.42	0.04	10.4	C iv 1550	1.70314	
25	4227.48	0.01	0.70	0.03	24.4	C iv 1548	1.73057	
26	4234.54	0.02	0.43	0.03	14.9	C iv 1550	1.73060	
27	4239.89	0.02	0.18	0.02	11.2			c
28	4275.59	0.03	0.16	0.03	6.2	Fe ii 2344	0.82389	
29	4277.55	0.02	0.50	0.04	13.9	Fe ii 2344	0.82473	
30	4321.40	0.01	0.18	0.02	10.4			c
31	4345.69	0.07	0.27	0.05	5.7	Fe ii 2382	0.82380	
32	4347.86	0.02	0.57	0.04	14.1	Fe ii 2382	0.82471	b
33	4374.51	0.03	0.09	0.02	5.4			c
34	4398.22	0.02	0.43	0.02	19.0	C iv 1548	1.84086	
35	4405.59	0.04	0.22	0.03	8.7	C iv 1550	1.84090	
36	4438.30	0.10	0.25	0.05	5.0			
37	4534.11	0.04	0.10	0.02	5.2			
38	4535.71	0.03	0.26	0.03	8.6	C iv 1548	1.92966	
39	4543.19	0.05	0.12	0.03	5.0	C iv 1550	1.92963	
40	4621.73	0.07	0.21	0.04	5.3			
41	4690.30	0.07	0.16	0.03	5.2			
42	4717.46	0.07	0.36	0.04	8.1	Fe ii 2586	0.82377	
43	4720.00	0.03	0.52	0.04	12.7	Fe ii 2586	0.82475	
44	4742.35	0.02	0.22	0.02	11.7	Fe ii 2600	0.82386	
45	4744.57	0.01	0.73	0.02	30.3	Fe ii 2600	0.82471	
46	4813.59	0.06	0.16	0.03	5.4			
47	4840.20	0.02	0.58	0.03	21.5	C iv 1548	2.12634	
48	4848.22	0.03	0.40	0.03	13.5	C iv 1550	2.12632	

TABLE 2.5—*Continued*

No.	λ_{obs}(Å)	$\sigma(\lambda)$	W_{obs}(Å)	$\sigma(W)$	S/N	ID	z_{abs}	Notes
49	4901.98	0.07	0.12	0.02	6.0			
50	5100.02	0.01	0.86	0.03	31.0	Mg II 2796	0.82381	
51	5102.44	0.01	1.11	0.03	33.6	Mg II 2796	0.82468	
52	5113.07	0.02	0.61	0.03	21.5	Mg II 2803	0.82380	
53	5115.52	0.01	0.97	0.02	29.5	Mg II 2803	0.82467	
54	5125.37	0.03	0.20	0.02	8.3			

[a]Doublet component below 5σ equivalent width threshold.
[b]Probable blend.
[c]Possible spurious line.
[d]Probable chance coincidence.

TABLE 2.6

ABSORPTION LINES OF TOL 1029−2654

No.	λ_{obs}(Å)	$\sigma(\lambda)$	W_{obs}(Å)	$\sigma(W)$	S/N	ID	z_{abs}	Notes
1	3817.90	0.02	0.39	0.04	8.7	Lyα	2.14057	
2	3820.44	0.05	1.07	0.08	13.4	Lyα	2.14266	
3	3823.16	0.05	0.39	0.06	6.7	Lyα	2.14490	
4	3832.87	0.08	0.31	0.05	5.8	Lyα	2.15289	
5	3848.18	0.04	0.43	0.04	11.5	Lyα	2.16548	
6	3855.10	0.03	1.96	0.05	39.2	Lyα	2.17117	
7	3871.39	0.02	0.82	0.04	20.4	Lyα	2.18457	
8	3887.01	0.04	0.26	0.04	5.9	Lyα	2.19742	
9	3890.31	0.06	0.50	0.06	8.2	Lyα	2.20014	
10	3892.18	0.05	0.32	0.05	6.7	Lyα	2.20167	
11	3903.09	0.04	4.26	0.09	47.3	Lyα	2.21065	
12	3907.56	0.05	0.38	0.05	8.3	Lyα	2.21432	
13	3911.47	0.06	0.23	0.05	5.1	Lyα	2.21754	
14	3925.07	0.06	2.10	0.07	28.7	Lyα	2.22873	
15	3934.74	0.03	0.34	0.04	9.8	Lyα	2.23668	
16	3939.49	0.03	0.23	0.03	7.7	Lyα	2.24059	
17	3941.18	0.04	1.05	0.05	19.8	Lyα	2.24198	
18	3950.48	0.06	1.58	0.09	17.6	Lyα	2.24963	
19	3955.50	0.04	1.07	0.06	17.5	Lyα	2.25376	
20	3958.61	0.07	0.35	0.06	5.7	Lyα	2.25632	
21	3971.08	0.03	3.69	0.07	95.6	Lyα	2.26658	
22	3981.61	0.02	0.76	0.05	13.9	Lyα	2.27524	
23	3982.78	0.02	1.02	0.06	16.6	Lyα	2.27620	
24	3984.07	0.05	0.34	0.04	9.5	Lyα	2.27726	
25	3985.73	0.03	0.28	0.03	9.1	Lyα	2.27863	
26	3991.62	0.02	0.60	0.03	18.3	Lyα	2.28347	
27	3998.84	0.01	1.17	0.03	40.3	Lyα	2.28941	
28	4001.84	0.02	0.76	0.03	23.5	Lyα	2.29188	
29	4006.39	0.02	1.14	0.03	33.8	Lyα	2.29562	
30	4008.22	0.03	0.56	0.03	17.4	Lyα	2.29713	
31	4012.52	0.04	0.52	0.04	13.2	Lyα	2.30067	
32	4014.38	0.02	0.37	0.04	10.0	Lyα	2.30220	
33	4015.34	0.05	0.28	0.05	5.7	Lyα	2.30298	
34	4020.16	0.05	1.10	0.06	18.3	Lyα	2.30695	
35	4022.25	0.04	0.54	0.05	11.0	Lyα	2.30867	
36	4025.23	0.03	0.23	0.04	6.2	Lyα	2.31112	
37	4026.07	0.04	0.31	0.04	7.0	Lyα	2.31181	
38	4030.17	0.03	2.09	0.06	34.8	Lyα	2.31518	
39	4038.84	0.05	0.38	0.05	7.3	C II 1334	2.02641	d
40	4048.61	0.02	0.82	0.03	26.8	Lyα	2.33035	
41	4055.76	0.02	1.13	0.03	33.1	Lyα	2.33623	
42	4058.90	0.05	0.20	0.03	7.1	Lyα	2.33882	
43	4063.51	0.02	0.18	0.02	8.4	Lyα	2.34261	
44	4065.21	0.03	0.19	0.03	7.5	Lyα	2.34401	
45	4067.24	0.02	0.83	0.03	29.4	Lyα	2.34568	
46	4074.39	0.02	1.19	0.03	36.7	Lyα	2.35156	
47	4077.68	0.02	2.22	0.04	58.0	Lyα	2.35427	
48	4080.75	0.06	0.30	0.04	7.6	Lyα	2.35679	

TABLE 2.6—*Continued*

No.	λ_{obs}(Å)	$\sigma(\lambda)$	W_{obs}(Å)	$\sigma(W)$	S/N	ID	z_{abs}	Notes
	4082.52	0.06	0.33	0.04	7.5	Lyα	2.35825	
50	4085.36	0.02	1.00	0.03	29.4	Lyα	2.36058	
51	4099.10	0.03	0.51	0.04	11.7	Lyα	2.37189	
52	4100.63	0.03	0.89	0.07	12.9	Lyα	2.37314	
53	4113.23	0.03	1.68	0.05	33.6	Lyα	2.38351	
54	4115.70	0.05	0.69	0.07	9.3	Lyα	2.38554	
55	4117.79	0.02	1.47	0.04	39.1	Lyα	2.38726	
56	4121.98	0.02	2.86	0.05	57.2	Lyα	2.39071	
57	4134.68	0.04	1.54	0.05	33.1	Lyα	2.40115	
58	4139.53	0.03	0.23	0.03	8.1	Lyα	2.40514	
59	4144.95	0.02	0.61	0.03	23.3	Lyα	2.40960	
60	4151.48	0.03	0.41	0.03	12.5	Lyα	2.41497	
61	4152.37	0.02	0.20	0.03	8.0	Lyα	2.41570	
62	4156.77	0.02	1.41	0.03	42.2	Lyα	2.41932	
63	4159.52	0.02	2.86	0.04	48.5	Lyα	2.42159	
64	4167.67	0.05	0.19	0.03	5.6	Lyα	2.42829	
65	4177.79	0.04	0.79	0.06	12.8	Lyα	2.43661	
66	4179.49	0.08	0.54	0.07	7.4	Lyα	2.43801	
67	4187.14	0.03	0.48	0.04	10.9	Lyα	2.44431	
68	4188.50	0.08	0.31	0.06	5.5	Lyα	2.44542	
69	4200.66	0.02	1.21	0.03	38.3	Lyα	2.45543	
70	4211.65	0.04	0.19	0.03	7.5	Lyα	2.46447	
71	4212.74	0.03	0.18	0.02	7.4	Lyα	2.46536	
72	4215.34	0.01	0.80	0.03	29.8	Lyα	2.46750	
73	4216.84	0.06	0.15	0.03	5.4	Si iv 1393	2.02552	
74	4218.34	0.02	0.25	0.03	8.5	Si iv 1393	2.02660	
75	4225.13	0.02	0.64	0.02	32.0	Si ii 1190	2.54929	
76	4227.72	0.02	1.65	0.03	55.1	Lyα	2.47769	
77	4229.77	0.04	0.26	0.02	13.2	Lyα	2.47937	
78	4232.58	0.02	1.77	0.03	59.5	Lyα	2.48168	
79	4235.36	0.02	0.78	0.02	39.4	Si ii 1193	2.54931	
80	4239.92	0.01	0.15	0.01	12.2	Lyα	2.48772	
81	4243.82	0.01	0.77	0.02	33.0	Si iv 1402	2.02531	
82	4245.61	0.02	0.15	0.02	7.6	Si iv 1402	2.02659	b
83	4250.57	0.04	0.82	0.05	16.4	Lyα	2.49648	
84	4256.61	0.03	0.92	0.04	23.6	Lyα	2.50145	
85	4259.55	0.04	0.76	0.04	19.9	Lyα	2.50387	
86	4272.75	0.03	0.14	0.02	6.1	Lyα	2.51473	
87	4282.40	0.03	1.28	0.04	32.0	Lyα	2.52267	
88	4285.28	0.03	1.40	0.04	35.5	Lyα	2.52504	
89	4293.36	0.04	0.19	0.03	6.5	Lyα	2.53168	
90	4328.91	0.05	1.07	0.11	9.8	Lyα	2.56092	
91	4330.27	0.04	0.60	0.08	7.3	Lyα	2.56204	
92	4335.26	0.03	3.77	0.07	53.8	Lyα	2.56615	
93	4338.28	0.05	0.32	0.04	7.7	Lyα	2.56863	
94	4340.92	0.03	2.36	0.05	47.2	Lyα	2.57080	
95	4345.32	0.03	0.29	0.03	10.6	Lyα	2.57442	
96	4352.59	0.01	0.50	0.02	23.2	Lyα	2.58040	
97	4363.29	0.01	1.65	0.02	81.6	Lyα	2.58921	

TABLE 2.6—*Continued*

No.	λ_{obs}(Å)	$\sigma(\lambda)$	W_{obs}(Å)	$\sigma(W)$	S/N	ID	z_{abs}	Notes
	4365.74	0.05	0.13	0.02	7.3	Lyα	2.59122	
99	4416.54	0.05	0.11	0.02	5.8			
100	4473.71	0.01	1.01	0.02	61.5	Si II 1260	2.54937	
101	4495.85	0.05	0.09	0.02	5.0			
102	4530.17	0.08	0.26	0.04	5.9			
103	4621.69	0.01	0.75	0.03	25.2	O I 1302	2.54923	
104	4629.42	0.03	0.47	0.03	14.0	Si II 1304	2.54916	
105	4671.60	0.04	0.32	0.03	10.2	C IV 1548	2.01744	
106	4673.09	0.04	0.39	0.04	11.9	C IV 1548	2.01840	
107	4679.36	0.04	0.21	0.03	7.6	C IV 1550	2.01744	
108	4680.86	0.04	0.31	0.03	10.6	C IV 1550	2.01840	
109	4684.07	0.01	0.71	0.02	37.4	C IV 1548	2.02549	
110	4685.11	0.02	0.43	0.05	8.9	C IV 1548	2.02616	
111	4685.81	0.02	0.87	0.06	14.9	C IV 1548	2.02661	
112	4686.65	0.02	0.17	0.02	6.9	C IV 1548	2.02716	
113	4691.85	0.01	0.58	0.02	31.1	C IV 1550	2.02549	
114	4692.90	0.02	0.30	0.04	7.3	C IV 1550	2.02617	
115	4693.60	0.02	0.81	0.05	15.9	C IV 1550	2.02662	
116	4694.43	0.02	0.07	0.01	6.8	C IV 1550	2.02715	
117	4736.54	0.01	0.82	0.02	39.9	C II 1334	2.54921	
118	4947.57	0.07	0.13	0.02	5.4	Si IV 1393	2.54981	
119	4969.70	0.04	0.09	0.02	5.0			
120	4979.53	0.03	0.13	0.02	7.4	Si IV 1402	2.54978	
121	5031.45	0.05	0.10	0.02	5.1			

[a] Doublet component below 5σ equivalent width threshold.
[b] Probable blend.
[c] Possible spurious line.
[d] Probable chance coincidence.

TABLE 2.7
C IV ABSORPTION SYSTEMS

z_{min} (1)	z_{max} (2)	z_{abs} (3)	$\sigma(z_{abs})$ (4)	Number (5)	β (6)	$W_0(1548)$ (7)	$W_0(1550)$ (8)	Reliability (9)
				Tol 1037–2704; $z_{em} = 2.193$				
1.46	2.19	1.48248	0.00001	2	0.2465	0.24	0.19	probable
		1.48323	0.00001	2	0.2462	0.16	0.12	probable
		1.63336	0.00001	2	0.1904	0.11	0.05	probable
		1.63434	0.00001	2	0.1900	0.55	0.50	probable
		1.91249	0.00001	7	0.0917	0.26	0.22	certain
		1.97145	0.00002	4	0.0718	0.16	0.13	certain
		1.97216	0.00001	6	0.0716	0.34	0.23	certain
		2.00336	0.00002	2	0.0612	0.09	0.07	probable
		2.02509	0.00001	2	0.0540	0.07	0.04	probable
		2.02785	0.00001	5	0.0531	0.32	0.29	certain
		2.02847	0.00001	5	0.0529	0.22	0.15	certain
		2.03915	0.00003	1	0.0493	0.06	$\cdots$	possible
		2.07059	0.00002	4	0.0391	0.54	0.47	certain
		2.07716	0.00003	4	0.0369	0.22	0.11[a]	probable
		2.07858	0.00003	4	0.0365	0.40	0.20[a]	certain
		2.08321	0.00003	4	0.0350	2.15[b]	1.22	certain
		2.10663	0.00001	2	0.0274	0.06	0.04	probable
		2.11561	0.00001	2	0.0245	0.05	0.04	probable
		2.12818	0.00001	6	0.0205	0.58	0.47	certain
		2.13593	0.00001	7	0.0180	0.70	0.57	certain
		2.13910	0.00001	10	0.0170	0.75	0.68	certain
		2.14030	0.00002	9	0.0166	0.20	0.17	certain
		2.14239	0.00001	4	0.0160	0.07	0.03	certain
				Tol 1038–2712; $z_{em} = 2.331$				
1.46	2.31	1.75530	0.00002	2	0.1875	0.09	0.09	probable
		1.77688	0.00003	2	0.1800	0.09	0.09	probable
		1.77764	0.00003	2	0.1797	0.18	0.16	probable
		1.85055	0.00002	2	0.1545	0.07	$\cdots$	possible
		1.89309	0.00003	1	0.1400	0.04	$\cdots$	possible
		1.89353	0.00002	2	0.1399	0.05	0.04	probable
		1.95490	0.00001	5	0.1192	0.29	0.21	certain
		1.95610	0.00001	3	0.1188	0.04	0.02	certain
		1.96047	0.00001	4	0.1174	0.17	0.12	certain
		2.01378	0.00001	4	0.0997	0.79	0.63	certain
		2.01623	0.00001	2	0.0989	0.09	0.06	probable
		2.07660	0.00011	4	0.0793	1.87[c]	1.87[c]	certain
		2.14674	0.00005	5	0.0568	0.42	0.40	certain
				Tol 1035–2737; $z_{em} = 2.149$				
1.46	2.15	1.70313	0.00001	2	0.1515	0.23	0.16	probable
		1.73058	0.00001	2	0.1416	0.26	0.16	probable
		1.84089	0.00001	2	0.1026	0.15	0.08	probable
		1.92965	0.00002	2	0.0721	0.09	0.04	probable
		2.12631	0.00001	4	0.0072	0.19	0.13	certain
				Tol 1029–2654; $z_{em} = 2.586$				
1.82	2.31	2.01744	0.00002	2	0.1709	0.11	0.07	probable
		2.01840	0.00002	2	0.1706	0.13	0.10	probable
		2.02543	0.00001	4	0.1684	0.23	0.19	certain
		2.02616	0.00001	2	0.1681	0.14	0.10	probable
		2.02660	0.00001	5	0.1680	0.29	0.27	certain
		2.02716	0.00001	2	0.1678	0.06	0.02	probable

[a]The C IV $\lambda1550$ component is blended with the C IV $\lambda1548$ line of the $z_{abs} = 2.08301$ system. It has been assigned an equivalent corresponding to half that of the unblended C IV $\lambda1548$.

[b]C IV $\lambda1548$ is blended with the C IV $\lambda1550$ lines of the $z_{abs} = 2.07741$ and 2.07820 systems. It has been assigned the measured equivalent width of the blended C IV $\lambda1548$ minus the contributions by C IV $\lambda1550$.

[c]The C IV $\lambda\lambda1548$, 1550 doublet is not resolved. Each component has been assigned half the equivalent width of the doublet.

TABLE 2.8

C IV ABSORPTION SYSTEM SAMPLES

Criteria	Sample	#	$< z_{abs} >$	W_*	$\sigma(W_*)$	N_*	$\sigma(N_*)$
All definite & probable systems	S1	44	1.958	0.33	0.04	77	22
$\beta c > 5000\,\mathrm{km\,s^{-1}}$	S2	41	1.947	0.33	0.04	73	20
$\beta c > 5000\,\mathrm{km\,s^{-1}}$, $W_0 > 0.15\,\text{Å}$	S3	21	1.961	0.39	0.04	53	11
$\beta c > 5000\,\mathrm{km\,s^{-1}}$, $W_0 > 0.15\,\text{Å}$, $\Delta v > 1000\,\mathrm{km\,s^{-1}}$	S4	16	1.937	0.41	0.06	40	13

TABLE 2.9
CIV ABSORPTION LINE MATCHES

Tol 1037-2704	Tol 1038-2712	Tol 1035-2737	Tol 1029-2654
1.48248 1.48323			
1.63336 1.63434			
		1.70313	
	1.75530	1.73058	
	1.77688 1.77764		
	1.85055	1.84089	
1.91249	1.89309 1.89353	1.92965	
1.97145 1.97216	1.95490 1.95610 1.96047		
2.00336			
2.02509 2.02785 2.02847 2.03915	2.01378 2.01623		2.01744 2.01840 2.02549 2.02616 2.02660 2.02716
2.07059 2.07716 2.07858 2.08321	2.07660		
2.10663			
2.11561			
2.12818 2.13593 2.13910 2.14030 2.14239	2.14674	2.12630	

CHAPTER 3

COMMON LYMAN ALPHA ABSORPTION TOWARD THE QUASAR PAIR Q1343+2640A,B: EVIDENCE FOR LARGE AND QUIESCENT CLOUDS[1]

Nadine Dinshaw[2], Chris D. Impey[2], Craig B. Foltz[3], Ray J. Weymann[4], and Frederic H. Chaffee[3]

---

[2]Steward Observatory, University of Arizona, Tucson, AZ 85721

[3]Multiple Mirror Telescope Observatory, University of Arizona, Tucson, AZ 85721

[4]Carnegie Observatories, 813 Santa Barbara St., Pasadena, CA 91101-1292

Abstract

We present observations of the Lyman α forest of the close quasar pair Q1343+2640A (z_{em} = 2.029) and B (z_{em} = 2.031). We detect 8 absorption lines of Lyman α common to both spectra and not attributable to metal line systems in the redshift range $1.7 < z < 2.1$, and 4 lines which are seen in one spectrum but not the other. At the 9.5″ separation of the two quasars, this implies a firm lower limit on the characteristic size of the Lyα clouds of $40\,h^{-1}$ kpc (where $h \equiv H_0/100$ km s^{-1} Mpc^{-1}, $q_0 = 0.5$) at a redshift $z \simeq 1.8$. The upper limit on the cloud size is much more uncertain due to the small number of observed lines, but taking the observed fraction of common lines at face value in the context of a simple model, the absorbers are shown have characteristic radii of about $125\,h^{-1}$ kpc. Significant velocity and equivalent width variations are seen with an rms velocity difference of ~ 65 km s^{-1} between the common absorption lines along the two lines of sight.

3.1 Introduction

The majority of the absorption lines of Lyman α seen in the spectra of high redshift quasars are thought to arise in cosmologically-distributed, intervening "clouds," the origin and physical nature of which remain controversial. Distinguishing between competing models for the absorbers requires some knowledge of the size of the Lyα clouds. Currently, the best limits on the cloud sizes, derived from observations along the two lines of sight to gravitationally-lensed and projected pairs of quasars, lie anywhere in the range from 25 to $500\,h^{-1}$ kpc (Smette *et al.* 1992; Shaver & Robertson 1983).

In this chapter, we present spectra of the Lyα forest of the quasar pair Q1343+2640A,B which was discovered in a CFHT survey for faint quasars by Crampton *et al.* (1988). The quasars have redshifts of 2.029 and 2.031 and are separated on the sky by $9.5''$, corresponding to a linear separation of $\sim 40\,h^{-1}$ kpc for $q_0 = 0.5$. Despite the fact that the quasars are faint ($B \sim 20.2$), this pair is particularly well-suited for this type of study since it samples the clouds on linear scales comparable to the expected characteristic cloud sizes predicted by several theoretical scenarios (Sargent *et al.* 1980; Ikeuchi & Ostriker 1986; Rees 1986; Bond, Szalay & Silk 1987).

3.2 Observations and Reductions

Spectra of Q1343+2640A and B were obtained during the period from 1994 March 11 to June 2 UT with the Multiple Mirror Telescope, using the Blue Channel Spectrograph equipped with a highly-optimized Loral 3072 × 1024 CCD. An 832 line mm^{-1} grating blazed at 3900Å in second order was used, along with a $1''$ slit, yielding a spectral resolution of 1 Å FWHM (0.35 Å $pixel^{-1}$), over the wavelength range $\sim 3300-4100$Å. First-order light was blocked by a solid $CuSO_4$ filter. Total integration times of 68400 s and 64800 s were accumulated on A and B, respectively. Exposures of a He-Ar-Cu calibration lamp were taken before and after each object exposure. No flux calibration standard stars were observed.

The spectra were reduced with the IRAF software package using standard techniques. Uncertainties in the wavelengths were primarily due to asymmetries in the line profiles of the comparison arc lamp and amounted to no more than $\sigma \simeq 0.15\,\text{Å}$. The resulting spectra of Q1343+2640A and B are shown in Figure 3.1.

The continuum was defined for each quasar using a cubic spline fit and each pixel in the spectrum was subsequently searched for absorption using line-finding routines based on the algorithms employed in the HST Quasar Absorption Line Key Project (Schneider $et\ al.$ 1993). Equivalent widths and line positions were determined by fitting single or, in the case of obvious blends, multiple Gaussian profiles to all the candidate absorption lines. A preliminary line list, useful for eliminating absorption features that were members of metal line systems, was assembled from lines with observed equivalent widths, $W > 3.5\sigma_W$. We then culled a subset of these lines with $W > 5\sigma_W$ to form the more conservative list presented in Table 3.1. Two lines which fell below this threshold but which satisfied our definition of a common absorption system (described below) were retained in order to investigate the impact of excluding possible Lyα pairs on our determination of the cloud size because they did not meet the $5\sigma_W$ equivalent width limit. We show later that the equivalent widths of the common features between the two lines of sight exhibit significant scatter about a line with unity slope, so the equivalent width cutoff itself introduces uncertainty into the observed number of common lines. Ideally, it would be better to use a complete set of lines with rest equivalent widths above some fixed value. However, given the significant variations in the S/N levels across the spectra, so limiting the line list reduces the number of lines to an intolerably low level.

Line identifications were made using the set of standard quasar absorption lines given in Morton $et\ al.$ (1988). Our identifications of metal-line systems agree well with Crotts $et\ al.$ (1994), taking into account the higher resolution of our data which occasionally resolved close blends.
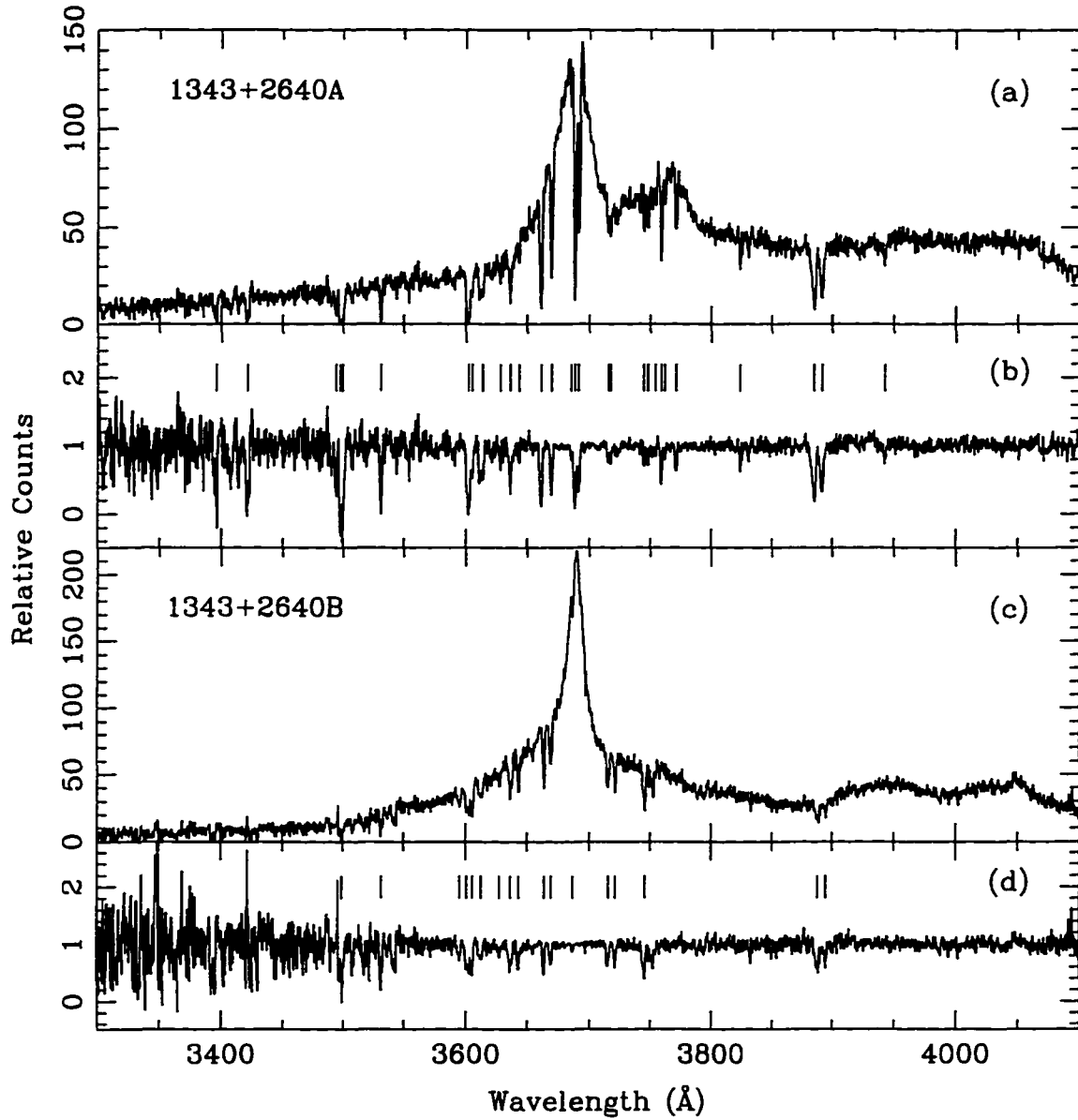
FIGURE 3.1—Spectra of Q1343+2640A and B. Panels (a) and (c) show the spectra in raw counts. In panels (b) and (d), the spectra have been divided by the continuum fits. Tickmarks in (b) and (d) indicate absorption features with equivalent widths, $W > 5\sigma_W$. The wavelengths are vacuum and heliocentric.

TABLE 3.1

ABSORPTION LINES OF QUASAR PAIR Q1343+2640A,B

A No.	λ_{obs}(Å)	σ_λ	W_{obs}(Å)	σ_W	S/N	ID	z_{abs}	B No.	λ_{obs}(Å)	σ_λ	W_{obs}(Å)	σ_W	S/N	ID	z_{abs}	A-B Δv(km/s)
1	3395.98	0.19	1.83	0.31	5.8	Lyα	1.7935				< 1.95					
2	3421.19	0.19	2.96	0.36	8.2	Lyα	1.8142				< 2.50					
3	3494.02	0.13	1.29	0.21	6.1	Lyα	1.8742				< 1.42					
4	3497.58	0.10	2.02	0.34	6.0	Lyα	1.8771				< 1.35					
5	3499.77	0.13	2.76	0.38	7.4	Lyα	1.8789	1	3499.40	0.19	1.94	0.35	5.5	Lyα[2]	1.8786	31 ± 20
6	3531.57	0.08	1.73	0.17	10.5	Lyα	1.9050	2	3532.31	0.20	1.28	0.22	5.9	Lyα	1.9057	−63 ± 18
			< 0.63					3	3595.07	0.21	0.62	0.12	5.1	Lyα	1.9573	
7	3601.73	0.09	3.42	0.20	16.7	Lyα	1.9628	4	3600.78	0.17	0.88	0.16	5.3	Lyα	1.9620	79 ± 16
8	3605.08	0.12	0.76	0.14	5.6	Lyα	1.9655	5	3605.28	0.09	1.21	0.11	11.0	Lyα	1.9657	−16 ± 12
9	3613.30	0.15	1.26	0.24	5.4	Lyα	1.9723	6	3612.52	0.25	0.86	0.13	6.4	Lyα	1.9716	64 ± 27
10	3627.86	0.14	0.40	0.09	4.4	Lyα	1.9843	7	3627.50	0.18	0.44	0.08	5.9	Lyα	1.9840	30 ± 19
11	3636.19	0.08	1.53	0.11	13.9	Lyα	1.9911	8	3636.60	0.11	1.42	0.10	13.5	Lyα	1.9914	34 ± 11
12	3643.14	0.14	0.31	0.07	4.1	Lyα	1.9968	9	3643.36	0.08	0.81	0.06	12.4	Lyα	1.9970	−18 ± 13
13	3661.10	0.03	1.95	0.06	35.5	Si III 1206	2.0345									
			< 0.24					10	3663.85	0.04	0.79	0.04	17.4	Lyα[3,4]	2.0138	
14	3669.48	0.03	1.23	0.04	30.8	Lyα	2.0185	11	3669.56	0.06	0.71	0.05	15.9	Lyα[3]	2.0185	−6 ± 5
15	3685.36	0.05	0.25	0.02	10.0	Lyα	2.0316	12	3686.99	0.08	0.16	0.02	8.0	Lyα	2.0329	−132 ± 2
16	3688.54	0.01	2.29	0.03	76.5	Lyα[1]	2.0342				< 0.11					
17	3691.58	0.01	1.25	0.03	50.0	Lyα[1]	2.0367				< 0.11					
18	3715.07	0.11	0.35	0.06	5.3	C IV 1548	1.3996	13	3715.50	0.09	0.82	0.06	12.6	C IV 1548	1.3999	
19	3717.19	0.11	0.47	0.07	6.8	C IV 1548	1.4010									
								14	3721.36	0.07	0.65	0.06	11.8	C IV 1550	1.3997	
20	3744.88	0.06	0.36	0.04	8.0	C IV 1548	1.4189	15	3745.71	0.08	1.51	0.24	6.3	C IV 1548	1.4194	
21	3747.71	0.09	0.50	0.05	10.0	C IV 1548	1.4207									
22	3754.06	0.10	0.19	0.04	5.4	C IV 1550	1.4208									
23	3758.98	0.04	0.91	0.04	20.2	N V 1238	2.0343									
24	3761.92	0.09	0.27	0.04	6.9	N V 1238	2.0367									
25	3770.98	0.05	0.73	0.05	16.1	N V 1242	2.0343									
26	3824.03	0.06	0.43	0.06	7.8	Si II 1260	2.0339									
27	3884.94	0.08	2.73	0.13	20.3	C IV 1548	1.5093									
								16	3887.94	0.20	1.41	0.22	6.3	C IV 1548	1.5113	
28	3891.33	0.09	2.05	0.12	17.8	C IV 1550	1.5093									
								17	3894.65	0.23	0.72	0.15	5.0	C IV 1550	1.5114	
29	3942.39	0.19	0.43	0.09	5.1	Fe II 2600	0.5162									

NOTE.—Upper W_{obs} limits are for 5σ significance level. For the sample of 5σ lines, the line pairs A5-B1, A6-B2, A7-B4, A8-B5, A9-B6, A11-B8, A14-B11 and A15-B12 are coincidences and A2, A4, B9 and B10 are anticoincidences according to the definitions outlined in the text. If we include the two 4σ lines, then line pairs A10-B7 and A12-B9 are coincidences with B9 no longer being an anticoincidence. Superscripts denote the following: 1. Member of metal-line absorption system; 2. Probable blend with Si IV 1393 of C IV system $z = 1.5114$; 3. Possible member of C IV doublet; and 4. Probable blend with Si II 1526 of C IV system $z = 1.3998$.

3.3 Common Lyman-α Absorption

Table 3.1 lists 14 Lyα forest lines in A and 12 in B with equivalent widths $> 5\sigma_W$ from $z \simeq$ 1.79 to the emission redshifts of the quasars. The distribution of velocity differences, Δv, of the absorbers between the two lines of sight was calculated from the fitted wavelengths of the features. For any given line, Δv was calculated only between the line itself and the 'nearest neighbor' line in the spectrum of the other quasar, thereby restricting a given Lyα line to belong to at most one pair. The histogram of Δv calculated using all the detected Lyα forest lines in Table 3.1 shows a peak with FWZI of $\sim 150\,\mathrm{km\ s^{-1}}$, mean of $-1\pm17\,\mathrm{km\ s^{-1}}$ and median of 30 km s^{-1}, and no additional pairs out to velocity differences of $\sim 2000\,\mathrm{km\ s^{-1}}$. The estimated number of *random* Lyα pairs with $|\Delta v| < 150\,\mathrm{km\ s^{-1}}$ is small, less than ~ 0.2, so we assume all the Lyα lines above the 5σ equivalent width limit with a corresponding match within the velocity difference ±150 km s^{-1} to be coincident to both spectra.

Under this criterion, of the 5σ Lyα absorption lines in Table 3.1, eight are common. An ambiguity in the velocity matches arises in one case: Lyα line 12 in B could have been matched with either the lines 15 ($\Delta v = -132\,\mathrm{km\ s^{-1}}$) or 16 ($\Delta v = +126\,\mathrm{km\ s^{-1}}$) in A. It is possible that this is either a spurious match or reflects real clustering of Lyα forest lines on small scales. We decided to pair lines 12 (in B) and 15 (in A) since their equivalent widths are more closely matched. In addition to the eight common absorption lines, there are two "possible" cases where a match was found in velocity but one component has an equivalent width less than 5σ, but more than 4σ (lines 10 and 12 in A). Assuming identical clouds, a firm lower limit on the diameter of the absorbers equal to the angular-diameter distance between the two lines of sight may be established, independent of any assumptions about the variation of the cloud density with impact parameter; in this case, $D \sim 40\,h^{-1}$ kpc. We note that although we refer to "cloud size" in this chapter, we cannot distinguish between coherent entities and correlated but distinct structures, *i.e.*, large ensembles of smaller clouds.

We chose to designate an absorption feature to be *not* in common to both spectra, or anticoincident, if the line is present in one spectrum at the 5σ level and if a line of that strength would have been a 5σ line in the other spectrum, but no corresponding 5σ line is seen within the velocity difference $\pm 150\,\mathrm{km\ s^{-1}}$. Four 5σ Lyα lines, not identified with metal-line systems, met the above criteria.

The size of the Lyα clouds was estimated by means of Monte Carlo simulations. We assumed the simplest (admittedly unphysical) model wherein all clouds are identical, spherical and have constant column density. The simulations are very similar in detail to those reported by Smette *et al.* (1992), and result in the determination of the ratio, f, of the number of coincidences, N_C, to the number of coincidences plus anticoincidences, N_A, which when compared to the observed ratio gives the characteristic cloud size. Simulations were performed for cloud radii in the range $20 \leq R \leq 500$ kpc in steps of 20 kpc. At each R, 10,000 realizations were carried out, each consisting of randomly-selected positions for $N_C + N_A$ clouds. The mean value of f and the range of f in which 95% of the realizations fell were calculated and are plotted in Figure 3.2.

Two samples were considered: In the first case, we consider only pairs where both components have equivalent widths $> 5\sigma$; specifically, $N_C = 8$ and $N_A = 4$, giving $f = 0.67$. The characteristic radius R from Figure 3.2 is $125\,h^{-1}$ kpc with lower and upper limits of $80 < R < 610\,h^{-1}$ kpc. In the second case we included the two "possible" common absorption features giving a total number of lines of 13 with $N_C = 10$ and $N_A = 3$, or $f = 0.77$. The characteristic cloud radius is larger since f increases: $R \simeq 190\,h^{-1}$ kpc, with lower and upper limits of $120 < R < 1535\,h^{-1}$ kpc. (Note that for $q_0 = 0$, these numbers increase by $\sim 50\%$.)

Putting aside the simple-minded assumptions of the simulation (*i.e.*, spherical clouds, no evolution in cloud size, hard-edged clouds) the significance of the upper limits on the cloud size given above is accurate only if we know the fraction of coincident lines exactly. In fact, there is an intrinsic uncertainty in our determination of f arising from the small
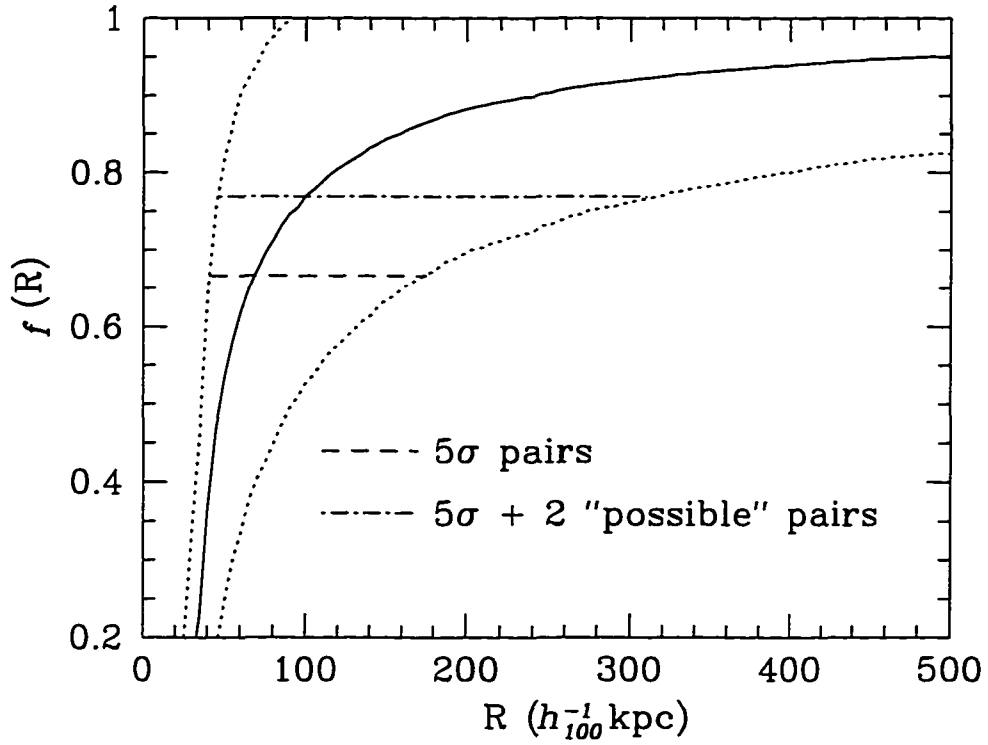
FIGURE 3.2—Fraction of common absorbers as a function of cloud radius. The solid curve gives the ratio f of the number of coincidences to the sum of the coincidences and anticoincidences as a function of cloud radius for the two samples described in the text. The dotted curves indicate the lower and upper limits on the radius of the absorbers at the 95% confidence level. A cosmological model with $H_0 = 100\,\mathrm{km\ s^{-1}\,Mpc}$ and $q_0 = 0.5$ was assumed.

number of absorbers detected in the redshift window sampled by our observations. For example, if only one of our coincident pairs was in fact an anticoincidence (*i.e.*, $N_C = 7$ and $N_A = 6$), f would drop to 0.54 with an attendant upper limit of about $250\,h^{-1}$ kpc. Conversely, if two of the lines we call anticoincident were in fact coincident (*i.e.*, $N_C = 9$ and $N_A = 2$), f would rise to 0.82 and the upper limit to about $3330\,h^{-1}$ kpc. Therefore, an error of ± 1 pair results in an uncertainty of more than a factor of ten in the inferred upper limit. For $f > 0.95$, the upper limit on the cloud radius is indeterminate.

Differences in equivalent widths and wavelengths of the common absorption features probe the column density and bulk motion along lines of sight separated by scales of 40 kpc. Existing data from Foltz *et al.* (1984) and Smette *et al.* (1992) indicate that the clouds are remarkably homogeneous and quiescent on scales of a few kpc. Our results suggest that we are sampling the clouds on spatial scales for which these properties do change. The rest equivalent widths of the common features along each sight line are plotted against each other on Figure 3.3. A χ^2 test shows that the distribution is inconsistent with a line with unity slope at more than a 99.9% significance level (reduced $\chi^2 = 36$), implying that on scales of ~ 40 kpc the column densities through the clouds do not correlate as well as they do when sampled on the $1 - 2$ kpc scale of the Smette *et al.* (1992) study. The rms velocity difference is 65 km s^{-1} for the 8 coincident lines and 60 km s^{-1} when the two possible coincidences are included. The 1σ uncertainty in the wavelength calibration is about 13 km s^{-1} and the typical uncertainty in the Gaussian fits is ~ 20 km s^{-1}, which when combined in quadrature give a total uncertainty of ~ 24 km s^{-1}, so the rms velocity differences deviate from zero at the 2.7σ and 2.5σ levels, respectively. The significance of this result is not overwhelming, but we interpret it as an indication that we are seeing real, albeit small, differences in the projected radial velocities of the clouds on scales of $\simeq 40\,h^{-1}$ kpc.
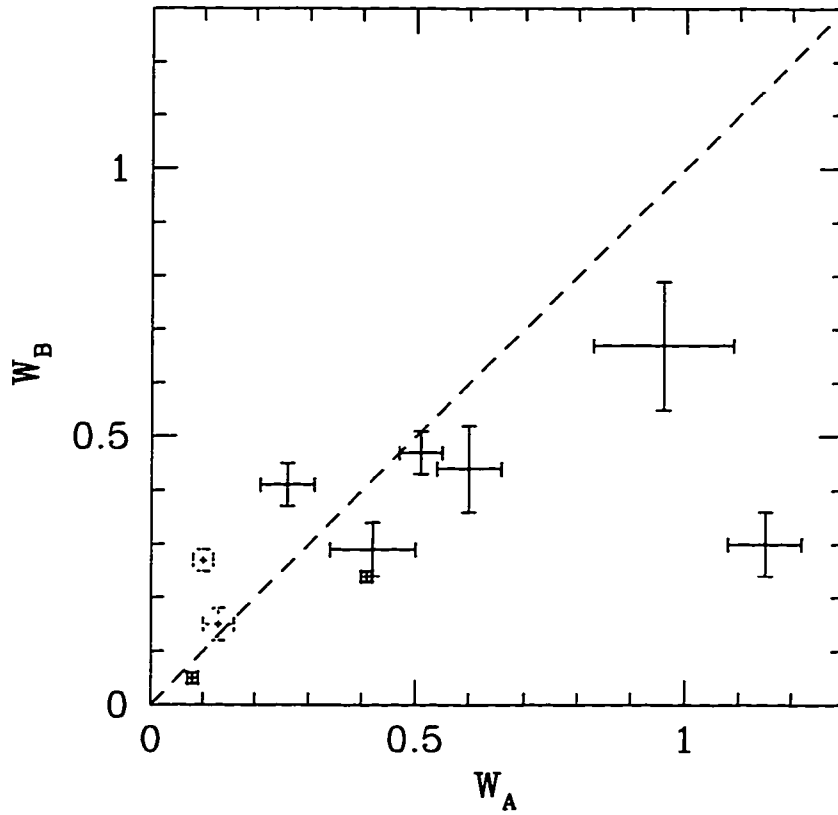
FIGURE 3.3—Correlation between the rest equivalent widths of the common lines in Q1343+2640A and B. The dotted error bars represent the two "possible" cases of common absorption. The dashed line has unit slope.

3.4 Discussion

The observations presented here give a direct and model-independent lower limit on the absorber diameter of $\sim 40\,h^{-1}$ kpc, suggesting further that they may be very large, with sizes up to a hundred kpc or more. We also detect differences in the column density and radial velocity of the absorbing gas on these scales. Every leading model has difficulty explaining Lyα clouds that are as large and quiescent as these observations imply.

The characteristic radius of $100-200\,h^{-1}$ kpc is substantially larger than that predicted by two popular models: clouds confined by a hot intergalactic medium (Sargent *et al.* 1980), and gas confined by mini-halos of cold dark matter (Rees 1986). The characteristic velocity difference of $60 - 65$ km s^{-1} is also a severe constraint. For example, clouds in the disks or virialized halos of normal galaxies would produce velocity dispersions of $200 - 300$ km s^{-1} (Mo & Morris 1994). Recent N-body simulations, which treat baryons and dark matter as gravitationally-coupled fluids, have looked at the dynamics of galaxies, or baryonic lumps that will become galaxies (Evrard *et al.* 1994). At $z \sim 2$ and on scales of $50-500$ kpc, the one-dimensional pairwise peculiar velocity dispersion is $200-400$ km s^{-1}.

Recently, Morris & van den Bergh (1994) have speculated that a significant fraction of Lyα absorbers might be associated with tidal debris in small groups of galaxies. Even in a low velocity dispersion environment, a conservative upper limit of 150 km s^{-1} on the velocity difference between separate lines of sight is difficult to accomodate. The archetype for this environment, the Local Group, has a line of sight velocity dispersion of about 150 km s^{-1} (Zaritzsky 1994). Double galaxies, including those with tidal tails and distortions and common halos, have characteristic radial velocity differences of $200 - 300$ km s^{-1} (Tifft 1985). However it is not clear whether the tidally stripped material will reflect the velocity differences of the parent galaxies. If the absorbers have simple geometries near the upper end of the allowed range, ~ 500 kpc, then the gas must be in a state that approximates pure Hubble flow.

CHAPTER 4

THE LARGE SIZE OF LYMAN ALPHA GAS CLOUDS AT INTERMEDIATE REDSHIFTS[1]

Nadine Dinshaw[2], Craig B. Foltz[3], Chris D. Impey[2], Ray J. Weymann[4], and Simon L. Morris[5]

---

[2] Steward Observatory, University of Arizona, Tucson, AZ 85721

[3] Multiple Mirror Telescope Observatory, University of Arizona, Tucson, AZ 85721

[4] Carnegie Observatories, 813 Santa Barbara St., Pasadena, CA 91101-1292

[5] Dominion Astrophysical Observatory, 5071 W. Saanich Rd., Victoria, B.C V8X 4M6, Canada

The absorption lines of Lyman-alpha observed in the spectra of high redshift quasars are thought to arise in cosmologically-distributed, intervening "clouds," the origin and physical nature of which are still unknown. Various models have been proposed, including pressure-confined clouds in a hot intergalactic medium (Ikeuchi & Ostriker 1986), relics of primordial density fluctuations associated with the cold dark matter (CDM) scenario for the biased formation of galaxies (Bond, Szalay & Silk 1988), gravitationally-confined clouds in CDM minihalos (Rees 1986), and shocks resulting from explosive galaxy formation (Lake 1988). To distinguish between these models requires some knowledge of the cloud size and geometry. Here we present ultraviolet spectra of the Lyman-alpha forest of the quasar pair Q0107−025A,B in which we detect four absorption lines common to both spectra in the redshift range $0.5 \leq z \leq 0.9$, and six lines which are seen in the spectrum of one quasar but not the other. Assuming that these are Lyα lines, the directly-measured lower limit on the characteristic radii of the clouds is between 140 and $160\,h^{-1}$ kpc (where $h \equiv H_0/100$ km s^{-1} Mpc^{-1}, $q_0 = 0.5$). The typical velocity difference between the common absorption lines along the two lines of sight is only about 100 km s^{-1}. These direct measurements lead to a picture of absorbing clouds that are both larger in extent and more quiescent than can easily be explained by current theoretical models.

The close pair of quasars, Q0107−025A,B ($z_{em} = 0.956, 0.952$; angular separation $1\rlap{.}''29$), were observed on 1994 February 12 with the Faint Object Spectrograph (FOS) on the reburbished *Hubble Space Telescope* (*HST*). The G190H grating was used on the red side of the FOS with the 1″ circular aperture. The reciprocal dispersion of the G190H is 0.36 Å pixel^{-1}, corresponding to a spectral resolution (FWHM) of 1.4 Å, or ~ 200 km s^{-1}. A total of 222 minutes integration time was accumulated on A and 108 minutes on B covering the wavelength range 1625 − 2300 Å. Figure 4.1 shows the flux calibrated *HST*

spectra.

Absorption lines were fitted by Gaussians using algorithms identical to those of the *HST QSO Absorption Line Key Project* (Bahcall *et al.* 1993). To avoid introducing spurious absorption lines into the analysis, we considered only those lines detected at the $> 5\sigma$ confidence level, and we also restricted our sample to lines with wavelengths longward of 1800 Å, shortward of which the S/N degrades rapidly and the identification of Lyα lines is confused by the presence of higher order Lyman lines. This procedure ensures that in the range $1800 - 2300$ Å, all lines with $W_o \geq 0.33$Å should be detected at the 5σ limit in *both* objects. In addition, since absorption line systems containing metal lines may have different properties than the Lyman α forest lines, we selected for further discussion only those lines that we believe are neither members of metal-line containing systems, higher order Lyman series lines, nor, of course, Galactic absorption lines. The lines so selected are listed in Table 4 and marked by ticks in Figure 4.1.

The lines listed in Table 4 are believed to be Lyα absorption lines for the following reasons: (1) the lines are not attributable to Galactic absorption features; (2) in some cases (lines 4, 5, 6, 7 in A and 4, 6, 7 in B), there are statistically real lines attributable to higher order Lyman lines at the same redshift; (3) given the number of Lyα forest lines per unit redshift determined from other investigations (Bachall *et al.* 1993), we expect to see about 9 ± 3 Lyα lines with rest equivalent width > 0.32 Å in each quasar's spectrum in the wavelength range from $1800 - 2300$ Å, and we observe seven lines in both A and B; and (4) we have not identified any metal lines associated with the Lyα lines, though our current wavelength coverage is not extensive enough to search for either the C IV or Mg II doublet.

Table 4 contains four pairs of lines which are seen at very similar wavelengths in each spectrum. In all cases the redshift differences between the two features comprising the pair are small, $\Delta z < 0.0009$. The probability of getting *four* or more pairs of lines out of a total sample of 14 within this redshift difference is $\sim 10^{-7}$. We interpret these as
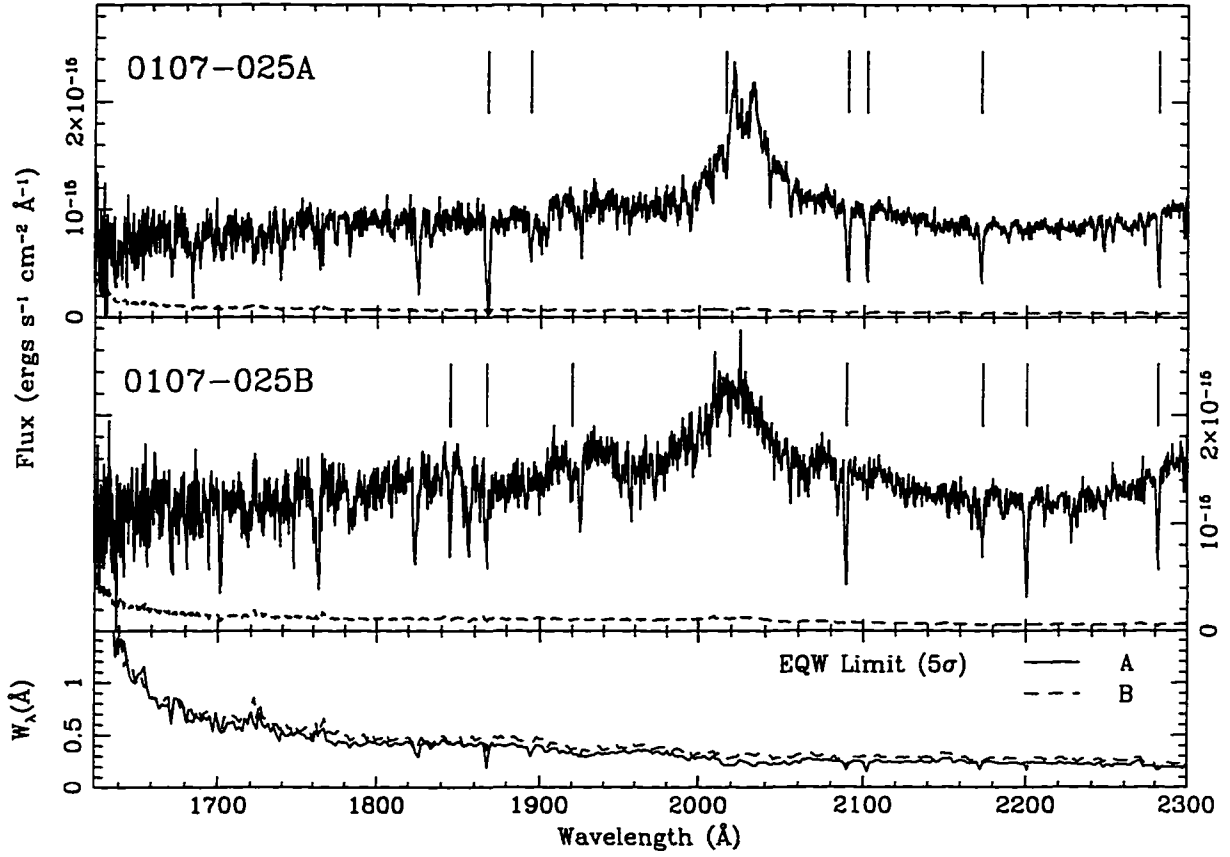
FIGURE 4.1—*HST* FOS spectra of Q0107−025A and B as a function of vacuum, heliocentric wavelength. The dotted line in each panel shows the 1-σ errors. Tickmarks indicate significant (> 5σ) absorption features with rest equivalent widths, $W_o \geq 0.33$ Å. Several strong lines which are not marked can be identified as higher order Lyman lines. The emission feature near 2020 Å is Lyman β+Ovi $\lambda\lambda$ 1031, 1037. An exposure of a PtCrNe comparison lamp was obtained immediately following one exposure of each of A and B to minimize the uncertainty in the wavelength calibration due to nonrepeatability in the positioning of the filter-grating wheel which was moved before each target was observed. The spectra were reduced via the STSDAS pipeline processing facility in IRAF using post-COSTAR flat-field and inverse sensitivity files. The bottom panel shows the equivalent width threshold (5σ) for an unresolved line.

TABLE 4.1

LYMAN-ALPHA ABSORPTION LINES OF QUASAR PAIR Q0107−025A,B

A No.	$\lambda(\text{Å})$	σ_λ	$W_0(\text{Å})$	σ_{W_0}	z_{abs}	B No.	$\lambda(\text{Å})$	σ_λ	$W_0(\text{Å})$	σ_{W_0}	z_{abs}	A–B $\Delta v(\text{km/s})$
			< 0.28			1	1845.17	0.06	0.44	0.04	0.5178	
1	1867.83	0.04	1.74	0.05	0.5364	2	1867.32	0.10	0.66	0.07	0.5360	82 ± 17
2	1894.34	0.10	0.60	0.05	0.5583				< 0.28			
			< 0.22			3	1919.99	0.33	0.38	0.08	0.5794	
3	2016.20	0.16	0.34	0.04	0.6585				< 0.18			
4	2090.33	0.03	0.94	0.03	0.7195	4	2089.55	0.03	0.79	0.03	0.7188	112 ± 4
5	2102.14	0.03	0.72	0.03	0.7292				< 0.16			
6	2172.52	0.03	0.65	0.03	0.7871	5	2173.58	0.07	0.40	0.03	0.7880	−146 ± 7
			< 0.14			6	2200.36	0.03	0.88	0.03	0.8100	
7	2282.03	0.02	0.67	0.02	0.8772	7	2281.61	0.03	0.58	0.02	0.8768	55 ± 5

cases where the lines of sight to the two quasars pierce the same absorber, so the lower limit on the transverse *diameter* of an absorber seen along both lines of sight is simply the proper separation of the lines of sight at the redshift of the absorber. For the common pairs observed here, this separation is $280 - 320$ kpc implying that the lower limits on the transverse *radii* range from about $140 h^{-1}$ kpc for the lowest redshift pair at $z = 0.536$ to more than $160 h^{-1}$ kpc for the pair at $z = 0.877$ (for $q_0 = 0.5$; assuming $q_0 = 0$, these limits become 160 and $200 h^{-1}$ kpc, respectively). These lower limits are independent of any assumptions about the cloud structure or geometry.

The radial velocities measured along the two lines of sight reflect differences in bulk motions (*e.g.* rotation, expansion or contraction) of the absorbing gas seen over scales equal to the separation of the lines of sight. The limit on the accuracy of these measurements is dominated by two types of errors: (1) a systematic uncertainty due to *HST* pointing errors causing the two quasar images to be placed differently within the $1''$ aperture of the FOS, and (2) random uncertainties arising in the wavelength calibration and line-fitting procedures. Since the observations of the two quasars used the same guide star, the *HST* pointing error projected along the dispersion direction is expected to introduce an uncertainty of 0.28 Å or about 42 km s^{-1} (FOS Instrument Team, private communication, 1994). Since this effect is systematic, shifting all of the lines in one spectrum relative to those in the other, it should be manifest in the mean of the velocity differences of the common lines, which range from -146 km s^{-1} to 112 km s^{-1} (Table 4). The mean velocity difference is only 26 km s^{-1}. Furthermore, the measured shift between the wavelengths of the Galactic Al II $\lambda 1671$ line is 20 ± 36 km s^{-1}. Both of these lead us to believe that there is no large systematic shift between the two spectra. The random uncertainty in the measured radial velocity *difference* between two lines is conservatively estimated to be about 17 km s^{-1} while the rms velocity difference for the four coincident pairs is 104 km s^{-1}. Therefore, we conclude that we are seeing statistically significant, albeit small, velocity differences over scales of several hundred kpc.

In the foregoing discussion we have consistently referred to 'cloud radii' rather than 'correlation lengths'. The present observations do not allow us to directly discriminate between single coherent clouds versus correlated but distinct structures. Assuming the former and that the clouds are identical and spherical, it is possible, using standard maximum likelihood techniques (McGill 1990), to estimate the most probable value as well as the upper and lower 95% confidence limits for the radius, R, of the clouds. Here, by "radius" we simply mean the impact parameter which produces column densities corresponding to our equivalent width detection limit. The probability distribution $P(R)$ [solid curve] and its cumulative distribution [dashed curve] for $q_0 = 0.5$ are plotted in Figure 4.2. The most probable value of R given by the peak of the solid curve is $350\,h^{-1}$ kpc. The 95% confidence lower and upper bounds on the cloud radius estimated from the dashed curve correspond to $270 < R < 860\,h^{-1}$ kpc. For $q_0 = 0.0$ the radii are larger by about 20%.

Previous constraints on Lyα forest absorber sizes (Shaver & Robertson 1983; Foltz et al. 1984; Crotts 1989; Smette et al. 1992), also based on the presence of common absorption lines in the spectra of physical or gravitationally-lensed pairs of quasars suggest cloud sizes about an order of magnitude smaller. Recent observations of the lensed pair HE 1104-1805 have been used to infer a 2σ model-dependent lower limit on the cloud radius, at redshift $z \simeq 2.5$, of $25\,h^{-1}$ kpc (Smette et al. 1995) and two very recent independent studies of the quasar pair 1343+2640 A,B separated by $9.5''$ suggest cloud radii of at least $\sim 20\,h^{-1}$ kpc at $z \simeq 2$ (Bechtold et al. 1994; Dinshaw et al. 1994).

For typical Doppler widths, neutral hydrogen column densities and expected values of the ionizing radiation field at these redshifts (Madau 1992), static self-gravitating clouds are expected to be smaller than this, especially with any dark matter binding (cf. Weymann et al. 1995; eq. 8); pressure confinement would make them smaller still. However, if the clouds are in the process of collapsing they would be larger than these simple estimates for static structures.
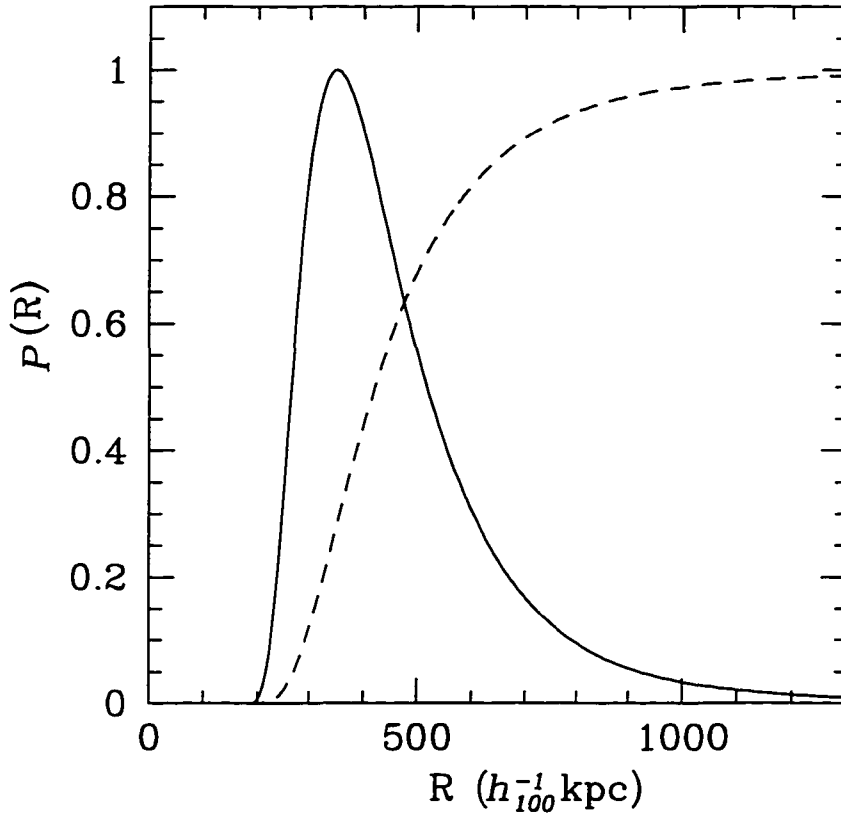
FIGURE 4.2—Probability distribution $P(R)$ normalized to one at its peak as a function of cloud radius for the four coincident and six anticoincident lines observed in the spectra of Q0107–025A,B (solid curve). The cumulative probability distribution is also plotted (dashed curve) from which lower and upper limits on the radius of the absorbers can be estimated. A cosmological model with $H_0 = 100\,\mathrm{km\ s^{-1}\ Mpc}$ and $q_0 = 0.5$ was assumed.

Alternatively, the large characteristic sizes implied by Figure 4.2 may be more indicative of correlation lengths than actual cloud sizes. There is evidence that luminous galaxies have effective cross sections for producing Lyα with $W_o \geq 0.3$ Å of several hundred kpc (Lanzetta et al. 1994), and it has also been suggested that pressure-confined tidal debris resulting from mergers or close encounters of galaxies spread over several hundred kpc may be involved (Morris & van den Bergh 1994). For models such as these, the large characteristic size for the Lyα structures which our observations establish is not especially surprising. However, the small projected velocity differences may be more difficult to understand, since clouds unaffected by drag in the disks or virialized halos of normal galaxies would have velocity dispersions of $200 - 300$ km s^{-1}(Mo & Morris 1994). Similarly, the characteristic line-of-sight velocities associated with small groups of galaxies, or with dwarf galaxies orbiting around luminous galaxies, are typcially 150 km s^{-1}(Zaritsky 1994). We must note, however, that our observed typical velocity difference of 104 km s^{-1} is based upon only four pairs of lines and so may not be highly statistically significant.

Regardless of which, if any, of the models above may prove to be correct, our observations suggest velocity differences of less than a few hundred km s^{-1} over scales of several hundred kpc. By contrast, examination of the distribution of the small number of Lyα line profiles currently observed with the HST Goddard High Resolution Spectrograph at 20 km s^{-1} resolution reveals that: (1) the typical Doppler width distribution is about the same as that at high redshifts, i.e. centered at about 30 km s^{-1} with a small dispersion; and (2) there is very little evidence for structure (e.g. an excess of line pairs with separation 50-300 km s^{-1}). So there is a marked contrast between the transverse versus line-of-sight velocity correlation properties of the absorbers, though it must be noted that the transverse properties result from studies of the relatively strong lines reported here while the line-of-sight properties are deduced from high spectral resolution studies of weaker lines. If these arise from different populations, then the comparison of their properties may be invalid, but, taken at face value, this evidence suggests that we are dealing

with coherent structures of low dimensionality, such as sheets or filaments, though the observations could also be explained by flattened disks supported by rotational velocities of (allowing for projection effects) order 200 km s^{-1} but with random velocities which are much smaller than this along each line of sight.

We are in the process of obtaining GHRS observations of this pair of quasars which extend to lower redshifts as well as supporting ground-based observations which may help to resolve some of the questions raised here.

CHAPTER 5

ADDITIONAL OBSERVATIONS AND ANALYSIS OF THE LYMAN ALPHA ABSORBERS TOWARD THE QSO PAIR Q0107−025A,B[1]

Nadine Dinshaw[2], Ray J. Weymann[3], Chris D. Impey[2], Craig B. Foltz[4], Simon L. Morris[5], and Tom Ake[6]

[2]Steward Observatory, University of Arizona, Tucson, AZ 85721

[3]Carnegie Observatories, 813 Santa Barbara St., Pasadena, CA 91101-1292

[4]Multiple Mirror Telescope Observatory, University of Arizona, Tucson, AZ 85721

[5]Dominion Astrophysical Observatory, 5071 W. Saanich Rd., Victoria, B.C V8X 4M6, Canada

[6]Goddard Space Flight Center, Code 681/CSC, Greenbelt, MD 20771

Abstract

We present further analysis and discussion of the properties of the absorption lines in the QSO pair Q0107−025A, B (z_{em} = 0.956, 0.952; angular separation 1.'29)based upon spectroscopy obtained with the Faint Object Spectrograph of the *Hubble Space Telescope* (*HST*). We also present observations at shorter wavelengths taken with the *HST* Goddard High Resolution Spectrograph low resolution grating, as well as Multiple Mirror Telescope spectra of the pair with the intent of looking for metal-line counterparts to the Lyα absorption systems. The most interesting feature revealed by the GHRS spectra is a weak Lyman limit system with a redshift of z = 0.400. The Lyman limit system itself is seen only in Q0107−025B, but the corresponding Lyα line can be seen in the FOS spectra of both Q0107−025A and B indicating that the lower column density material is more extended than the higher column density material. The impact parameters of these associations give further indication of the large size of the low to moderate redshift Lyα absorbers. From the presence of common absorption in the FOS spectra, we obtain lower limits on the radius of the absorbers of $140 - 160\,h^{-1}$ kpc ($h \equiv H_0/(100$ km s^{-1} Mpc^{-1}); q_0 = 0.5), where we have assumed large coherent clouds. From a sample of 5σ lines with $W_0 > 0.32$ Å, we counted five systems (including a probable system) common to both spectra within velocity differences less than ±150 km s^{-1}, and six systems which were not in common to both spectra. Using a simple maximum likelihood analysis, we estimated a radius of $505\,h^{-1}$ kpc for spherical absorbers with 95% confidence lower and upper limits of $360 < R < 1535\,h^{-1}$ kpc. For disk-like absorbers, we derived a most probable radius of $715\,h^{-1}$ kpc and confidence limits of $470 < R < 2295\,h^{-1}$ kpc. We also present a new statistical technique to test the relative likelihood of three geometric models. In particular, we consid-

ered spherical absorbers, with and without a distribution in size, as well as pseudo-filamentary and disk-like absorbers. Spherical absorbers with uniform radius cannot represent the observations and are ruled out. The model which provided the most favorable fit to the observations was found to be randomly-inclined disks with characteristic radius $850\,h^{-1}$ kpc with 95% confidence lower and upper bounds of $600 < R < 1200\,h^{-1}$ kpc. Our results are in agreement with recent cosmological simulations in which $Ly\alpha$ absorption arises in diverse structures with a range of scales.

5.1   Introduction

A great deal of progress has been made in understanding the physical properties and evolutionary characteristics of the material producing the Lyα absorption systems seen in QSO spectra. Recent ground-based results from very high resolution and S/N echelle spectra indicate significant metal enrichment and clustering on small velocity scales even for high redshift low column density systems (Cowie et $al.$ 1994; Tytler et $al.$ 1995), but there is no direct evidence on the relationship of these clouds to galaxies. At low redshifts, the data suggest a fairly intimate connection between many intermediate column density Lyα clouds and galaxies (Lanzetta et $al.$ 1995; Le Brun, Boisse & Bergeron 1995; Bowen, Blades & Pettini 1996), though a number of low column-density clouds have been found in or near voids in the galaxy distribution (Morris et $al.$ 1993; Stocke et $al.$ 1995). Encouraging progress has been made in N-body simulations which incorporate gas hydrodynamics (Cen et $al.$ 1994; Zhang, Anninos & Norman 1995; Hernquist et $al.$ 1996; Miralde-Escudé et al. 1996), and some of the characteristics of the Lyα forest observations are reproduced quite well.

Despite this progress, the actual origin and physical nature of the clouds is far from clear; it is not even clear if the Lyα absorption seen at low redshifts in HST spectra represents the same phenomenon as that seen at high redshifts. Critical information for understanding the nature of the Lyα absorption is the geometry and kinematics of the absorbers, which can be constrained by studying two or more lines of sight with small angular separation.

Until fairly recently it appeared that the characteristic transverse sizes of absorbers at redshifts $\gtrsim$ 2 were a few tens of kpcs. Recent observations have shown that the characteristic sizes are somewhat larger. In particular Bechtold et $al.$ (1994) and Dinshaw et $al.$ (1994) find a characteristic radius[1] of order $100\,h^{-1}$ kpc at $z \simeq 2$. Still more

---

[1]The meaning of the "characteristic radius" is somewhat imprecise. In the present context it refers to the most likely impact parameter for an assembly of assumed identical spherical clouds which yield Lyα

recently, Dinshaw *et al.* (1995; hereafter Paper I) observed lines of sight towards the QSOs Q0107–025A, B (z_{em} = 0.956, 0.952; angular separation 1."29) and determined for the first time characteristic sizes at much smaller redshifts. The results implied a characteristic radius of at least $\sim$ 150 h^{-1} kpc and perhaps as large as 1 Mpc over the redshift range $0.5 < z < 0.9$.

At face value, these results give a weak indication that the characteristic transverse sizes of the Lyα absorbers may increase with decreasing redshift, and there is growing evidence from *HST* observations of paired lines of sight at redshifts $1.1 < z < 1.7$ that the evolution in the cloud radius may be real (Dinshaw *et al.* 1996). However, Fang *et al.* (1996) have suggested that the more significant correlation is one between inferred cloud size and line-of-sight separation, which they attribute to a distribution in cloud size.

It is not yet clear if the majority of the Lyα absorbers at redshifts $\lesssim$ 1 arise from the same mechanisms which produce the high redshift absorbers. Study of the relation of the distribution of the absorbing material along more than one line of sight with galaxies may give us some clues about the topology and kinematic structure of the absorbers. We are currently surveying the neighboring galaxies in the field of Q0107–025A, B in order to study the spatial correlation between the galaxies and the Lyα absorbers seen in *HST* GHRS spectra of the pair. The results will be presented in a forthcoming paper.

The remainder of the chapter is organized as follows: In §5.2, we describe the observations taken with the FOS and GHRS, and present lists of all the lines in those data. In the same section, we also present ground-based observations obtained with the Multiple Mirror Telescope. In §5.3, we describe in detail the method used to identify the lines. In §5.4, we define subsamples of the data and derive a definition for common systems; we also discuss the properties of Lyman limit and metal-line systems in that section. In §5.5, we estimate the sizes of the Lyα clouds, investigate their column density and velocity structure. Finally, in §5.6, we summarize and discuss our results. Throughout this

---

absorption above some equivalent width threshold – typically $\sim$0.3 Å.

chapter, we assume a cosmological model with $H_0 = 100$ km s^{-1} Mpc^{-1} and $q_0 = 0.5$, except where explicitly stated, and express the dependence upon the Hubble constant by means of the parameter $h \equiv H_0/(100$ km s^{-1} Mpc$^{-1})$.

5.2 Data

In this section, we present observations of the Lyα forest obtained with the FOS and GHRS on the *HST*, as well as ground-based data taken with the MMT in order to search for metal systems associated with the Lyα absorption lines. The program QSOs are listed in Table 5.1, along with their J2000 coordinates, Gunn g magnitudes, and redshifts. The coordinates were measured by the support staff at the Space Telescope Science Institute (STScI) using the Guide Star Selection System Astrometric Support Package (GASP), and are accurate to $1''$. The improved coordinates give an angular separation of the lines of sight of $1\rlap{.}''29$. Magnitudes and redshifts are from Surdej *et al.* (1986). A journal of all the observations presented in this chapter is given in Table 5.2.

5.2.1 The FOS Spectra

5.2.1.1 Observations and Data Reduction

A preliminary account of the FOS observations was reported in Dinshaw *et al.* (1995; hereafter Paper I). A more detailed description of the observations is provided here. We obtained ultraviolet observations of Q0107−025A,B on 1994 February 12 with the post-COSTAR Faint Object Spectrograph (FOS) on the *Hubble Space Telescope* (*HST*), using the red Digicon detector, $1''$ circular aperture, and G190H grating. This configuration yielded a spectral resolution (FWHM) of 1.4 Å, or 200 km s^{-1}, over the wavelength range from 1625 − 2300 Å. The spectra were obtained in 40 minute exposures with a total of 222 minutes accumulated on A and 108 minutes on B. The signal-to-noise ratio (SNR) in the spectrum of Q0107−025A is at least 12 per pixel in the continuum shortward of ~ 2000 Å and approaches 25 per pixel at longer wavelengths. The SNR for Q0107−025B

was slightly poorer: 10 and 22 per pixel shortward and longward, respectively, of ~ 2000 Å.

The FOS spectra were reduced at the STScI via the STSDAS pipeline processing facility in IRAF. Post-COSTAR "superflats" (Lindler *et al.* 1995) and inverse sensitivity files were used to flat field and flux calibrate the data, respectively. A correction was also performed for dead and disabled diodes using the reference file recommended for data obtained after 13 September 1993.

A potentially significant source of uncertainty in the zero point of the wavelength scale is caused by nonrepeatability in the positioning of the filter-grating wheel. This error can be unacceptably large, amounting to 0.35 diodes, if calibration exposures are not obtained at the same time as the target exposure (FOS Instrument Handbook, Version 6.0 June 1995). Given the need for accurate measurements of the zero-point shift between the two spectra and the fact that only one Galactic absorption line falls within the wavelength range of the G190H grating, the acquisition of simultaneous calibration exposures was important for this program. Therefore, we obtained one exposure of a PtCrNe comparison lamp for each target, and required that the filter-grating wheel be not moved between target exposures. The wavelengths were then recalibrated using the lamp exposures. The rms error in the wavelength coefficients was ~ 0.06 Å, or ~ 9 km s^{-1}. Since the same comparison lines were used to calibrate both spectra, the wavelength calibration is expected to introduce a systematic error common to both spectra and should not affect the *differences* in radial velocities of the lines found to be in common to both spectra (defined in § 5.4.2).

By far, the dominant uncertainty in the wavelength zero-point is due to *HST* pointing errors that arise from the relative placement of the two QSO images in the 1″ aperture of the FOS. Since the same guide star was used during the exposures of both QSOs, this error is expected to be about 0.40 Å (private communication with FOS Instrument Team), yielding an error projected along the dispersion direction of up to 0.28 Å or ~ 42 km s^{-1}. This effect is a systematic in the sense that it shifts all of the lines in one spectrum relative

to those in the other. The observed wavelength of the only Galactic line accessible with the G190H grating (Al II $\lambda1671$) gives a measured shift between the spectra of Q0107–025A and B of 20 ± 36 km s^{-1}, well within the estimated uncertainty from pointing errors. [The Fe II $\lambda\lambda2344$, 2374 lines have been identified in some HST data (Bahcall *et al.* 1992), but we see no evidence for them in our spectra.] We made no attempt to correct for a zero-point shift in the wavelengths since the Al II $\lambda1671$ lines in both A and B appear to be contaminated by the Lyγ line associated with the common redshift system at $z_{abs} = 0.719$. Given the measured shift between the Galactic line is small, we believe that there is no large systematic shift between the two spectra.

Figures 5.1 and 5.2 show the flux calibrated spectra and their 1σ error arrays derived from photon statistics. The broad emission lines at 2020 Å are blends of O VI $\lambda\lambda1031, 1037$, with possibly some contribution from Lyβ. The emission feature in Q0107–025A shows a double-peaked structure, where the peaks correspond well in redshift to the O VI doublet. This is the first case we are aware of where the blend of O VI $\lambda1031$ and O VI $\lambda1037$ in emission appears resolved. The continuum fits and significant lines are also shown in the figures. We describe the procedure used to fit the continuum and selection significant lines in the next section.

5.2.1.2 Continuum Fitting and Selection of Significant Absorption Lines

An interactive program written by T. Aldcroft (Aldcroft 1993) was used to fit the continua shown in Figures 5.1 and 5.2. The program iteratively fits cubic splines to the average of a specified number of datapoints, where the tightness of the fit is determined by the number of points used in the average. Points deviating negatively by more than two standard deviations from the estimated continuum were rejected from subsequent iterations until the RMS positive and negative residuals in the remaining points were equal. The fit typically converged in less than four iterations. In order to establish whether the undulations in the spectra are weak emission features, we compared our data with the composite of
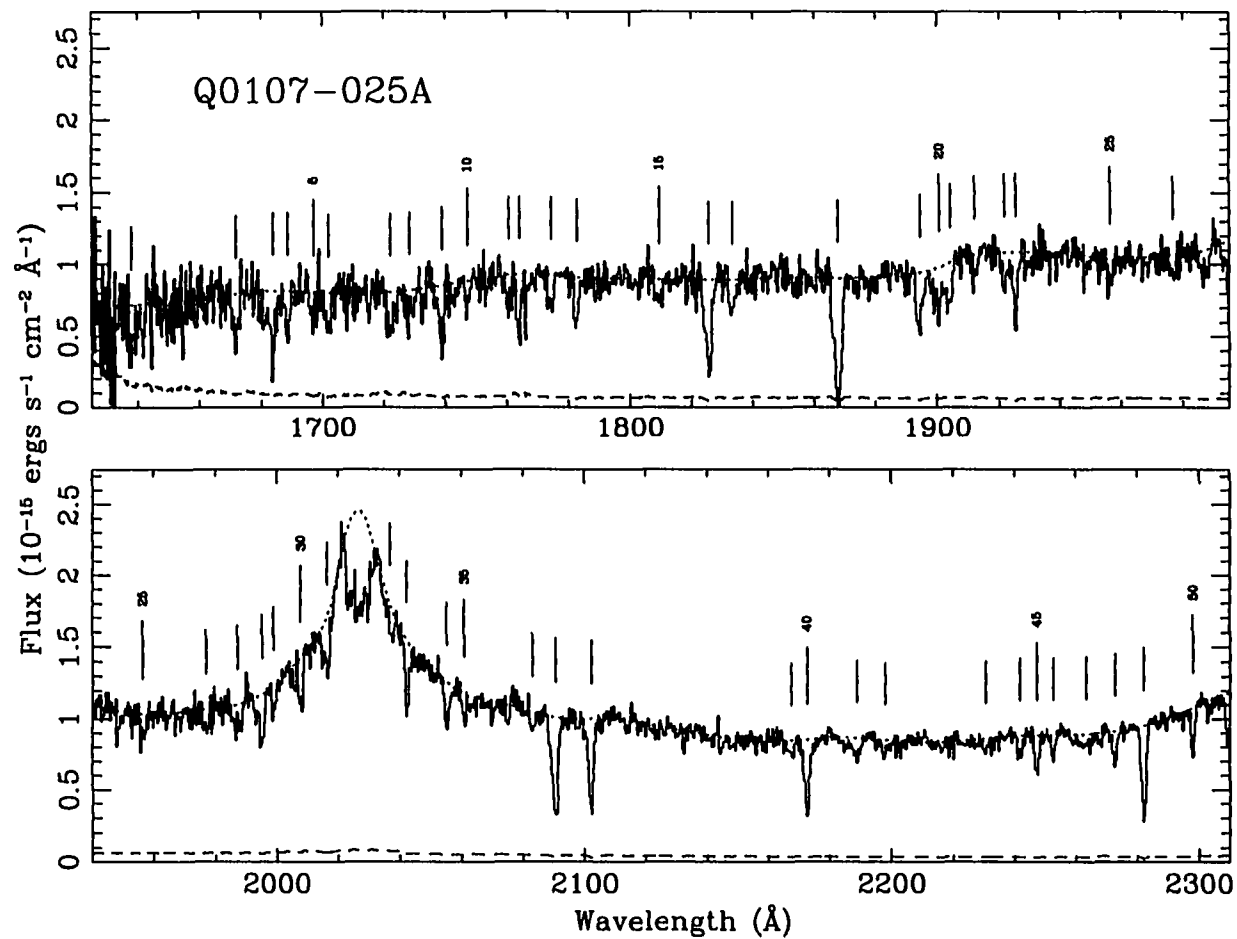
FIGURE 5.1—Spectrum of Q0107−025A obtained with the *HST* FOS as a function of vacuum wavelength. The dotted line shows the 1-σ error in the flux. The dotted line is the continuum fit. Tickmarks indicate absorption features detected at or above the 3.5σ confidence level. The emission features near 2020 Å is Ovi λλ1031,1037, with possibly some contribution from Lymanβ.
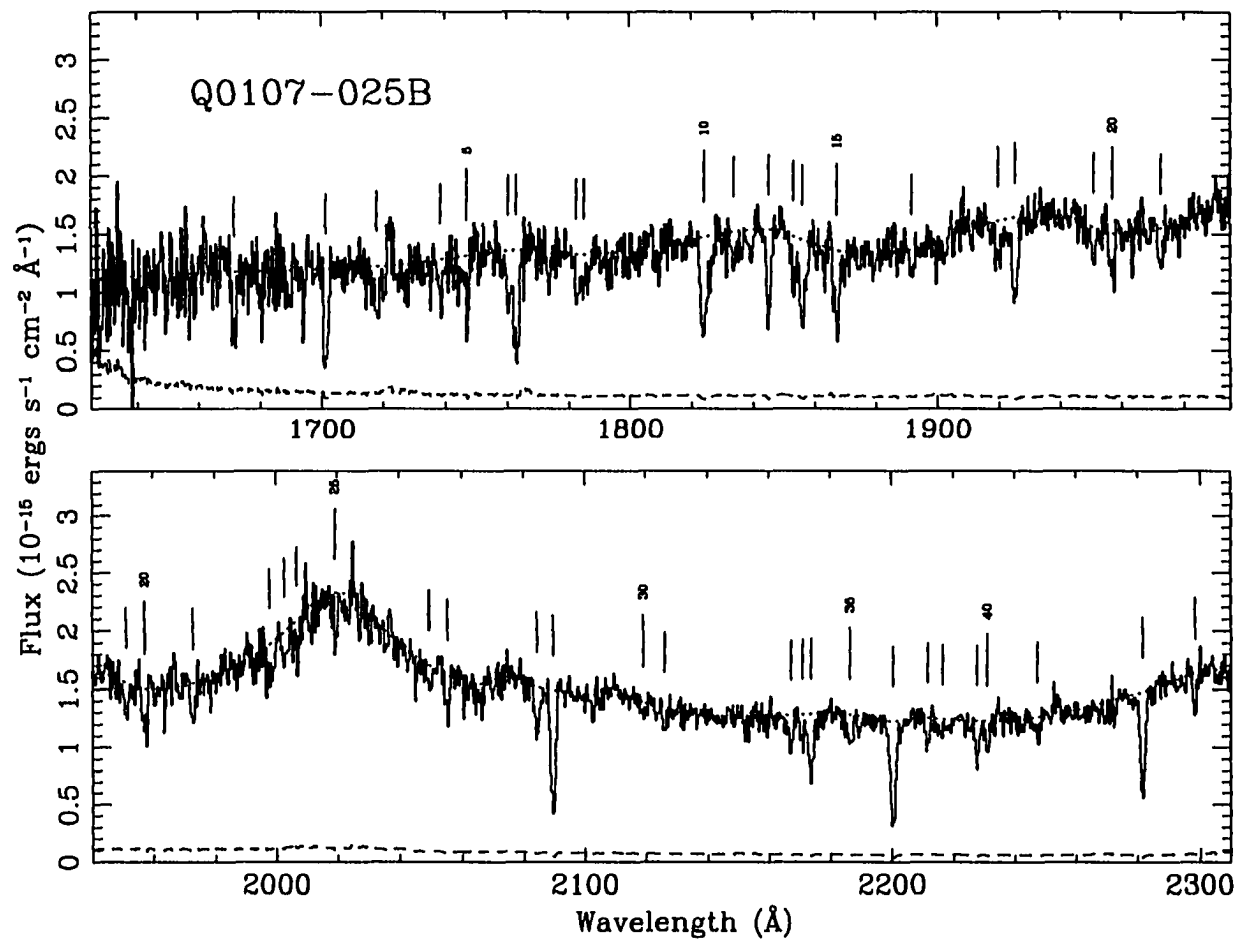
FIGURE 5.2—As Figure 5.1, for Q0107−025B.

5 *HST* FOS spectra taken with the G160L grating (Hamann, Zuo & Tytler 1995). By adjusting the continuum level to compensate for differences in the equivalent width and slope, the composite spectrum looked remarkably like those of Q0107−025A and B. The agreement however was not sufficient to use the composite as the true continuum, but was useful in guiding the placement of the continuum fits. The program also allows for manual modifications which were necessary in the emission lines. Our best guess of the true emission profiles are shown in Figures 5.1 and 5.2. In the spectrum of Q0107−025A, we did not attempt to fit between the peaks of the O VI $\lambda\lambda 1031$, 1037 emission lines, but we excluded the region from 2020 − 2032 Å in constructing the line list.

We searched for significant lines in the normalized spectra using the interactive line-finding and fitting software of T. Aldcroft which uses algorithms similar to the HST Quasar Absorption Line Key Project (cf. Schneider *et al.* 1993). The instrumental line spread function (LSF) was convolved with the data and error arrays to get the equivalent width W_i and corresponding uncertainty $\sigma(W)_i$ of an unresolved line at each pixel. The regions satisfying the criterion $W_i/\sigma(W)_i > 3.5$ were flagged as candidate lines. All the candidate absorption lines were then fitted in an interactive manner by single or, in the case of obvious blends, multiple Gaussians unconstrained in FWHM, equivalent width and central wavelength. The signal-to-noise ratio defined according to the Key Project as (Schneider *et al.* 1993)

$$\text{SNR} = \frac{W}{\sigma(W)}$$

where W is the measured equivalent width and $\sigma(W)$ is the 1σ uncertainty in the equivalent width was computed for each line and those absorption features with SNR > 3.5 were included in the line lists for Q0107−025A and B given in Tables 5.3 and 5.4, respectively. This list was useful in identifying the absorption lines in these spectra as well as the GHRS data. Below, we define subsamples of 3.5σ and 5σ Lyα absorption lines drawn from these line lists to be used later in our statistical analyses.

In a number of cases, the best fit to a line was a single Gaussian with an unphysically

large FWHM. [Doppler parameters determined by fitting Voigt profiles to Lyα lines in echelle spectra are typically less than $b = 60$ km s^{-1} (Hu et $al.$ 1995).] Unless the line-finding software separated the lines into smaller components, we counted them as single lines in Tables 5.3 and 5.4, although in higher resolution data these lines will likely be resolved into narrower components. Only in those cases where the blended components were flagged by the line selection software did we attempt a multicomponent fit, and then only when the reduced χ^2 of the fit was smaller for the multicomponent fit than for a single Gaussian. There were also cases where the FWHM of a line was narrower than that of the instrumental line spread function (LSF). A histogram of FWHMs showed a smooth distribution with a peak between 1.4 and 1.8 Å, and a sharp cutoff for widths < 1.3 Å. We included all the lines with FWHM above this cutoff value, with the assumption that the lines with widths between 1.3 and 1.4 Å are probably real, but their line profiles are artificially narrow because they have been contaminated by noise or because the continuum has been fit too low across the line. This represents a departure from the approach taken by the Key Project, where the width of the fitted Gaussian was kept fixed at the instrumental LSF. Because we selected lines according to their SNR, this approach would have overestimated the significance of the narrow lines, by underestimating the error in the fit.

In order to evaluate the completeness and reliability of the line lists, we performed several tests on the data. First, an independent check of the line lists was made using the software "JASON" developed for the HST Quasar Absorption Line Key Project (cf. Bahcall et $al.$ 1995, and references therein). We are grateful to B. Jannuzi for providing us with the JASON line lists. The program is fully automated and therefore offers a less subjective approach to line selection and fitting. The JASON line lists were derived using the normalized data used to generate Tables 5.3 and 5.4. Therefore, a comparison of the lines selected and measured by the two programs should be independent of the continuum fit.

The original analysis detected 93 lines among the two lines of sight. The Key Project software recovered 92 of those lines and found an additional 18 lines not listed in Tables 5.3 and 5.4. Of the extra 18 lines, 15 were fitted by JASON with the widths of the Gaussians profiles fixed at the instrumental LSF, which, as discussed above, tends to overestimate the SNRs of the lines. Since the line widths were always allowed to vary in our analysis, those lines would not be expected to be included in our line lists. Almost all the lines had equivalent widths less than 0.20 Å; for one, $W_{obs} \simeq 0.25$ Å. The remaining three lines selected only by the independent check were fitted as single, broad features with line widths > 5 Å. In our analysis, these features were modeled by two components whose SNR did not exceed the 3.5σ confidence level. The equivalent widths of the components were less than 0.20 Å. The only line not found by JASON (see footnote in Table 5.3) is located in the noisy part of the spectrum of Q0107−025A, shortward of 1800 Å.

Among the lines found by both searches, the central wavelengths and equivalent widths of the lines agreed within the uncertainties in all but four cases. The discrepancies can all be traced to differences in the treatment of broad or blended features. In general, the Key Project software fit a single component, whereas we found two components to be a better representation of the line. In one particularly noisy part of the spectrum, the fit to a line appeared unrealistically broad, since JASON systematically increases the region in which a line is fit if another line is found within a given wavelength window. In our interactive treatment of the data, we were able to exercise greater control in the size of the fitting window. In none of the cases, did the differences in the fit affect the *number* of lines among the two line lists, though it did cause differences in the equivalent widths of the lines.

In order to evaluate the effect of continuum placement on the line lists, we dropped the continuum everywhere by 3%, as a means of providing a reasonable lower bound to the true continuum level in each spectrum, and repeated the search for significant features. A number of lines dropped out of the sample, giving an indication of the lines that were

most secure and independent of the continuum. The lines not found in the new search have been flagged by a question mark in Tables 5.3 and 5.4. Typically, their equivalent widths were less than 0.36 Å; the three above this equivalent width were broad features and could be artifacts of the continuum fit. Finally, we inverted the spectra and again search for significant "emission" features. We found three with equivalent widths less than 0.28 Å.

Based on these tests, we estimate the reliability and completeness of the line lists above a rest equivalent width of ~ 0.24 Å to be at least 90%.

5.2.2 The GHRS Spectra

5.2.2.1 Observations

In order to extend the redshift coverage of the Lyα lines along these two sight lines down to redshifts near zero, we have obtained spectra with the *HST* Goddard High Resolution Spectrograph (GHRS) using the G140L grating and the large science aperture (LSA). The usable spectral range is from about 1220 − 1495 Å. These two objects (especially Q0107−025A) are faint and near the limit of what can reasonably be observed with GHRS. Consequently, the SNR for Q0107−025A is quite poor. Nevertheless, some interesting features have been observed.

Q0107−025B was observed on 22 September 1994 UT and Q0107−025A was observed on 15 November 1994 UT. Quarter diode substepping was used with the FP-SPLIT option. A total of 9124 seconds was obtained for each object for each pixel (substep). The mean background rate was approximately $0.007 \, \mathrm{pixel}^{-1} \, \mathrm{s}^{-1}$ and the SNR ranged from ~ 3 at 1220 Å to a peak of 7 at 1350 Å and 4 at 1480 Å for Q0107−025B with corresponding SNR levels of ~ 3, 4 and 3 for Q0107−025A. One pixel is approximately 0.14 Å and the line spread function has been approximated by a Gaussian with a FWHM of 10 pixels yielding a spectral resolution of 1.4 Å, or a velocity resolution of $\sim 300 \, \mathrm{km \, s}^{-1}$ (Gilliland 1995). The spectra were reduced at the Goddard Space Flight Center using the IDL

software developed by the GHRS team (Blackwell *et al.* 1993).

5.2.2.2 Selection of Significant Absorption Lines

The spectra for these two objects are shown in Figure 5.3. The spectra have been smoothed using a three-pixel running boxcar for the purpose of display only; the original data were used in the selection of significant lines. From this figure it is immediately obvious that there is a Lyman limit in Q0107−025B which is missing (or very much weaker) in Q0107−025A. We have generated line lists using exactly the same procedure as in § 5.2.1.2. However, because of the low SNR of these spectra we have been less conservative and listed all absorption features with formal significance greater than only 3σ. Table 5.5 shows the resulting line list with the columns for each object being respectively the line number, wavelength, formal 1σ uncertainty in the wavelength due to counting statistics, the *observed* equivalent width and associated uncertainty, the formal SNR of the line, the proposed identification, and the redshift. The limits on the equivalent widths of lines which are *not* seen along one line of sight when they are seen along the other line of sight are also 3σ limits. Clearly, the reality of some of the lines near the low end of the significance threshold must be treated with some caution and should be verified by obtaining better data in the future.

Relative wavelength shifts between the GHRS spectra of Q0107−025A and B are somewhat uncertain. The difference in the interstellar C II λ1334 velocities between Q0107−025A and B (119 km s^{-1}) deviates by about 3σ from the formal expected uncertainty in the difference. (The Si II λ1260 line in Q0107−025A gives an even more discrepant result but the profile is complex and noisy). We have therefore shifted the Q0107−025A wavelength scale by 119 km s^{-1} to the red to force agreement with the Q0107−025B wavelength scale.

Inspection of Table 5.5 shows that many of the stronger lines in Q0107−025B are associated with the higher Lyman series of the 1701.52Å Lyman α line in the FOS spectrum
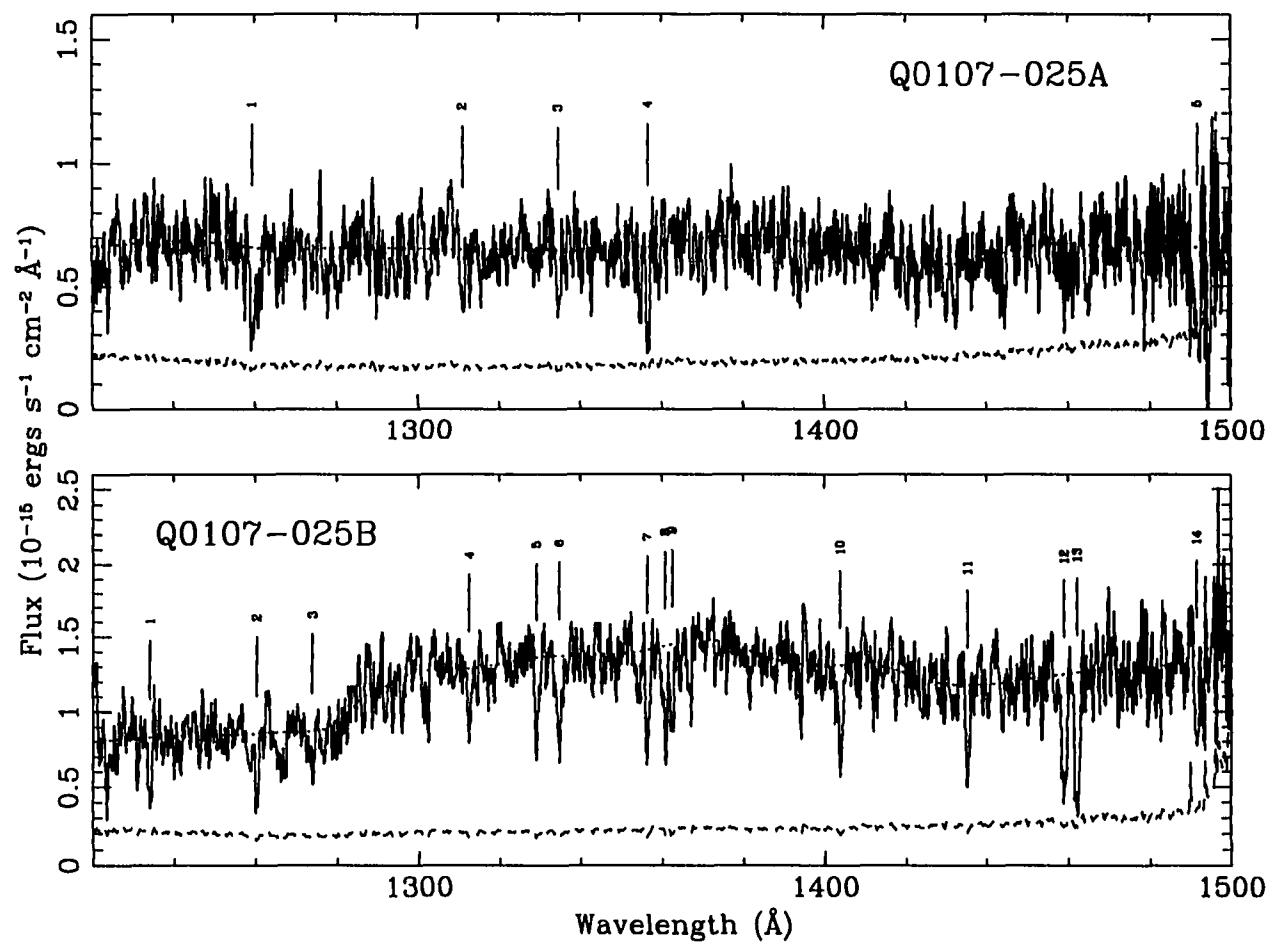
FIGURE 5.3—Spectra of Q0107−025A (*upper panel*) and B (*lower panel*) obtained with the *HST* GHRS as a function of vacuum wavelength. The dashed line in each panel shows the 1σ errors, and the dotted line gives the continuum fit. The spectra have been smoothed using a three-pixel running boxcar.

of Q0107−025B at a redshift of 0.3997. The measured redshifts of the Lyman series from β through ϵ were quite consistent among themselves, but were shifted about 75 km s^{-1} to the blue relative to the wavelength scale for the FOS Q0107−025B observation. We therefore applied a shift of 75 km s^{-1} to the red to both the GHRS spectra (in addition to the 119 km s^{-1} shift to Q0107−025A noted above) to bring them into agreement with the FOS scale. *All these shifts have already been applied in Table 5.5.*

The optical depth of the Lyman limit in Q0107−025B was estimated by fitting the Q0107−025B continuum with a constant flux between 1300 Å and 1400 Å (corresponding to rest wavelengths in the Lyman limit system of 928 Å and 1000 Å), extrapolating it to shorter wavelengths, performing a similar fit between 1228 Å and 1270 Å (corresponding to rest wavelengths 877 Å to 907 Å) and measuring the ratio at rest 910 Å. We obtain an optical depth of 0.48 ± 0.06 corresponding to an HI column density of $\log N(\text{H\,I})_B = 16.88 \pm 0.06$. The uncertainty is a rough estimate based upon slightly different fitting windows and fits made by three of us independently.

A similar fit to Q0107−025A gives a ratio of fluxes shortward and longward of the Lyman limit with an optical depth zero to within the errors. We estimate a conservative *upper* limit on the optical depth of the Lyman limit in Q0107−025A to be $\tau \simeq 0.1$, or $\log N(\text{H\,I})_A \leq 16.20$. A simple naive *lower* limit on the column density towards Q0107−025A follows from assuming that the Lyα line in Q0107−025A is in reality a number of unsaturated components. This limit requires $\log N(\text{H\,I})_A > 13.90$. Assuming a single component with a Doppler parameter of 35 km s^{-1} would imply a value of $\log N(\text{H\,I})_A = 14.52$. This would imply an equivalent width of the corresponding Lyβ line in Q0107−025A at 1435 Å of about 0.24 Å. There is no indication of a line at that wavelength; an unresolved line would have been only a 1.7σ fluctuation.

We will adopt $\log N(\text{H\,I})_A = 14.5$ as the approximate column density for the $z = 0.3997$ system towards Q0107−025A, bearing in mind the limits and corresponding large uncertainties just described.

5.2.3 Ground-Based Spectra of Q0107−025A,B

Optical spectra of the pair were obtained at the Multiple Mirror Telescope using the Blue Channel of the MMT Spectrograph equipped with a 3072 × 1024 optimized Loral CCD detector. Q0107−025A and B were observed for a total of 6600 and 4800 seconds, respectively, over the wavelength range 4150 − 5650 Å on 29 September 1994 and for 9600 and 5400 seconds in the range 3250 − 4250 Å on 2 October 1994. An 832 gpm grating was used in the second order on both nights along with a 1″ entrance slit; this combination gives a spectral resolution of 1 Å (FWHM). Data reduction followed standard procedures. Relative flux calibration was carried out using the spectrophotometric standard star Hiltner 600. Note that the standard was also observed through the narrow slit so that absolute fluxes derived from the spectroscopy will be unreliable. The resulting spectra are plotted in Figure 5.4.

The SNR of the ground-based spectrum is fairly low at the blue end of the spectrum (SNR $\simeq$ 3.5 and 8 in Q0107−025A and B, respectively at 3300 Å), but it reaches respectable values at wavelengths longward of about 3500 Å. The 5σ observed equivalent width limit on a 2-Å-wide line is about 0.6 Å and 0.33 Å at 3500 Å in Q0107−025A and B, respectively, 0.40 Å and 0.17 Å at 3750 Å, and lower than 0.20 Å and 0.10 Å at all wavelengths longward of about 4000 Å.

The spectra were searched for significant lines that could correspond to Mg II $\lambda\lambda2796$, 2802 doublets from any of the systems identified from the *HST* data; none were found. A conservative statement is that no doublets could be identified at greater than the 5 σ confidence level with rest equivalent widths larger than 0.30 Å at redshifts larger than $z = 0.34$. Note that at the highest redshift corresponding to a common Lyα detection, $z = 0.877$, the 5 σ limits on the rest equivalent width of an individual line in a Mg II doublet are 0.08 and 0.05 Å for Q0107−025A and B.

An expanded plot of the region of the spectrum of Q0107−025B containing any Mg II absorption in the $z = 0.3997$ Lyman limit system is shown in Figure 5.5. The 5σ observed
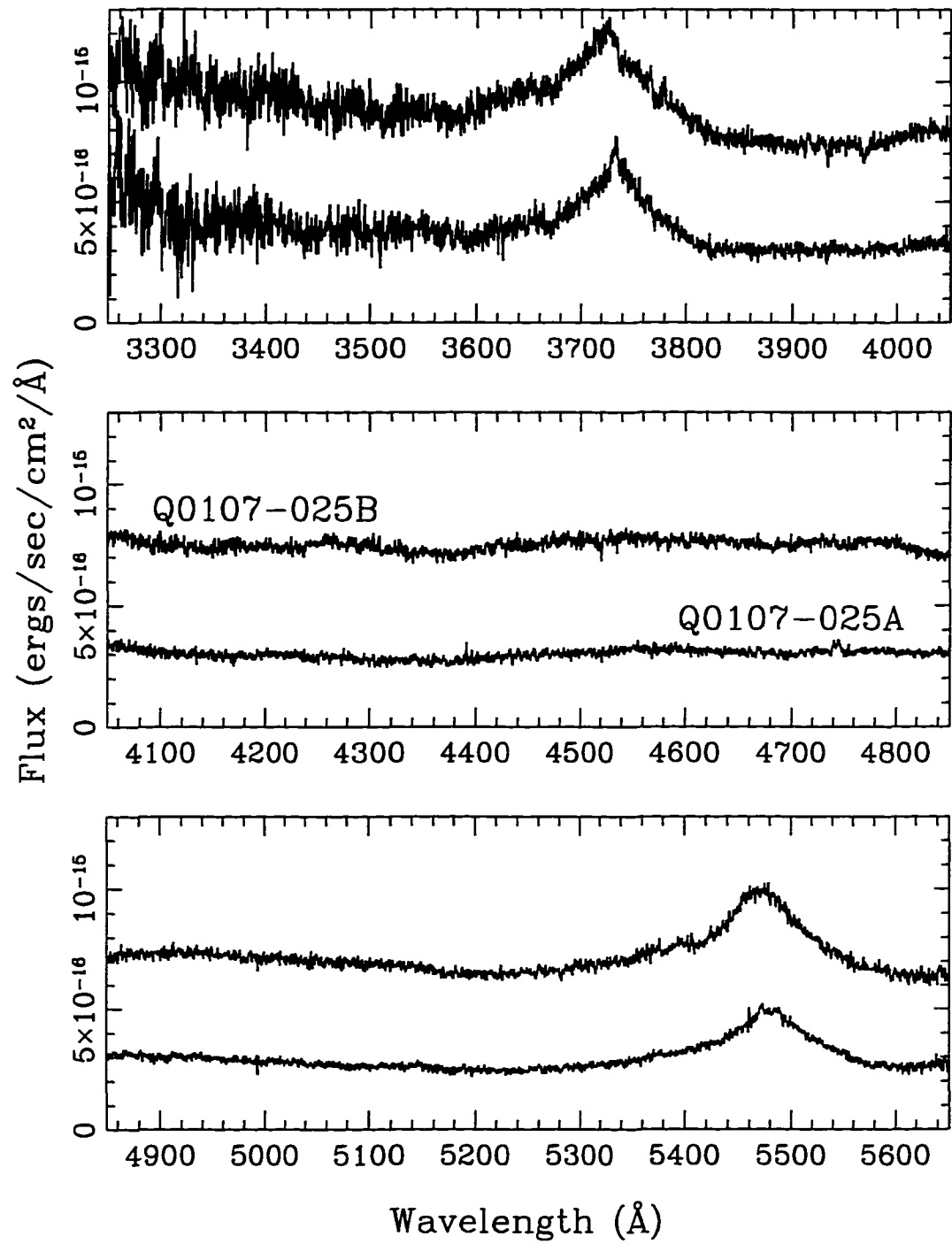
FIGURE 5.4—MMT spectra of Q0107–025A and B as a function of vacuum wavelength. The dotted line in each panel shows the 1σ errors.

equivalent width limit is about 0.15 Å, corresponding to a rest equivalent width limit of 0.11 Å. This spectral region in Q0107−025B contains a saturated Ca II H & K doublet arising in the Galaxy. However the doublet is not seen in A. The galactic latitude of this sightline is ∼ 64°, and if the clouds are at a distance of 300 pc, the linear separation of the sightlines is only 0.1 pc.

5.3 Identification of Absorption Lines

The line identifications posed a significant challenge given the limited spectral range and level of blending in the FOS data. We have followed closely the approach implemented in the Key Project program "*ZSEARCH*" for identifying the lines with the exception that our identifications were carried out manually. We used the set of ultraviolet absorption lines corresponding to the strongest transitions of the most abundant elements (Morton, York & Jenkins 1988; Table 4). We first searched the spectra for Galactic interstellar lines. Then, starting from the red ends of the spectra, we searched for Lyα-Lyβ pairs with relative equivalent widths consistent with their known oscillator strengths. Since the spectra do not extend sufficiently redward to cover the Lyα emission lines of Q0107−025A and B, there is an ambiguity in the identifications of the lines shortward of the Lyβ emision line; some of those lines could be Lyβ's for which corresponding Lyα's would not be observable. For this reason, searches for Lyβ-Lyγ pairs were also made. Finally, the spectra were scanned for doublets of C IV λλ1548, 1550, Si IV λλ1393, 1402, N V λλ1238, 1242, and O VI λλ1031, 1037. If any tentative metal features were identified, we searched for other plausible lines in the system.

In order for an identification to be accepted, we required that the discrepancy between the candidate and observed identifications had to be less than three times the estimated 1σ uncertainty in the measured wavelength. In most cases, the agreement was considerably better. We also checked that the strengths of the absorption lines of the same ion identified within a given system were ordered according to the rules of atomic physics,
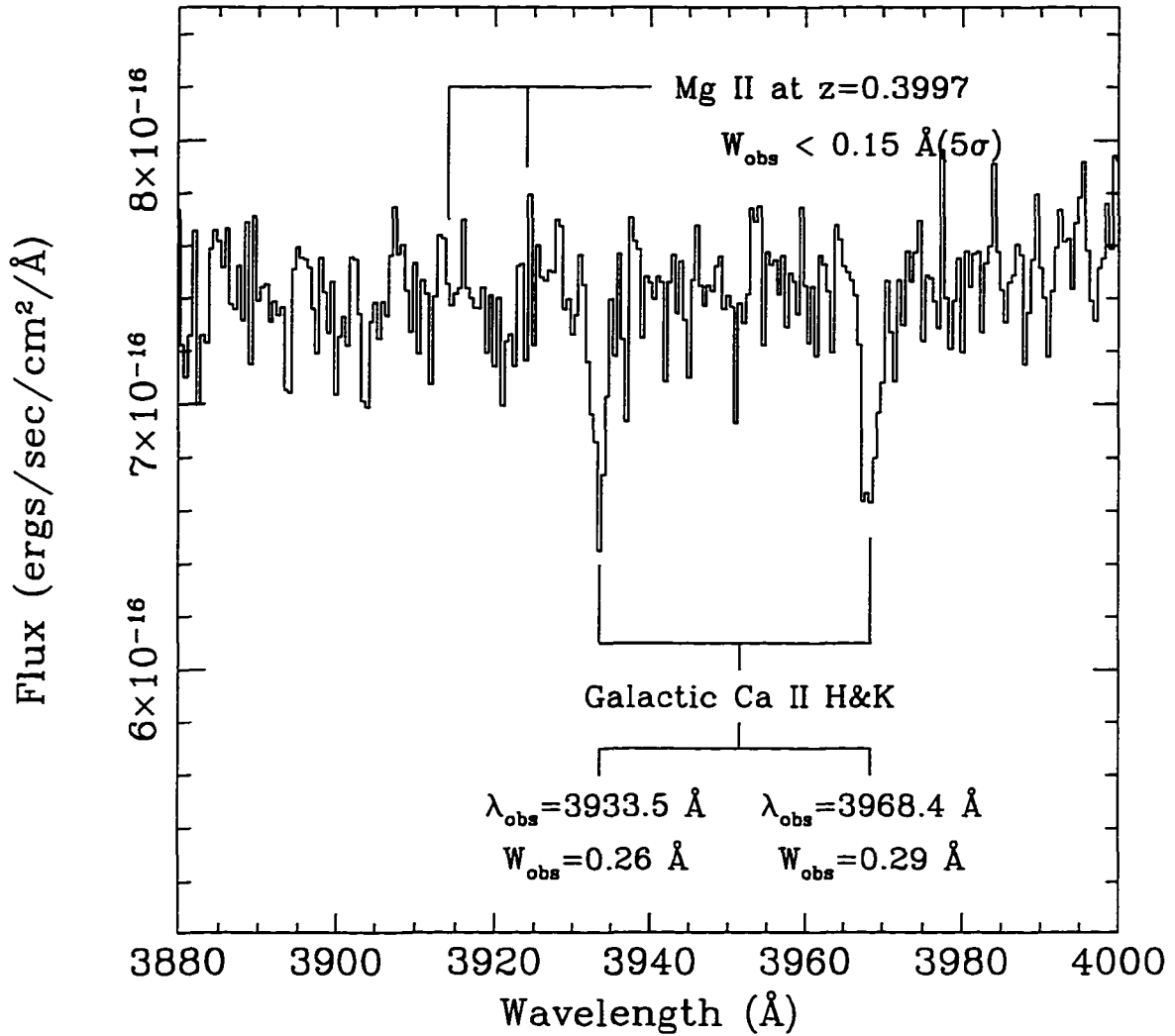
FIGURE 5.5—Expanded plot of the region of the spectrum of Q0107—025B containing any Mg II absorption in the $z = 0.3997$ Lyman limit system. The 5σ observed equivalent width limit is about $0.15\,\text{Å}$, corresponding to a rest equivalent width limit of $0.11\,\text{Å}$. Note that this spectral region contains a saturated Ca II H & K doublet arising in the Galaxy.

taking into account uncertainties in the measured equivalent widths and well as possible blends. Therefore, if a candidate C IV doublet was identified, we checked that C IV λ1548 was stronger than C IV λ1550; and similarly for the doublets of Si IV, N V, and O VI; if candidate Lyman series lines were identified, we verified that their strengths decreased in the order: Lyα, Lyβ, Lyγ, Lyδ, etc; and, finally, we checked that the strengths of candidate C II, N II, Si II, and Fe II lines were consistent with their known oscillator strengths.

Tables 5.3 and 5.4 list the parameters of the absorption lines detected in the GHRS and FOS spectra of A and B, respectively, including the central vacuum wavelengths and their 1σ uncertainties, the equivalent widths and their 1σ uncertainties, the SNR and FWHM of the line, the proposed identification, and finally the absorption redshift. There were a number of cases where a line was multiply identified. In these cases, both identifications have been listed in the tables. We found 50 absorption lines above the 3.5σ equivalent width threshold in the FOS spectrum of Q0107−025A, 34 of which are Lyα absorption systems. In addition we identified three C IV doublet systems, one with associated Lyα absorption. In the other two cases, Lyα was not observable. In the FOS spectrum of Q0107−025B, a total 43 absorption lines were detected and 31 Lyα absorption systems identified, one with associated metal lines.

The lack of spectral coverage out to the Lyα emission lines of the QSOs introduces uncertainty into the identifications of some of the lines shortward of Lyβ emission. In particular, there are two possible Lyβ-Lyγ pairs in the spectrum of Q0107−025A with velocities of 200 and 1500 km s^{-1} longward of the emission redshift. Because a redshift with respect to the Lyα emission of 1500 km s^{-1} is larger than typically observed for Lyα systems and because the strengths of the lines belonging to the Lyβ-Lyγ pairs are inconsistent with their f-values, we chose to identified the lines as Lyα. In the putative system at $z_{abs} = 0.9573$, the Lyγ line is too strong, whereas the Lyγ line $z_{abs} = 0.9657$ is weaker than expected. In both cases there is evidence that the stronger lines are blends or multiple systems. Observations out to the Lyα emission lines are required to confirm

either possibility. Further *HST* observations in the spectral range $2225 - 3275\,\text{Å}$, being obtained in Cycle 5, should resolve many of these ambiguities.

Two lines, one in Q0107−025A and the other in Q0107−025B, located at 1825 Å and identified as Lyγ of systems $z_{\mathrm{abs}} = 0.8772$ in Q0107−025A and $z_{\mathrm{abs}} = 0.8757$ in Q0107−025B have equivalent widths twice that expected from the strengths of the Lyα and Lyβ lines of the same systems. The lines show definite asymmetries and are likely blends. For this reason, we have given the lines a second identification of Lyα at $z_{\mathrm{abs}} = 0.5009$ in Q0107−025A and $z_{\mathrm{abs}} = 0.5004$ in Q0107−025B. We comment on these systems in greater detail in § 5.4.3.

The tentative identifications of two C IV systems in Q0107−025A are worthy of further discussion. The $z_{\mathrm{abs}} \simeq 0.227$ system was identified by a C IV $\lambda\lambda1548$, 1550 doublet and C II $\lambda1334$ line. Lyα also appears to be present in the GHRS data of both Q0107−025A and B at the 3.2σ significance level. Despite the presence of C II $\lambda1334$, lines from other low ionization ions, *e.g.*, Si II, Fe II, Al II, and Al III, are all absent. Similarly the Si IV $\lambda\lambda1393$, 1402 doublet is not observed. We searched for the Mg II doublet in our ground-based data, but did not find it to a limiting equivalent width (3σ) of 0.4 Å. From apparent structure in the C IV doublet lines, this system may break up into several components, but higher SNR is required to confirm this. The velocity difference of the system, based on the Lyα lines, is 52 ± 20 km s^{-1}.

The system at $z_{\mathrm{abs}} \simeq 0.289$ was identified solely by the presence of the C IV doublet. Based upon the fact that Lyα is not accessible by our data and the strengths of the component lines agree with their oscillator strengths within the uncertainties of their measured equivalent widths, this system would be accepted according to the rules of the Key Project. Moreover, the probability of getting an agreement of $\delta z \leq 0.0003$ between two lines by random chance is $[2 \times 0.0003/0.5] \times N_l = 6\%$ where $N_l = 55$ is the number of lines in the spectrum of Q0107−025A. Taking into account the fact that the probability of line ratio being ordered correctly is 0.5, the *a posteriori* probability of getting a C IV

doublet purely by chance is even smaller, $\sim 3\%$.

5.4 Characteristics of the Absorption Systems

In this section, we define two complete samples of Lyα absorption lines which we will use in the next section to set limits on the size of the Lyα lines (§ 5.4.1). We also derive a working definition of systems we consider common and not in common to the spectra of both Q0107−025A and B (§ 5.4.2), and briefly comment on the common systems (§ 5.4.3). Finally, we discuss the metal-line and Lyman limit systems found in the spectra and comment on the limits that can be placed on the extent of those systems (§ 5.4.4).

5.4.1 Samples of Lyman Alpha Absorption Systems

In this section, we construct two subsamples of Lyα absorptions lines from Tables 5.3 and 5.4, each having a different rest equivalent width detection limit. If we define the characteristic radius of an absorber in terms of the impact parameter that gives rise to a line with equivalent width above a given detection limit, then the subsamples can be used to estimate the cloud radii corresponding to different column densities. In constructing these samples, we ensured that none of the Lyα lines were associated with metal-containing systems because it is not clear whether these systems share the same properties as those that do not contain metals. As a practical matter, this did not affect either sample. We did not include the absorption lines detected in the GHRS spectra in these samples since those data are less homogeneous, although we found one new Lyα system in common and a possible second metal-containing system (see §§ 5.4.3, 5.5.1).

First we define a sample of strong lines which we call the "strong-line" sample. This conservative list was published in Paper I and is reproduced in Table 5.6, with slight differences. This list consists of a complete sample of 5σ lines with rest equivalent widths greater than 0.32 Å in the region 1800 − 2300 Å. Figure 5.6a shows the observed 5σ equivalent width thresholds for unresolved lines as a function of wavelength for Q0107−025A

and B. All of the differences between Table 5.6 and the table in Paper I appear in the measured equivalent widths of the lines and reflect changes in the continuum fits, particularly in the emission features. In addition, Table 5.6 includes two probable $Ly\alpha$ absorption systems, not listed in the table of Paper I. The secure and strong lines that make up this list are unlikely to arise by statistical fluctuations; moreover, this list is likely to be essentially complete.

Because of the small size of the "strong-line" sample we also define a larger, but less secure, sample of 3.5σ lines which we list in Table 5.7. We required lines in this sample to have rest equivalent widths greater than $0.24\,\text{Å}$, also satisfied in the wavelength range from $1800 - 2300\,\text{Å}$. Figure 5.6b shows the observed 3.5σ equivalent width thresholds for unresolved lines as a function of wavelength for Q0107−025A and B. As discussed in the previous section, these lines are less likely to be affected by continuum placement, but this "weak-line" sample is more likely to contain lines with are not real and to omit real lines.

The results of our analysis hinge on whether the absorption features are correctly identified as $Ly\alpha$ lines. The number of $Ly\alpha$ absorption features is consistent with other estimates of the line density. The FOS data have comparable SNR to those of the *HST* Quasar Absorption Line Key Project. Using the results of Paper I of the Key Project (Bahcall *et al.* 1993), we expect to see about 9 ± 3 $Ly\alpha$ systems in each QSO spectrum in the range $1800 \le \lambda \le 2310\,\text{Å}$ and with $W_0 > 0.32\,\text{Å}$ (effectively the criteria for a line to be included in the strong sample). We count 7 such systems (plus an additional probable system) toward both Q0107−025A and B, consistent with the Key Project results.

5.4.2 Definition of Coincident and Anticoincident Systems

The close separation of the quasars allows an estimate of the transverse dimensions of the $Ly\alpha$ absorbers, based on the number systems observed to be in common and not in common to both spectra. A line is defined to belong to a common, or coincident, system
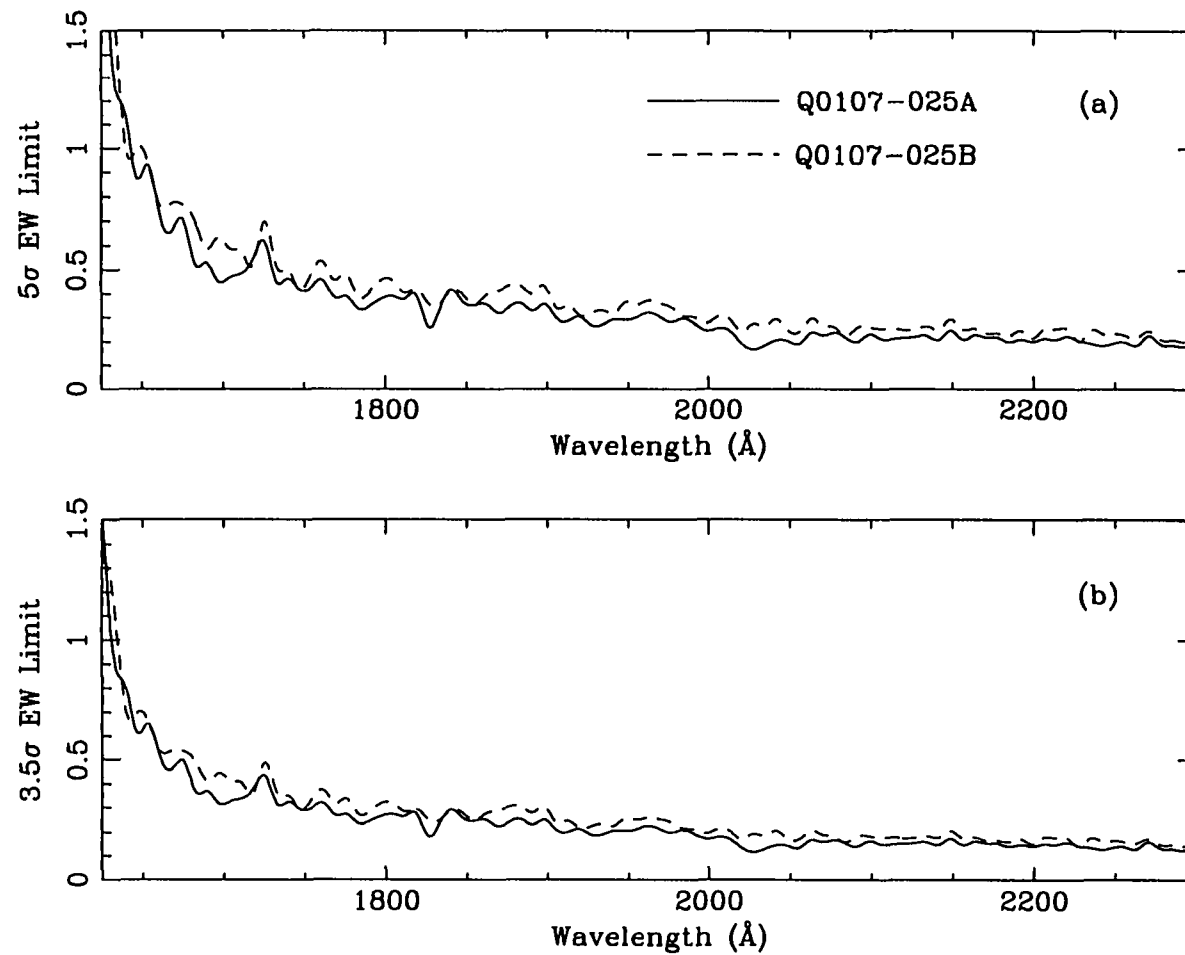
FIGURE 5.6—(a) Equivalent width thresholds (5σ) for an unresolved line as a function of wavelength for the *HST* FOS spectra of Q0107−025A (*solid line*) and Q0107−025B (*dashed line*). (b) Equivalent width thresholds (3.5σ) for an unresolved line as a function of wavelength for the *HST* FOS spectra of Q0107−025A (*solid line*) and Q0107−025B (*dashed line*).

when a corresponding line is present in the other line of sight within some predetermined velocity difference. Conversely, a line is defined to be *not* in common, or anticoincident, if there is no corresponding line within the same velocity difference. In this section, we define the velocity difference that delineates coincident and anticoincident systems.

Ideally, we should be guided by the expected velocity dispersions between physically associated absorbing clouds, but there is little theoretical information or empirical evidence bearing on this question at this redshift. On the one hand, Lanzetta *et al.* (1995) used a velocity window of $|\Delta v| = 1000$ km s^{-1} as their criterion for assigning an absorption system to a galaxy, though in practice, the velocity difference of most galaxy-aborption pairs were found to lie within $|\Delta v| = 250$ km s^{-1}. Similarly, Christiani *et al.* (1995) detected significant clustering of the high redshift Lyα absorbers with $N(\text{H I}) \gtrsim 10^{14}$ cm^{-2} on scales out to 500 km s^{-1}. On the other hand, Dinshaw *et al.* 1994 found that a histogram of nearest-neighbor pairs of all the lines in their sample showed a peak within $|\Delta v| = 150$ km s^{-1} and no additional pairs out to $|\Delta v| > 2000$ km s^{-1}. A similar velocity criterion $|\Delta v| = 200$ km s^{-1} was also used by Bechtold *et al.* 1994 and Fang *et al.* 1996. The smaller velocity window is consistent with results of hydrodynamical simulations, which show the median velocity difference of common systems along adjacent lines of sight separated by several hundred kpcs to be $|\Delta v| < 100$ km s^{-1}(Miralda-Escudé *et al.* 1996).

In attempting to derive an optimal velocity window, we are implicitly assuming that the structures responsible for the Lyα absorption are well-bounded structures with finite, determinable dimensions. Instead, hydrodynamical simulations draw a picture of the Lyα absorbers as complex structures with varied dimensions (Miralda-Escudé *et al.* 1996). Therefore, the velocity window we ultimately adopt must be a compromise between a velocity difference that is large enough to accept common systems that are physically related, but not so large that a significant number of random coincidences are included. We derived the optimal velocity difference in the following manner: For each line in the

spectrum of Q0107—025A, we calculated the velocity difference Δv between it and its nearest neighbor in the spectrum of Q0107—025B, requiring that each line belong to only one pair. We carried out the same analysis for 1000 samples of randomly-placed absorption lines, preserving the number of lines in each line of sight. We also required that the sensitivity range for detecting absorption lines be the same as in the observations.

The distributions of velocity differences Δv for the observed and expected pairs are shown in Figures 5.7 for the strong- and weak-line samples in bins of $\Delta v = 50$ km s^{-1}. The figure shows five pairs within a velocity difference of 150 km s^{-1}, including the probable system at $z_{abs} = 0.501$. The velocity separation of the probable system, $\Delta v = 99 \pm 23$ km s^{-1}, is uncertain because it was derived from blended lines (cf. §§ 5.3, 5.4.3). In the strong-line sample, there are no additional pairs out to velocity differences of ~ 4000 km s^{-1}. However, in the weak-line sample, Figure 5.7 shows a possible coincidence at a velocity difference of 320 km s^{-1}, and another at 1460 km s^{-1}. A velocity window of 1500 km s^{-1} is larger than used in any other study (e.g. Fang et al. 1996; Lanzetta et al. 1995; Le Brun et al. 1996), and would include an unacceptable number of random coincidences. Within a velocity difference of $|\Delta v| < 150$ km s^{-1} corresponding to the peak in the distribution, we expect 0.2 random coincidences in the strong-line sample which contains 8 lines per spectrum. This number grows to 0.4 for the weak-line sample which contains approximately 16 lines per spectrum. For $|\Delta v| < 500$ km s^{-1}, the number of expected pairs is 2.5, consistent with the possible sixth coincidence (with $\Delta v = 320$ km s^{-1}) in the weak-line sample arising randomly. As a practical matter, our experiments with different velocity windows always result in the four original (plus one probable) pairs within a velocity difference of ± 150 km s^{-1}. Therefore, we adopt $\Delta v = 150$ km s^{-1} as the velocity window for a coincidence, consistent with the value used by Dinshaw et al. 1994 and Fang et al. (1996). Under this criterion, both samples have an identical number of coincidences; however, the number of anticoincidences is doubled between the strong- and weak-line samples.
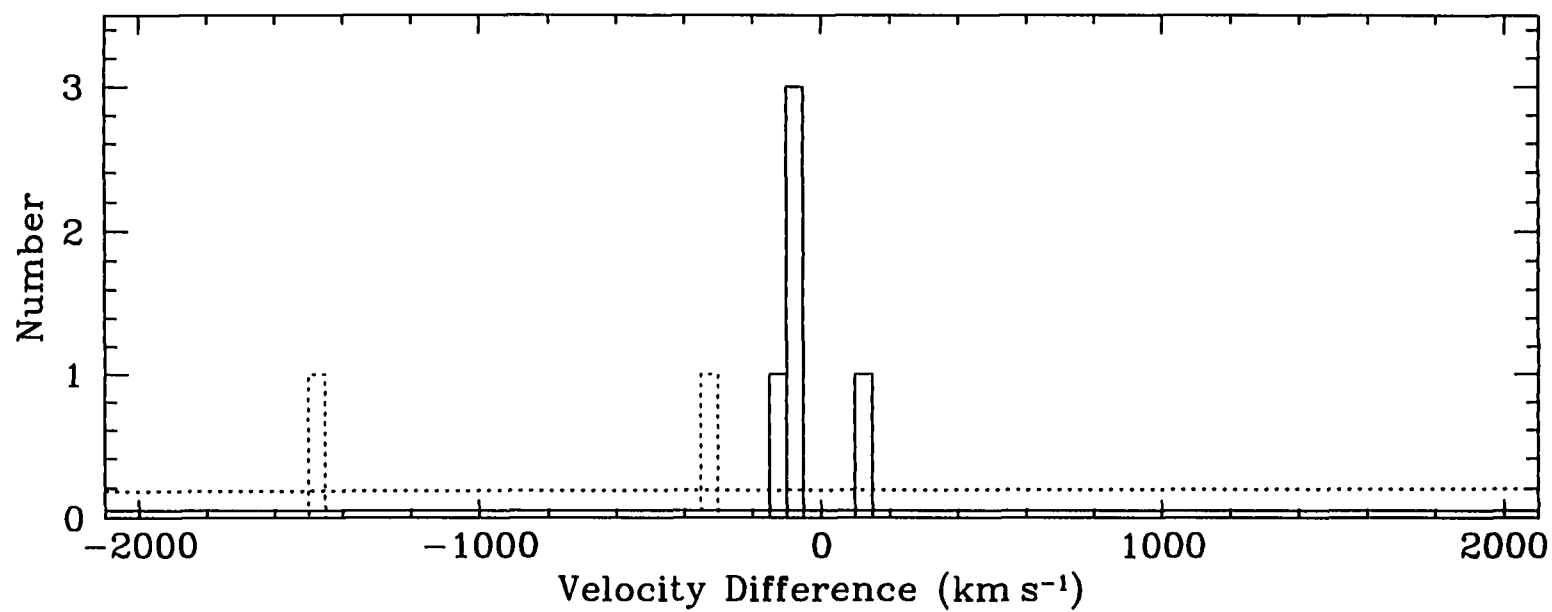
FIGURE 5.7—Histogram of velocity differences for the strong-line (*solid histogram*) and weak-line (*solid and dashed histogram*) samples. The number of expected velocity pairs for each sample is shown as a straight line.

The measured velocity differences among the coincident lines range from -150 km s^{-1} to 111 km s^{-1} (Table 5.6 and 5.7). The mean velocity difference is 26 km s^{-1}, smaller than the expected error due to mispointing of *HST*. The rms velocity difference about the mean is 104 km s^{-1}. (Including the one probable coincidence whose velocity difference is based on blended lines, the rms velocity difference is 97 km s^{-1}.) Assuming the uncertainties in the line fitting and wavelength calibration are random, the expected uncertainties in the radial velocity difference of a pair of lines is conservatively estimated to be ~ 17 km s^{-1}. We therefore conclude that we are seeing statistically significant velocity differences over scales of several hundred kpc.

5.4.3 Notes on Common Lyman-Alpha Systems

In this section, we comment on the common Lyα absorption systems found in the strong- and weak-line samples. We also include the one common system that is present in the GHRS data and that is not contaminated by metals.

$z_{\rm abs} \simeq 0.116$. This common system is observed in the GHRS data. No lines associated with this system other than Lyα are detected. The velocity difference is 86 ± 20 km s^{-1}.

$z_{\rm abs} = 0.501$. This is a probable system, based solely on the presence of Lyα, which is severely blended with the Lyγ lines of $z_{\rm abs} = 0.877$ in both spectra. We believe this is a common Lyα system because the strengths of the Lyγ lines are considerably stronger than the other lines identified with the $z_{\rm abs} = 0.877$ system, and the profiles show clear asymmetries. We have attempted to deblend the lines although we did not list the deblended components in Tables 5.3 and 5.4, because the line selection software did not identify the components. Our best fits to the line profiles give Lyα components at 1824.43 ± 0.10 Å in A and 1823.94 ± 0.10 Å in B. The wavelengths of components at 1825.94 ± 0.05 Å (A) and 1826.01 ± 0.20 Å (B) correspond well to Lyγ lines belonging to the systems $z_{\rm abs} = 0.8769$

in A and $z_{abs} = 0.8772$ in B, respectively.

$z_{abs} \simeq 0.536$. This is a strong system for which only Lyα is observed. The higher order Lyman series lines would lie shortward of the wavelength range covered by the FOS spectra and none are seen in the GHRS data. The velocity difference is 90 ± 16 km s^{-1} for the system.

$z_{abs} \simeq 0.719$. This system contains Lyα, Lyβ and Lyγ. The large equivalent width of Lyβ in the spectrum of B suggests that it is probably blended. The Lyγ's are both blended with Galactic Al II λ1670 absorption. Given this blending, the system's velocity difference of 111 ± 6 km s^{-1} is based only on the Lyα lines

$z_{abs} \simeq 0.788$. This system includes Lyα, Lyβ and Lyγ. Lyδ is also seen in B but appears to blended with Lyη of the system at $z_{abs} = 0.8772$. Si II λ1193 and 1260 are possibly present in A, but such an identification is doubtful given the lack of Mg II absorption in the ground-based data. Neither Si II λ1190 nor 1206 is observed, consistent with the oscillator strengths of Si II lines (Morton et $al.$ 1988). The weighted average velocity difference of Lyα and Lyβ is -145 ± 10 km s^{-1}.

$z_{abs} \simeq 0.877$. In addition to Lyα, the higher Lyman series lines Lyβ through Lyθ are present in one or both quasars. The equivalent widths of some of the lines are inconsistent with unblended Lyman series; Lyγ, Lyζ and Lyη are certainly contaminated. The unblended lines give a weighted average velocity difference of 51 ± 5 km s^{-1}.

5.4.4 Properties of the Metal-line and Lyman Limit Systems

There are some additional features present (all at levels above 5σ) which are of special interest in conjunction with the GHRS spectra. We observe a metal-containing system at $z_{abs} \simeq 0.400$ with a weak Lyman limit detected in Q0107−025B but not in A; in addition to the Lyα and the C IV doublet, we identified Si IV λ1393 (Si IV λ1402 appears to be present at the 2.7σ significance level) along the sightline to B. C II λ1334 is also possibly

present in the spectrum of B but blended with Lyα at $z_{abs} = 0.5360$. Lyα and C IV $\lambda1548$ are seen in the spectrum of Q0107−025A but C IV $\lambda1550$ is blended with a Lyα at a different redshift. The system's velocity difference of 65 ± 25 km s^{-1} is based on the Lyα and C IV $\lambda1548$ lines.

The fact that we see common Lyα (and possibly C IV) in the lines of sight to Q0107 − 025A and B, but the associated LLS is present only in B implies an upper limit on the size of the LLS of $R = 125\,h^{-1}$ kpc. We also have information about the tranverse sizes of structures with very different column densities. From this system, it appears that the extent of the absorbing gas producing the Lyα and C IV systems is larger than that of the LLS, which is consistent with their relative cross sections derived from the statistics of the absorbers (cf. Steidel 1993). This furthermore implies that the lower column density material extends out to greater distances than the higher column density material. The equivalent widths of the Si IV and C II lines are too small to make any conclusions on the linear extent of the absorbers producing them.

Using the prime focus spectrograph COSMIC on the Hale 5-m telescope and the multiobject spectrograph on the CFHT 3.6-m telescope, we have begun a survey of galaxies near the lines of sight to Q0107−025A and B in order to identify galaxies in the same volume of space as the Lyα absorbers seen in *HST* GHRS data. The objects have been selected using the galaxy classification software package FOCAS on an undispersed V image taken with the same spectrograph, and were chosen to be brighter than 21.5 V magnitudes and to lie within a region of 8 × 10 arcminutes centered approximately on Q0107−025A, B. So far, we have obtained 31 redshifts. Although the redshift sample is still sparse, we observe several galaxies within 1 Mpc of absorption systems in the GHRS data. We have so far failed to identify a galaxy which can plausibly be associated with the $z = 0.400$ Lyman limit system in B noted above. Either this galaxy is of rather low luminosity or it is quite compact and nearly aligned with the QSO Q0107−025B, and a more careful point spread function subtraction will be required for it's detection. This

work will be published in a forthcoming paper.

5.5 Likelihood Analysis

In this section, we determine the sizes of the Lyα absorbers for a number of simple models using two maximum likelihood methods. In § 5.5.1, we consider models that are certainly too naive, but are conceptually simple: a single population of absorbers with spherical and disk geometries that are uniform in size and have constant column density. We also correct an error in Paper I. In § 5.5.2, we again consider a single population of spherical, disk-like and pseudo-filamentary absorbers, but this time assuming the absorbers have power-law column density profiles.

5.5.1 Likelihood Estimates for Models with Constant Column Density

As in Paper I, we assume the absorbers are coherent "clouds", since, with our current data set, we cannot really distinguish between coherent versus correlated structures. Aside, from this basic assumption, the presence of common systems in the lines of sight to Q0107−025A, B immediately implies a lower limit to the sizes of the Lyα absorbers, corresponding to pathlength separation at the redshifts of the common systems. For the lowest redshift pair ($z = 0.536$), the lower limit on the *radius* of the absorbers corresponds to $140\,h^{-1}$ kpc and for the highest redshift pair ($z = 0.877$), it is $160\,h^{-1}$ kpc. The presence of a comparable number of features that are in common and not in common to both spectra suggests that we may be fortuitously sampling spatial scales that are of order of the characteristic size of the absorbers. Assuming absorbers of uniform size, we have used maximum likelihood statistics to calculate the most probable radius, R, of the Lyα forest clouds for both spherical and disk geometries.

The probability that a spherical cloud is intersected by both lines of sight, given that it is intersected by one line of sight is given by McGill (1990) as

$$\phi_s(X) = \frac{2}{\pi}[\arccos[X(z)] - X(z)\sqrt{1 - X(z)^2}] \tag{5.1}$$

where $X(z) \equiv S(z)/2R$ and $S(z)$ is the line of sight separation at the redshift of the absorber. Note that eq. (5.1) only holds for $0 \leq X \leq 1$ and is zero everywhere else. For disks, the probability is given by McGill (1990) as

$$\phi_d(X) = \int_{-\pi/2}^{\pi/2} \frac{\cos\theta}{\pi} \left[\arccos\left[\frac{X(z)}{\cos\theta}\right] - \frac{X(z)}{\cos\theta}\sqrt{1 - \frac{X(z)^2}{\cos^2\theta}} \right] d\theta \qquad (5.2)$$

for $X < \cos\theta$ and zero everywhere else.

At this point, we would like to correct an error made in Paper I, and called to our attention by M. Fardal. In that paper, we used the probability ϕ_s to calculate the most probable radius. The relevant question is: "If a line appears in a *given* spectrum, what is the probability that a corresponding line appears in the other spectrum?" Therefore, only the anticoincidences from *one* line of sight should have been used, and *not* both lines of sight as was done in Paper I. Clearly a disadvantage of using this probability is that it throws out valuable information. In order to incorporate all of the available information, we must define a probability that addresses the question: "If a line appears in *either* spectrum, what is the probability that a corresponding line appears in the other spectrum?" By simple geometrical arguments, this is easily shown to be given by

$$\psi_{s,d} = \frac{\phi_{s,d}}{2 - \phi_{s,d}} \qquad (5.3)$$

This error resulted in our estimating the radius of the clouds to be 40% smaller than that had we used the correct expression.[2]

The probability of getting the observed number of coincidences and anticoincidences is then given by the likelihood function (McGill 1990)

$$\mathcal{L}(R) = \prod_i \psi[X(z_i)] \prod_j \{1 - \psi[X(z_j)]\} \qquad (5.4)$$

---

[2]This lead to a similar error in the Monte Carlo simulations performed in Dinshaw *et al.* (1994). There the cloud sizes were underestimated by 70%. The most probable radius for the Lyα absorbers in the lines of sight toward Q1343+2640A,B for the case of 8 coincidences and 4 anticoincidences should be 125 h^{-1} kpc with 95% confidence lower and upper bounds of $80 < R < 610\,h^{-1}$ kpc.

where z_i is the redshift of the ith line "coincidence", and z_j is the redshift of the jth "anticoincidence".

The results of the likelihood analysis for both samples and geometries are summarized in Figures 5.8 and 5.9, and Table 5.8. In the strong-line sample, we found four coincidences and one probable coincidence. In addition, we observed three lines in both Q0107–025A and B with no corresponding match in the other spectrum. Figure 5.8 shows the likelihood distribution $\mathcal{L}(R)$ and its cumulative distribution for spheres and randomly inclined disks. The most probable radius is $445\,h^{-1}$ kpc for spherical absorbers. From the cumulative distribution, we derive 95% lower and upper confidence limits of $340 < R < 1360\,h^{-1}$ kpc. Taking into account the one probable coincidence, we calculate a characteristic radius of $505\,h^{-1}$ kpc with 95% confidence limits of $360 < R < 1535\,h^{-1}$ kpc (Figure 5.8). For randomly inclined disks, the cross section for interception is smaller, therefore it is not surprising that the characteristic radius determined for that model is correspondingly larger: $R = 625\,h^{-1}$ kpc with 95% confidence limits of $420 < R < 2025\,h^{-1}$ kpc for four coincidences; including the probable coincidence, the most likely radius becomes $R = 715\,h^{-1}$ kpc with 95% confidence limits of $470 < R < 2295\,h^{-1}$ kpc.

Figure 5.9 shows the maximum likelihood results for the weak-line sample. Dropping the rest equivalent width threshold to 0.24 Å, we found no additional coincidences despite the fact that the number of lines detected in both lines of sight doubled. In total, we found four (and one probable) coincidences and 20 anticoincidences. For the first case (four coincidences), the most probable radius is $320\,h^{-1}$ kpc assuming spherical absorbers. The 95% lower and upper bounds on the inferred radius are $250 < R < 520\,h^{-1}$ kpc. Including the one possible coincidence, the radius measured is $350\,h^{-1}$ kpc with corresponding 95% confidence limits of $270 < R < 560\,h^{-1}$ kpc. For randomly inclined disks, the radii become: $R = 330\,h^{-1}$ kpc with 95% confidence limits of $255 < R < 550\,h^{-1}$ kpc for four coincidences, and $R = 355\,h^{-1}$ kpc with confidence limits of $275 < R < 595\,h^{-1}$ kpc including the probable coincidence. We have assumed $q_0 = 0.5$; for $q_0 = 0$, the radii
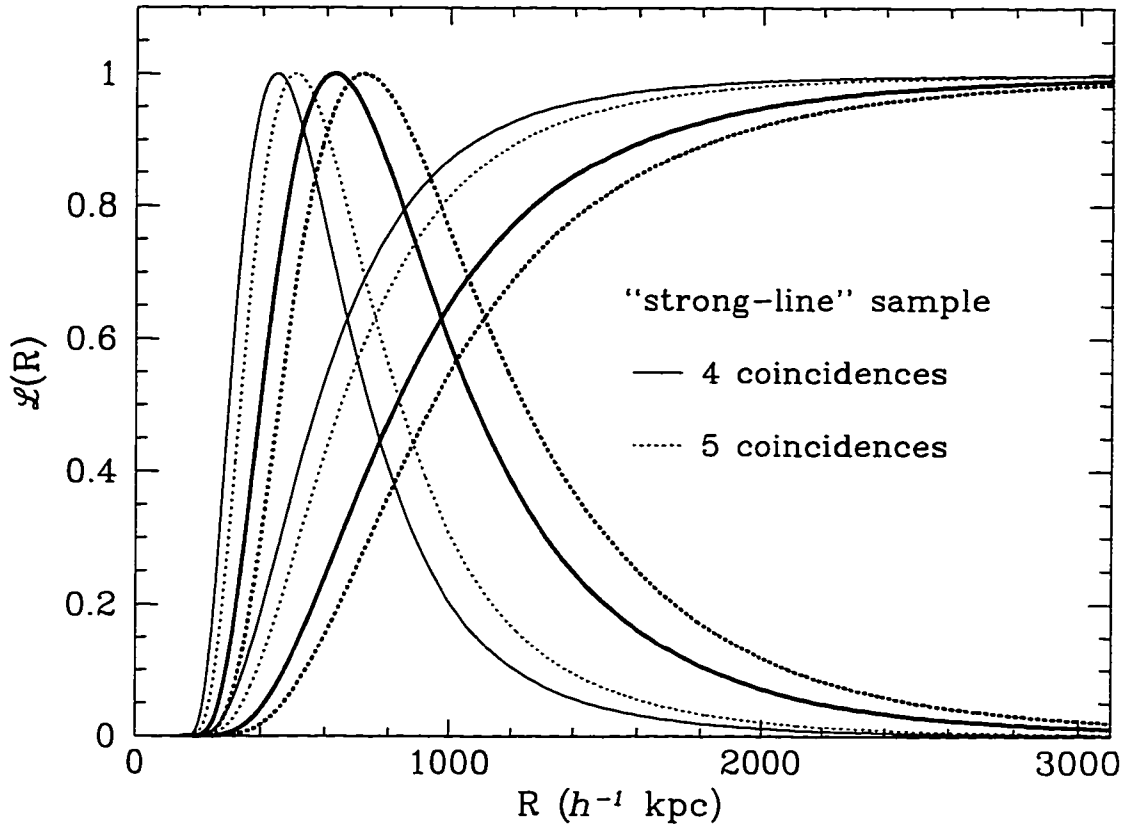
FIGURE 5.8—Likelihood distribution $\mathcal{L}(R)$ for spherical absorbers (*thin curves*) and randomly-inclined disks (*thick curves*), normalized to unity at its peak, as a function of cloud radius for the strong-line sample. Two cases are considered: (1) Four coincident and six anticoincident lines (*solid curves*); The cumulative probability distribution (*monotonically increasing solid lines*) is also plotted from which lower and upper limits on the radius of the absorbers can be estimated. (2) Five coincidences and six anticoincidences (*dotted curves*).

quoted are 20% bigger.

The size estimates between the strong- and weak-line samples seem to suggest that the lower column density absorbers are *smaller* in extent than the high column density systems, contrary to what was found for the $z = 0.400$ LLS (§ 5.4.4). Given that this result is not very significant ($< 3\sigma$) and the fact that the weak-line sample is not complete (though there is no obvious reason that incompleteness would bias toward more anticoincidences), we hesitate to draw any conclusions at this time. Instead, we await further FOS observations of the pair in Cycle 5, which will raise the significance of many of the weaker lines and should help to resolve this issue.

5.5.2 Likelihood Estimates for Models with Column Density Distributions

In this section, we present a new statistical method adapted from Maoz & Rix (1995) for comparing the observations with specific models which utilizes the information given in the equivalent widths of the lines in order to test basic properties of the Lyα absorbers. This allows not only an estimate of the radius of the absorbers, but also an evaluation of the likelihood of different geometric models for the clouds. In this way, our method improves upon the diagnostic technique presented by Charlton, Churchill & Linder (1995) because it provides a statistical basis for the comparison in addition to a measure of the best radius for the clouds for a given model. Some of the power of the technique arises from the fact that few observational points are required. However there are other limitations which we discuss below that do not allow a definitive analysis at this time.

The observed correlation in the rest frame equivalent widths of the Lyα absorption systems is shown in Figure 5.10 for both the coincidences and anticoincidences. The equivalent widths of the common systems show clear deviations from unit slope, indicating that the lines are not highly correlated. They also exhibit a general trend for the scatter in $|W_A - W_B|$ to be greater for large $\max(W_A, W_B)$ that is a generic result of a smooth column density profile for the absorbers, and not an irregular column density
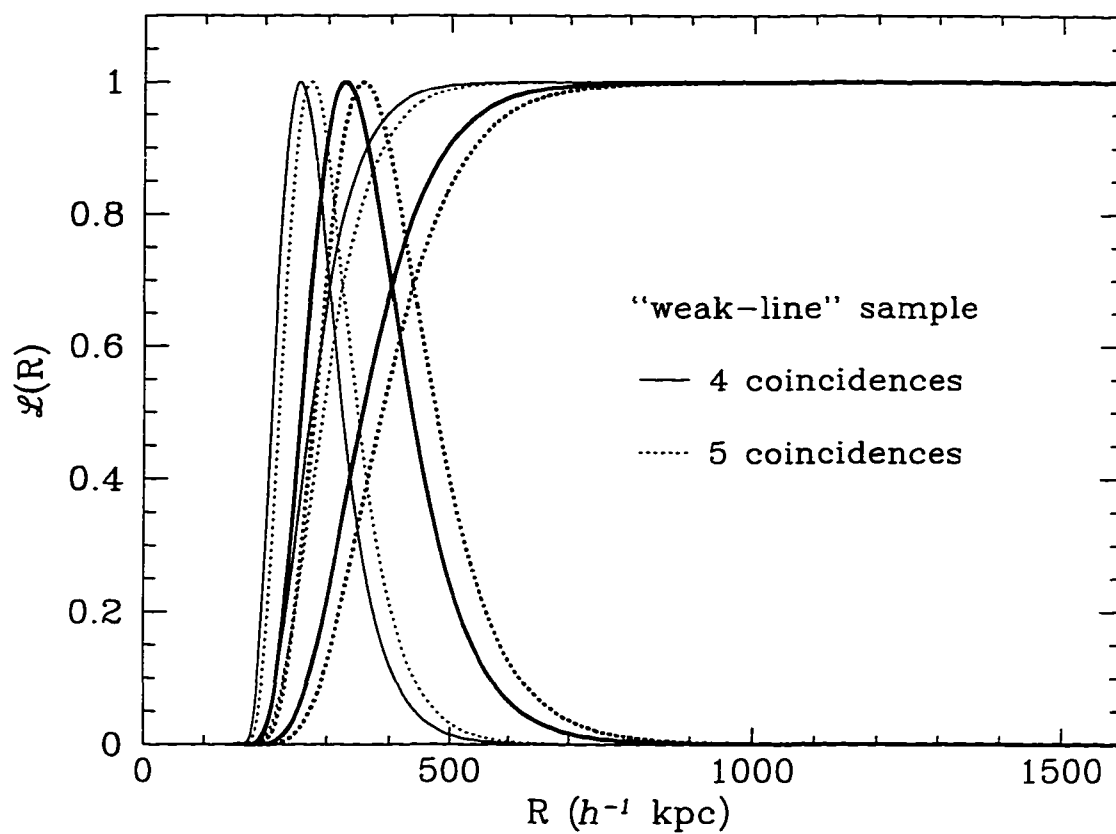
FIGURE 5.9—As Figure 5.8, for sample the weak-line sample. Again, two cases are considered: (1) Four coincident and 20 anticoincident lines (*solid curves*). (2) Five coincidences and 20 anticoincidences (*dotted curves*).

distribution. Therefore, on scales of a few hundred kpcs, there appears to be a column density gradient within the Lyα absorbers. It is difficult to know how much of the trend for the high equivalent width pairs to have large absolute equivalent width differences is due to blending (an issue we revisit below). Another feature of this plot that is worth pointing out is that the lines detected in Q0107—025A appear to be stronger than those found in B. This could arise from inaccurate placement of the continuum due to the fact that the noise level in Q0107—025B is higher making it more difficult to delineate the continuum level.

For simplicity and so that we can easily compare our results with those of Charlton *et al.* (1995), we assumed absorber models with a power-law column density profile

$$N(r) = N_{\text{lim}} \left(\frac{r}{R_0}\right)^{-\gamma} \tag{5.5}$$

where N_{lim} is the limiting column density of the sample and R_0 is the radius of the absorber. We considered the cases $\gamma = 3, 4, 5, 6$, which correspond to column density distributions $f(N_{\text{H I}})dN_{\text{H I}} \propto N_{\text{H I}}^{-\beta}dN_{\text{H I}}$ with $\beta = 2, 1.67, 1.5, 1.33$, which bracket the power-law index of the observed column density distribution ($\beta = 1.7$; Petitjean *et al.* 1993; Rauch *et al.* 1993). We considered three geometries for the absorbers: spheres, randomly-inclined disks and pseudo-filamentary structures (approximated as disks with fixed inclination [$\cos i = 0.2$]). Inherent in this definition is that for spherical clouds and filaments, the absorbers have constant radius, defined to be the impact parameter corresponding to N_{lim}. For inclined disks, the column density increases across the absorber as $\sec\theta$ (while the cross-sectional area of the absorber decreases as $\cos\theta$) and we must make the transformation $N_{\text{lim}} \to N_{\text{lim}}/\cos\theta$ in eq. (5.5). Since the impact parameter at which N_{lim} is observed is greater depending on the inclination of the disk, the cross sections of the absorbers vary as the inclination. Obviously, for $r \to 0$, $N_{\text{H I}} \to \infty$, so a line of sight was never allowed to intersect the disk at an impact parameter smaller than that corresponding to $N_{\text{H I}} > 10^{20}$ cm^{-2} which exceed that largest observed column density.

For each model, we tested the set of parameters (*e.g.*, R_0, γ, i) which predicts a
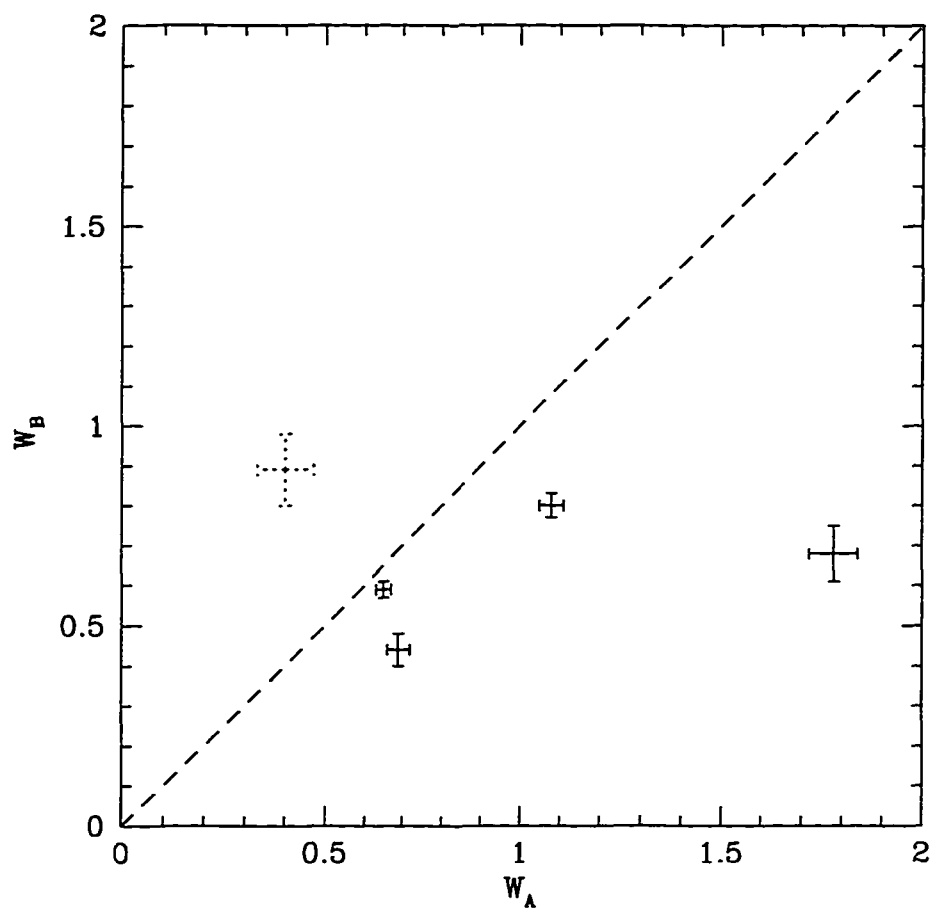
FIGURE 5.10—Correlation between the rest equivalent widths of the common lines in Q0107−025A and B. The dotted error bars represent the probable coincident system for which the equivalent widths are highly uncertain. The dashed line has unit slope.

particular distribution of pairs of column density along the two lines of sight. We can then compare the observations with the simulated distribution to determine the best model or reject models. We evaluate the relative likelihood of these models using a likelihood function defined as

$$\mathcal{L} \equiv \sum_i \ln[p_i(W_1, W_2)] + \sum_j \ln[p_j(W_1, W_2 < W_{\lim})] \tag{5.6}$$

where $p_i(W_1, W_2)$ is the probability that a particular model gives a coincidence with equivalent widths of the lines of W_1 and W_2, and similarly $p_j(W_1, W_2 < W_{\lim})$ is the probability that the model gives an anticoincidence with equivalent width of W_1 in one line of sight and no detected line in the other, i.e., $W_2 < W_{\lim}$. Due to symmetries in the column density distributions, we arrange the observed and simulated equivalent widths such that $W_1 \equiv \max(W_A, W_B)$ and $W_2 \equiv \min(W_A, W_B)$. The most likely set of parameters is determined by maximizing the likelihood function, where the uncertainties in the parameters are determined by the relation $2(\mathcal{L}_{\max} - \mathcal{L})$ (Rix et al. 1996). The likelihood function gives the relative likelihood of the models, but does not provide the absolute likelihood for any model.

We estimated the probabilities of the observed coincidences and anticoincidences from the column density distributions along two lines of sight for each of the geometric models considered in the following way: The column density distributions were simulated by means of the Monte Carlo techniques outlined by Smette et al. (1992). For the spherical model, we randomly selected two points, r_A and r_B, separated by $S(z)$ corresponding to separation between the LOS, on a circular disk of radius $R_0 + S(z)$ where R_0 is the radius of the absorber. When either r_A or r_B happened to lie within the radius R_0 (such that a coincidence or anticoincidence was always obtained), then the column density at r_A or r_B were determined from eq. (5.5). The simulations for randomly-inclined disks and filaments were similarly carried out, but this time the geometry was that of ellipses on the sky with semi-major and minor axes of $R_0 + S(z)$ and $R_0/\cos\theta + S(z)$, respectively. For simplicity,

we fixed the line-of-sight separation of the QSO to be $S(z = 0.7) \simeq 300\,h^{-1}$ kpc, despite the fact that our observations cover the redshift range $0.5 < z < 0.9$.

5.5.2.1 The Column Density Distributions

Figure 5.11 shows the loci of the column densities along the two lines of sight on plots of $\log N_A$ versus $\log N_B$ for spherical (top panels), pseudo-filamentary (middle panels), and disk-like (bottom panels) absorbers. To illustrate the effect of varying R_0 and γ, the distributions have been derived for $R_0 = 300$, 1200 and $3000\,h^{-1}$ kpc corresponding to 1, 4 and 10 times the line-of-sight separation of the QSO pair, and power-law indices of $\gamma = 4$ and 5. Immediately, we can see striking differences between panels.

In Figure 5.11, the dashed lines corresponds to the rest equivalent width threshold of the strong-line sample. The points lying above and to the right of the dashed lines represent coincidences, and those falling below the horizontal dashed line or to the left of the vertical dashed line are anticoincidences. Points in the unpopulated square box near the origin are disallowed by the condition that at least one of the lines of sight have column density above N_{lim}. In order to adequately populate regions of low probability which tended to occur at high column densities, the first impact parameter r_A was selected randomly from an exponential distribution [$r_A = \exp(x)$ where x was a random number from -10 to 0] and the points in the distribution weighted by r_A^2 to account for the nonuniform selection. We checked that this was correct by making sure we recovered the column density distribution with the value of β appropriate for the power-law exponent used. The probability of a coincidence $p_i(W_1, W_2)$ was determined by counting the number of systems in a square region, 0.08 Å on a side, corresponding to the typical uncertainty in the observed equivalent widths. The probability of an anticoincidence $p_j(W_1, W_2 < W_{\text{lim}})$ was obtained by counting the total number of systems in vertical swaths of the same width. The probabilities were normalized by the sum of all the weights. We found that highly inclined disks sometimes gave very large weights that dominated the sum, and produced
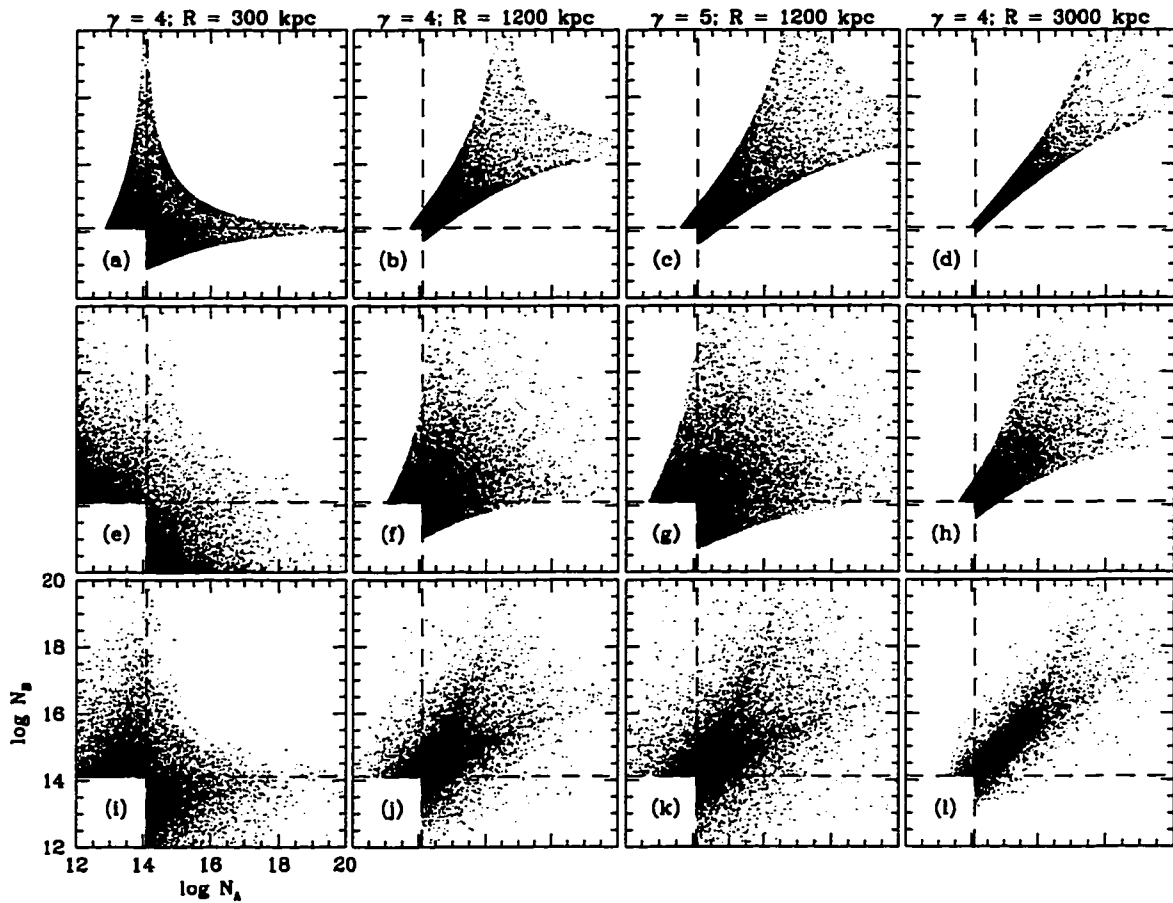
FIGURE 5.11—Column density distributions for spherical halo model (*top row of panels*), filamentary structures (*middle row of panels*) and randomly-inclined disks (*bottom row of panels*). The dashed lines represent the column density threshold ($N_{lim} = 1.26 \times 10^{14}$ cm^{-2} for $b = 35$ km s^{-1}) for the strong-line sample. The points lying above and to the right of the dashed lines represent coincidences, and those falling below the horizontal dashed line or to the left of the vertical dashed line are anticoincidences. Points in the unpopulated square box near the origin are disallowed by the condition that at least one of the lines of sight have column density above N_{lim}.

statistically meaningless fluctuations in the probabilities even for very large numbers of realizations. To alleviate this problem, we restricted the inclinations of the disks to lie in the range $0.1 < \cos i < 1$.

Figure 5.11a – d shows the simulated distribution for spherical absorbers. The first point to note about this figure is the presence of sharp boundaries delineating regions of significant and zero probability. Also for large absorbers, there never occurs a case where there is an anticoincidence where the detected line has a large column density. However, for spheres with radius comparable to the line-of-sight separation, it is possible to get anticoincidences with a high column density in the observed line, but not high column density coincidences. Moreover, the probability density for points below the limiting column density is higher meaning the chance of observing anticoincidences is higher for small clouds.

Figure 5.11e – h shows the expected column density distribution for pseudo-filamentary structures with semi-major axis five times that of the semi-minor axis. The probability density for anticoincidences is very high, as expected, for small filaments. Again, there are sharp boundaries to the probability density at the lower edges as well as near the correlation line for the filament model. The ridges (which are more apparent in Figure 5.12) representing higher probabilities correspond approximately to the expected distribution for a sphere with radius equal to the semi-minor axis of the projected ellipse. Unlike the spherical model, the probability density is spread over a larger region for a given radius because of the inclination effect which allows for greater variations in the column densities over smaller areas. Therefore it is possible to obtain circumstances where both anticoincidences and coincidences with large column density lines can be observed.

Figure 5.11i – l shows the expected column for randomly inclined disks. These produce less well-defined boundaries because the column density across the structure and the radius of the absorber depends on the inclination. The high density ridges straddling the correlation line reflect the probability density for disks inclined at the median inclination.

This model clearly gives the most diverse structures ranging from spheres to filament-like structures.

There are a couple of gross features that appear in Figure 5.11 regardless of the geometry of the absorbers: 1) For radii progressively larger than the line-of-sight separation, the column densities become more highly correlated. The correlation is generally higher for low column densities where the lines of sight sample the outer regions of the absorbers and where the drop off in the column density across the absorber is not as steep as in the center of the cloud. 2) The effect of increasing γ is to increase the cross-section for detecting high column density systems. This produces is a greater spread in the distribution for larger γ since a larger range of column densities is sampled for steeper profiles.

5.5.2.2 Likelihood Limits

Figure 5.12 shows the equivalent width distribution for spherical (*top panels*), pseudo-filamentary (*middle panels*), and disk-like (*bottom panels*) absorbers. We plotted the distribution in terms of equivalent width so that we can compare the simulated distribution with the observations. Superimposed on the simulated distributions are the equivalent widths of the observed coincidences and anticoincidences for the strong-line sample. The odd appearance of the distributions is caused by the transition at $W_1 \simeq 1$ from the flat part of the COG to the square root part. Furthermore, in these plots, r_A was selected according to a exponential distribution so that the region $W_1 \gtrsim 1$ would be adequately populated. For this reason, the regions of high density of points do not represent the true probability density.

The present data were obtained at a spectral resolution that does not allow a detailed curve of growth (COG) analysis. Instead, we used an approximation having an accuracy of better than 10% to evaluate the COG in the range of optical depths from $0.1 \leq \tau \leq 40$ (Chernomodik & Ozernoy 1993)

$$W = \frac{\sqrt{2}b\lambda}{c} \left[\ln \left(1 + \frac{\pi}{2}\tau^2 \right) \right]^{1/2} \tag{5.7}$$

167
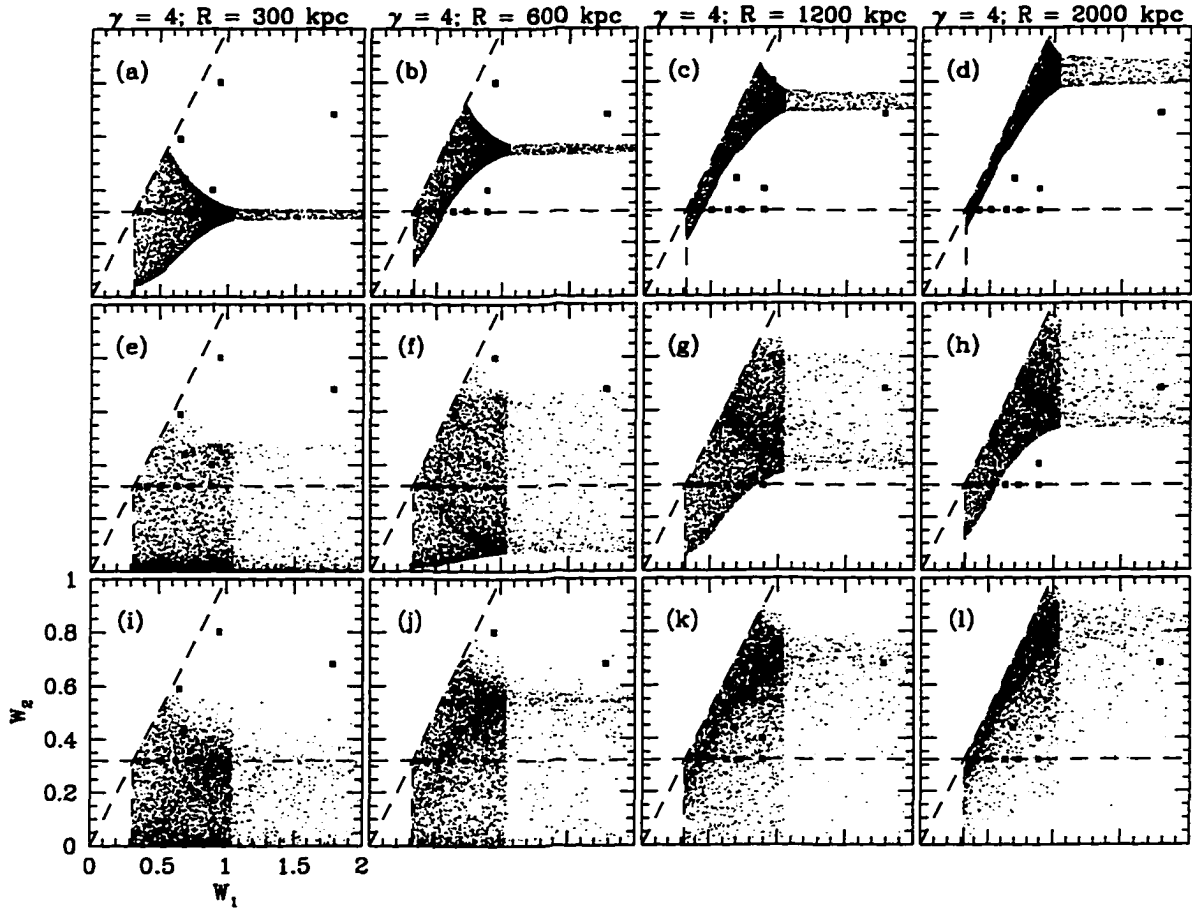
FIGURE 5.12—Equivalent width distributions for spherical halo model (*top row of panels*), filamentary structures (*middle row of panels*) and randomly-inclined disks (*bottom row of panels*). The observed and simulated equivalent widths are arranged such that $W_1 \equiv \max(W_A, W_B)$ and $W_2 \equiv \min(W_A, W_B)$. The horizontal dashed lines represent the rest equivalent width threshold ($W_0 > 0.32$ Å) of the strong-line sample. The points lying above the dashed lines represent coincidences, and those falling below the horizontal dashed line are anticoincidences. Superimposed on the simulated distributions and indicated by the solid squares are the equivalent widths of the observed coincidences and anticoincidences for the strong-line sample.

where λ is the wavelength of the line, c is the speed of light and $\tau = 1.497 \times 10^{-2} \lambda f N / b$ is the optical depth and $f = 0.416$ is the the oscillator strength for the Lyα transition. The approximation provides a smooth transition between the linear and flat parts of the COG. For $\tau > 40$, we used the usual equations given in Spitzer (1978) to calculate equivalent widths. For simplicity, we also assume a single Doppler width of $b = 35$ km s^{-1}, which corresponds to the average b-value derived from several high resolution studies of the Lyα forest at high redshift (Carswell *et al.* 1991; Rauch *et al.* 1993; Hu *et al.* 1995). For $b = 35$ km s^{-1}, the rest equivalent width limits of the strong- and weak-line samples correspond to $N_{\text{lim}} = 1.26 \times 10^{14}$ cm^{-2} and 0.66×10^{14} cm^{-2}, respectively.

Figure 5.12a - d show the distribution for progressively larger radii of spherical absorbers. It is clear from this figure that *it is impossible to represent the observations by a spherical model with uniform size*. Absorbers with radii less than $\sim 1000\ h^{-1}$ kpc cannot produce the high column density systems because the cross-sections for those systems are too small. Conversely, absorbers with radii greater than $\sim 450\ h^{-1}$ kpc cannot account for the high column density anticoincidences. However, large column density anticoincidences within a spherical structure can be obtained if the absorbing structure has less than unity covering factor. Similar conclusions were drawn by Charlton *et al.* (1995) using observations of the high redshift QSO pair Q1343+2640A, B.

Figure 5.12e - h shows the equivalent width distribution for pseudo-filamentary absorbers. For this model, there is a single radius for which all the observed coincidences and anticoincidences fall onto the region of non-zero probability. The likelihood functions for exponents $\gamma = 3, 4, 5, 6$ are shown in Figure 5.13 for the strong- and weak-line samples. Large jumps in the likelihood function occur when an observed coincidence or anticoincidence falls into or out of the region of non-zero probability density (regions outside those populated by points were assigned a probability of 10^{-12} in order to avoid eq. 5.6 becoming indeterminant). The peak of the likelihood function gives the most probable radius for the pseudo-filamentary geometry. The most likely model occurs for the steepest profile

($\gamma = 6$). The most probable radius was determined for this model by fitting a parabola to the peak of the likelihood function. For both the strong- and weak-line samples, the radius along the major axis is $1150\,h^{-1}$ kpc with 95% confidence lower and upper limits of $800 < R < 1480\,h^{-1}$ kpc, corresponding to $230\,h^{-1}$ kpc along the minor axis with limits of $160 < R < 295\,h^{-1}$ kpc.

Figure 5.12i - l shows the equivalent width distribution for randomly-inclined disks. Once again, a single radius can be found for which all the observed coincidences and anti-coincidences fall onto the area of non-zero predicted probability. The likelihood functions for $\gamma = 3, 4, 5, 6$ are shown in Figure 5.14 for the strong- and weak-line samples. As above, the most likely model corresponds to $\gamma = 6$. For $\gamma = 6$, the most likely radius determined by fitting a parabola to the peak of the likelihood function of the strong-line sample is $850\,h^{-1}$ kpc with 95% confidence lower and upper bounds of $600 < R < 1200\,h^{-1}$ kpc. The most probable radius for the weak-line sample is similarly $850\,h^{-1}$ kpc with 95% confidence limits of $720 < R < 1340\,h^{-1}$ kpc. In the likelihood analysis, randomly-inclined disks are only slightly favored over filamentary structures.

Finally, we tested whether spherical clouds with a range of sizes could be consistent with the observations. We randomly selected radii according to two distributions: (1) exponential, and (2) power law with indices $\alpha = -4, -3, \ldots, 5, 6$. The exponential distribution gave a poor representation of the observations. For the power-law distribution, the likelihood as a function of α is a parabola with maximum likelihood at $\alpha = 3$. In Figures 5.13 and 5.14, we have superimposed the maximum likelihood estimate for the case of $\alpha = 3$ for three values of γ on the likelihood functions for pseudo-filaments and randomly-inclined disks. Clearly, a range of absorber sizes can yield comparable likelihoods as those obtained for the filament and disk geometries. Because the maximum likelihoods determined for each of the geometries considered are very similar, we cannot definitively say one model is favored over the other; however, we can rule out the most simplistic model of spherical clouds of fixed radius.
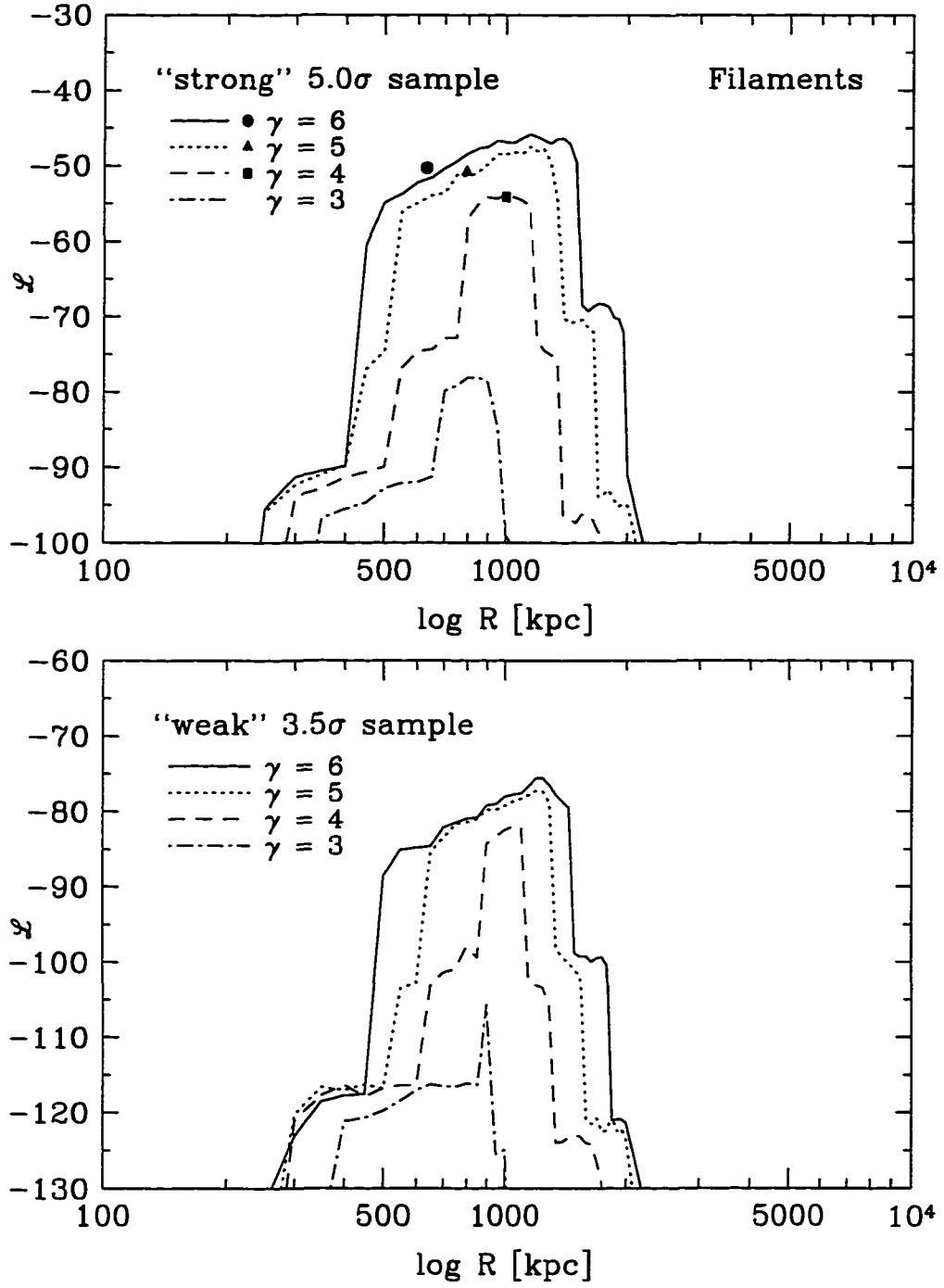
FIGURE 5.13—Likelihood functions for pseudo-filamentary absorbers with power-law column density profiles $N(r) \propto r^{-\gamma}$ for $\gamma = 3, 4, 5, 6$. Superimposed are the maximum likehood estimates for spherical absorbers with a power-law distribution of radii with index $\alpha = 3$ for three values of γ.
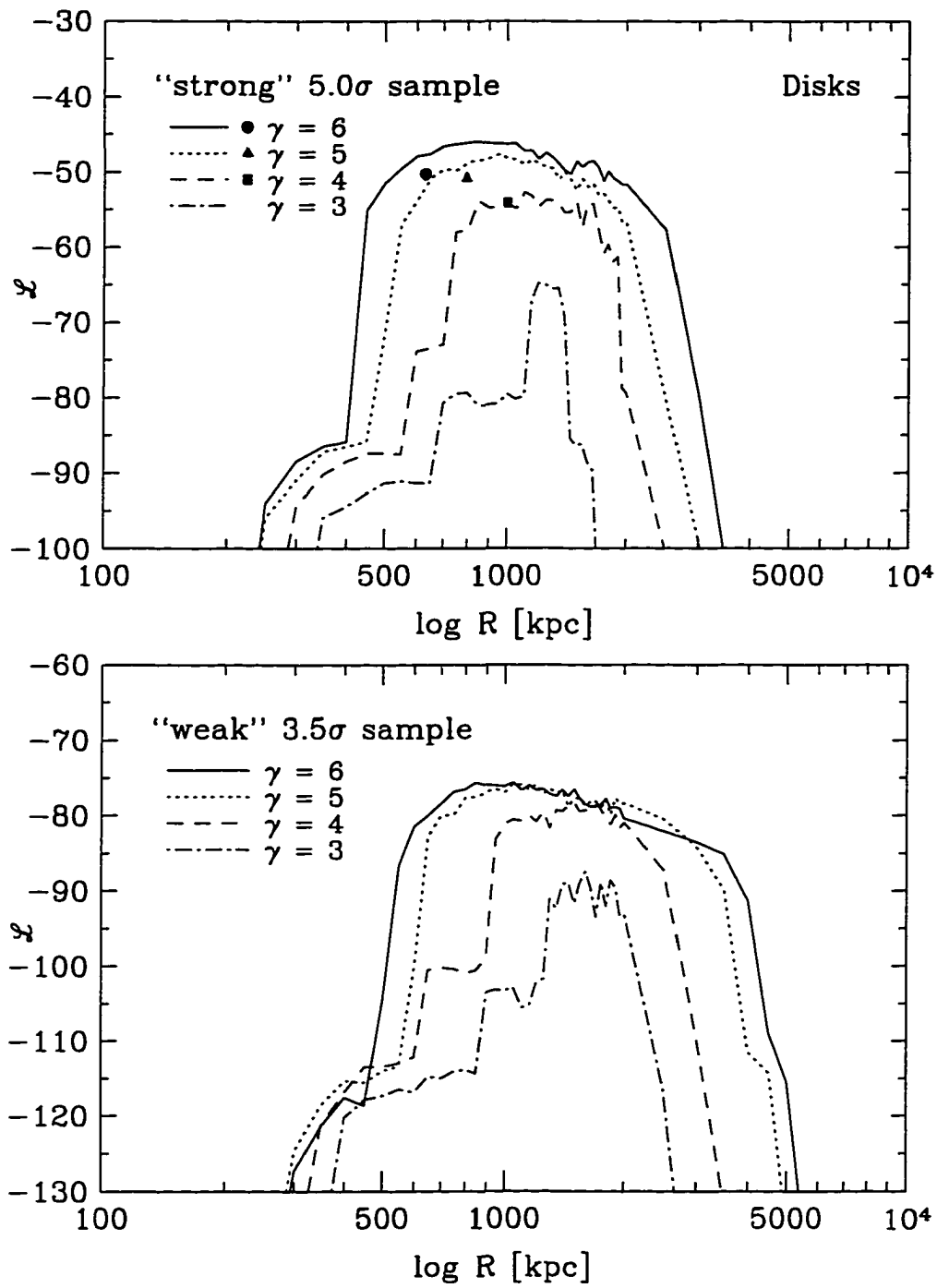
FIGURE 5.14—As Figure 5.13, likelihood functions for randomly-inclined disks.

The most important result of this analysis is that the model which best fits the observations is obtained for the least restrictive model considered, *i.e.*, randomly inclined disks. The implication of this result is that the Lyα absorbers are diverse structures. Randomly inclined disks give a range of cross sections and varying projected sizes that eliminate the sharp edges and forbidden regions produced by spherical structures and filaments of a single size. This is consistent with the picture of Lyα absorbers arising from recent hydrodymanical simulations that have found that some of the Lyα absorption is produced in the halos of galaxies and some arises in the filaments and sheets between galaxies (Cen *et al.* 1995; Hernquist *et al.* 1995; Miralde-Escudé *et al.* 1996).

Although we have chosen in this chapter to model the Lyα absorbers with power-law column density profiles, the likelihood technique presented here can easily be expanded to test other models, such as, exponential disks with central column densities selected according to the observed column density distribution. Future analysis should also account for the error associated with the observed equivalent widths by convolving the probabilities, $p_i(W_1, W_2)$ and $p_j(W_1, W_2 < W_{lim})$, with a distribution of errors in measured equivalent widths. This likelihood technique can also be expanded to include the information contained in the velocity differences of the common systems in order to diagnose the kinematics of the absorbers.

5.6 Summary and Discussion

We have obtained *HST* observations with the FOS and GHRS of the QSO pair Q0107 − 025A, B in an attempt to measure the transverse sizes of the Lyα absorbers. In addition, ground-based observations have been obtained from 3200 Å to the Mg II emission redshifts of the QSOs in order to look for possible metal lines associated with the Lyα lines. From the presence of common absorption in the FOS spectra, we obtained lower limits on the radius of the clouds of $140 - 160\,h^{-1}$ kpc. The presence of anticoincident systems allows a measure of the characteristic sizes of the Lyα absorbers. We defined two

samples of Lyα absorption lines, and estimated the most probable radius of the absorbers for both samples. Defining a coincidence as common systems within a velocity window of 150 km s^{-1}, consistent with other studies (Dinshaw et al. 1994; Fang et al. 1996) and numerical simulations, we counted five coincidences (including a probable coincidence) and six anticoincidences in the sample of strong lines with $W_0 > 0.32$ Å. Using a simple maximum likelihood analysis for spherical and disk-like absorbers, we obtained estimates of the characteristic radius of 505 h^{-1} kpc and 715 h^{-1} kpc, respectively. For the weak-line sample with $W_0 > 0.24$ Å, we found the same number of coincidences and 20 anticoincidences, which gave a somewhat smaller size estimate of 275 h^{-1} kpc for spherical absorbers and 355 h^{-1} kpc for randomly-inclined disks.

We also presented a new statistical technique to test the relative likelihood of three geometric models. In particular, we considered spherical absorbers, with and without a distribution in size, as well as pseudo-filamentary and disk-like absorbers. An important result is that spherical absorbers with uniform radius cannot represent the observations and, therefore, are ruled out. The model which provided the most favorable fit to the observations was found to be randomly-inclined disks with characteristic radius 850 h^{-1} kpc and 95% confidence limits of $720 < R < 1340$ h^{-1} kpc, although filaments also provided a good fit. Qualitative comparisons by Charlton et al. (1995) of spherical and disk-like geometries with both smooth and irregular column density distributions led to the same conclusion that smooth disk-like structures are consistent with existing observations of QSO pairs at $z \simeq 2$. This result is not that surprising in view of recent cosmological simulations in which the Lyα absorption arises in complex structures with a range of scales. Further observations of QSO pairs are required to discriminate between pseudofilaments and disks, as well as more sophisticated models in which there are two relevant length scales: a length measuring the characteristic distance over which the column density drops by, e.g., a factor two compared to its maximum value, and a length measuring the characteristic distance to the next maximum peak in the column density. These results of

the likelihood analysis are preliminary, and are meant to demonstrate the viability of the method as a powerful new statistical tool for analysing the data of QSO pairs.

Several of the Lyα absorption systems appear to lie in the Lyman limit regime, *i.e.*, with column densities above 10^{17} cm^{-2}. If these systems are indeed LLSs, we should see a decrement in the flux in the GHRS data as well as corresponding Mg II absorption lines, since the Mg II absorbers are thought to be the same population of objects as the LLSs (Steidel 1993). Inspection of the flux levels in the FOS and GHRS spectra of both quasars reveals no evidence for either reduced flux or the characteristic signature of LLSs. (The LLS at $z_{\rm LLS} = 0.400$ in Q0107–025B, discussed in § 5.4.4, was not included in either the strong- or weak-line samples). Moreover, we see no evidence for corresponding Mg II systems which would be observable in our MMT data down to an equivalent width of ~ 0.30 Å. Finally, many of the apparent high column density sytsems have line widths that exceed the instrumental LSF. Therefore, it is more likely that they are blends of narrower components which could be resolved in higher resolution data. Because the line density is so low, the blends could not be due to just chance superposition, and provides indirect evidence for strong correlations of the Lyα forest on velocity separations of $\Delta v < 400$ kms. Clustering has been detected in the *HST* Key Project catalog of absorbers ($0 < z < 1.3$) on scales of $250 - 500$ km s^{-1} (Ulmer 1996). For clustered absorbers, the range of sizes of the Lyα absorbers determined from the likelihood analysis in this section would be overestimated since the strong lines tend to drive the estimated radius upward.

In order to extend the observations to lower redshifts and therefore smaller transverse dimensions, we also obtained GHRS data of the pair. Although the SNR of the GHRS observations is insufficient to measure cloud sizes, we can nevertheless place some interesting limits. First, we observed three Lyα absorption systems in one line of sight and not the other, although a line of the same strength could have been seen. We also found two common systems with small velocity differences less than 150 km s^{-1}. The pathlength separation at the redshifts of the common systems are about $100\,h^{-1}$ kpc. However, we

need a better SNR in the spectrum of Q0107−025A before we can compare the statistics about size estimates with FOS estimate at higher redshift. More interesting is the presence of the $z = 0.400$ LLS in the spectrum of Q0107−025B, but not in A, despite the existence of both Lyα and possibly C IV features in both spectra. This suggests that lower column density systems maybe found at larger impact parameters than systems with higher column densities, in agreement with hydrodynamical simulations (e.g. Cen et al. 1995) and the statistics of the Lyα and LLS absorbers (Steidel 1993). See, for example, the contour diagrams of neutral hydrogen column density published in Cen et al. (1995) and Miralde-Escudé et al. (1996) which show that the lower column density contour extend out to larger distances than the higher column density contours, contrary to what is expected for uniform clouds pressure-confined by hot halo gas (Cowie et al. 1995).

The characteristic size of the Lyα absorbers derived in this chapter are incompatible with those predicted by the pressure-confined model (Sargent et al. 1980; Ikeuchi & Ostriker 1986) and the standard CDM minihalo model (Rees 1986; Miralda-Escudé & Rees 1993), originally proposed to explain the high redshift Lyα systems. The models predict an impact parameter at which a sightline intercepts a column density 10^{14} cm^{-2} to lie in the range $5 - 50\,h^{-1}$ kpc for typical Doppler widths and reasonable assumptions about the mean intensity of the backround radiation field. Structures of the size derived in this chapter are not expected to be dynamically stable against gravitational collapse or tidal disruption. Such large sizes can be understood if the gas is in the process of collapse or expansion.

At low redshift, there is increasing evidence that the Lyα systems are associated with luminous galaxies, though the degree of association remains a contentious issue. Lanzetta et al. (1995) find that Lyα absorption originates in the extended envelopes of luminous galaxies for impact parameters $\lesssim 160\,h^{-1}$ kpc, with the implication that most if not all Lyα systems are associated with galaxies. In contrast, Morris et al. (1995; see also Mo & Morris 1994) estimate that no more than 20% of the Lyα absorbers are associated

with luminous galaxies, and some of the absorbers have been found in voids (Morris et al. 1995; Stocke et al.1995). The apparent contradiction may be explained by the fact that the Morris et al. and Stocke et al. results are more sensitive to lower column density absorbers, whereas Lanzetta et al. sample column densities of $N(\text{H\,I}) \gtrsim 10^{14}$ cm^{-2} comparable to the equivalent width threshold of the strong-line sample. If the luminous galaxies are responsible for the high column density absorbers, their envelopes would have to be huge to be consistent with the sizes derived in this chapter.

Similar studies of the relationship between Lyα absorbers and individual galaxies have recently been published by Le Brun et al. (1995) and Bowen et al. (1996). Neither study found evidence for a correlation between Lyα equivalent width and impact parameter. In fact, their results are consistent with the Lyα absorbers distributed in large-scale filaments or sheets, rather than residing in any particular galaxy. In this scenario, the Lyα absorption systems could plausibly arise in the gaseous bridges between galaxies or in tidal debris built up in small groups of galaxies (Morris & van den Bergh 1994). The upper limit on the baryonic density ($\Omega_b \leq 0.036 h^{-2}$; Walker et al. 1991) also places severe constraints on the geometry of the absorbers. Using reasonable estimates of the ionization background, Rauch and Haehnelt (1995) argue that there are not enough baryons to fill a spherical volume of order $0.5\,h^{-1}$ Mpc radius, even if all the baryons are contained in the Lyα absorbers. Thus, the Lyα absorption must arise in highly flattened structures with transverse extent approximately ten times the thickness of the clouds.

Flattened structures such as filaments, sheets or pancakes arise naturally in cosmological simulations of gravitational collapse (Cen et al. 1995; Hernquist et al. 1995; Miralda-Escudé et al. 1996). In the simulations, the absorption systems with column densities of $N(\text{H\,I}) \simeq 10^{13} - 10^{15}$ cm^{-2} are produced in a variety of complex structures including filaments, sheets of shocked gas resembling Zel'dovich pancakes and velocity caustics in low density regions. The characteristic size of a filament is of order $1\,h^{-1}$ Mpc long and $50 - 100\,h^{-1}$ kpc thick. Because of the low overdensities of the absorbers, many are still

expanding with the Hubble flow. Although the simulations have only been evolved to $z = 2$ and are therefore not entirely comparable to our $z < 1$ observations, they are nevertheless remarkably consistent with our results.

Differences between the line-of-sight velocities of the absorption features provide information about any systematic motions of the absorbing gas over scales equal to the separation of the lines of sight. The velocity difference on scales of a few kpc from paired lines of sight to the gravitationally-lensed quasars Q2345+007A,B (Foltz et al. 1984), UM673A,B (Smette et al. 1992), and most recently HE1104−1805 (Smette et al. 1995) can be ascribed to measurement errors and a reasonable upper bound to Δv is 20 km s^{-1}. In Dinshaw et al. (1994), evidence for a marginally significant velocity difference of 65 km s^{-1} was detected in the physical pair Q1343+266A,B with separation $\sim 40h^{-1}$ kpc. The results presented here provide evidence for a statistically significant velocity difference of ~ 100 km s^{-1} over scales of several hundred kpc, and confirm the trend in Δv as a function of line-of-sight separation. The correlation of rms velocity difference with line-of-sight separation can be understood if the internal motions of the absorbers are systematic over large scales (see for example, Charlton et al. 1995).

The trend in Δv is consistent with what one would expect for disk-like absorbers with a bulk rotational, inflow or outflow velocity component (Charlton et al. 1995). Similarly, it is consistent with structures expanding with the Hubble flow. The velocity difference expected from Hubble expansion in any gravitationally clustering model (Haehnelt 1996) is $\Delta v = H(z)D_\perp \tan \alpha$ where $D_\perp$ is the perpendicular separation of an absorber situated on the two sightlines and α is the angle between the normal to the surface of the absorber and the line of sight. Therefore for larger line-of-sight separations, we expect systematically larger rms velocity diferences of the common pairs, as is observed. The trend in velocity is similarly observed in the cosmological simulations. Miralda-Escudé et al. (1996) plot the median velocity separation of coincident lines as a function of line-of-sight separation. The velocity differences are unobservably small on the scales sampled by gravitationally-

lensed QSOs, consistent with the results of Smette *et al.* (1993, 1995). The velocity differences grow on larger scales, qualitatively similar to the existing observations, however the theorectical results are not directly comparable to the data, since the simulated data have been analyzed in different ways than the Gaussian profile fitting method used in this chapter.

We are currently obtaining further observations of Q0107−025A, B in order to raise the confidence level of many of the weak lines in the FOS data, specifically so that the question of whether the low column density absorption lines share the same properties as those with high column density may be addressed. We are also obtaining data with the G270H grating to extend the spectral coverage of the FOS data out to the Lyα emission lines of the QSOs in order to eliminate existing ambiguities in the line identification. Finally, we are obtaining FOS data of a third bright QSO ($z = 0.728, B_J = 18.4$) lying a few arcminutes from Q0107−025A, B. The existence of this quasar offers a unique opportunity to probe distance scales out to 1 Mpc, and to sample two dimensions transverse to the line of sight. These observations, along with those being carried out on other QSOs with still larger separations (*e.g.*, Turnshek *et al.*, in preparation), should yield additional clues as to the distribution and topology of the clouds at low redshifts.

composite FOS spectrum. Finally, we thank Tom Aldcroft and Jill Bechtold for making their spectral analysis software available to us.

TABLE 5.1

Program QSOs

QSO	R.A. (J2000)	Decl. (J2000)	g	z_{em}
Q0107-025A.....	$01^h 10^m 13\overset{s}{.}16$	$-02°19'54\overset{.}{.}3$	17.9	0.956
Q0107-025B.....	01 10 16.27	-02 18 52.2	17.3	0.952

TABLE 5.2

JOURNAL OF SPECTROSCOPIC OBSERVATIONS

QSO	Date	Instrument	Grating	Exposure (s)	Wavelength (Å)	Resolution (Å)
Q0107-025A......	1994 Feb 12	FOS	G190H	13320	1625 – 2300	1.4
	1994 Nov 15	GHRS	G140L	9124	1220 – 1495	1.4
	1994 Sep 29	MMT	832	6600	4150 – 5650	1.0
	1994 Oct 02	MMT	832	9600	3250 – 4250	1.0
Q0107-025B......	1994 Feb 12	FOS	G190H	6480	1625 – 2300	1.4
	1994 Sep 22	GHRS	G140L	9124	1220 – 1495	1.4
	1994 Sep 29	MMT	832	4800	4150 – 5650	1.0
	1994 Oct 02	MMT	832	5400	3250 – 4250	1.0

TABLE 5.3

ABSORPTION LINES OF Q0107–025A IN FOS DATA

No.	λ_{obs} (Å)	σ_λ (Å)	W_{obs} (Å)	σ_W (Å)	SNR	FWHM (Å)	ID	z_{abs}	Remarks
1	1637.98	0.38	1.37	0.38	3.6	2.99	C II 1334	0.2274	
2	1671.76	0.15	0.98	0.15	6.5	1.96	Al II 1670	0.0006	
	1671.76	0.15	0.98	0.15	6.5	1.96	Lyγ	0.7190	
3	1683.81	0.10	1.22	0.14	8.6	1.87	Lyα	0.3851	b
4	1688.70	0.14	0.65	0.12	5.4	1.50	Lyα	0.3889	
5	1697.16	0.25	0.53	0.13	3.9	2.04	Lyδ	0.7870	
6	1701.94	0.18	0.73	0.13	5.6	2.11	Lyα	0.4000	c
7	1722.10	0.19	0.86	0.16	5.4	2.24	Lyα	0.4167	d
8	1728.30	0.37	0.80	0.20	4.0	3.21	Lyα	0.4216	g
9	1738.77	0.08	0.94	0.10	9.6	1.70	Lyγ	0.7879	
	1738.77	0.08	0.94	0.10	9.6	1.70	Lyη	0.8773	
10	1747.08	0.16	0.32	0.09	3.7	1.30	Lyζ ?	0.8771	
11	1760.58	0.18	0.47	0.10	4.6	1.71	Lyϵ	0.8774	
12	1763.94	0.10	0.87	0.11	8.0	1.66	Lyβ	0.7197	
13	1774.16	0.17	0.54	0.10	5.6	1.98	Lyβ	0.7297	
14	1782.75	0.09	0.58	0.08	7.6	1.43	Lyδ	0.8771	
15	1809.50	0.29	0.44	0.11	3.9	2.40	Lyα ?	0.4884	
16	1825.62	0.05	1.84	0.09	21.1	2.41	Lyα	0.5017	
	1825.62	0.05	1.84	0.09	21.1	2.41	Lyγ	0.8772	
17	1833.36	0.15	0.54	0.09	6.1	1.93	Lyβ	0.7874	
18	1867.83	0.04	2.73	0.09	30.7	2.61	Lyα	0.5365	
19	1894.36	0.10	0.98	0.09	11.4	2.28	Lyα	0.5583	h
20	1900.66	0.11	0.51	0.07	7.3	1.42	C IV 1548	0.2274	e
21	1904.13	0.10	0.49	0.07	6.8	1.62	C IV 1550	0.2276	e,i
22	1912.11	0.20	0.30	0.07	4.2	1.71	Lyα ?	0.5729	j
23	1921.88	0.16	0.45	0.10	4.8	1.78	Lyα	0.5811	
24	1925.53	0.05	0.74	0.06	11.9	1.40	Lyβ	0.8772	
25	1956.36	0.25	0.36	0.09	4.2	2.00	Lyα ?	0.6093	l
26	1976.83	0.21	0.32	0.07	4.4	1.87	Lyα ?	0.6262	l
27	1987.04	0.30	0.48	0.09	5.3	3.31	Lyα	0.6346	l
28	1995.02	0.09	0.54	0.07	8.1	1.55	C IV 1548	0.2886	l, m
29	1998.83	0.16	0.24	0.06	4.3	1.39	C IV 1550 ?	0.2889	l, m
30	2007.65	0.10	0.41	0.06	7.2	1.45	Lyα	0.6515	l, n
31	2016.22	0.14	0.78	0.07	11.9	3.30	Lyα	0.6589	o, r
32	2036.73	0.33	0.36	0.07	5.1	3.40	Lyα ?	0.6754	a
33	2042.17	0.06	0.50	0.04	11.9	1.41	Lyα	0.6799	
34	2055.16	0.08	0.48	0.05	10.3	1.76	Lyα	0.6906	
35	2060.79	0.13	0.24	0.05	5.3	1.36	Lyα	0.6952	
36	2083.00	0.17	0.19	0.05	4.0	1.37	Lyα ?	0.7135	a
37	2090.33	0.03	1.64	0.05	32.7	2.22	Lyα	0.7195	
38	2102.14	0.03	1.26	0.05	27.5	1.82	Lyα	0.7292	
39	2167.37	0.23	0.31	0.06	5.1	2.40	C IV 1548	0.3999	p
40	2172.52	0.04	1.24	0.05	26.2	1.95	Lyα	0.7871	
41	2188.78	0.23	0.40	0.09	4.5	2.40	Lyα	0.8005	
42	2197.92	0.26	0.31	0.06	5.0	2.69	Lyα ?	0.8079	
43	2230.44	0.23	0.22	0.05	4.2	2.03	Lyα ?	0.8347	
44	2241.55	0.13	0.32	0.05	6.8	1.76	Lyα	0.8439	
45	2247.07	0.06	0.48	0.04	12.3	1.42	Lyα	0.8484	

TABLE 5.3—*Continued*

No.	λ_{obs} (Å)	σ_λ (Å)	W_{obs} (Å)	σ_W (Å)	SNR	FWHM (Å)	ID	z_{abs}	Remarks
46	2252.61	0.09	0.29	0.04	7.4	1.34	Lyα	0.8530	
47	2263.13	0.51	0.50	0.13	3.9	5.09	Lyα ?	0.8616	f, q
48	2272.73	0.07	0.39	0.04	9.6	1.47	Lyα	0.8695	
49	2282.03	0.02	1.22	0.04	33.2	1.68	Lyα	0.8772	
50	2298.01	0.05	0.39	0.03	11.6	1.30	Lyα	0.8903	

NOTES TO TABLE 5.3

a. Possibly spurious.

b. Possible blend with $Ly\beta$ of $z = 0.6411$.

c. System contains absorption from heavy elements.

d. Possible blend with $Ly\beta$ of $z = 0.6799$.

e. $Ly\alpha$ line corresponding to C IV doublet present in GHRS data.

f. Feature may disappear with slight change in the continuum.

g. Feature was not found by Key Project software JASON.

h. Possible blend with $Ly\beta$ of $z = 0.8484$.

i. Uncertain identification. Possibly $Ly\gamma$ ($z = 0.9578$) with redshift $\sim 200\,\mathrm{km\ s^{-1}}$ longward of the emission redshift of QSO.

j. Uncertain identification. Possibly $Ly\gamma$ ($z = 0.9661$) with redshift $\sim 1500\,\mathrm{km\ s^{-1}}$ longward of the emission redshift of QSO.

l. Possibly $Ly\beta$.

m. Probable C IV doublet. Doublet ratio > 2. $Ly\alpha$ would not lie in available FOS or GHRS data.

n. Uncertain identification. Possibly $Ly\beta$ ($z = 0.9573$) with redshift $\sim 200\,\mathrm{km\ s^{-1}}$ longward of the emission redshift of QSO.

o. Uncertain identification. Possibly $Ly\beta$ ($z = 0.9657$) with redshift $\sim 1500\,\mathrm{km\ s^{-1}}$ longward of the emission redshift of QSO.

p. Doublet component C IV 1550 would be blended with $Ly\alpha$ at $z = 0.7871$.

q. Probable blend since FWHM of line is $5.09\,\text{Å}$. No attempt at deblending was made since individual components are not obviously visible.

TABLE 5.4

ABSORPTION LINES OF Q0107–025B IN FOS DATA

No.	λ_{obs} (Å)	σ_λ (Å)	W_{obs} (Å)	σ_W (Å)	SNR	FWHM (Å)	ID	z_{abs}	Remarks
1	1671.62	0.13	0.89	0.15	6.0	1.60	Al II 1670	0.0005	
	1671.62	0.13	0.89	0.15	6.0	1.60	Lyγ	0.7188	
2	1701.52	0.07	1.31	0.12	11.2	1.72	Lyα	0.3997	c, m
3	1718.05	0.33	1.05	0.20	5.2	3.13	Lyα	0.4133	
4	1738.53	0.18	0.50	0.11	4.4	1.64	Lyγ	0.7876	
	1738.53	0.18	0.50	0.11	4.4	1.64	Lyη	0.8770	
5	1747.00	0.11	0.63	0.10	6.2	1.42	Lyζ	0.8771	e
6	1760.37	0.14	0.52	0.12	4.5	1.39	Lyγ	0.8101	
7	1763.05	0.09	1.58	0.16	10.2	2.19	Lyβ	0.7188	e
8	1782.72	0.21	0.48	0.13	3.7	1.45	Lyδ	0.8771	
9	1785.07	0.43	0.78	0.21	3.7	3.38	Lyα	0.4684	
10	1824.19	0.09	1.72	0.11	15.7	2.97	Lyα	0.5006	d
	1824.19	0.09	1.72	0.11	15.7	2.97	Lyγ	0.8757	
11	1833.85	0.19	0.36	0.09	4.0	1.61	Lyβ	0.7879	
12	1845.16	0.07	0.78	0.08	10.3	1.41	Lyα	0.5178	f
13	1853.22	0.12	0.49	0.09	5.4	1.44	Lyα	0.5244	
14	1856.20	0.10	1.20	0.11	11.0	2.28	Lyβ	0.8094	
15	1867.30	0.10	1.05	0.11	10.0	2.00	Lyα	0.5360	g
16	1891.86	0.23	0.32	0.09	3.5	1.64	Lyα ?	0.5562	h
17	1919.84	0.24	0.62	0.11	5.6	2.68	Lyα	0.5792	
18	1925.28	0.08	0.97	0.09	11.2	2.05	Lyβ	0.8769	
19	1950.91	0.19	0.29	0.08	3.8	1.46	Si IV 1393 ?	0.3997	k, m
20	1957.02	0.21	0.47	0.10	4.7	2.15	Lyα	0.6099	l
21	1972.63	0.15	0.37	0.07	5.0	1.57	Lyα	0.6227	l
22	1997.88	0.28	0.49	0.11	4.7	2.85	Lyα	0.6436	l
23	2002.71	0.28	0.30	0.08	3.7	2.15	Lyα ?	0.6474	a, l
24	2006.52	0.31	0.33	0.10	3.5	2.33	Lyα ?	0.6508	a, l
25	2019.15	0.16	0.33	0.06	5.5	1.80	Lyα	0.6609	
26	2049.44	0.32	0.25	0.07	3.5	2.30	Lyα ?	0.6858	
27	2055.24	0.12	0.34	0.05	6.2	1.48	Lyα	0.6906	
28	2084.30	0.10	0.55	0.06	8.9	1.92	Lyα	0.7145	
29	2089.55	0.03	1.37	0.05	27.6	1.75	Lyα	0.7188	
30	2119.07	0.29	0.23	0.07	3.6	2.14	Lyα ?	0.7431	a
31	2126.15	0.16	0.30	0.06	4.9	1.66	Lyα ?	0.7490	
32	2166.97	0.12	0.45	0.06	7.4	1.90	C IV 1548	0.3997	m
33	2170.79	0.15	0.38	0.07	5.4	1.88	C IV 1550	0.3997	m
34	2173.57	0.06	0.78	0.07	10.9	1.72	Lyα	0.7880	
35	2186.21	0.16	0.53	0.07	7.8	2.52	Lyα	0.7984	
36	2200.36	0.03	1.61	0.05	31.2	2.00	Lyα	0.8100	
37	2211.41	0.11	0.30	0.05	6.1	1.34	Lyα	0.8191	
38	2216.38	0.49	0.40	0.10	4.3	4.35	Lyα ?	0.8216	
39	2227.65	0.08	0.48	0.05	9.3	1.57	Lyα	0.8325	
40	2231.05	0.12	0.38	0.05	6.9	1.65	Lyα	0.8352	
41	2247.36	0.22	0.27	0.06	4.5	2.00	Lyα ?	0.8487	
42	2281.61	0.03	1.10	0.04	25.2	1.70	Lyα	0.8768	
43	2298.26	0.09	0.27	0.04	6.6	1.32	Lyα	0.8905	

NOTES TO TABLE 5.4

a. Possibly spurious.

c. System contains absorption from heavy elements.

d. Associated Lyγ present in GHRS data.

e. Components are too strong with respect to other lines in this system and are almost certainly blends.

f. Possible blend with Lyβ of $z = 0.7984$.

g. Possible blend with C II 1334 of $z = 0.3997$.

h. Possible blend with Lyβ of $z = 0.8484$ in A or $z = 0.8487$ in B.

k. Si IV $\lambda1402$, the other member of the doublet, appears to be present at 2.7σ confidence level.

l. Possibly Lyβ.

m. Member of Lyman limit system. Higher order Lyman series lines Lyβ through Lyε present in GHRS data.

TABLE 5.5
ABSORPTION LINES OF Q0107−025A,B IN GHRS DATA

No.	λ_{obs}(Å)	σ_λ(Å)	A W_{obs}(Å)	σ_W(Å)	SNR	ID	z_{abs}	No.	λ_{obs}(Å)	σ_λ(Å)	B W_{obs}(Å)	σ_W(Å)	SNR	ID	z_{abs}	A − B Δv(km/s)
			< 0.74					1	1234.27	0.16	0.62	0.16	3.8	Lyβ	0.2033	
1	1259.80	0.10	0.82	0.15	5.3	Si II 1260	−0.0005	2	1260.61	0.07	0.58	0.11	5.5	Si II 1260	0.0001	−164 ± 4
			< 0.58					3	1274.29	0.11	0.32	0.10	3.2	Lyα	0.0482	
2	1311.37	0.16	0.46	0.14	3.2	Lyα	0.0787				< 0.38					
			< 0.62					4	1312.73	0.09	0.32	0.08	4.2	Lyε[b]	0.3998	
			< 0.65					5	1329.35	0.06	0.46	0.07	6.2	Lyδ[b]	0.3997	
3	1335.03	0.14	0.44	0.14	3.2	C II 1334	0.0004	6	1335.03	0.12	0.72	0.11	6.8	C II 1334	0.0004	0 ± 41
4	1357.05	0.07	0.68	0.12	5.5	Lyα	0.1163	7	1356.70	0.07	0.56	0.08	6.9	Lyα	0.1160	86 ± 20
			< 0.73					8	1361.19	0.12	0.70	0.14	5.1	Lyγ[b]	0.3996	
			< 0.65					9	1362.88	0.13	0.47	0.13	3.7	Lyα	0.1211	
			< 0.61					10	1404.13	0.11	0.77	0.12	6.6	Lyα	0.1550	
			< 0.77					11	1435.72	0.09	0.55	0.11	5.0	Lyβ[b]	0.3997	
			< 0.89					12	1459.29	0.10	1.03	0.15	7.1	Lyγ[c]	0.5004	
			< 0.92					13	1462.50	0.08	1.18	0.14	8.3	Lyα	0.2030	
5	1492.21	0.24	1.17	0.37	3.2	Lyα[a]	0.2275	14	1491.90	0.14	0.52	0.15	3.4	Lyα	0.2272	52 ± 20

[a] Associated C IV doublet present in FOS data.

[b] Member of Lyman limit system. Associated Lyα and C IV doublet present in FOS data.

[c] Associated Lyα absorption line present in FOS data.

NOTE.— This table lists lines detected at or above 3σ confidence level. The wavelengths have been shifted to the red by 75 km s^{-1} in order to register them with the FOS data. Upper equivalent width limts are 3σ confidence level.

TABLE 5.6

"Strong-line" Sample of Coincident and Anticoincident Lyman-Alpha Systems

No.	$\lambda(\text{Å})$	$\sigma_\lambda(\text{Å})$	A $W_0(\text{Å})$	$\sigma_W(\text{Å})$	SNR	z_{abs}	No.	$\lambda(\text{Å})$	$\sigma_\lambda(\text{Å})$	B $W_0(\text{Å})$	$\sigma_W(\text{Å})$	SNR	z_{abs}	A · B $\Delta v\,(\text{km s}^{-1})$
15	1824.54	0.10	0.40	0.07	5.8	0.5009	9	1823.94	0.10	0.89	0.09	9.6	0.5004	99 ± 23
			< 0.24				12	1845.16	0.07	0.51	0.05	10.3	0.5178	
17	1867.83	0.04	1.78	0.06	30.7	0.5365	15	1867.30	0.10	0.68	0.07	10.0	0.5360	90 ± 16
18	1894.36	0.10	0.63	0.06	11.4	0.5583				< 0.22				
			< 0.23				17	1919.84	0.24	0.39	0.07	5.6	0.5792	
30	2016.20	0.07	0.39	0.04	9.9	0.6589				< 0.20				
36	2090.33	0.03	0.95	0.03	32.7	0.7195	28	2089.55	0.03	0.80	0.03	27.6	0.7188	111 ± 6
37	2102.14	0.03	0.73	0.03	27.5	0.7292				< 0.18				
40	2172.52	0.04	0.69	0.03	26.2	0.7871	34	2173.57	0.06	0.44	0.04	10.9	0.7880	-150 ± 11
			< 0.14				37	2200.36	0.03	0.89	0.03	31.2	0.8100	
49	2282.03	0.02	0.65	0.02	33.2	0.8772	42	2281.61	0.03	0.59	0.02	25.2	0.8768	53 ± 5

NOTE. — This table lists 5σ lines with $W_0 > 0.32\,\text{Å}$. Upper equivalent width limits are 5σ confidence level.

TABLE 5.6
"WEAK-LINE" SAMPLE OF COINCIDENT AND ANTICOINCIDENT LYMAN-ALPHA SYSTEMS

No.	$\lambda(\text{Å})$	$\sigma_\lambda(\text{Å})$	A $W_0(\text{Å})$	$\sigma_W(\text{Å})$	SNR	z_{abs}	No.	$\lambda(\text{Å})$	$\sigma_\lambda(\text{Å})$	B $W_0(\text{Å})$	$\sigma_W(\text{Å})$	SNR	z_{abs}	A - B $\Delta v\,(\text{km s}^{-1})$
14	1809.50	0.29	0.30	0.07	3.9	0.4885				< 0.25				
15	1824.54	0.05	0.40	0.07	5.8	0.5009	9	1824.19	0.09	0.89	0.09	9.6	0.5004	99 ± 23
			< 0.24				11	1845.16	0.07	0.51	0.05	10.3	0.5178	
			< 0.23				12	1853.22	0.12	0.32	0.06	5.4	0.5244	
17	1867.83	0.04	1.78	0.06	30.7	0.5365	14	1867.30	0.10	0.68	0.07	10.0	0.5360	90 ± 16
18	1894.36	0.10	0.63	0.06	11.4	0.5583				< 0.22				
			< 0.23				16	1919.84	0.11	0.39	0.07	5.6	0.5792	
22	1921.88	0.16	0.28	0.06	4.8	0.5809				< 0.22				
			< 0.20				19	1957.02	0.21	0.29	0.06	4.7	0.6099	
26	1987.04	0.30	0.29	0.06	5.3	0.6345				< 0.20				
							21	1997.88	0.28	0.30	0.07	4.7	0.6434	
29	2007.65	0.10	0.25	0.04	7.2	0.6515				< 0.20				
30	2016.21	0.15	0.39	0.04	9.9	0.6585				< 0.20				
32	2042.17	0.06	0.30	0.02	11.9	0.6799				< 0.20				
33	2055.16	0.08	0.28	0.03	10.3	0.6906				< 0.19				
							26	2084.30	0.10	0.32	0.03	8.9	0.7145	
36	2090.33	0.03	0.95	0.03	32.7	0.7195	27	2089.55	0.03	0.80	0.03	27.6	0.7188	111 ± 6
37	2102.14	0.03	0.73	0.03	27.4	0.7292				< 0.18				
39	2172.52	0.04	0.69	0.03	26.2	0.7871	32	2173.57	0.05	0.44	0.04	10.9	0.7880	−150 ± 11
			< 0.14				33	2186.21	0.16	0.29	0.04	7.8	0.7984	
			< 0.14				34	2200.36	0.03	0.89	0.03	31.2	0.8100	
			< 0.14				36	2227.65	0.08	0.26	0.03	9.3	0.8324	
44	2247.07	0.06	0.26	0.02	12.3	0.8484				< 0.16				
45	2263.13	0.51	0.27	0.07	3.9	0.8616				< 0.14				
47	2282.03	0.02	0.65	0.02	33.2	0.8772	39	2281.61	0.03	0.59	0.02	25.2	0.8768	53 ± 5

NOTE. This table lists 3.5σ lines with $W_0 > 0.24\,\text{Å}$. Upper equivalent width limits are 3.5σ confidence level.

TABLE 5.8

RADIUS ESTIMATES OF THE LYMAN ALPHA ABSORBERS

	N_{coin}	N_{anti}	R [h^{-1} kpc]	Spheres $R - 2\sigma$	$R + 2\sigma$	R [h^{-1} kpc]	Disks $R - 2\sigma$	$R + 2\sigma$
"strong" sample: $q_0 = 0.5$	4	6	445	340	1360	625	420	2025
	5	6	505	360	1535	715	470	2295
$q_0 = 0.0$	4	6	535	370	1610	745	495	2390
	5	6	600	410	1810	850	560	2680
"weak" sample: $q_0 = 0.5$	4	20	255	210	395	330	255	550
	5	20	275	220	425	355	275	595
$q_0 = 0.0$	4	20	310	255	475	395	305	655
	5	20	325	265	510	425	325	710

CHAPTER 6

HUBBLE SPACE TELESCOPE[1] ULTRAVIOLET SPECTROSCOPY OF THE QUASAR PAIR LB 9605, LB 9612: EVOLUTION IN THE SIZES OF THE LYMAN-ALPHA ABSORBERS?

Nadine Dinshaw[2], Craig B. Foltz[3], Chris D. Impey[2], and Ray J. Weymann[4]

Abstract

Ultraviolet spectroscopy has been obtained with the Faint Object Spectrograph of the *Hubble Space Telescope* in the Lyα forest of the quasar pair, LB 9605 ($z_{em} = 1.834$) and LB 9612 ($z_{em} = 1.898$), in order to measure the sizes of the Lyα absorbers. The quasars are separated by $1\rlap{.}'65$ on the sky corresponding to a proper separation of $412\,h^{-1}$ kpc at $z = 1.83$ (where $h \equiv H_0/100$ km s^{-1} Mpc^{-1}; $q_0 = 0.5$). We detected five Lyα absorption lines common to both spectra within a velocity difference of 400 km s^{-1} in the redshift range $1.1 < z < 1.7$, and 20 lines which are seen in the spectrum of one quasar but not the other. The number of coincidences expected for randomly distributed absorbers in this redshift interval is 3.2 ± 1.2, implying a less than 2σ significance for the observed coincidences. If none of the observed coincidences are real, then we can place an upper limit on the cloud radii with 95% confidence of $\sim 280\,h^{-1}$ kpc for redshifts $1.1 < z < 1.7$. If, on the other hand, all of the observed coincidences are real, then a maximum likelihood estimate of the characteristic cloud radii in the context of identical, spherical clouds give a most probable radius of $380\,h^{-1}$ kpc with 95% confidence that the characteristic radius lies in the range $305 < R < 590\,h^{-1}$ kpc. Taken together with a low redshift estimate and new ground-based estimates, the upper limit on the cloud size provides tantalizing evidence for evolution in the radius of the Lyα clouds with cosmic time, in the sense that the characteristic size of the Lyα absorbers increases with decreasing redshift.

6.1 Introduction

The Lyα forest absorption lines, observed in the spectra of all quasars at wavelengths shortward of the emission redshift of the quasar, have important implications for cosmology since they may be used to trace the formation and evolution of structure from $z \simeq 5$ to the present (Cen *et al.* 1994). Recent studies of the Lyα clouds have changed our perception of their origin and physical characteristics considerably. At low redshifts, Lanzetta *et al.* (1995) have found that 35% and perhaps as many as 65% of intermediate column-density (log N(HI) $\gtrsim$ 14) Lyα absorption systems arise in the extended envelopes of bright galaxies, whereas low column-density clouds have been found in or near voids in the galaxy distribution (Morris *et al.* 1993; Stocke *et al.* 1995). Very high resolution observations taken with the Keck telescope imply significant metal enrichment of the clouds (Tytler *et al.* 1995; Cowie *et al.* 1995), and there is growing evidence for clustering of the high-column density clouds, though not as strongly or on the same scale as luminous galaxies (Chernomordik 1995; Christiani *et al.* 1995). Finally, observations of a quasar pair with the *Hubble Space Telescope* have lead to a picture of absorbing clouds at $z \simeq 0.5$ that are larger in extent than previously thought, and surprisingly quiescent (Dinshaw *et al.* 1995; hereafter D95). Recent N-body + hydrodynamic simulations produce, as a natural extention of a hierarchical clustering, Lyα forest structures in the form of sheets and filaments with coherence lengths as great as 1 Mpc (Cen *et al.* 1994; Zhang, Anninos & Norman 1995; Hernquist *et al.* 1996; Miralde-Escudé *et al.* 1996).

Lines of sight to quasar pairs provide a powerful diagnostic of cloud sizes and kinematics as derived from the number of Lyα systems observed to be in common between the two LOSs and the velocity difference between the common systems. In this chapter, we use the quasar pair, LB 9605 and LB 9612, to set limits on the sizes of the Lyα absorption clouds in the critical redshift interval $1.1 < z < 1.7$, lying between a low-redshift *HST* measurement (D95) and two recent ground-based estimates (Dinshaw *et al.* 1994, hereafter D94; Bechtold *et al.* 1994). This pair belongs to a group of four quasars pro-

jected within 2″8 on the sky. LB 9605 and LB 9612 have redshifts $z_{em} = 1.834$ and 1.898, respectively, and are separated by 1″65 on the sky, corresponding to a proper separation of $412\,h^{-1}$ kpc at $z = 1.83$. Spectra of all four quasars in the group were recently analyzed by Elowitz, Green & Impey (1994) for clustering of the Lyα absorbers on scales ranging from $400\,h^{-1}$ kpc out to $30\,h^{-1}$ Mpc. No evidence was found for a correlation of the Lyα clouds on the scales of clusters or superclusters, implying the absorbers are smaller in extent than those structures. The LB pair is particularly important for further study since there are currently no firm upper limits on the sizes of the Lyα clouds.

The observations and reductions are described in § 6.2, and the methods used to select and identify the absorption lines are discussed in § 6.3. In § 6.4, we place constraints on the sizes of the Lyα clouds, and finally, in § 6.5, we summarize and discuss our main results. Throughout this chapter, we express all dimensions in terms of the dimensionless Hubble constant $h \equiv H_0/(100$ km s^{-1} Mpc^{-1}) assuming a deceleration parameter of $q_0 = 0.5$.

6.2 Observations and Reductions

LB 9605 was observed on 1995 January 25 and LB 9612 on 1994 December 9 with the Faint Object Spectrograph (FOS) on the reburbished *Hubble Space Telescope* (*HST*). The observations were taken through the 1″ circular aperture with the red Digicon and G270H grating, and covered the wavelength range $2225 - 3275$ Å. The reciprocal dispersion of the G270H grating is 0.5 Å pixel^{-1}, corresponding to a spectral resolution of 2.0 Å (FWHM). The same guide stars were used in order to minimize radial pointing errors arising from relative placements of the quasars in the aperture. A total of 140 minutes integration time was accumulated on LB 9605 and 49 minutes on LB 9612. Table 6.1 lists the J2000 coordinates, apparent visual magnitudes and emission redshifts of the program quasars. The coordinates were obtained from the Space Telescope Science Institute using its Guide Star Selection Systems Astrometric Support Package (GASP) and should be accurate to about 1″.

The spectra were reduced via the STSDAS pipeline processing facility, using post-COSTAR "superflats" (Lindler *et al.* 1993) and inverse sensitivity files. In order to minimize the uncertainty in the wavelength calibration due to nonrepeatability in the positioning of the filter-grating wheel, we recalibrated the data using one exposure of a PtCrNe comparison lamp obtained at the same time as one exposure of each target. The filter-grating wheel was not moved between the target and lamp exposures. The rms error in the wavelength calibration is 0.14 Å. A zero-point offset between the spectra was calculated from the numerous Galactic absorption features observed with the G270H grating (described below).

Figures 6.1 and 6.2 shows the flux-calibrated spectra of LB 9605 and LB 9612, respectively, and the 1σ uncertainty in the flux. The emission lines near 2900 Å in LB 9605 and 3000 Å in LB 9612 are blends of Lyβ + Ovi $\lambda\lambda1031, 1037$. The spectrum of LB 9612 exhibits a strong Lyman-limit system (LLS) at $z_{\rm LLS} \simeq 1.7259$ (which we discuss in more detail in § 6.3). The continuum of each spectrum was determined by fitting cubic splines to binned datapoints that did not reside inside absorption features. We used the interactive program written by T. Aldcroft (Aldcroft 1993) for this procedure, as well as to select and measure the lines (see § 6.3). The continua of LB 9605 and LB 9612 are shown as dotted curves in Figures 6.1 and 6.2. Because of the difficultly in simultaneously obtaining a good fit over the entire spectrum, some manual adjustments in the continuum were made within heavily blended regions, in the emission line profiles and in the LLS of LB 9612.

Observations of the quasars with the G190H grating were also obtained, but are not presented here because the LLS in the spectrum of LB 9612 removes most of the flux below 2500 Å, rendering the data unsuitable for the purpose of this chapter.
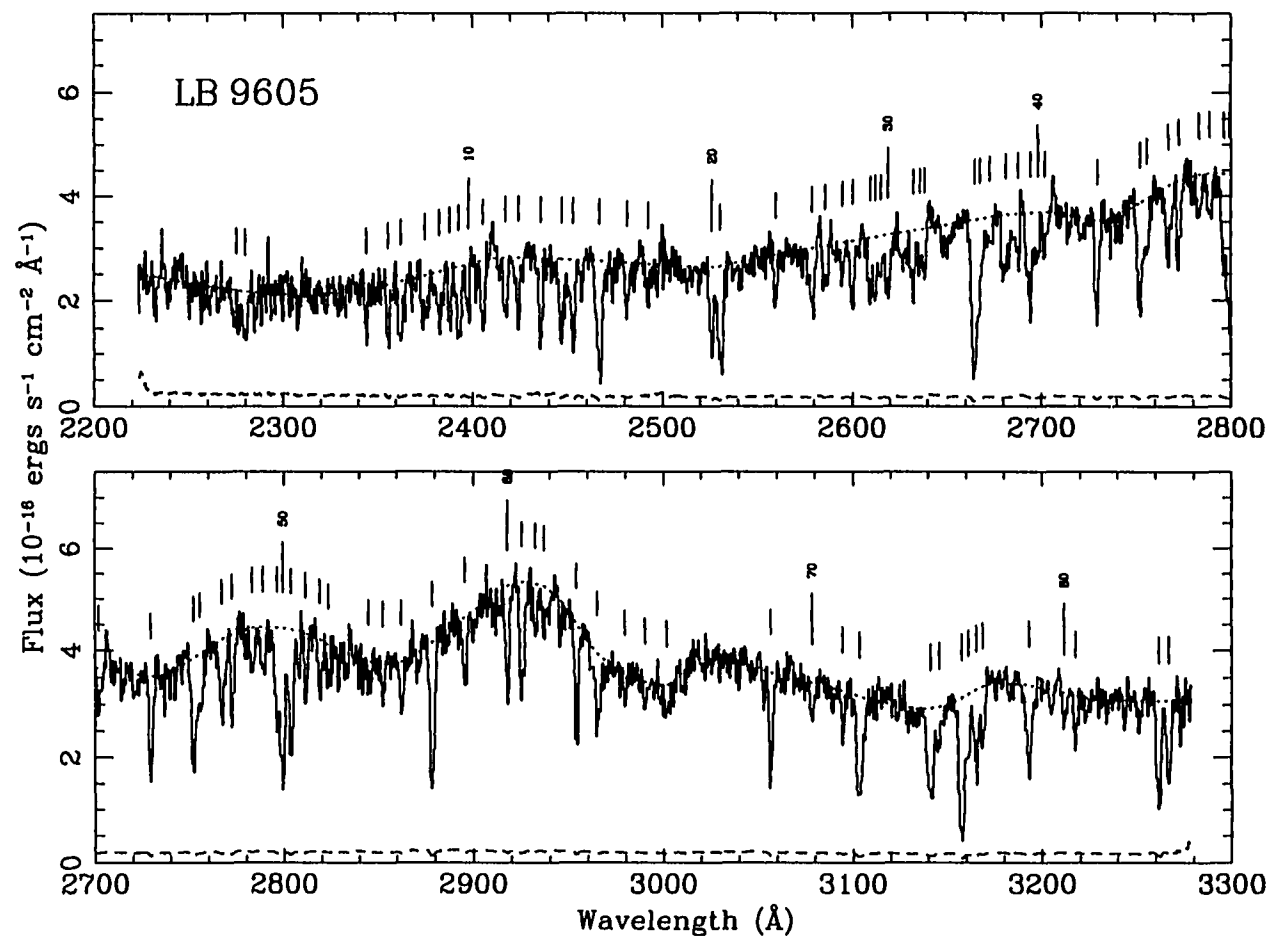
FIGURE 6.1—*HST* FOS spectrum of LB 9605 as a function of vacuum wavelength. The dashed line in each panel is the 1-σ error in the flux. The dotted line is the continuum fit. Tickmarks indicate absorption features detected at the 3.5σ or greater confidence level. The emission feature near 2900 Å is Lymanβ + Ovi $\lambda\lambda$1031, 1037.
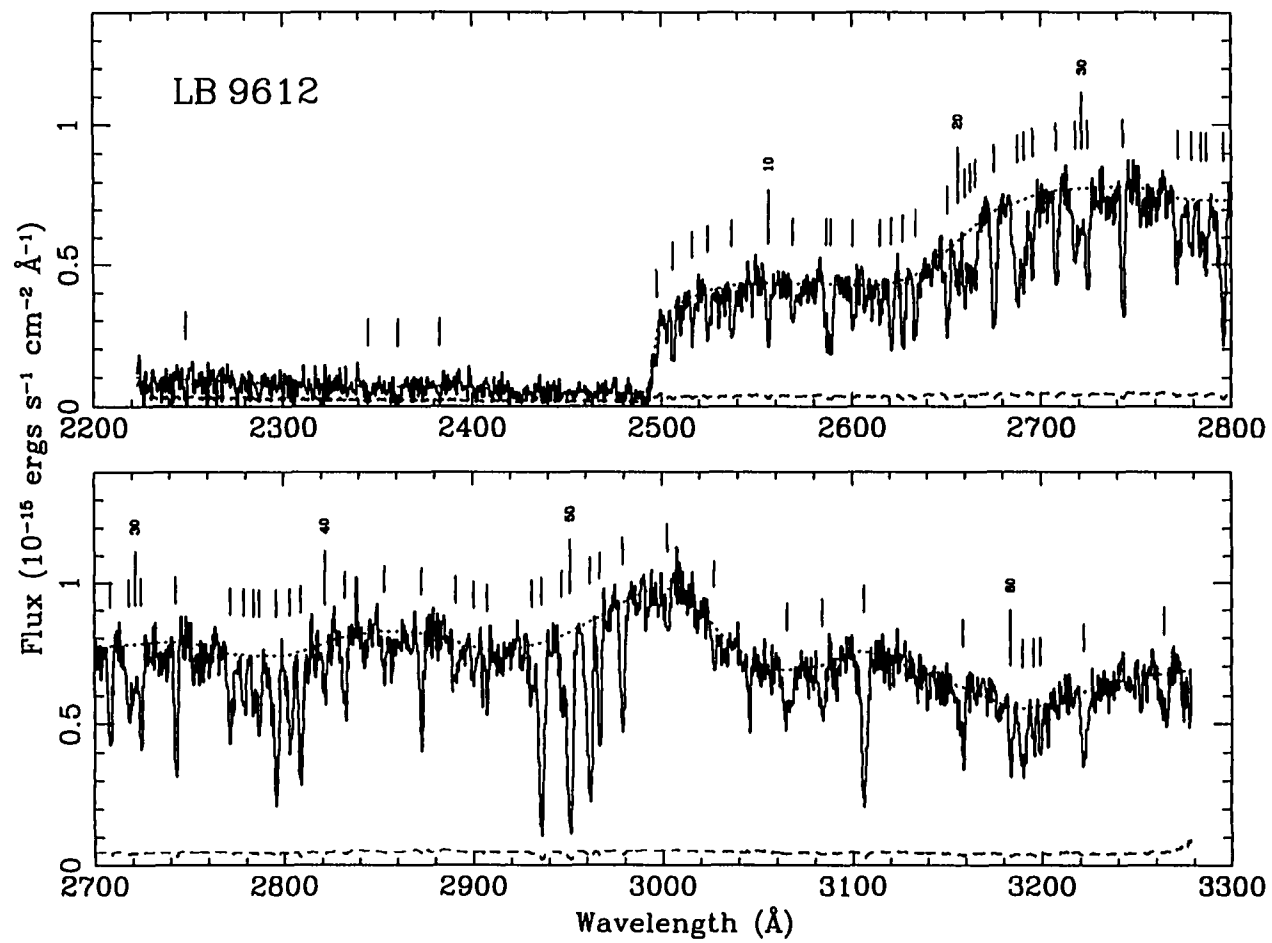
FIGURE 6.2—Same as Figure 6.1 for LB 9612. The emission feature near 3000 Å is Lymanβ + Ovi $\lambda\lambda1031,1037$.

6.3   Line Selection and Identification

A detailed description of the line selection and identification procedures is presented in a separate paper (Dinshaw *et al.* 1996); we provide only a brief description here. The spectra were divided by their respective continuum fits, and the normalized spectra searched for significant lines using the method of optimal extraction used for the *HST* Quasar Absorption Line Key Project data and described by Schneider *et al.* (1993). An interactive fit was performed with single, or in the case of obvious blends, multiple Gaussians unconstrained in FWHM, equivalent width and central wavelength to all the candidate absorption features. Preliminary lists of the absorption features detected at or above the 3.5σ confidence level in LB 9605 and LB 9612 are presented in Tables 2 and 3, and the lines in the tables are marked by ticks in Figures 6.1 and 6.2, respectively. The quoted confidence levels represent the signal-to-noise ratio (SNR) of the lines defined as $SNR = W/\sigma(W)$ where W is the equivalent width and $\sigma(W)$ the 1σ uncertainty in the measured W. [This is to be distinguished from the significance level SL used by the Key Project and defined in Schneider *et al.* (1993)]. The 3.5σ line lists were constructed solely for the purpose of identifying the lines, and are by no means complete, in the sense that they may include spurious lines or miss real lines. Only those lines at or above the 5σ confidence level are considered secure.

The instrumental resolution for the configuration used to obtain the data is listed in the FOS Instrument Handbook (Version 6.0 June 1995) as being 2.0 Å. We found, however, that about 25% of the lines have line widths smaller than the FWHM of the instrumental line spread function (LSF). This could arise from a variety of factors including noise and fitting the continuum too low. The approach of the Key Project in these situations is to fit the narrow lines again with the FWHM fixed at the instrumental LSF. A consequence of this approach to our analysis having defined the significance of a line by its SNR is that the SNR of many of the weaker lines are overestimated, some by as much as 50%, because the uncertainty in the measurement of the equivalent is artifically smaller having

removed one degree of freedom in the fit. In order to find a more acceptable solution, we plotted a histogram of the FWHMs of all the lines. The histogram shows a smooth distribution of FWHMs with a peak at 2.2 Å and a sharp break in the number of lines with FWHM less than 1.6 Å. Assuming that many of the lines with FWHM < 1.6 Å are likely spurious, we included in Tables 1 and 2 only those lines with FWHM $\geq$ 1.6 Å. At most, this excluded 8 lines from the linelist of LB 9605 and 6 lines from that of LB 9612. By allowing the FWHM to vary during the line fitting, we have ensured that we have not overestimated the significance of the line with FWHM < 2.0 Å, such that it could appear in our 5σ line list (defined below), but we note that the equivalent widths of those lines are likely underestimated.

The identification of the lines was problematic due to the limited spectral range and significant level of crowding in our data. To minimize the uncertainty in the line identifications, we extended the wavelength coverage of the data out to the Lyα emission using the spectra published by E95). However, the wavelength calibration of the ground-based data is poor, so some of the identifications remain uncertain, as indicated in the footnotes in Tables 1 and 2. We have followed closely the approach implemented in the Key Project program *ZSEARCH* (Bahcall *et al.* 1996) for identifying the lines, with two exceptions: we carried out the identifications manually, and we used a subset of 53 strong ultraviolet absorption lines from Morton, York & Jenkins (1988). We first searched the spectra for plausible Galactic interstellar lines. Then, we looked for Lyβ lines that corresponded to the Lyα systems identified by E95, before searching for new systems. Starting from the red ends of the FOS spectra, we treated each significant absorption line as a candidate Lyα line and searched for higher order Lyman series lines corresponding to that system. Once we identified a system, we checked that relative equivalent widths of the lines in a system were consistent with their known oscillator strengths. Finally, the spectra were scanned for doublets of C IV $\lambda\lambda$1548, 1550, Si IV $\lambda\lambda$1393, 1402, N V $\lambda\lambda$1238, 1242, and O VI $\lambda\lambda$1031, 1037, and features associated with those systems. We found 15 Lyα absorp-

tion systems in both LB 9605 and LB 9612 with $W_0 > 0.32$ Å, consistent with the expected number ($\sim 16 \pm 4$) given the number density of Lyα lines per unit redshift determined from the Quasar Absorption Line Key Project (Bahcall *et al.* 1993), which lends some confidence to our line identifications.

We identified one LLS in the spectrum of LB 9612; the higher Lyman series lines Lyβ through Lyη associated with this system are present in the spectrum. From these lines, we derive a redshift of $z_{LLS} = 1.7259 \pm 0.0001$ for the LLS. The optical depth of the LLS was estimated from the ratio of the fluxes shortward F_- and longward F_+ of the LLS:

$$\exp(-\tau_{LLS}) \equiv \frac{F_-}{F_+}. \tag{6.1}$$

F_+ was estimated by fitting the continuum between 2550 Å and 2600 Å assuming constant flux, and F_- was determined in the wavelength region from 2350 Å to 2500 Å. Dividing the flux in the continuum from the flux estimated in the LLS, we obtain an optical depth of $\tau_{LLS} = 2.00 \pm 0.07$. This corresponds to an H I column density of $\log N(\text{HI}) = 17.50 \pm 0.02$. The uncertainty was estimated by varying the locations and widths of the fitting windows.

To avoid introducing spurious absorption lines into the analysis, we considered for further study only those lines detected at or above 5σ confidence level. Because the S/N degrades rapidly shortward of the LLS, we also restricted our sample to lines with wavelengths greater than 2500 Å. In this way, we can be sure that in the range $2500 - 3270$ Å, all lines with $W_0 > 0.32$Å are detected with 5σ confidence in *both* objects. Figure 6.3 shows the observed equivalent width threshold (5σ) for an unresolved line as a function of wavelength for LB 9605 (solid line) and LB 9612 (dashed line). Lines meeting both criteria are listed in Table 4. We note that this is identical to the way in which lines were selected for Q0107–025A,B (D95), so that we can make a direct comparison with those observations.

In Table 4, we have also culled out all Galactic absorption lines and higher order Lyman series lines. Since absorption line systems containing metal lines may have different properties than the Lyα-only lines, we selected only those lines that we believe are not
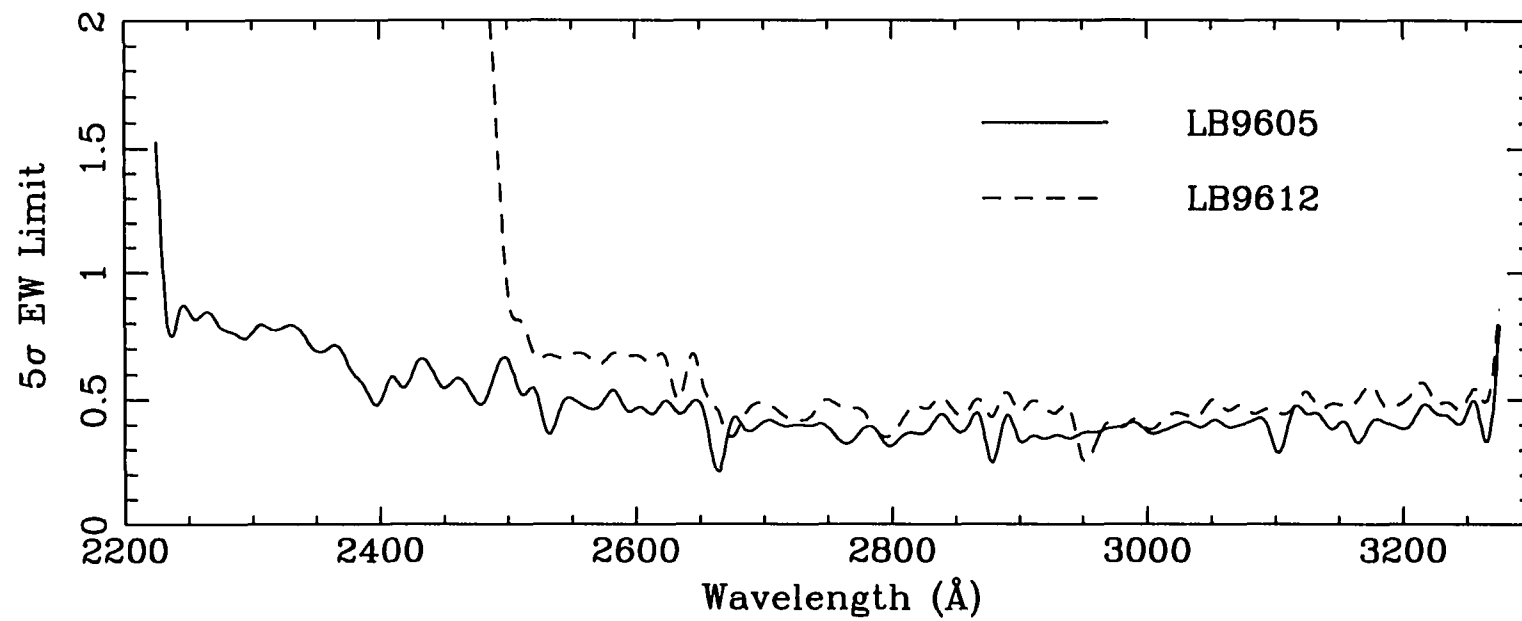
FIGURE 6.3—Equivalent width thresholds (5σ) for an unresolved line as a function of wavelength for LB 9605 (*solid line*) and LB 9612 (*dashed line*).

members of metal-line containing systems. E95 found no metal-line systems in LB 9605, and one C IV doublet in LB 9612 at z_{abs} = 1.4146. Their ground-based data has a 3σ limiting equivalent width of 0.6 − 0.7 Å over the observed wavelength range 3220 − 5500 Å.

There are numerous Galactic absorption features in the wavelength range covered by the G270H grating: Fe II $\lambda 2344$, $\lambda 2374$, $\lambda 2382$, $\lambda 2586$, $\lambda 2600$, Mg II $\lambda\lambda 2796$, 2803, and Mg I $\lambda 2853$. Using only the Galactic feature found outside the LLS, we measured the zero-point shift between the spectra of LB 9605 and LB 9612 to be -26 ± 6 km s^{-1}. In Table 4, we have shifted the lines of LB 9612 to the blue by 26 km s^{-1} to register them with the lines of LB 9605.

6.4 Limits on the Sizes of the Lyman-Alpha Clouds

The goal of this chapter is to put new constraints on the size of Lyα absorbers at the intermediate redshifts $1.1 < z < 1.7$. This is not a trivial task at these redshifts because of the high density of lines, which make the assignment of common systems difficult. In D94 and D95, we defined a Lyα absorption feature to be common, or coincident, if there was a corresponding line in the other spectrum within a velocity difference of ± 150 km s^{-1}. Similarly, we designated a system to be *not* in common, or anticoincident, if there was no corresponding match within the same velocity difference. In all cases, the assignments of coincident and anticoincident systems were unambiguous, in the sense that the histogram of velocity pairs peaked in the range ± 150 km s^{-1}, with no more pairs out to several thousand km s^{-1}. On the other hand, the pairwise velocity histogram of the Lyα lines in LB 9605 and LB 9612 shows no clear peak (see below). In order to establish the optimum window in which to define coincident and anticoincident pairs, we compare in Figure 6.4a the cumulative velocity difference distribution of the Lyα absorption systems in Table 4, with the distribution expected for randomly-placed absorbers. The velocity differences were computed between each line in LB 9605 and its nearest neighbor in LB 9612, such that every line belonged to one, and only one, pair.
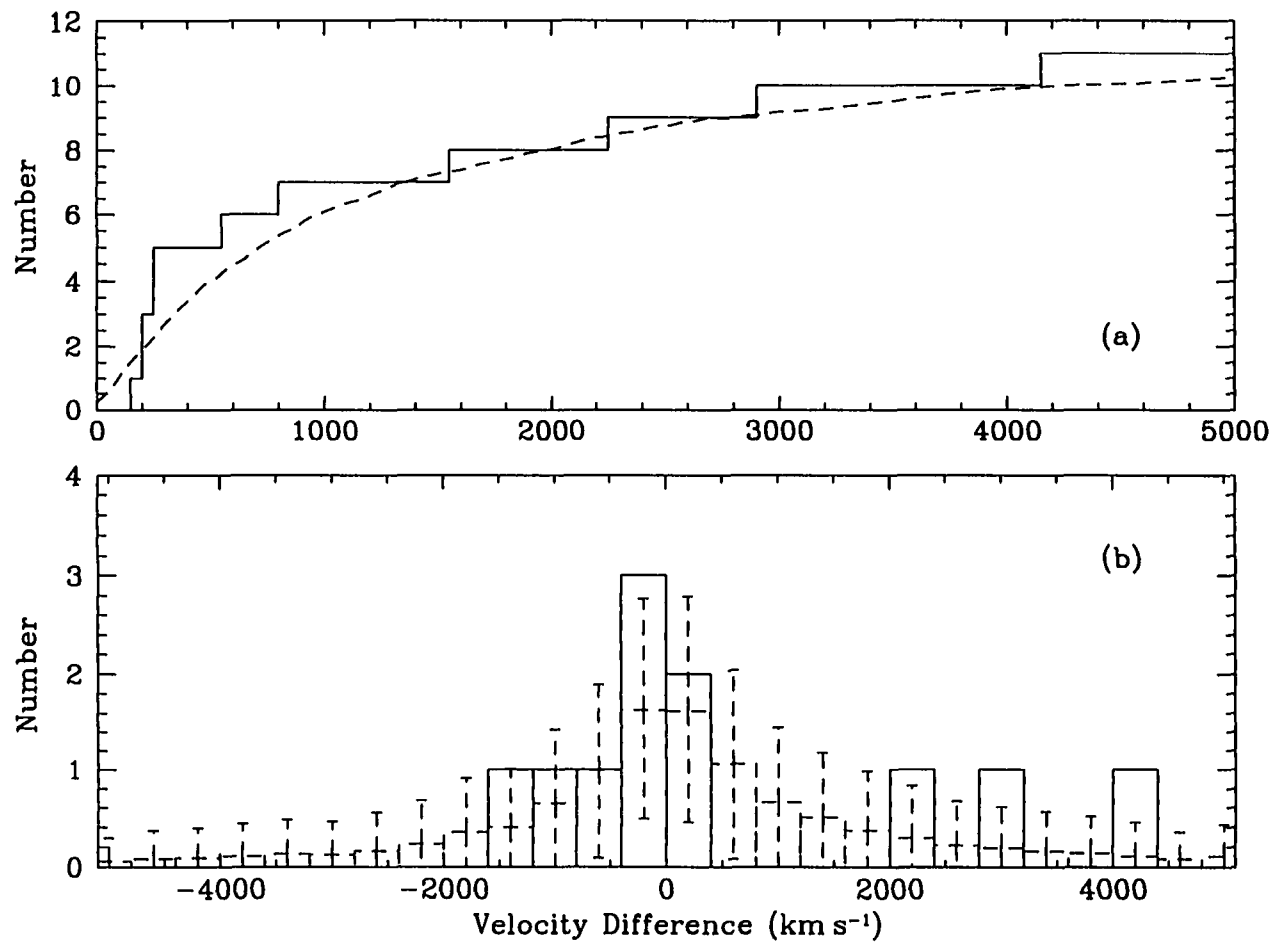
FIGURE 6.4—(a) Cumulative distribution of observed (*solid line*) and random (*dashed line*) velocity differences between each line in one line of sight and its nearest neighbor in the other line of sight. (b) Distribution of observed (*solid line*) and random (*dashed line*) velocity differences in 400 km s^{-1} bins.

The expected distribution was estimated from 1000 samples of 15 systems per LOS drawn randomly from the same redshift intervals as the observations. These intervals do not correspond to the entire spectral coverage of the data since, shortward of 2900 Å, Lyα lines (with $W_0 > 0.32$ Å) could not have been detected because of crowding from Lyβ and Galactic absorption lines. Therefore, in calculating the number of random coincidences, we did not allow lines to fall where Lyα lines were not detected, namely, 2550 − 2650 Å and 2700 − 2900 Å in LB 9605, and 2520 − 2620 Å and 2750 − 2900 Å in LB 9612.

Figure 6.4a shows that if we restrict the size of the velocity window in which we define a coincidence to be too small, we minimize the number of random coincidences, N_r, but we may also exclude some real coincidences. For example, for $\Delta v = 150$ km s^{-1}, which corresponds to the velocity separations in which common systems were observed in other quasar pairs (cf. D94 and D95), we find no coincident systems, with the result that we can only quote an upper limit on the sizes of clouds. Alternatively, if we expand the velocity window in which we define a coincidence, we can be more confident that we are counting all the common systems, but we are also more likely to include random coincidences. In fact, for $\Delta v = 1500$ km s^{-1} which corresponds to the velocity dispersions of the largest structures observed at $z < 2$ (e.g., rich clusters of galaxies [Zabludoff et al. 1993]), we see 6 pairs and expect 7.3 ± 1.6, consistent with no real coincidences, and once again we obtain only an upper limit on the absorber size. From Figure 6.4a, the intermediate Δv that maximizes the number of coincident systems above the number of random coincidences is roughly 400 km s^{-1}.

The histograms of observed and expected velocity pairs in bins of $\Delta v = 400$ km s^{-1} are shown in Figure 6.4b. The distribution of velocity differences shows 5 pairs in the velocity range $-400 < \Delta v < 400$ km s^{-1}, and pairs at $\Delta v \simeq -550$, -845, and -1586 km s^{-1}. We note one ambiguity in the assignment of a coincidence. Line 15 in LB 9612 could have been matched with either line 14 ($\Delta v = -220$ km s^{-1}) or 15 ($\Delta v = 260$ km s^{-1}) in LB 9605. The former match was selected because it has a smaller velocity separation; if we were to

have paired the systems according to D94, such that their equivalent widths were more closely matched, then we would have called lines 15 in both quasars coincidences. In total, there are 5 possible coincidences between the two spectra within a velocity difference of $|\Delta v| < 400$ km s^{-1}, and 20 anticoincidences. The number of random coincidences expected in that interval is $N_r = 3.2 \pm 1.2$. Therefore, the coincidences observed toward the paired LOS to LB 9605 and LB 9612 are of marginal significance, $< 2\sigma$, especially given the *a posteriori* selection of an optimum Δv matching window.

In addition to the high probability of random coincidences, there are two uncertain line identifications that could affect the coincident count. Lines 14 and 15 in LB 9605 and line 8 in LB 9612 can be identified as members of C IV doublets at $z_{abs} \simeq 0.91$ and 1.11, respectively. The redshift agreement between the components of the doublets is excellent (< 0.0002). Two of the lines have been identified as belonging to certain Lyα systems and were accordingly identified following the priorities of the Key Project identification procedure. If these are shown to be C IV, then the number of coincidences drops to three, which is consistent with the a number of expected coincidences for randomly distributed absorbers.

The maximum significance we obtain for an excess number of common pairs above that expected for randomly placed absorbers is $\sim 2\sigma$. This implies that in most cases a single cloud does not intercept both LOS and the clouds are small compared to the LOS separation. Under this hypothesis, the equivalent widths of the coincident pairs should be uncorrelated (Charlton *et al.* 1995). Figure 6.5 shows the correlation between the rest equivalent widths of the common systems in LB 9605 and LB 9612. Out of the five apparent coincidences, three have equivalent widths that agree with one another to within their respective errors. Using the observed equivalent width distribution of Lyα lines determined by the Key Project (Bahcall *et al.* 1993), we find that the probability of obtaining three pairs whose equivalent widths lie within the quoted errors is not negligible $\sim 0.8\%$. However, recall the ambiguity in the pairing of the lines: although line 15 in

LB 9612 was matched with line 14 in LB 9605, it equally well could have been matched with line 15 in LB 9605. In this latter case, we find there are four coincidences with similar equivalent widths, and the probability drops to 0.1%, indicating that the coincidences may not arise randomly.

For this reason, our attempt to establish a cloud size at these redshifts remains insecure, and we consider three possibilities: (1) all the coincidences are real; (2) two of the coincidences are real (after correcting the 5 observed coincidences for 3 random coincidences); and (3) none of the observed coincidences are real. We calculated the characteristic radius using the maximum likelihood method outlined in Dinshaw *et al.* (1996), which is based on the counts of coincidences, N_C, and anticoincidences, N_A. In the following analysis, we assume the common Lyα lines arise in single coherent clouds, and that the clouds are spherical and uniform in size. In this way, we may define the cloud radius R as the impact parameter that give rise to lines with rest equivalent widths greater than or equal to our rest equivalent width detection limit. If however, the structures are small "cloudlets" that are spatially clustered, then our limits are more indicative of correlation lengths. More data are required to establish with confidence which of these two models apply.

Figure 6.6 shows the probability distribution, $\mathcal{P}(R)$, as a function of cloud radius for the three cases considered above: (1) If we consider all of the coincidences to be real, then $N_C = 5$ and $N_A = 20$, and the most probable radius of the clouds is $380\,h^{-1}$ kpc. The cumulative probability distribution, also plotted in Figure 6.6 indicates with 95% confidence that the radius falls in the range $305 < R < 590\,h^{-1}$ kpc. (2) If we subtract the number of expected pairs ($N_r = 3$) from the total coincident count, such that $N_C = 2$, $N_A = 26$, then we obtain a smaller characteristic radii of $275\,h^{-1}$ kpc with 95% confidence lower and upper limits of $240 < R < 385\,h^{-1}$ kpc. (3) Finally, if none of observed coincidences are real, then we derive 95% confidence upper limits on the cloud radius of $R = 280\,h^{-1}$ kpc.
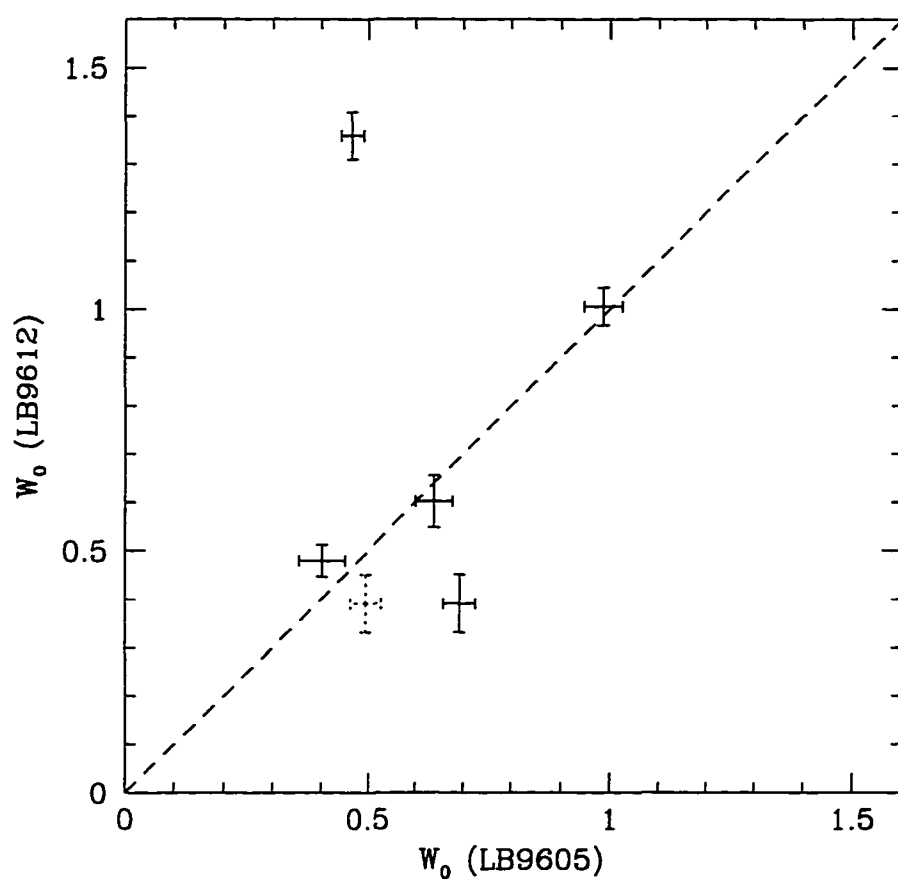
FIGURE 6.5—Correlation between the rest equivalent widths of the common lines in LB 9605 and LB 9612. The dotted error bars represent the alternate matching between lines 15 in both LB 9605 and LB 9612. The dashed line has unit slope.
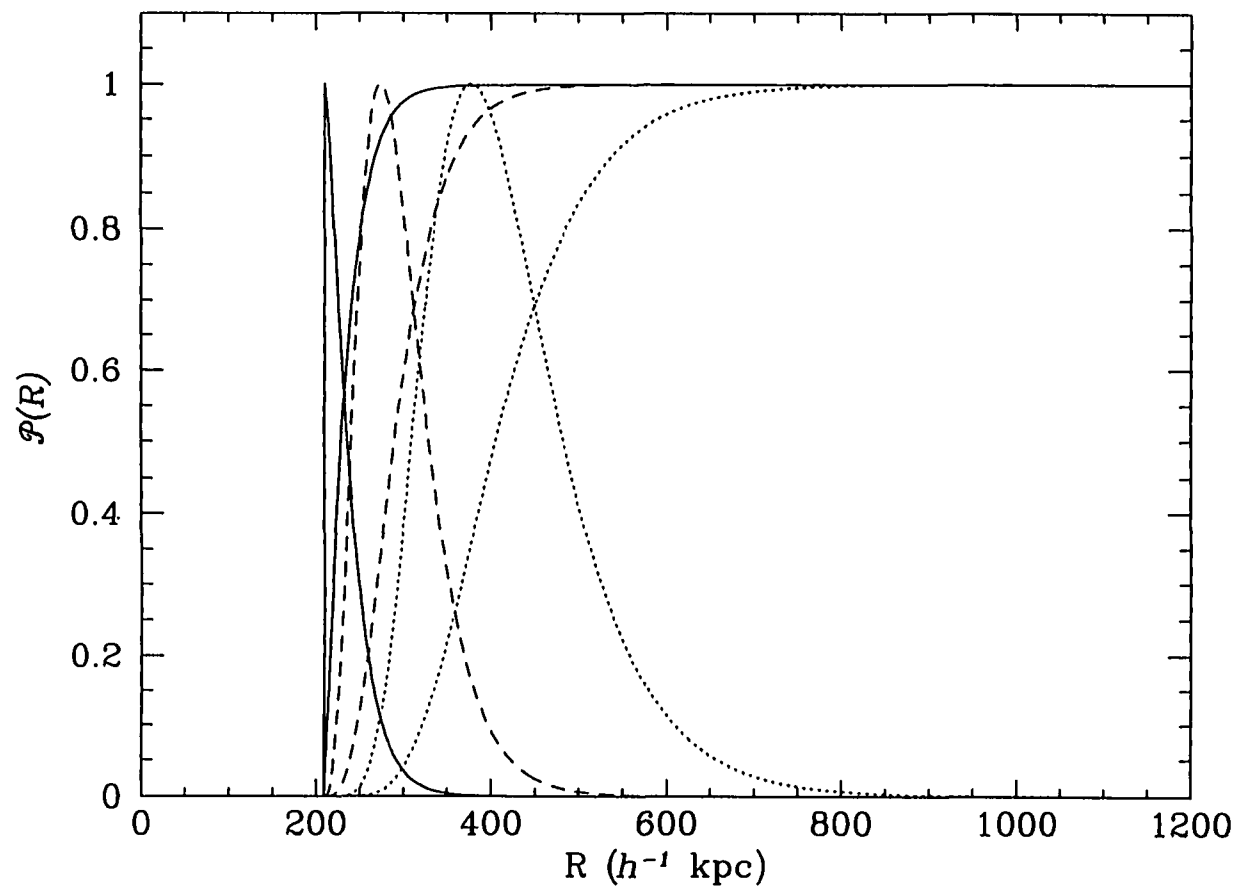
FIGURE 6.6—Probability distribution $\mathcal{P}(R)$, normalized to unity at its peak, as a function of cloud radius for three cases: (1) Five coincident and 20 anticoincident lines (*dotted curve*); The cumulative probability distribution (*monotonically increasing dotted line*) is also plotted from which lower and upper limits on the radius of the absorbers can be estimated. (2) Two coincidences and 26 anticoincidences (*dashed curves*). (3) The upper limit in the radius of the clouds if none of the coincidences are real (*solid curve*).

In the above analysis, we have not used any of the information contained in the equivalent widths of the lines. The high degree of correlation between the equivalent widths of the common pairs and the low probability of this occuring randomly suggests the Lyα clouds must be considerably larger than the radius derived above assuming all coincidences are real, perhaps by as much as a factor of 10 − 100 (Charlton *et al.* 1995). Moreover, the clouds must have remarkably smooth column density distributions on scales of several hundred kpc. Previous studies have found that even on scales as small as $40\,h^{-1}$ kpc out to scales of $330\,h^{-1}$ kpc, the equivalent widths show significant deviations from the correlation line (D94; Fang *et al.* 1996; Dinshaw *et al.* 1996). Another argument against all the coincidences being real is based on the velocity differences of the common systems. Lanzetta *et al.* (1993) has found the redshift agreement between coincident galaxies and Lyα absorption systems to be $\Delta v < 250\,\mathrm{km\ s^{-1}}$. Similarly, the hydrodynamical simulations show the peculiar motions of the Lyα structures to be typically less than $150\,\mathrm{km\ s^{-1}}$ (Miralda-Escudé *et al.* 1996), so our use of $400\,\mathrm{km\ s^{-1}}$ likely overestimates the number of real coincidences. For these reasons, we favor the interpretation that none of the coincidences are real (case 3) which gives an upper limit on the cloud radius of $280h^{-1}$ kpc, but we cannot rule out larger clouds that are are remarkably smooth on scales of the LOS separation of the quasar pair. Nor can we reject a model involving a distribution of cloud sizes. The high level of correlation in the equivalent widths for the observed coincidences, which make up $\lesssim 20\%$ of the total sample, could be explained if there is a rare population of large, homogeneous clouds in addition to a population of small clouds which dominates the counts (but see § 6.5). We have been reluctant to introduce any more parameters into the analysis at this time given the limited data sample.

Differences in equivalent widths and relative velocities of the common systems provide information about the homogeneity and internal kinematics of the clouds since the quasar LOS pierce the Lyα absorbers at different locations. From studies of gravitationally-lensed quasars whose characteristic pathlength separations at the redshift of the ab-

sorbers are a few kpc, the clouds are homogeneous and their internal motions are small, $<$ $10-20$ km s^{-1} (Smette *et al.* 1992, 1995; Bechtold & Yee 1996). In D94, we presented evidence for significant inhomogeneities in the clouds, as well as a marginally significant rms velocity difference of 65 km s^{-1} from observations of the physical pair Q1343+2640A,B with separation $\sim 40h^{-1}$ kpc. From the common lines of Q0107−025A,B, we found a statistically significant velocity difference of ~ 100 km s^{-1} over scales of several hundred kpc, implying that the clouds are still remarkably quiescent on these scales. The rms velocity difference, $\Delta v_{\rm rms} \simeq 260$ km s^{-1}, of the five apparently coincident lines in the spectra of LB 9605 and LB 9612 also exceeds the typical velocity error, but interpretation of this result is hampered by our uncertainty over how many, if any, of the coincidences are real.

6.5 Summary and Discussion

Recent ground-based observations of a high-redshift quasar pair Q1343+2640 A ($z_{\rm em} = 2.029$) and B ($z_{\rm em} = 2.031$), interpreted in terms of the same simple-minded model assumed above (*i.e.*, identical, spherical absorbers) suggest a characteristic radius of the clouds of $125\,h^{-1}$ kpc, with 95% lower and upper bounds of $80 < R < 610\,h^{-1}$ kpc at $z \simeq 2$ (D94; see also Bechtold *et al.* 1994 and Fang *et al.* 1996). Observations of a lower redshift pair Q0107−025A ($z_{\rm em} = 0.956$) and B ($z_{\rm em} = 0.952$) in the redshift range $0.5 \leq z \leq 0.9$, imply lower limits on the transverse radius of the clouds of $140\,h^{-1}$ to $160\,h^{-1}$ kpc. Maximum likelihood estimates of the characteristic radii for spherical clouds, give a most probable radius of $440\,h^{-1}$ kpc with 95% confidence that the characteristic radius lies in the range $300 < R < 1340\,h^{-1}$ kpc. (We point out that the radii quoted here are different from those given in D94 and D95 because of an error in our derivation of the probability of obtaining a coincidence [see Dinshaw *et al.* 1996 for details].)

We note that the characteristic radius estimated from the data of Q1343+2640A,B was

obtained using all the 5σ lines with no rest equivalent width detection limit imposed. In contrast, in our analysis of the data in this chapter and of Q0107−025A,B, we considered only the region of the spectrum where all 5σ lines with $W_0 > 0.32$ Å would be detected. In order to compare the cloud radii inferred from Q1343+2640A,B, Q0107−025A,B and the results presented in this chapter, we must make the samples uniform. If we impose the same detection criteria on the Q1343+2640A,B data, then we must discard all lines in Table 1 of D94 with $\lambda < 3525$ Å and $W_0 \leq 0.32$ Å. This has the effect of cutting the number of lines in the new sample by more than a factor of two. The new sample contains 2 coincidences and 4 anticoincidences, from which we derive a most probable radius of $50\,h^{-1}$ kpc, with 95% confidence limits of $30 < R < 230\,h^{-1}$ kpc. B94 have also looked at this pair. Imposing the same detection criteria on their linelist (Crotts et al. 1994; Table 1) and discarding the spectrum $\lambda < 3500$ Å, 3 coincidences and 2 anticoincidences remain. The radius implied by this sample is $100\,h^{-1}$ kpc, with 95% lower and upper bounds of $60 < R < 2620\,h^{-1}$ kpc. The difference in the number of coincidences and anticoincidences is *entirely* due to the different spectral resolutions of the data. One of the coincidences in the B94 data appears to be a blend of two coincidences in our higher resolution data, with one of the lines in each pair falling below the equivalent width limit (cf. line pair B16-A9 in Crotts et al. (1994) and pairs A7-B4 and A8-B5 in D94). This discussion serves to highlight some of the pitfalls of this kind of analysis, particularly when dealing with such small numbers of lines.

Figure 6.7 shows the estimated radius of the Lyα clouds in three redshift regimes, where the value of the radius estimated by D94 for the pair Q1343+2640A,B has been plotted since it is consistent with the radii derived above, but has smaller error bars. These observations span a large redshift range $0.5 < z < 2.1$, corresponding to roughly a third of the age of the universe, and imply evolution in the radius of the Lyα clouds from $\sim 100\,h^{-1}$ kpc at $z \simeq 2$ to $\sim 450\,h^{-1}$ kpc at $z \simeq 0.7$. There are two other estimates of the clouds radius at $z \sim 2$ published in Fang et al. (1996). However, it may be misleading to

plot these estimates in Figure 6.7 because those radii were calculated assuming a cutoff rest equivalent width of $W_0 > 0.40$ Å (compared to the value $W_0 > 0.32$ Å used in this chapter), and there is evidence for a correlation of cloud radius with column density, with the high column density clouds being larger in extent than the low column density clouds (Dinshaw et al. 1996). If $q_0 = 0$, the apparent evolution in clouds radius is less pronounced.

An alternative interpretation for this trend is given in Fang et al. (1996). They note that the characteristic radii inferred from quasar pairs depend on the LOS separations, in the sense that pairs with larger proper separation give larger cloud radii. This can be explained if there is a distribution of cloud sizes, or the clouds are clustered. In the first case, a population of small clouds will produce a higher incidence of anticoincidences for both closely separated pairs as well as widely separated pairs resulting in a smaller inferred radius. However, as long as there is a population of large clouds with transverse sizes greater than the LOS separation, the lower limit of the cloud size cannot be less than the transverse separation of the pair. Therefore, estimates based on observations of widely separated pairs will be biased toward larger cloud radii. A similar bias holds for clouds that are correlated over a range of scales.

In Figure 6.8, we have reproduced Fang et al.'s Figure 5 which shows the apparent trend in inferred cloud radius with pair separation. The radii were estimated for six pairs with angular separations ranging from $\sim 10''$ to $3'$. In order to obtain a uniform sample only those lines with rest equivalent widths $W_0 > 0.40$ Å were used. Coincidences were defined within a velocity difference of $\Delta v < 150$ km s^{-1}. In the sample of Lyα lines for LB 9605, LB 9612, there are no coincidences within this velocity difference, implying an upper limit on the inferred radius for redshifts $1.1 < z < 1.7$. With the addition of this new point in Figure 6.8, the trend of radius versus separation is less significant. The upper limit derived in this chapter argues against there being a population of large clouds at high redshift. The lack of a population of large clouds is an apparent contradiction with
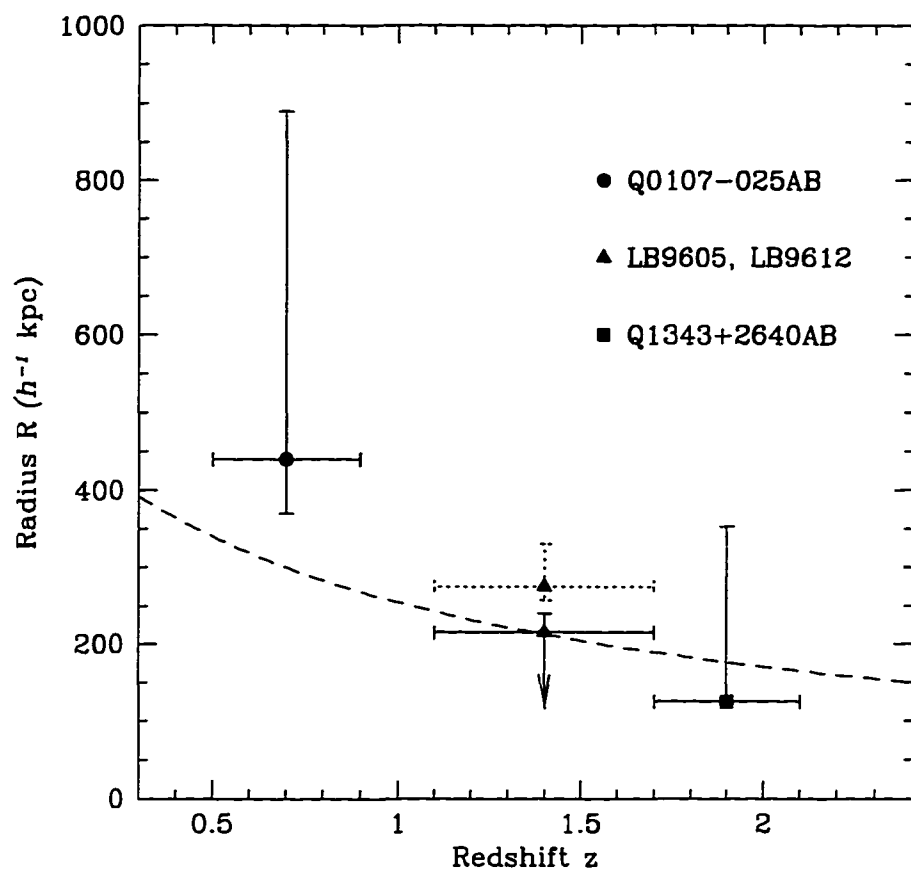
FIGURE 6.7—Estimates of the cloud radius in three redshift intervals. The dotted error bars give the limits on the clouds radius for two coincidences and 26 anticoincidences (*i.e.*, having corrected the 5 observed coincidences for 3 random coincidences [cf. § 6.4]). The dashed line represents a freely expanding Hubble sphere with arbitrary normalization.

the estimates based on the group Q1623+2651A,B and Q1623+2653. More data of this group and other high-redshift widely-separated pairs are required to settle this.

Recent hydrodynamical simulations with hierarchical clustering are able to reproduce the essential properties (*e.g.*, distributions of column density and Doppler parameter) of the Lyα forest. In these simulations, the low column density clouds arise in sheet-like or filamentary structures with coherence lengths consistent with those estimated from quasar pairs (Cen *et al.* 1994, Hernquist *et al.* 1996, Miralde-Escudé *et al.* 1996). To date, the simulations have not been evolved below $z = 2$, so it is difficult to interpret the apparent evolutionary growth of the Lyα absorbers in terms of those models. However, since gravity has the effect of amplifying initial anisotropies, the correlation or coherence lengths of these anisotropies may be expected to grow in size as gravitational clustering evolves (Pauls & Melott 1995). Moreover, the simulations show that many of the low column density Lyα lines are produced in regions of low overdensity ($\rho/\bar{\rho} \sim 1 - 10$), that are not in dynamical equilibrium, and those low-column density absorbers are still expanding with residual Hubble flow (Hernquist *et al.* 1996). Pancake-like structures are expected to be expanding about 30% faster than the Hubble flow (Haehnelt 1996). Superimposed on Figure 6.7 is the expected evolution of the cloud radius for a freely expanding Hubble sphere, $R \propto (1 + z)^{-1}$. The observed evolution in cloud radius is well-represented by free Hubble expansion at redshifts $z < 2$, though better limits are needed in order to constrain the evolutionary character of the Lyα cloud sizes.

Some of the growth in cloud radius may also be related to the decline in the UV background. The space density of quasars and the star formation rates peak at redshifts $z > 2$, and falls off at lower redshifts. Impey *et al.* (1996) have suggested that the transition in the absorber number density evolution (from rapid evolution at $z \gtrsim 2$ to a flattening of dN/dz at low redshifts) could be related to the drop in the background UV flux causing the clouds to become more neutral. Thus, a fixed column density (corresponding to the rest equivalent width detection limit) would be measured at a larger impact parameter.
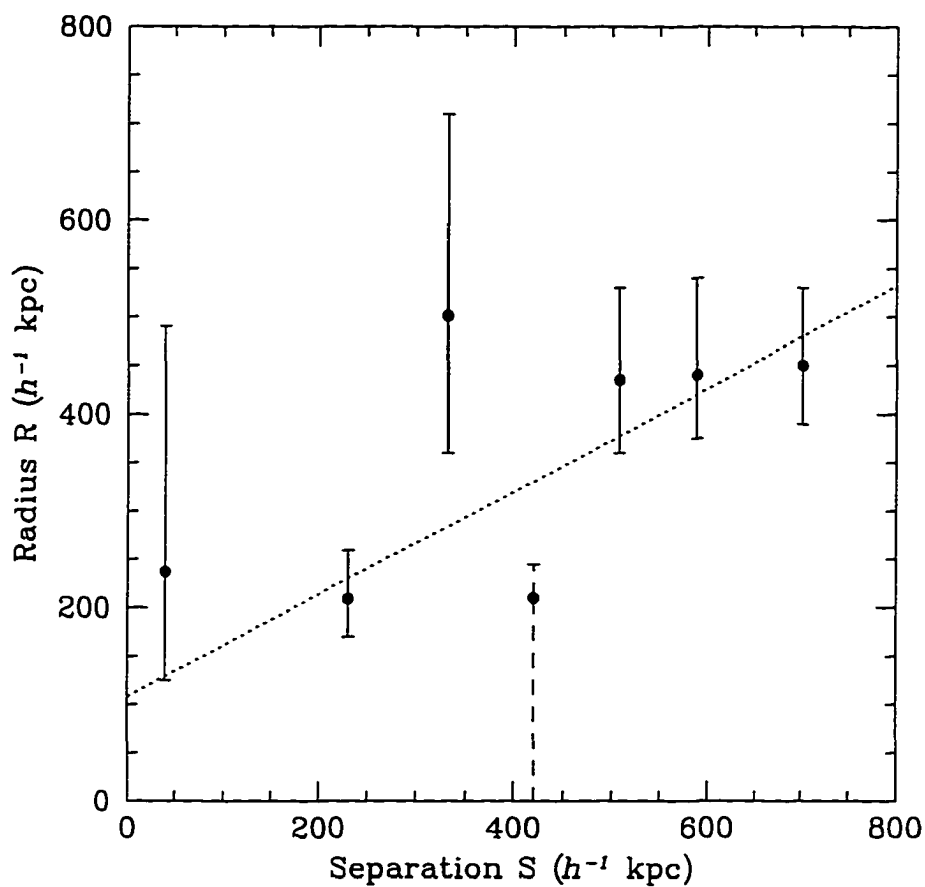
FIGURE 6.8—Inferred radius as a function of pair separation reproduced from Fang *et al.*
(1996; Figure 5). The dotted line indicates the least-squares fit to the six quasar pairs
considered in that paper. The 1σ upper limit derived in this chapter from the LB 9605,
LB 9612 pair is indicated with the dashed error bar.

The apparent increase in the radius therefore does not necessarily correspond to a physical growth, but may result from an increase in the neutral hydrogen fraction of the clouds. The combination of a net increase in the size of the clouds with a change in the ionization level may explain the leveling off of the number density of Lyα systems at low redshift.

In summary, we have presented FOS G270H spectra of the quasar pair, LB 9605 and LB 9612 in order to measure the sizes of the Lyα clouds. The quasars are separated by $1\rlap.''65$ corresponding to a linear separation of $412\,h^{-1}$ kpc at $z = 1.83$. We detected five coincident absorption lines within a velocity difference of 400 km s^{-1} in the redshift range $1.1 < z < 1.7$, and 20 anticoincidences. The significance of the observed coincidences is less than 2σ. On this basis, we argued that none of the observed coincidences are likely real, and we placed an upper limit on the cloud radii of $280\,h^{-1}$ kpc assuming spherical absorbers. Together with estimates at $z \simeq 0.7$ and 2.1, this suggests evolutionary growth in the radius of the Lyα clouds with cosmic time. However, we could not exclude the possibility that all the observed coincidences are real, from which we obtained a characteristic radius of $380\,h^{-1}$ kpc with 95% confidence that it lies in the range $305 < R < 590\,h^{-1}$ kpc. Observations of more pairs, particularly at redshifts $z > 2$, will be required to confirm the apparent evolution in cloud radius presented here. The analysis will be difficult due to the problems of blending and metal-line contamination, and will likely require the development of new statistical techniques.

TABLE 6.1

PROGRAM QSOs

QSO	R.A. (J2000)	Decl. (J2000)	V	z_{em}
LB 9605.....	$15^h 19^m 13^s.4$	$23° 46' 57''.4$	18.4	1.834
LB 9612.....	15 19 19.4	23 46 03.3	16.4	1.898

TABLE 6.2

Absorption Lines of LB 9605

No.	λ_{obs} (Å)	σ_λ (Å)	W_{obs} (Å)	σ_W (Å)	S/N	FWHM (Å)	ID	z_{abs}	Remarks
1	2275.27	0.42	1.32	0.30	4.5	4.13	Lyα	0.8716	
2	2279.95	0.25	1.12	0.25	4.4	2.59	Lyα	0.8755	
3	2344.46	0.10	0.72	0.10	6.9	2.00	Fe II 2344	0.0001	b
4	2356.01	0.10	0.89	0.12	7.8	1.61	Lyα	0.9380	
5	2362.61	0.15	1.47	0.15	9.8	3.02	Lyα	0.9435	
6	2375.35	0.22	1.39	0.17	8.2	3.75	Fe II 2374	0.0004	
7	2383.08	0.21	1.37	0.16	8.5	3.68	Fe II 2382	0.0001	
8	2388.41	0.11	0.80	0.11	7.5	1.67	Lyα	0.9647	
9	2393.13	0.11	1.63	0.13	12.5	2.94	Lyϵ	1.5518	
10	2397.94	0.13	0.73	0.11	6.9	1.87	Lyθ	1.5976	
11	2405.58	0.10	1.15	0.11	10.5	2.30	Lyη	1.5972	c
12	2417.43	0.12	1.06	0.11	9.3	2.38	Lyα	0.9886	
13	2424.10	0.13	0.97	0.11	8.8	2.27	Lyδ	1.5524	
14	2435.76	0.09	1.25	0.12	10.4	1.97	Lyϵ	1.5973	
15	2446.85	0.13	1.94	0.15	13.2	3.57	Lyα	1.0128	
16	2452.77	0.08	1.61	0.11	14.2	2.56	Lyα	1.0176	
17	2466.79	0.06	2.87	0.11	25.0	3.41	Lyδ	1.5973	d
18	2481.34	0.14	0.79	0.10	7.6	2.21	Lyγ	1.5514	
19	2492.46	0.21	0.57	0.13	4.6	1.99	Lyβ	1.4300	
20	2526.01	0.07	1.48	0.11	13.9	2.28	Lyγ	1.5973	
21	2530.66	0.07	2.66	0.12	21.5	3.48	Lyα	1.0817	
22	2559.90	0.10	0.66	0.08	8.0	1.66	Lyα	1.1058	e
23	2579.10	0.14	1.31	0.11	11.5	3.25	Lyβ	1.5144	
24	2586.06	0.14	0.66	0.09	7.3	2.11	Fe II 2586	-0.0002	
25	2594.79	0.21	0.52	0.10	5.5	2.33	Lyα	1.1345	a
26	2600.21	0.09	1.06	0.09	11.9	2.32	Fe II 2600	0.0000	
	2600.21	0.09	1.06	0.09	11.9	2.32	Lyη	1.8064	f
27	2609.53	0.12	0.84	0.11	7.8	2.05	Lyγ	1.6832	
28	2612.06	0.21	0.74	0.10	7.5	1.95	Lyζ	1.8064	f
29	2614.96	0.28	0.71	0.17	4.1	2.91	Lyα	1.1510	
30	2618.86	0.14	1.19	0.12	10.2	3.19	Lyβ	1.5532	
31	2632.13	0.15	1.15	0.11	10.3	3.26	Lyϵ	1.8067	f,g
32	2635.80	0.21	0.51	0.13	4.0	2.26	Lyγ	1.7102	h
33	2638.37	0.15	0.57	0.10	5.9	1.95	Lyα	1.1703	
34	2664.37	0.16	2.41	0.36	6.7	2.70	Lyβ	1.5976	
	2664.37	0.16	2.41	0.36	6.7	2.70	Lyδ	1.8054	f,i
35	2667.18	0.20	1.31	0.24	5.5	2.61	Lyβ	1.6003	j
36	2672.86	0.39	0.54	0.14	3.9	3.34	Lyγ	1.7483	k,l
37	2681.16	0.18	1.61	0.13	12.7	4.87	Lyα	1.2055	
38	2687.44	0.19	0.68	0.10	6.7	2.69	Lyα	1.2107	
39	2693.99	0.14	1.85	0.16	11.5	3.68	Lyβ	1.6264	
40	2698.18	0.22	0.73	0.15	4.8	2.69	Lyα	1.2195	
41	2701.91	0.18	0.62	0.09	7.1	2.59	Lyδ	1.8449	m
42	2729.43	0.06	1.27	0.07	17.7	2.16	Lyγ	1.8065	f
43	2752.08	0.12	1.51	0.16	9.3	2.72	Lyβ	1.6831	n
44	2755.63	0.27	0.88	0.17	5.2	3.14	Lyβ	1.6865	o
45	2767.14	0.13	1.15	0.09	12.7	3.42	Lyγ	1.8453	m
46	2772.47	0.08	0.79	0.07	12.0	1.92	Lyβ	1.7029	p

TABLE 6.2—*Continued*

No.	λ_{obs} (Å)	σ_λ (Å)	W_{obs} (Å)	σ_W (Å)	S/N	FWHM (Å)	ID	z_{abs}	Remarks
47	2782.95	0.29	0.70	0.10	6.7	4.01	Lyβ	1.7132	h
48	2788.92	0.20	0.59	0.09	6.8	2.84	Lyβ	1.7190	q
49	2796.36	0.26	0.84	0.06	13.1	2.03	Mg II 2796	0.0000	
50	2799.23	0.06	2.22	0.11	20.6	3.12	Lyβ	1.7290	r
51	2803.65	0.06	1.50	0.08	18.6	2.50	Mg II 2803	0.0000	
	2803.65	0.06	1.50	0.08	18.6	2.50	Lyβ	1.7333	y
52	2811.51	0.10	0.52	0.06	8.3	1.63	Lyβ	1.7410	j,t
53	2819.07	0.13	0.58	0.07	7.9	2.16	Lyβ	1.7484	k
54	2823.55	0.21	0.44	0.08	5.5	2.33	Lyβ	1.7527	u
55	2845.18	0.27	0.34	0.09	3.9	2.21	Lyβ	1.7738	
56	2852.58	0.22	0.34	0.06	5.5	2.00	Mg I 2853	-0.0001	
57	2862.39	0.14	0.52	0.07	7.1	1.97	Lyβ	1.7906	v
58	2878.56	0.05	1.85	0.07	25.7	2.62	Lyβ	1.8064	f
59	2895.67	0.12	0.70	0.07	9.5	2.42	Lyβ	1.8231	w
60	2917.89	0.07	0.98	0.06	15.6	2.23	Lyβ	1.8447	m
61	2925.43	0.08	1.23	0.07	17.3	2.90	Lyα	1.4064	
62	2932.63	0.16	0.44	0.07	6.6	2.21	Lyα	1.4124	a
63	2937.05	0.18	0.45	0.07	6.3	2.34	Lyα	1.4160	a
64	2954.03	0.05	1.13	0.06	18.1	2.01	Lyα	1.4300	
65	2965.15	0.13	0.98	0.12	8.0	2.65	Lyα	1.4391	
66	2979.51	0.21	0.27	0.07	3.8	1.60	Lyα	1.4509	a
67	2990.06	0.20	0.28	0.07	3.9	1.62	Lyα	1.4596	a
68	3001.71	0.42	0.88	0.14	6.3	5.60	Lyα	1.4692	
69	3056.80	0.05	1.33	0.07	18.7	2.16	Lyα	1.5145	
70	3078.44	0.19	0.49	0.09	5.7	2.29	Lyα	1.5323	
71	3094.48	0.11	0.51	0.07	7.2	1.63	Lyα	1.5455	
72	3103.38	0.07	2.52	0.10	24.9	3.88	Lyα	1.5528	
73	3141.14	0.11	2.52	0.16	15.5	3.97	Lyα	1.5839	
74	3145.52	0.28	0.65	0.15	4.2	2.83	Lyα	1.5875	
75	3157.56	0.06	3.13	0.14	23.1	3.32	Lyα	1.5974	
76	3161.10	0.14	0.83	0.14	5.8	2.28	Lyα	1.6003	
77	3165.15	0.12	1.08	0.13	8.6	2.30	Lyα	1.6036	
78	3168.41	0.18	0.93	0.14	6.7	2.69	Lyα	1.6063	
79	3193.10	0.10	1.68	0.10	17.4	3.46	Lyα	1.6267	
80	3211.63	0.22	0.38	0.09	4.3	1.92	Lyα	1.6419	
81	3217.55	0.15	0.58	0.09	6.5	1.99	Lyα	1.6467	
82	3261.73	0.06	1.86	0.09	20.9	2.57	Lyα	1.6831	x
83	3266.95	0.09	1.33	0.10	13.1	2.50	Lyα	1.6874	x

NOTES TO TABLE 6.2

a. Possibly spurious.

b. Possible blend with $Ly\zeta$ of system $z \simeq 1.5528$.

c. $Ly\eta$ is too strong with respect to other lines in this system and is almost certainly a blend.

d. Possible blend with $Ly\beta$ of system $z \simeq 1.4062$.

e. System may contain absorption from heavy elements.

f. Corresponding $Ly\alpha$ identified as system $z \simeq 1.8078$ in E95.

g. Possible blend with $Ly\beta$ of system $z \simeq 1.6865$.

h. Corresponding $Ly\alpha$ identified as system $z \simeq 1.7183$ in E95.

i. $Ly\delta$ is too strong with respect to other lines in this system and is almost certainly a blend.

j. Possible blend with $Ly\gamma$ of $z \simeq 1.7411$.

k. Corresponding $Ly\alpha$ identified as system $z \simeq 1.7522$ in E95.

l. Possible blend with $Ly\beta$ of systems $z \simeq 1.6062$ and 1.6034.

m. Corresponding $Ly\alpha$ identified as system $z \simeq 1.8465$ in E95.

n. Corresponding $Ly\alpha$ identified as system $z \simeq 1.6908$ in E95.

o. Corresponding $Ly\alpha$ identified as system $z \simeq 1.6956$ in E95.

p. Corresponding $Ly\alpha$ identified as system $z \simeq 1.7097$ in E95.

q. Corresponding $Ly\alpha$ identified as system $z \simeq 1.7245$ in E95.

r. Corresponding $Ly\alpha$ identified as system $z \simeq 1.7334$ in E95. $Ly\beta$ is stronger than $Ly\alpha$ and is possibly a blend.

s. Possibly $Ly\beta$.

t. Corresponding $Ly\alpha$ identified as system $z \simeq 1.7447$ in E95.

u. Corresponding $Ly\alpha$ identified as system $z \simeq 1.7567$ in E95.

v. Corresponding $Ly\alpha$ identified as system $z \simeq 1.7942$ in E95.

w. Corresponding $Ly\alpha$ identified as system $z \simeq 1.8241$ in E95.

x. Uncertain identification. Possibly C IV $\lambda\lambda$ 1548, 1550 at $z \simeq 1.1068$. C II $\lambda1334$ is possibly blended with $Ly\beta$ of system $z \simeq 1.7411$.

y. Corresponding $Ly\alpha$ identified as system $z \simeq 1.7366$ in E95.

z. Corresponding $Ly\alpha$ identified as system $z \simeq 1.7768$ in E95.

TABLE 6.3
ABSORPTION LINES OF LB 9612

No.	λ_{obs} (Å)	σ_λ (Å)	W_{obs} (Å)	σ_W (Å)	S/N	FWHM (Å)	ID	z_{abs}	Remarks
1	2248.79	0.25	1.65	0.44	3.7	2.06	Lyα	0.8498	b
2	2345.39	0.26	1.55	0.44	3.5	2.02	Fe II 2344	0.0006	b
3	2360.84	0.29	2.90	0.55	5.3	3.26	Lyα	0.9420	b
4	2382.91	0.28	1.44	0.29	4.9	2.00	Fe II 2382	0.0001	b
5	2497.47	0.26	0.79	0.22	3.6	1.92	Lyα	1.0544	b
6	2506.26	0.10	1.20	0.14	8.8	1.90	Lyα	1.0616	
7	2516.39	0.14	0.71	0.12	5.8	1.67	Lyθ	1.7259	c
8	2524.79	0.17	1.08	0.15	7.4	2.54	Lyη	1.7259	c
9	2537.26	0.13	1.18	0.14	8.7	2.45	Lyζ	1.7260	c
10	2556.22	0.10	1.12	0.12	9.6	1.98	Lyϵ	1.7258	c
11	2568.97	0.19	0.76	0.14	5.6	2.27	Lyβ	1.5045	
12	2586.74	0.21	1.04	0.22	4.8	2.25	Fe II 2586	0.0000	
	2586.74	0.21	1.04	0.22	4.8	2.25	Lyβ	1.5219	
13	2588.93	0.12	1.22	0.17	7.2	2.00	Lyδ	1.7259	c
14	2600.63	0.14	0.85	0.12	7.0	2.09	Fe II 2600	0.0002	
	2600.63	0.14	0.85	0.12	7.0	2.09	Lyβ	1.5354	
15	2614.96	0.20	0.57	0.12	4.7	1.99	Lyα	1.1510	
16	2620.82	0.09	1.23	0.11	11.0	2.09	Lyβ	1.5551	
17	2627.06	0.10	1.33	0.12	11.4	2.28	Lyϵ	1.8013	d,e,f
18	2633.74	0.11	1.22	0.12	10.2	2.41	Lyα	1.1665	g
19	2650.89	0.09	1.42	0.11	12.9	2.44	Lyγ	1.7257	c
20	2656.57	0.16	0.89	0.12	7.6	2.60	Lyα	1.1853	
21	2660.07	0.12	0.90	0.12	7.8	2.06	Lyδ	1.8008	e
	2660.07	0.12	0.90	0.12	7.8	2.06	Lyι	1.8884	h
22	2662.88	0.35	0.62	0.09	6.7	2.00	Lyα	1.1905	
23	2665.54	0.16	0.87	0.13	6.5	2.31	Lyβ	1.5987	h
	2665.54	0.16	0.87	0.13	6.5	2.31	Lyθ	1.8874	h
24	2675.51	0.07	2.03	0.10	20.4	3.00	Lyη	1.8886	h,i
25	2687.63	0.29	1.94	0.32	6.0	3.75	Lyζ	1.8876	h,j,k
26	2691.49	0.32	1.21	0.24	5.0	3.14	Lyβ	1.6240	
27	2695.65	0.14	0.88	0.12	7.5	2.19	Lyα	1.2174	
28	2708.16	0.09	1.13	0.09	12.8	2.35	Lyϵ	1.8878	h
29	2718.35	0.24	1.27	0.18	7.2	3.74	Lyβ	1.6502	l
30	2721.50	0.35	0.36	0.09	4.1	1.98	Lyα	1.2387	
31	2724.54	0.09	1.17	0.10	11.6	2.36	Lyγ	1.8015	e
32	2742.97	0.05	1.35	0.08	17.8	2.02	Lyδ	1.8881	h
33	2771.91	0.14	1.31	0.11	11.8	3.44	Lyβ	1.7024	m
34	2779.01	0.18	0.73	0.10	7.2	2.63	Lyβ	1.7093	g
35	2784.01	0.40	0.53	0.09	6.7	1.77	Lyβ	1.7142	o
36	2786.85	0.13	0.88	0.11	8.1	2.30	Lyβ	1.7170	o
37	2795.97	0.08	1.99	0.14	14.0	2.60	Mg II 2796	-0.0001	
	2795.97	0.08	1.99	0.14	14.0	2.60	Lyβ	1.7259	c
38	2803.34	0.11	1.45	0.11	13.0	3.18	Mg II 2803	-0.0001	
39	2808.80	0.06	1.70	0.09	18.8	2.56	Lyγ	1.8881	h
40	2821.65	0.17	0.60	0.09	6.5	2.27	Lyα	1.3211	n
41	2832.22	0.15	0.96	0.10	9.5	2.89	Lyβ	1.7611	p
42	2853.32	0.27	0.53	0.10	5.2	2.83	Mg I 2853	0.0001	
43	2872.94	0.09	1.14	0.09	12.0	2.24	Lyβ	1.8009	e

TABLE 6.3—*Continued*

No.	λ_{obs} (Å)	σ_λ (Å)	W_{obs} (Å)	σ_W (Å)	S/N	FWHM (Å)	ID	z_{abs}	Remarks
44	2890.85	0.31	0.66	0.13	5.1	3.31	Lyα	1.3780	a,n
45	2900.41	0.25	0.41	0.09	4.4	2.28	Lyα	1.3859	a,n
46	2907.30	0.18	0.53	0.09	5.8	2.12	Lyα	1.3915	a,n
47	2931.07	0.21	0.80	0.12	6.9	3.14	Lyα	1.4111	n
48	2936.17	0.04	2.96	0.10	29.9	3.23	Lyα	1.4153	q,r
49	2947.00	0.19	0.79	0.12	6.4	2.69	Lyα	1.4242	n
50	2951.34	0.05	3.30	0.12	26.7	3.65	Lyα	1.4277	s
51	2961.71	0.05	2.74	0.10	28.8	3.53	Lyβ	1.8874	h,t
52	2967.00	0.06	1.17	0.08	15.6	2.09	Lyα	1.4406	t
53	2978.99	0.08	1.34	0.08	16.2	2.58	Lyα	1.4505	u
54	3002.70	0.28	0.45	0.09	4.9	2.81	Lyα	1.4700	a
55	3027.40	0.26	0.43	0.10	4.2	2.38	Lyα	1.4903	a
56	3065.72	0.31	1.34	0.16	8.5	5.52	Lyα	1.5218	
57	3083.91	0.22	0.95	0.12	7.9	3.57	Lyα	1.5368	
58	3105.99	0.06	2.57	0.10	25.8	3.43	Lyα	1.5550	
59	3158.49	0.09	0.76	0.10	7.8	1.63	Lyα	1.5981	
60	3183.78	0.12	0.85	0.10	8.7	2.07	Lyα	1.6190	
61	3190.15	0.16	1.58	0.14	11.6	3.81	Lyα	1.6242	
62	3195.78	0.17	0.51	0.10	5.3	1.87	Lyα	1.6288	a
63	3199.24	0.13	0.59	0.09	6.4	1.71	Lyα	1.6317	
64	3222.16	0.14	1.44	0.12	12.0	3.41	Lyα	1.6505	l
65	3264.40	0.32	1.05	0.16	6.7	4.34	Lyα	1.6853	v

NOTES TO TABLE 6.3

a. Possibly spurious.

b. Wavelength is highly uncertain since it lies in the Lyman limit.

c. Corresponding Lyα identified as system $z \simeq 1.7300$ in E95. The lines are associated with the LLS at $z_{LLS} = 1.7259$.

d. Components are too strong with respect to other lines in this system and are almost certainly blends.

e. Corresponding Lyα identified as system $z \simeq 1.8028$ in E95.

f. Possible blend with Lyγ of $z \simeq 1.7022$.

g. Possible blend with Lyγ of $z \simeq 1.7153$.

h. Corresponding Lyα identified as system $z \simeq 1.8897$ in E95.

i. Lyη is too strong with respect to other lines in this system and is almost certainly a blend.

j. Possible blend with Lyβ of $z \simeq 1.6190$.

k. Possible blend with Lyγ of $z \simeq 1.7612$.

l. Corresponding Lyα identified as system $z \simeq 1.6610$ in E95.

m. Corresponding Lyα identified as system $z \simeq 1.7093$ in E95.

n. Possibly Lyβ.

o. Corresponding Lyα identified as one system at $z \simeq 1.7210$ in E95, but is clearly a blend of two systems.

p. Corresponding Lyα identified as system $z \simeq 1.7628$ in E95.

q. Corresponding C IV doublet identified as $z \simeq 1.4146$ in E95.

r. System contains absorption from heavy elements.

s. Almost certainly not Lyβ with $z \simeq 1.8773$ since it would have been observed in E95.

t. Uncertain identification. Possibly C IV $\lambda\lambda$ 1548, 1550 at $z \simeq 0.9131$. No other lines associated with this system are detected, but Lyα would lie in the Lyman limit.

u. Possibly Lyβ corresponding to Lyα system at $z \simeq 1.9006$ in E95.

v. Corresponding Lyα identified as system $z \simeq 1.6921$ in E95.

w. Corresponding Lyα identified as system $z \simeq 1.7732$ in E95.

TABLE 6.4
Coincident and Anticoincident Lyman-Alpha Absorption Lines

			LB9605							LB9612				LB9605–LB9612
No.	λ(Å)	σ_λ(Å)	W_0(Å)	σ_W(Å)	S/N	z_{abs}	No.	λ(Å)	σ_λ(Å)	W_0(Å)	σ_W(Å)	S/N	z_{abs}	Δv(km s⁻¹)
			< 0.28				1	2506.04	0.10	0.58	0.07	8.8	1.0614	
1	2530.66	0.07	1.28	0.06	21.5	1.0817				< 0.32				
			< 0.19				2	2633.51	0.11	0.56	0.06	10.2	1.1663	
			< 0.19				3	2656.34	0.16	0.41	0.05	7.6	1.1851	
2	2681.16	0.18	0.73	0.06	12.7	1.2055				< 0.22				
			< 0.18				4	2695.42	0.14	0.40	0.05	7.5	1.2172	
3	2925.43	0.08	0.51	0.03	17.3	1.4064				< 0.19				
			< 0.14				5	2930.82	0.21	0.33	0.05	6.9	1.4109	
			< 0.14				6	2946.74	0.19	0.33	0.05	6.4	1.4240	
4	2954.03	0.05	0.47	0.02	18.1	1.4300	7	2951.08	0.05	1.36	0.05	6.7	1.4275	300 ± 4
5	2965.15	0.13	0.40	0.05	8.0	1.4391	8	2966.74[a]	0.06	0.48	0.03	15.6	1.4404	−161 ± 7
			< 0.16				9	2978.73[b]	0.08	0.55	0.03	16.2	1.4503	
6	3001.71	0.42	0.36	0.06	6.3	1.4692				< 0.16				
7	3056.80	0.05	0.53	0.03	18.7	1.5145				< 0.19				
			< 0.16				10	3065.45	0.31	0.53	0.06	8.5	1.5216	
			< 0.16				11	3083.64	0.22	0.37	0.05	7.9	1.5366	
8	3103.38	0.07	0.99	0.04	24.9	1.5528	12	3105.66	0.06	1.01	0.04	25.8	1.5547	−220 ± 4
9	3141.14	0.11	0.98	0.06	15.5	1.5839				< 0.19				
10	3157.56	0.06	1.21	0.05	23.1	1.5974				< 0.17				
11	3165.15	0.12	0.41	0.05	8.6	1.6036				< 0.19				
12	3168.41	0.18	0.36	0.05	6.7	1.6063				< 0.20				
13	3193.10	0.10	0.64	0.04	17.4	1.6267	13	3189.92	0.16	0.60	0.05	11.6	1.6240	298 ± 9
			< 0.15				14	3221.88	0.14	0.54	0.05	12.0	1.6503	
14	3261.73[c]	0.06	0.69	0.03	20.9	1.6831	15	3264.12	0.32	0.39	0.06	6.7	1.6850	−220 ± 15
15	3266.95[c]	0.09	0.49	0.04	13.1	1.6874				< 0.20				

NOTE. This table lists those lines with rest equivalent widths $W_0 > 0.32$ Å. Upper equivalent width limits are 5σ confidence level. (a) Possibly C IV $\lambda1550$ with redshift $z_{abs} = 0.91$. The C IV $\lambda1548$ component associated with this possible system has been identified as Lyβ belonging to the certain system at $z_{abs} \simeq 1.8875$ in Table 3. (b) Possibly Lyβ. (c) Possibly member of C IV doublet with redshift $z_{abs} = 1.11$.

CHAPTER 7

FUTURE WORK

In Chapter 2, we reported the detection of a marginally significant clustering signal on scales of $< 18\,h^{-1}$ Mpc based on 16 C IV absorbers distributed among 4 lines of sight toward the Tololo Group. In order to provide greater sensitivity to clustering (by increasing the number of C IV absorbers detected), a larger grid of background QSOs is required. Multifiber spectrographs offer the most efficient means of sampling many QSOs (~ 40 in a 2 deg^2 field) simultaneously with sufficient resolution and S/N to be sensitive to C IV absorption. Estimating the mean expected number of C IV systems in each of the lines of sight to be $n_{\mathrm{exp}} = 3$, the total number of line pairs in the spatial correlation function increases to $n_{\mathrm{pairs}} \sim 7000$, resulting in an *order of magnitude* improvement in the sensitivity of the correlation function to clustering. In addition to the Tololo field, measurements of the galaxy correlation function on scales of $10 - 50\,h^{-1}$ Mpc can be made in the directions of a number of promising fields identified by Romani *et al.* (1991).

The intervening supercluster hypothesis has been widely used to explain the overdensity of C IV absorption systems toward the pair Tol 1037−2704 and Tol 1038−2712; however, this theory is not universally accepted (Christiani *et al.* 1987; Robertson 1987). In particular, Tol 1037−2704 and Tol 1038−2712 both display broad absorption line (BAL) characteristics, which are generally thought to have an intrinsic origin. Spectroscopic work has so far not been able to distinguish between these two possibilities. Direct IR

imaging of the field will help identify the absorbers responsible for the C IV absorption. The observations require imaging in one optical passband (*e.g.*, *R*) and in the *K* band, since colors redder than $R - K \gtrsim 4.5$ are indicative of high redshift galaxies. Followup multiband imaging of identified clusters can provide information on cluster morphology and member galaxy colors to compare with simulations (Evrard & Charlot 1994) and clusters discovered by other means at $z > 1$.

As we have seen in the previous chapters, new measurements of the tranverse dimensions of the Lyα absorbers, recent supercomputer simulations and other studies aimed at understanding the nature of the Lyα absorbers have dramatically changed our perception of their origin and physical characteristics. They have also raised new questions: What are the clustering properties and geometry (*e.g.*, spherical, disk-like, filamentary) of the Lyα aborbers? In particular, is there a difference in the clustering and geometry between the high and low column density clouds? Do the radii of the clouds evolve with time? What is the relationship between the Lyα absorbers and galaxies and/or clusters of galaxies?

Future HST observations in Cycle 5 and Cycle 6 are being obtained to address some of these questions. Fortuitously, here is a *third* bright QSO lying a few arcminutes from Q0107$-$025A,B. The existence of this QSO offers the unique opportunity to probe distance scales out to 1 Mpc and provide additional clues as to the topology of the clouds at $z < 1$. Observations to improve the S/N of the FOS data presented in Chapters 5 and 6 are also being obtained to raise the confidence level of many of the weak lines, so that we can address the question of whether the low column density systems share the same properties as the high column density systems.

In addition to the FOS observations, parallel WFPC2 observations of one of the QSO fields targeted for spectroscopy are being obtained in Cycle 5. The WFPC2 will be used to take deep images in two filters, and will find galaxies with projected distances of $0.5 - 1.5\,h^{-1}$ Mpc from the QSO lines of sight. A ground-based program at Palomar

is locating galaxies in a 8 × 10 arcmins field centered on the same group (Chapter 5). Redshifts are being obtained down to $V = 21$, and have already led to the discovery of two clusters along the line of sight at $z = 0.20$ and $z = 0.23$. From the parallel WFPC2 exposures, galaxy colors and morphologies will be measured down to $V = 23.5$, ten times fainter than the Palomar survey and down to the limit of plausible galaxy spectroscopy. The result will be a new way to address the relationship between the Lyα absorbers and the large scale structure of normal galaxies.

In Chapter 6, we presented marginally significant evidence for evolution of the Lyα absorbers. Further ground-based observations of pairs and groups of QSOs are need to provide a firm upper limit on the sizes of the clouds. At redshifts $z > 1.7$, where Lyα absorption is observable from the ground, high resolution spectroscopy is essential because of the high density of lines and significant level of blending. There are few candidate pairs where both QSOs are bright, and have similar enough redshifts to avoid confusion with higher order Lyman series lines. However, the number of appropriate pairs grows if one is able to go to fainter magnitudes ($V > 18$). Therefore these kinds of observations will require the light-collecting power of latest generation of large telescopes. The field will continue to benefit from further observations of QSO pairs and groups with angular separations of < 1 to 10 arcmins, in order to probe cloud sizes ranging from tens of kpc to Mpc scales. Already, a number of suitable QSO groups have been identified in the Large Bright QSO Survey (Foltz et al. 1987), and new high-redshift pairs and groups will almost certainly be discovered in new surveys for QSOs. The observations will further constrain the Lyα cloud sizes at the critical redshifts ($z > 1.7$) needed to either confirm or refute the apparent evolution in the radius of the Lyα clouds.

The observations of closely spaced QSOs offer an unique opportunity to study the large scale distribution of the absorbers and to map their topology in three dimensions. For this purpose, the clustering properties of the absorbers should be examined not only along the lines of sight to the QSOs, but also in the transverse direction. If the high column density

systems originate in galaxies which are strongly correlated with each other, and the rest arise in physically diverse structures such as filaments of warm gas and sheets of cool gas confined between shocks, then it should be possible to distinguish between the origins by testing whether they share same clustering properties and physical geometry. As we saw in Chapter 5, different geometric and kinematic models give rise to specific predictions about the correlation of the equivalent widths and redshifts of the common systems along multiple lines of sight. At present however, the number of published observations of paired lines of sight are too small to distinguish between even the simplest models. Further HST data and observations from the ground are needed to improve the statistics of the common systems so that detailed diagnostics of the geometric and kinematic properties of the $Ly\alpha$ absorbers can be made.

Though encouraging progress has been made in trying to simulate the $Ly\alpha$ forest and coherent structures on scales out to 1 Mpc can be produced, few quantitative comparisons of the simulations with observations of multiple lines of sight have yet been made. New supercomputer simulations that include gas dynamics can be used to generate artificial spectra along lines of sight whose separations correspond to those of the observed QSO groups. The simulations already show a number of coincident lines between lines of sight separated by $\sim 150\,h^{-1}$ kpc, and the coincident features display significant variations in their depth and shape (Hernquist *et al.* 1996). High resolution data will be required for a detailed comparison of the shapes and equivalent widths between the observed and simulated line profiles for various line-of-sight separations. The results of the simulations, which are currently being evolved to $z = 2$, can also be compared to the observed characteristic sizes, clustering properties and topology of the $Ly\alpha$ absorbers at $z > 2$. The hydrodynamic simulations combined with data from ground-based telescopes promise to provide important constraints on the physical models of the $Ly\alpha$ absorbers.

REFERENCES

Aaronson, M., McKee, C. F., & Weisheit, J. C. 1975, ApJ, 198, 13

Aldcroft, T. 1993, Ph.D. Thesis, Stanford University

Bahcall, J. N. 1968, ApJ, 153, 679

Bahcall, J. N., Bergeron, J., Boksenberg, A., Hartig, G. F., Jannuzi, B. T., Kirhakos, S., Sargent, W. L. W., Savage, B. D., Schneider, D. P., Turnshek, D. A., Weymann, R. J., & Wolfe, A. M. 1993, ApJS, 87, 143

Bahcall, J. N., Bergeron, J., Boksenberg, A., Hartig, G. F., Jannuzi, B. T., Kirhakos, S., Sargent, W. L. W., Savage, B. D., Schneider, D. P., Turnshek, D. A., Weymann, R. J., & Wolfe, A. M. 1996, ApJ, 457, 19

Bahcall, N. A., & Soneira, R. M. 1983, ApJ, 270, 20

Bahcall, N. A., & Soneira, R. M. 1984, ApJ, 277, 27

Bahcall, N. A., & Bergett, W. S. 1986, ApJ, 300, L35

Bahcall, N. A. 1988, ARA&A, 26, 631

Baum, S. A. 1992, in Proceedings of NATO Advanced Study Institute, Clusters and Superclusters, ed. A.C. Fabian (Dordrecht, Kluwer), 171

Bergeron, J., & Boisse, P. 1991, A&A, 243, 344

Bergeron, J., & Stasinka, G. 1986, A&A, 169, 1

Bechtold, J. 1987, In *Proc. 3rd IAP Workshop, High Redshift and Primeval Galaxies*, eds. Kunth, D., Bergeron, J. & Rocca-Volmerange, B., (Gif-sur-Yvette, France, Editions Frontieres), 397

Bechtold, J. 1994, ApJS, 91, 1

Bechtold, J., & Ellingson, E. 1992, ApJ, 396, 20

Bechtold, J., Crotts, A. P. S., Duncan, R. C., Fang, Y. 1994, ApJ, 437, L83

Blackwell, J. et al. 1993, A User's Guide to the GHRS Software, Version 2.1 (Greenbelt: Goddard Space Flight Center)

Blades, J. C. 1988, in Proceedings of the QSO Absorption Line Meeting, QSO Absorption Lines: Probing the Universe, ed. J. C. Blades, D. A. Turnshek, & C. A. Norman (Cambridge, Cambridge University Press), 147

Bohuski, T. J., & Weedman, D. W. 1979, ApJ, 231, 653

Bond, J.R., Szalay, A.S., & Silk, J. 1988, ApJ, 324, 627

Bowen, D. V., Blades, J. C., & Pettini, M. 1996, ApJ, 464, 141

Broadhurst, T. J., Ellis, R. S., Koo, D. C., & Szalay, A. S. 1990, Nature, 343, 726

Carswell, R. F., Morton, D. C., Smith, M. G., Stockton, A. N., Turnshek, D. A., Weymann, R. J. 1984, ApJ, 278, 486

Cen, R., Miralda-Escudé, J., Ostriker, J. P., & Rauch, M. 1994, ApJ, 437, L9

Charlton, J. C., Churchill, C. W., & Linder, S. M. 1995, ApJ, 452, L81

Chernomordik, V. V., & Ozernoy, L. M. 1993, ApJ, 404, L5

Chernomordik, V. 1995, ApJ, 440, 431

Christiani, S., D'Odorico, S., Fontana, A., Giallongo, E., & Savaglio, S. 1995, in Proceedings of the ESO Workshop on QSO Absorption Lines, Meylan, G. (ed.), (Springer-Verlag: Heidelberg), 357

Christiani, S., Danziger, I. J., & Shaver, P. A. 1987, MNRAS, 227, 639

Cowie, L. L., Songaila, A., Kim, T.-S., & Hu, E. M. 1995, AJ, 109, 1522

Crampton D., Cowley, A. P., Hickson, P., Kindl, E., Wagner, R. W., Tyson, J. A., & Gullixson, C. 1988, ApJ, 330, 184

Crawford, C. S., Crehan, D. A., Fabian, A. C., & Johnstone, R. M. 1987, MNRAS, 224, 1007

Crotts, A. P. S. 1985, ApJ, 298, 732

Crotts, A. P. S. 1989, ApJ, 336, 550

Crotts, A. P. S., Bechtold, J., Fang, Y., & Duncan, R. C. 1994 ApJ, 437, L79

da Costa, L. N., Pellegrini, P. S., Sargent, W. L. W., Tonry, J., Davis, M., Meiksin, A., Latham, D. W., Menzies, J. W., & Coulson, I. A. 1988, ApJ, 327, 544

Davis, M., & Peebles, P. J. E. 1983, ApJ, 267, 465

de Lapparent, V., Geller, M. J., & Huchra, J. P. 1986, ApJ, 302, L1

Dinshaw, N., Impey, C. D., Foltz, C. B., Weymann, R. J., Chaffee, F. H. 1994, ApJ, 437, L87 (D94)

Dinshaw, N., Foltz, C. B., Impey, C. D., Weymann, R. J., Morris, S. L. 1995, Nature, 373, 223 (D95)

Dinshaw, N., & Impey, C. D. 1996, ApJ, 458, 73

Dinshaw, N., Foltz, C. B., Impey, C. D., & Weymann, R. J. 1996, ApJ, submitted

Dinshaw, N., Weymann, R. J., Impey, C. D., Foltz, C. B., Morris, S. L., & Ake, T., ApJ, in preparation

Elowitz, R. M., Green, R. F., & Impey, C. D. 1995, ApJ, 440, 458

Evrard, A. E., Summers, F. J., & Davis, M. 1994, ApJ, 422, 11

Fang, Y., Duncan, R. C., Crotts, A. P. S., & Bechtold, J. 1996, ApJ, 462, 77

Foltz, C.B., Weymann, R.J., Röser, H-J, and Chaffee, F.H. 1984, ApJ, 281, L1

Foltz, C. B., Weymann, R. J., Peterson, B. M., Sun, L., Malkan, M. A. & Chaffee, F. H. 1986, ApJ, 307, 504

Foltz, C. B., Weymann, R. J., Morris, S. L., & Turnshek, D. A. 1987, ApJ, 317, 450

Foltz, C. B., Hewett, P. C., Chaffee, F. H., & Hogan, C. J. 1993, AJ, 105, 22

Francis, P. J., & Hewett, P. C. 1995, AJ, in press

Geller, M. J., & Huchra, J. P. 1989, Science, 246, 897

Giovanelli, R., & Haynes, M. P. 1991, ARA&A, 29, 499

Heisler, J., Hogan, C. J., & White, S. D. M. 1989, ApJ, 347, 52 (HHW)

Gilliland. R. 1994, GHRS Instrument Science Report #063 and 1995 private communication to R. Weymann

Hernquist, L., Katz, N., Weinberg, D. H., & Miralda-Escudé, J. 1996, ApJ, 457, L51

Hu, E. M., Kim, T.-S., Cowie, L. L. 1995, AJ, 110, 1526

Horne, K. 1986, PASP, 96, 609

Ikeuchi, S., & Ostriker, J.P. 1986, ApJ, 301, 522

Impey, C.D., Petry, C.E., Malkan, M.A., & Webb, W. 1996, ApJ, in press

Jakobsen, P., Perryman, M. A. C., & Cristiani, S. 1988, ApJ, 326, 710 (J88)

Jakobsen, P., & Perryman, M. A. C. 1992, ApJ, 392, 432 (J92)

Jakobsen, P., Perryman, M. A. C., Ulrich, M. H., Macchetto, F., & Di Serego Alighieri, S. 1986, ApJ, 303, L27 (J86)

Jannuzi, B. T. 1996, In *Science with the Hubble Space Telescope – II, Space Telescope Science Institute*, eds. Benvenuti, P., Macchetto, F. D., & Schreier, E. J., in press

Kaiser, N., & Peacock, J. A. 1991, ApJ, 379, 482

Kopylov, A. I., Kuznetsov, D. Yu., Fetisova, T. S., Shvartsman, V. F. 1987, in Proc. Semin. Large Scale Structure of the Universe (Stavropol, USSR: Spec. Astrophys. Obs.), 39

Lake, G. 1988, ApJ, 327, 99

Lanzetta, K. M., Wolfe, A. M., Turnshek, D. A., Lu, L., McMahon, R. G., & Hazard, C. 1991, ApJS, 77, 1

Lanzetta, K. M., Bowen, D. V., Tytler, D., Webb, J. K. 1995, ApJ, 442, 538

Le Brun, V., Bergeron, J., Boise, P. 1996, A&A, 306, 691

Lindler, D., Bohlin, R., Hartig, G., & Keyes, C., 1993, FOS Instrument Science Report CAL/FOS-088, available from STScI

Loveday, J., Peterson, B. M., Efstathiou, G., & Maddox, S. J. 1992, ApJ, 390, 338

Lu, L., Wolfe, A. M., & Turnshek, D. A. 1991, ApJ, 434, 493

McGill, C. 1990, MNRAS, 242, 544

Meiksin, A., & Bouchet, F. R. 1995, ApJ, 448, L85

Miralda-Escudé, & Rees, M. J. 1993, MNRAS, 260, 617

Miralda-Escudé, J., Cen, R., Ostriker, J. P., & Rauch, M. 1996, ApJ, in press

Mo, H.J., & Morris, S.L. 1994, MNRAS, 269, 52

Maoz, D., & Rix, H.-W. 1993, ApJ, 416, 425

Morris, S. L., Weymann, R. J., Savage, B. D., & Gilliland, R. L. 1991, ApJ, 377, L21

Morris, S. L., Weymann, R. J., Dressler, A., McCarthy, P. J., Smith, B., Terrile, R. J., Giovanelli, R., & Irwin, M. 1993, ApJ, 419, 524

Morris, S.L., & van den Bergh, S. 1994, ApJ, 427, 696

Morton, D. C., York, D. G., & Jenkins, E. B. 1988, ApJS, 68, 449

Olivier, S. S., Primack, J. R., Blumenthal, G. R. & Dekel, A. 1993, ApJ, 408, 17

Ostriker, J. P., & Ikeuchi, S. 1983, ApJ, 268, L63

Pauls, J. L., & Melott, A. L., 1995, MNRAS, in press

Peebles, P. J. E. 1980, *The Large Scale Structure of the Universe*, (Princeton, NJ: Princeton University Press)

Petitjean, P., Mücket, J. P., & Kates, R. E. 1995, A&A, 295, L9

Postman, M., Huchra, J. P., & Geller, M. J. 1992, ApJ, 384, 404

Primack, J. R. 1995, private communication

Rauch, M., & Haehnelt, M. G. 1996, MNRAS, submitted

Rauch, M., Carswell, R. F., Webb, J. K., & Weymann, R. J. 1993, MNRAS, 260, 589

Rees, M.J. 1986, MNRAS, 218, 25

Rix, H.-W., Guhatharkurta, P., Colless, M., & Ing, K. 1996, MNRAS, submitted

Robertson, J. G. 1987, MNRAS, 227, 653

Romani, R. W., Filippenko, A. V., & Steidel, C. C. 1991, PASP, 103, 154

Sargent, W.L.W., Young, P., Boksenberg, M., & Tytler, D. 1980, ApJ, 42, 41

Sargent, W. L. W., & Steidel, C. C. 1987, ApJ, 322, 142 (S87)

Sargent, W. L. W., Boksenberg, A., & Steidel, C. C. 1988, ApJS, 68, 539 (SBS)

Schneider, D. P., Hartig, G. F., Jannuzi, B. T., Kirhakos, S., Saxe, D. H., Weymann, R. J., Bahcall, J. N., Bergeron, J., Boksenberg, A., Sargent, W. L. W., Savage, B. D. Turnshek, D. A., & Wolfe, A. M. 1993, ApJS, 87, 45

Shaver, P.A., & Robertson, J.G. 1983, ApJ, 268, L57

Smette, A., Surdej, J., Shaver, P. A., Foltz, C. B., Chaffee, F. H., Weymann, R. J., Williams, R. E., & Magain, P. 1992 ApJ, 389, 39

Smette, A., Robertson, J. G., Shaver, P. A., Reimers, D., Wisotzki, L., Köhler, Th. 1995, A&AS, 113, 199

Songalia, A., & Cowie, L. L. 1996, AJ, in press

Spitzer, L. Jr. 1978, Physical Processes in the Interstellar Medium, (John Wiley & Sons, Inc.), p. 53

Srianand, R. 1996, ApJ, 462, 68

Steidel, C. C. 1990, ApJS, 72, 1

Steidel, C. C., & Dickinson, M. 1992, ApJ, 394, 81

Steidel, C. C., & Sargent, W. L. W. 1991, AJ, 102, 1610

Steidel, C. C., & Sargent, W. L. W. 1992, ApJS, 80, 1

Steidel, C. C. 1993, in The Environment and Evolution of Galaxies, Shull, J. M., & Thronson, H. A. Jr. (eds.), (Kluwer Academic Publishers: Dordrecht), 263

Stocke, J. T., Shull, J. M., Penton, S., Donahue, M., Carilli, C., & van Gorkom, J. 1995, ApJ, 451, 24

Tifft, W.G. 1985, ApJ, 288, 65

Tytler, D., Fan, X.-M., Burles, S. Cottrel, L., Davis, C., Kirkman, D., & Zuo, L. 1995, in Proceedings of the ESO Workshop on QSO Absorption Lines, Meylan, G. (ed.), (Springer-Verlag: Heidelberg), 289

Ulmer, A. 1996, ApJ, submitted

Webb, J. K. 1987, In *Observational Cosmology, IAU Symposiumn No. 124*, eds. Hewitt, A., Burbidge, G. & Fang, L.-Z., (Reidel: Dordrecht, Holland), 803

Webb, J. K., & Barcons, X. 1991, MNRAS, 250, 270

Weymann, R. J., Carswell, R. F., & Smith, M. G. 1981, ARA&A, 19, 41

Williger, G. M., Hazard, C., Baldwin, J. A., & McMahon, R. G. 1996, ApJS, in press

Wolfe, A. M., Turnshek, D. A., Smith, H. E., & Cohen, R. D. 1986, ApJS, 61, 249

Young, P. J., Sargent, W. L. W., & Boksenberg, A. 1982, ApJ, 252, 10

Young, P. J., Sargent, W. L. W., Boksenberg, A., Carswell, R. F., & Whelan, J. A. J. 1979, ApJ, 229, 891

Zabludoff, A. I., Geller, M. J., Huchra, J. P., & Vogeley, M. S. 1993, AJ, 106, 1273

Zaritsky, D. 1994, The Local Group: Comparative and Global Properties, Third ESO/CTIO Workshop, in press

Zhang, Y., Anninos, P., & Norman, M. L. 1995, ApJ, 453, L57